PACIFIC EARTHQUAKE ENGINEERING RESEARCH CENTER

Documentation and Analysis of Field Case Histories of Seismic Compression during the 1994 Northridge, California, Earthquake

Jonathan P. Stewart
Patrick M. Smith
Daniel H. Whang
University of California, Los Angeles

and

Jonathan D. Bray
University of California, Berkeley

PEER 2002/09
OCT. 2002

Documentation and Analysis of Field Case Histories of Seismic Compression during the 1994 Northridge, California, Earthquake

Jonathan P. Stewart, Patrick M. Smith, and Daniel H. Whang
Department of Civil and Environmental Engineering
University of California, Los Angeles

Jonathan D. Bray
Department of Civil and Environmental Engineering
University of California, Berkeley

A report on research conducted under Grant No. 1434-HQ-GR-00037 from the U.S. Geological Survey, National Earthquake Hazards Reduction Program; Grant No. 9701568 from the National Science Foundation; and the Pacific Earthquake Engineering Research Center's Program of Applied Earthquake Engineering Research of Lifeline Systems

PEER Report 2002/09
Pacific Earthquake Engineering Research Center
College of Engineering
University of California, Berkeley

October 2002

ABSTRACT

USGS/NEHRP Award No. 1434-HQ-98-GR-00037

DOCUMENTATION AND ANALYSIS OF FIELD CASE HISTORIES OF SEISMIC COMPRESSION DURING THE 1994 NORTHRIDGE, CALIFORNIA EARTHQUAKE

PI: Jonathan P. Stewart
Civil & Environmental Engineering Department
University of California
Los Angeles, CA 90095-1593
Tel: (310) 206-2990 Fax: (310) 206-2222
jstewart@seas.ucla.edu

Seismic compression is defined as the accrual of contractive volumetric strains in unsaturated soil during strong shaking from earthquakes. While ground deformations from seismic compression have been reported in the literature, it contains few case histories in which the amount of ground deformation was known accurately from pre– and post–earthquake surveys. In this report, two such case histories are documented in detail and analyzed. Both case studies involve deep canyon fills in Santa Clarita, California, an area strongly shaken by the Northridge earthquake (peak accelerations on rock ≈ 0.3–0.7 g). The performance of the fills was quite different. In one case (denoted Site A) ground settlements up to ~18 cm occurred, which damaged a structure, while in the other case (Site B) settlements were < ~6 cm.

One important thrust of the present work involved cyclic simple shear laboratory testing of four reconstituted soil samples from the two subject sites. These samples all have fines contents near 50% (such that the fines fraction controls the soil behavior), but have varying levels of fines plasticity. Each specimen was compacted to a range of formation dry densities and degrees of saturation. The results significantly extend the seismic compression literature, which has consisted primarily of laboratory testing of clean uniform sands. The test results show that seismic compression susceptibility increases with decreasing density and increasing shear strain amplitude. Saturation is found to be important for soils with plastic fines but relatively unimportant for soils with nonplastic fines. Comparisons of test results for soils with and without fines suggest that for many cases, fines decrease seismic compression potential relative to clean sands. For soils with fines, it appears that seismic compression is most pronounced when the fines are nonplastic, or when the fines are plastic and the soil has a clod structure. We

observe clod structures in plastic soils compacted dry of the line of optimums or at low densities, but not in nonplastic soils.

The objectives of analyses performed for the two sites were (1) to investigate the degree to which seismic compression can explain the observed ground displacements and (2) to evaluate the sensitivity of calculated settlements to variability in input parameters as well as the dispersion of calculated settlements given the overall parametric variability. The analysis procedure that is used de-couples the calculation of shear strain from that of volumetric strain. The shear strain calculations involved one- and two-dimensional ground response analyses employing site-specific dynamic soil properties and a suite of input motions appropriate for the respective sites. Volumetric strains are evaluated from the shear strains using material-specific models derived from the simple shear laboratory test results.

Parametric variability in all significant model parameters is estimated, and the analyses are repeated according to a logic tree approach in which a weight is assigned to each possible realization of the model parameters. The analyses results provide probabilistic distributions of shear strain, volumetric strain, and settlement, the last of which can be compared to observed field settlements. Calculated ground settlements at Site B match observations between the 30th and 70th percentile levels. At Site A, the analyses successfully predict the shape of the settlement profile along a section, but the weighted average predictions are biased slightly low (match occurs at the 50th to 70th percentile level). We speculate that the underprediction likely results from imperfect knowledge of site stratigraphy and/or underestimation of volumetric strains from the laboratory tests as a result of the non-reproducibility of the field soil's clod structure.

Sensitivity studies reveal that the mean value of calculated settlements is highly sensitive to shear strain amplitude and compaction condition, while the standard deviation is mostly strongly influenced by variability in the shear strains. The median and standard deviation of shear strains, in turn, are strongly influenced by the site shear wave velocity profile, ground motion characteristics, and the method of site response analysis (i.e., 1-D versus 2-D). The various sources of parametric variability combine to form a coefficient of variation of about 0.5 to 1.0, being closer the low end of the range if 2-D analyses are performed (~0.5–0.7) and the upper end of the range if 1-D analyses are performed (~0.8–1.0).

NONTECHNICAL PROJECT SUMMARY

We investigate ground settlements at two canyon fills shaken by the Northridge, California, earthquake. The settlements are found to result from seismic compression, a process by which volumetric strain accrues in unsaturated soil during strong earthquake shaking. Insights into soil parameters affecting seismic compression are gained through a simple shear laboratory testing program involving soils from the sites. Back-analyses of site performance are able to capture the observed field settlement patterns. The analyses also provide insight into the ground motion and site parameters that significantly influence the seismic compression susceptibility of a fill section.

ACKNOWLEDGMENTS

Support for this work was provided by the U.S. Geological Survey, National Earthquake Hazards Reduction Program, Award No. 1434-HG-98-GR-00037; a CAREER grant from the National Science Foundation (NSF Award No. 9733113); the Pacific Earthquake Engineering Research Center's Program of Applied Earthquake Engineering Research of Lifeline Systems with funding from the Pacific Gas and Electric Company (PEER award number Z-19-2-133-96); and the UCLA Department of Civil & Environmental Engineering.

This work made use of Earthquake Engineering Research Centers Shared Facilities supported by the National Science Foundation under Award #EEC-9701568. The views and conclusions contained in this document are those of the authors and should not be interpreted as necessarily representing the official policies, either expressed or implied, of the U.S. Government.

The authors would like to thank the following individuals who provided materials that were of assistance in this research program: Del Yoakum of Geosoils, Jim Roberts of Jacobs Engineering, Mike Sisson, and Jerod Cascadden. We acknowledge the technical assistance to the laboratory testing program provided by Michael Riemer of the Pacific Earthquake Engineering Research Center. The supportive work of UCLA undergraduate and graduate students Trolis Niebla, Mathew Moyneur, and Annie Kwok is also acknowledged.

CONTENTS

LIST OF FIGURES

LIST OF TABLES

1 Introduction

Developments in seismic design and analysis procedures for earth structures have historically been motivated by concerns about the performance and stability of critical facilities such as earth dams and solid waste landfills. This is to be expected, given the dire consequences associated with failures of such structures. In this study, we examine compacted fills in developed hillside areas, a class of earth structure whose seismic performance has historically received relatively little attention, yet which are pervasive throughout urban centers in California and elsewhere. These fills are constructed to create level building pads, with geometric configurations often similar to the wedge or canyon fills shown in Figure 1.1. In California, the seismic performance of these earth structures has been recognized as a critical design issue. Such concerns are derived primarily from substantial economic losses to dwellings, pipelines, and other engineered improvements that can be traced to ground deformations in fill induced by the 1994 Northridge earthquake. Such deformations did not typically damage structures to the extent that life safety was threatened. However, economic losses (mostly borne by insurance carriers) were large as a result of homeowner expectations that damaged homes be returned to their pre–earthquake condition. The repair costs associated with such work typically totaled \$50,000 to \$100,000 per site, but often rose to full replacement value. Given this unsatisfactory performance, the California Seismic Safety Commission (SSC) recommended in their official Report to the Governor following the Northridge earthquake that “seismically induced deformation caused by seismic compaction of fill and underlying alluvium be considered in the design and construction of residential fills” (SSC, 1995).

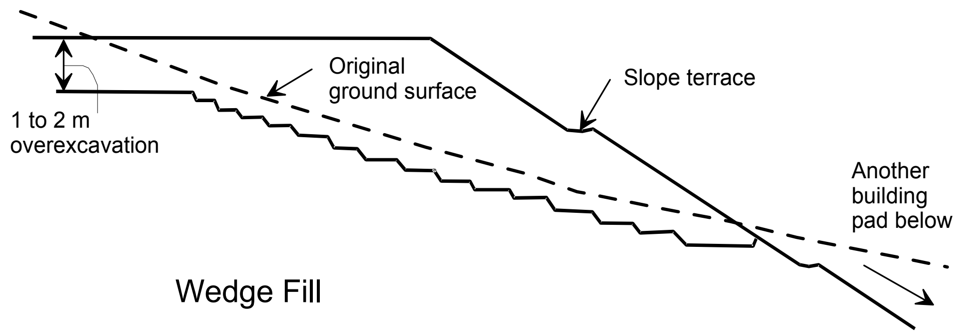

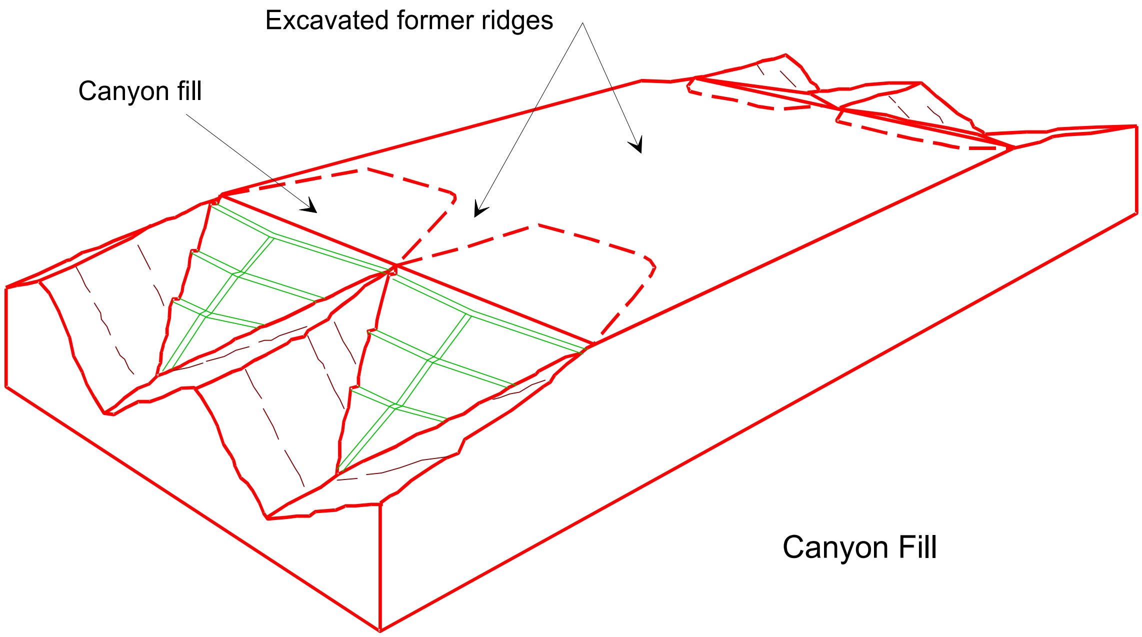

Fig. 1.1. Schematic illustration of wedge and canyon fill geometries

This report begins in Chapter 2 with a general discussion of the field performance of compacted fill soils during past earthquakes, with an emphasis on the 1994 Northridge earthquake. Common ground surface deformation patterns are identified, which can most often be attributed to volumetric strain accumulation in unsaturated, compacted fill soils — a process termed “seismic compression.” A key shortcoming of most previous field documentation studies of fill performance is the lack of pre– and post–earthquake survey measurements from which earthquake-induced ground displacements can be reliably quantified. This shortcoming provides motivation for the present study, which is focused on two sites for which displacements induced by the Northridge earthquake can be accurately estimated from survey measurements.

The work on these case histories had multiple objectives. Naturally, we thoroughly document the case histories (in Chapter 3), including the geotechnical site conditions established through field and laboratory testing, and the measured ground displacements. A second objective was to shed light on physical soil characteristics that affect seismic compression susceptibility through a simple shear laboratory testing program using fill soils from the sites. In Chapter 4, we present test results for clean sands, which provide a baseline set of data that can be used subsequently with test results for fill soils to evaluate the effects of fines on seismic compression. Test results for fill soils, presented in Chapter 5, provide substantial new insights into compositional and construction-related factors that affect seismic compression susceptibility in soils containing nonplastic and low-plasticity fines.

The third set of project objectives were realized through numerical analyses of site performance, with which we intended to (1) investigate the degree to which seismic compression can explain the observed ground displacements and (2) evaluate the sensitivity of calculated settlements to variability in input parameters as well as the dispersion of calculated settlements given the overall parametric variability. These case history analyses begin in Chapter 6, which describes the evaluation of ground motions for response analyses of the fill sites. Chapter 7 is directed principally towards realizing the first objective of the site analyses (comparison of computed settlements to observation). The analysis models for shear and volumetric strain are described; a logic tree methodology for treatment of parametric variability is described, including the assignment of model parameter values and their associated weights; and analysis results are given and interpreted for the response quantities of shear strain amplitude, volumetric strain, settlement, and peak horizontal acceleration. Finally, the computed settlement distributions are compared to observed values.

Chapter 8 is directed toward resolution of the second objective of the site analyses (evaluation of sensitivity and dispersion of analysis results). We evaluate the effects of various sources of parametric uncertainty (e.g., ground motion characteristics, soil shear wave velocity, modulus reduction/damping curves, and soil compaction conditions) on the median and standard deviation of shear and volumetric strain estimates. These sensitivity studies provide insight into the most critical input parameters for analysis of seismic compression settlements. Finally, the report is concluded in Chapter 9 with a synthesis of the scope and results of the research, recommendations for seismic compression analysis in engineering design practice, and recommendations for future research.

2 Prior Observations of the Seismic Performance of Compacted Fills

2.1 HISTORIC OBSERVATIONS

Few previous studies have focused specifically on the seismic performance of hillside fills or have attempted to document their performance on a broad scale, though the occurrence of ground deformations in fill has been noted following a number of earthquakes. Lawson (1908), in summarizing observations of ground cracking in hillside areas from the 1906 San Francisco earthquake, noted "roadways and artificial embankments were particularly susceptible to ... cracks." In summarizing observations from the 1952 Kern County, 1960 Chilean, and 1957 Hebgen Lake earthquakes, Seed (1967) noted "the effect of earthquakes on banks of well-compacted fill constructed on firm foundations in which no significant increases in pore-water pressure develop during the earthquake is characteristically a slumping of the fill varying from a fraction of an inch to several feet."

In a systematic survey of distress to single-family dwellings from the 1971 San Fernando earthquake, McClure (1973) noted the influence of fills on damage patterns, particularly when residences were constructed over cut/fill contacts. This study found that "...ground failure occurred on a higher percentage of sites that were on fill or cut and fill than on those sites which were on cut or natural grade" and "dwellings on cut and fill or fill had more relative damage than dwellings on cut or natural grade." In a separate report documenting earthquake effects in residential areas, Slosson (1975) noted that post–1963 fills (i.e., fills constructed to relatively strict post–1963 grading standards) performed markedly better than pre–1963 fills. Incidents of hillside fill movements during the 1989 Loma Prieta earthquake have been reported by several consultants; however, this information has not been compiled, and relatively little published information is available.

Prior to the present study, the best documentation of seismically induced ground displacement of a fill was from the Jensen Filtration Plant site during the 1971 San Fernando earthquake (Pyke et al., 1975). A fill blanket of up to 17 m thick was reported to have experienced settlements and lateral ground displacements along a survey baseline of about 13 cm. However, these displacements occurred on a section of fill that underwent lateral spreading as a result of liquefaction of underlying alluvium, which opened a ground crack near the survey baseline. Accordingly, Pyke et al. could only estimate the settlement due to seismic compression (9–10 cm). Clearly, even this relatively thoroughly documented and analyzed case history of seismic compression displacements must be interpreted with caution.

2.2 OBSERVATIONS FROM THE 1994 NORTHRIDGE EARTHQUAKE

2.2.1 Damage Distribution and Typical Fill Deformation Features

Stewart et al. (2001) documented the locations of about 250 sites where fill movements caused damage, as shown in Figure 2.1. Concentrated damage occurred on the north flank of the Santa Monica Mountains, along the north rim of the San Fernando Valley, and in the Santa Clarita Valley area. Other affected areas included the south flank of the Santa Monica Mountains and portions of Simi Valley. Much of the available data were gathered by consulting engineers in response to insurance claims. As such, the data provide a somewhat biased sample by which to assess fill performance (i.e., sites for which no claims were made are not included). Moreover, the data from most sites consist of general descriptions of distress and relative movements across improvements (such as houses), but absolute movements relative to a "fixed" reference are unavailable. Nonetheless, the data illustrate general characteristics of ground deformations that occurred in fill, and the effect of such deformations on structures.

Characteristics of fill movements at the sites plotted in Fig. 2.1 were similar. Characteristic fill deformation features are illustrated in Figure 2.2 and are discussed below:

- *Cracks near cut/fill contacts*: The most commonly observed location of ground cracks was at cut/fill contacts, or above the nearest bench to cut/fill contacts. In building pad areas, cut/fill cracks typically had < 8 cm of lateral extension and 3 cm of localized differential settlement of fill relative to cut. Damage to structures crossing these features was often significant (e.g., Figure 2.3). Where investigated with trenching or downhole logging, these cracks were found to become thinner with depth, and could be traced to depths of only 1–2 m. Hence, the cracks did not appear to be surface expressions of deep seated shear failures.

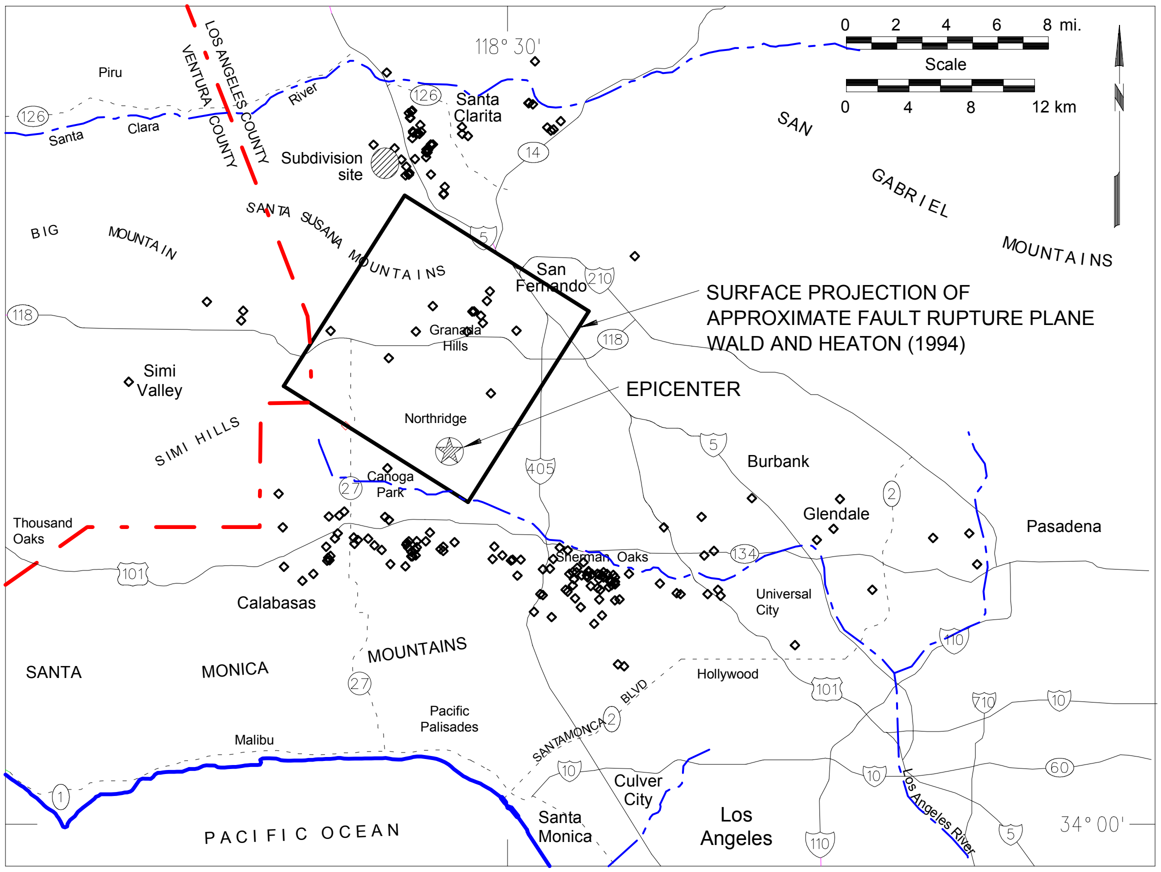

Fig. 2.1. Site locations where fill movements caused significant damage during Northridge earthquake

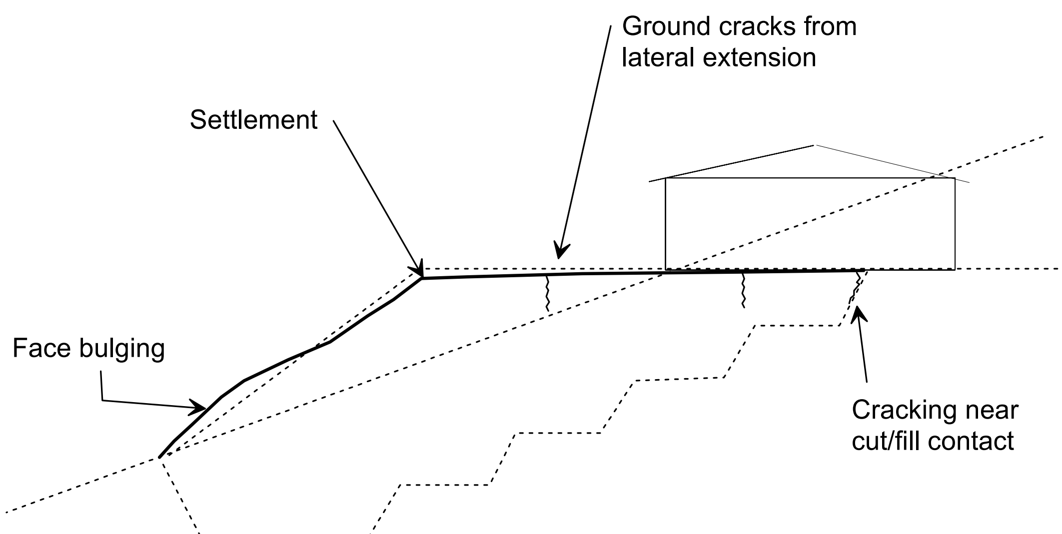

Fig. 2.2. Schematic showing typical damage to fill slope

- *Lateral extension in fill pad:* Evidence of lateral extension of fill pads was commonly observed in the form of tensile cracking parallel to the top of the slope, and the opening of relatively large (>3 cm) separations at cold joints between concrete slabs and footings (e.g., Figure 2.4), or between pools and pool decks. These features typically involved about 3–10 cm horizontal or vertical offsets, but significantly wider cracks (<30 cm) occurred at some sites. The setback of tensile cracking from the top of slope tended to increase with fill depth, and most houses constructed with Uniform Building Code-level setbacks (one third the slope height) were not damaged by this cracking.

Fig. 2.3. Cracked floor slab above cut/fill contact; displacements are 1.9 cm (V) and 5 cm (H)

Fig. 2.4. Evidence of extensional ground deformations at back of house; top of slope is to the left

- *Settlement:* Fill pad settlements increased with fill depth, resulting in differential settlements across the surface of fills. These settlements were often measured within houses by means of manometer floor level surveys. A typical criteria allows for 2.5 cm floor-level differentials within 6 m (0.4% floor slope), though Los Angeles County requires engineers to design for 1.25 cm settlement in 9 m (0.14% slope) (Pearson, 1995). Maximum floor slopes for fills were often as high as ~2%, which significantly exceeds normal tolerances for houses.
- *Face bulging/shortening:* Detailed slope face inspections were performed at a number of sites, and at a limited number of these, fill slope face bulging was evident from movements of concrete surface drains running cross-slope (terrace drains) and down-slope (downdrains). Terrace drains had cracks oriented perpendicular to the slope contours that widened in the downslope direction, providing evidence for face bulging of the center of the fill. Uplifted downdrains were observed in some large fills at approximately one third the slope height (Figure 2.5), indicating shortening of the lower slope face.

Fig. 2.5. Uplifted down drain indicating compression of fill slope face

2.2.2 Effect of Fills on Damage Patterns — Santa Clarita Subdivision Case Study

The Santa Clarita Valley area was strongly shaken by the Northridge earthquake, and experienced significant ground deformations in compacted fill. Recent development in outlying portions of the valley has often occurred in deeply incised canyon/ridge topography, which has required massive grading operations involving deep canyon fills. Engineered improvements constructed across fill and cut areas are often of fairly uniform design and construction. Such sites provide the opportunity to assess the impact of earth fills on the performance of improvements (such as pipelines and houses) by comparing damage statistics for cut and fill areas.

One such site is the 85.0 km^2 subdivision shown in Figure 2.6, the seismic performance of which has been documented by Stewart et al. (2001). At the time of the Northridge earthquake, 645 properties in the subdivision had been developed, with the construction having occurred between July 1986 and October 1987. The site is approximately 9 km from the surface projection of the Wald and Heaton (1994) Northridge fault rupture plane, and likely experienced peak ground accelerations on rock on the order of 0.3 to 0.5g (Chang et al., 1996). Original topography at the site consisted of numerous canyons and ridges, with a general increase in elevation to the west. Grading operations involved the construction of fills with maximum depths typically of about 15 to 21 m. The fill soils placed at the site are primarily sands and silty sands, with nonplastic fines contents on the order of 15–30%. Fill placed at the site was required to have a minimum relative compaction by the Modified Proctor standard of 90%. Water content was not controlled during construction, and cut areas were not overexcavated.

We have documented the performance of all major buried pipelines (water, sewer, stormdrain, and gas), and most building structures that were in place at the time of the 1994 Northridge earthquake. As shown in Figure 2.6, a total of 14 breaks were reported in the water distribution system (15, 20, or 25 cm diameter asbestos-concrete pipes), most of which are described as “shear failure.” All the breaks occurred in fill, generally near cut/fill contacts. The gas and storm drain lines primarily consist of relatively flexible PVC pipe, and no breaks were reported. A 152 cm diameter reinforced concrete storm drain, constructed in 2.4 m sections, passes through the subdivision. This pipe had only minor damage at grout joints, and this damage was uniformly distributed across the length of the pipe (i.e., no concentration of damage in fill areas). Apparently the strength and stiffness of this large-diameter reinforced concrete section was sufficient to resist damage associated with deformations in fill.

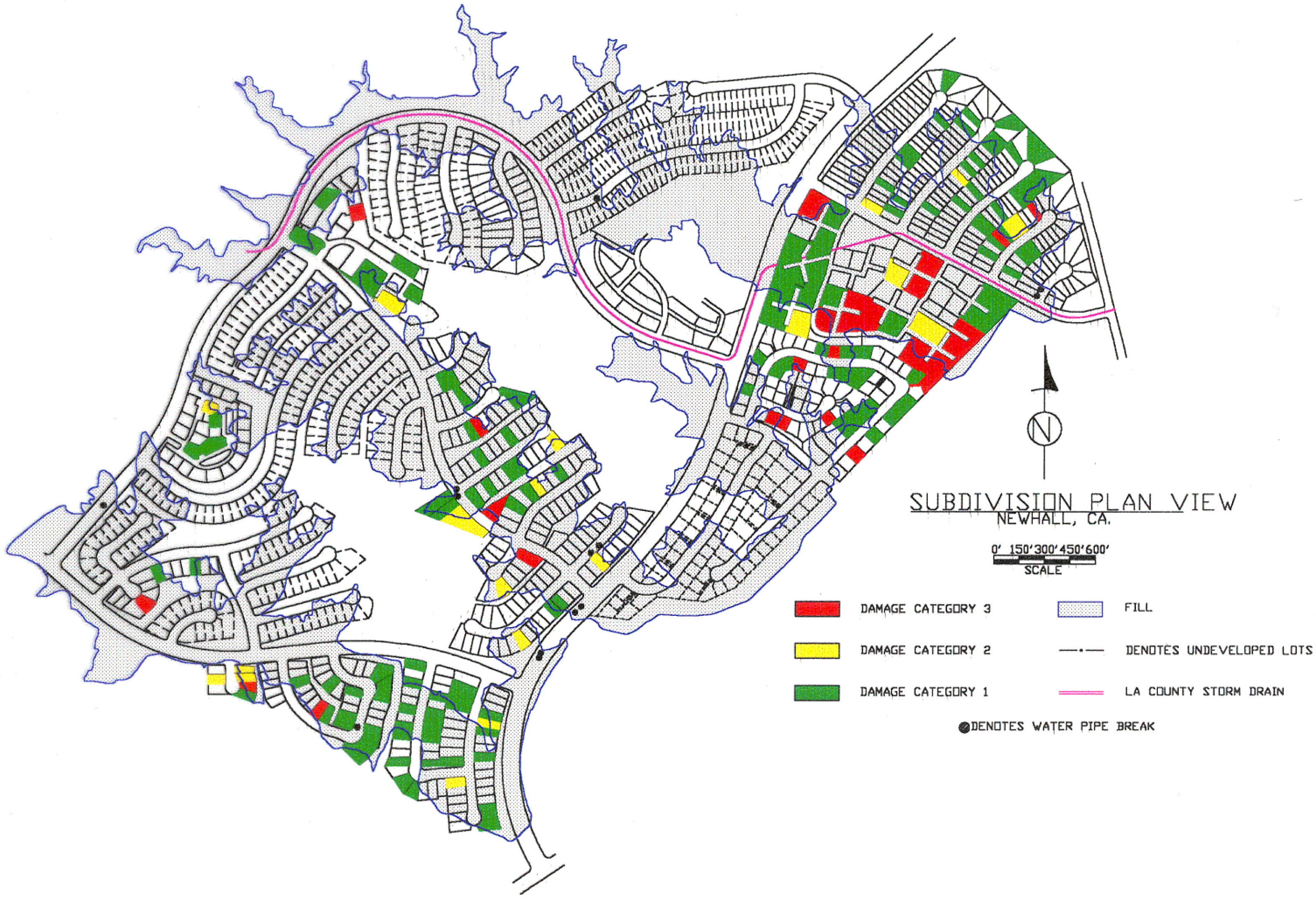

Fig. 2.6. Plan view of subdivision showing fill and cut zones and locations of damaged water pipes and structures

Damage to structures was evaluated based on inspection reports prepared by Los Angeles County staff within one month of the earthquake. Inspections were made upon the request of property owners seeking earthquake relief. Specific damages were documented (e.g., foundation cracks, wall cracks, collapsed chimneys), and monetary losses were estimated. Some properties were not inspected, presumably because of little or no earthquake damage. As shown in Figure 2.6, damage at each site was classified according to the four categories in Table 2.1.

Table 2.1. Damage statistics for subdivision as function of site condition. Indicated are numbers (and percentages in parentheses) of lots within each site category with different damage levels.

Site Condition	No Damage* (0)	Cosmetic Damage* (1)	Moderate Damage* (2)	Significant Damage* (3)	Total
Cut	193 (77%)	49 (20%)	3 (1%)	5 (2%)	250
Cut/Fill	159 (66%)	60 (25%)	11 (4%)	12 (5%)	242
Fill	100 (65%)	39 (25%)	8 (5%)	7 (5%)	154
All lots	452 (70%)	148 (23%)	22 (3%)	24 (4%)	646

*0. No damage. No observed distress, or no homeowner request for inspection.
1. Cosmetic damage. Cracks in walls and ceilings that do not threaten structural integrity.
2. Moderate damage. Cosmetic damage + damaged roof, chimney, floors, windows, or plumbing suggesting some ground deformation or intense shaking.
3. Significant damage. Moderate damage + cracked foundation and displacements observed in soil, suggesting significant ground deformation.

Also shown in Table 2.1 is the frequency with which the various damage levels were encountered in cut, fill, and cut/fill transition lots. These data indicate that the likelihood of significant damage (Damage Category of 2 or 3) on cut/fill or fill lots was more than twice that on cut lots.

The reported damage from this subdivision indicates that the presence of fill significantly affected the likelihood of damage to pipelines and building structures, as all reported pipeline breaks occurred in fill near cut/fill transitions, and the likelihood of significant structural damage on fill or cut/fill areas was more than twice that on cut areas.

2.3 DISCUSSION

The observations of seismic ground deformations in fill that had been compiled prior to this study were documented in the previous sections. These observations provide insight into the general characteristics of deformation features and the importance of these features for the built environment. Two ground failure mechanisms can be postulated to have caused these deformations:

- *Seismic compression*, i.e., contractive volumetric strains developed during cyclic loading of unsaturated, compacted soil, and
- *Permanent shear deformations*, either along distinct sliding surfaces or distributed across highly stressed zones in the fill.

Analyses by Stewart et al. (2001) found that for many common fill geometries, the general characteristics of the observed ground deformations could be best explained by the seismic compression mechanism. Permanent shear deformations are only likely to occur at a relatively small subset of sites with large static driving shear stresses relative to the soil strength (i.e., sites with low static factors of safety). As discussed further subsequently in the report (Section 7.1), permanent shear deformations at the two subject sites for this research are unlikely to have significantly contributed to observed ground deformations. Accordingly, in this study we focus on the more plausible seismic compression mechanism for these sites.

What the prior observations of seismic ground deformations in fill (outlined in the previous sections) generally fail to provide is unambiguous, quantifiable ground displacements attributable to seismic compression. While ground position surveys can readily be performed following an earthquake, pre–earthquake surveys are not generally available from which earthquake-induced displacements can be assessed. In the absence of such data, only limited insights into ground deformation processes are possible, and calibration of analysis procedures is impossible. The present study is focused on two sites for which displacements induced by the Northridge earthquake can be accurately estimated from pre– and post–earthquake surveys. These sites provide a unique opportunity to gain insight into the seismic compression problem, and to compare the outcome of seismic compression analyses to field performance data.

3 Site Performance and Site Conditions

In this chapter, two sites are identified where the amount of ground deformation induced by the 1994 Northridge earthquake can be reliably estimated from pre– and post–earthquake surveys. The results of geotechnical investigations of the site conditions are described, and the field performance of each site is documented.

3.1 SITE SELECTION

In Section 2.2, we reviewed the general characteristics of ground deformations observed in fill following the 1994 Northridge earthquake. The field performance data used in the compilation of those deformation patterns were based on post–earthquake reconnaissance by the authors and others and site-specific studies by engineering consultants. Those data do not enable precise evaluations of earthquake-induced deformations, due to a lack of pre–earthquake fill position surveys. The availability of such data, along with complementary post–earthquake surveys, therefore, represents the principal criteria employed here for site selection. Two sites meeting these criteria were found:

1. Site A: A canyon fill constructed in 1990–91 just north of Santa Clarita
2. Site B: A canyon fill constructed in 1993 near Santa Clarita

The locations of these sites relative to the surface projection of the Northridge fault rupture plane are shown in Figure 3.1.

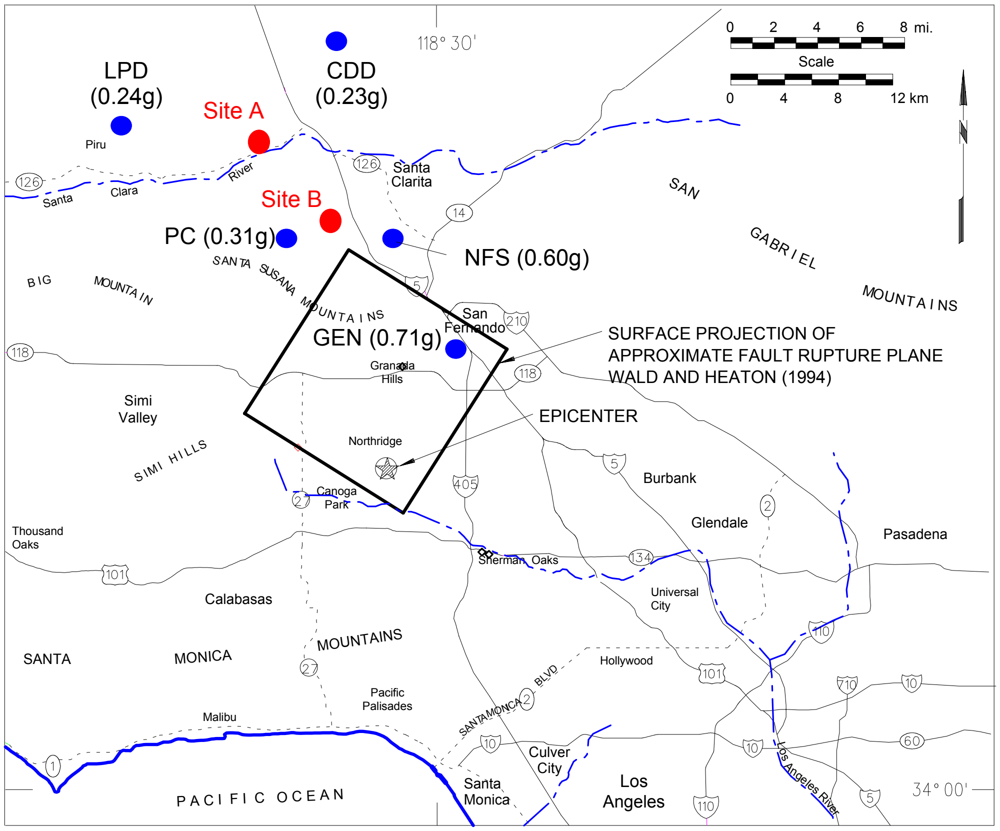

Fig. 3.1. Locations of Sites A and B and selected strong motion stations (with geometric mean peak horizontal accelerations from 1994 Northridge earthquake in parentheses)

3.2 SITE A CHARACTERISTICS

Site A is located in the Santa Clarita Valley, north of the Santa Clara River and west of Interstate Highway 5. The site is approximately 12.2 km from the 1994 Northridge earthquake fault rupture plane, based on the fault rupture model by Wald and Heaton (1994).

3.2.1 Stratigraphy

Plan views of the approximately 121,400 m^2 site, and cross sections through the site, are shown in Figures 3.2 and 3.3, respectively. The topographic and depth-of-fill data are based on as-built construction drawings provided by Jacobs Engineering. Original topography at the site consisted of several deeply incised canyons, with a general increase of elevation to the north. The level final grade was realized with cuts into the hillside at the north and west ends of the site, and large fills extending to depths of up to 24 m at the south and west ends of the site.

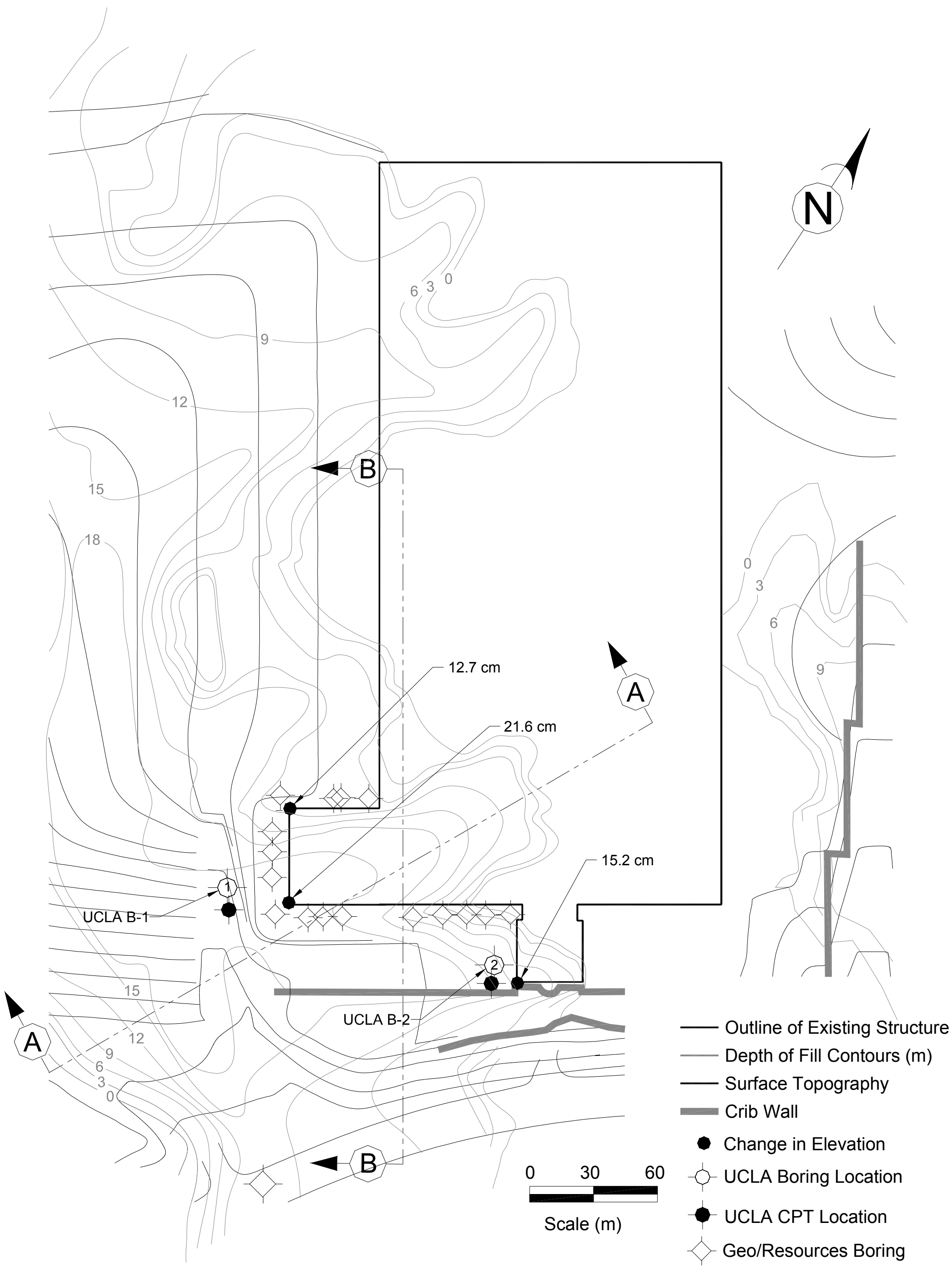

Fig. 3.2(a). Plan view of Site A, showing fill thickness contours, locations of subsurface exploration, and selected settlement values between 1991 and 1994

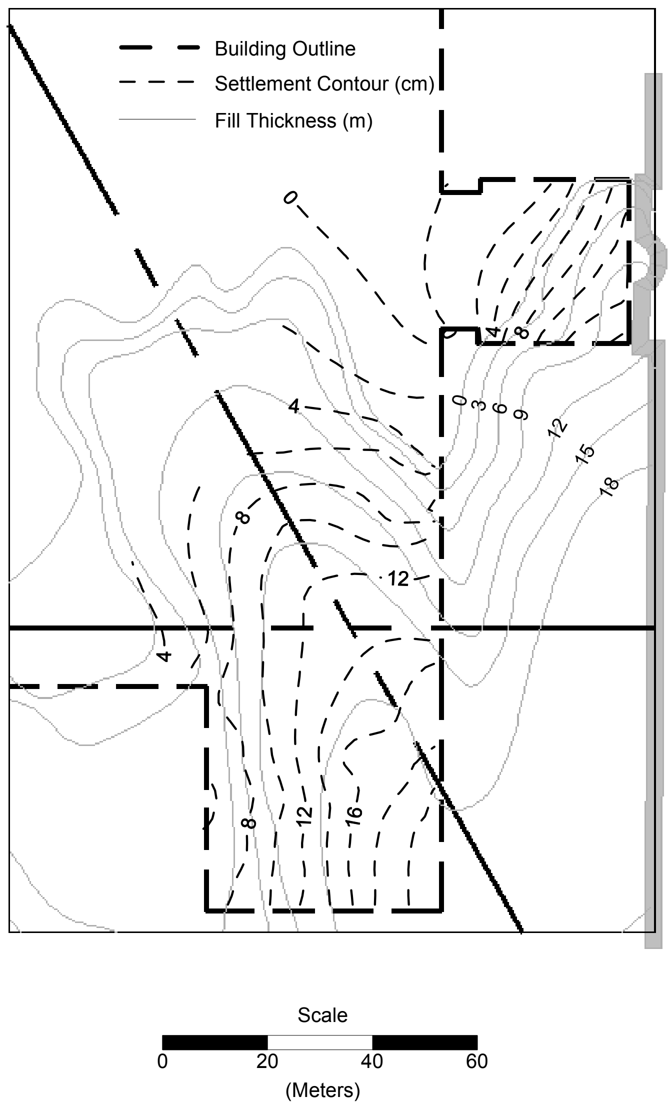

Fig. 3.2(b). Detail view of south corner of building at Site A showing contours of fill thickness, and observed settlements between October 1991 and January 1994 (in cm). The bold lines through the figure are cross-section locations from Figure 3.2(a).

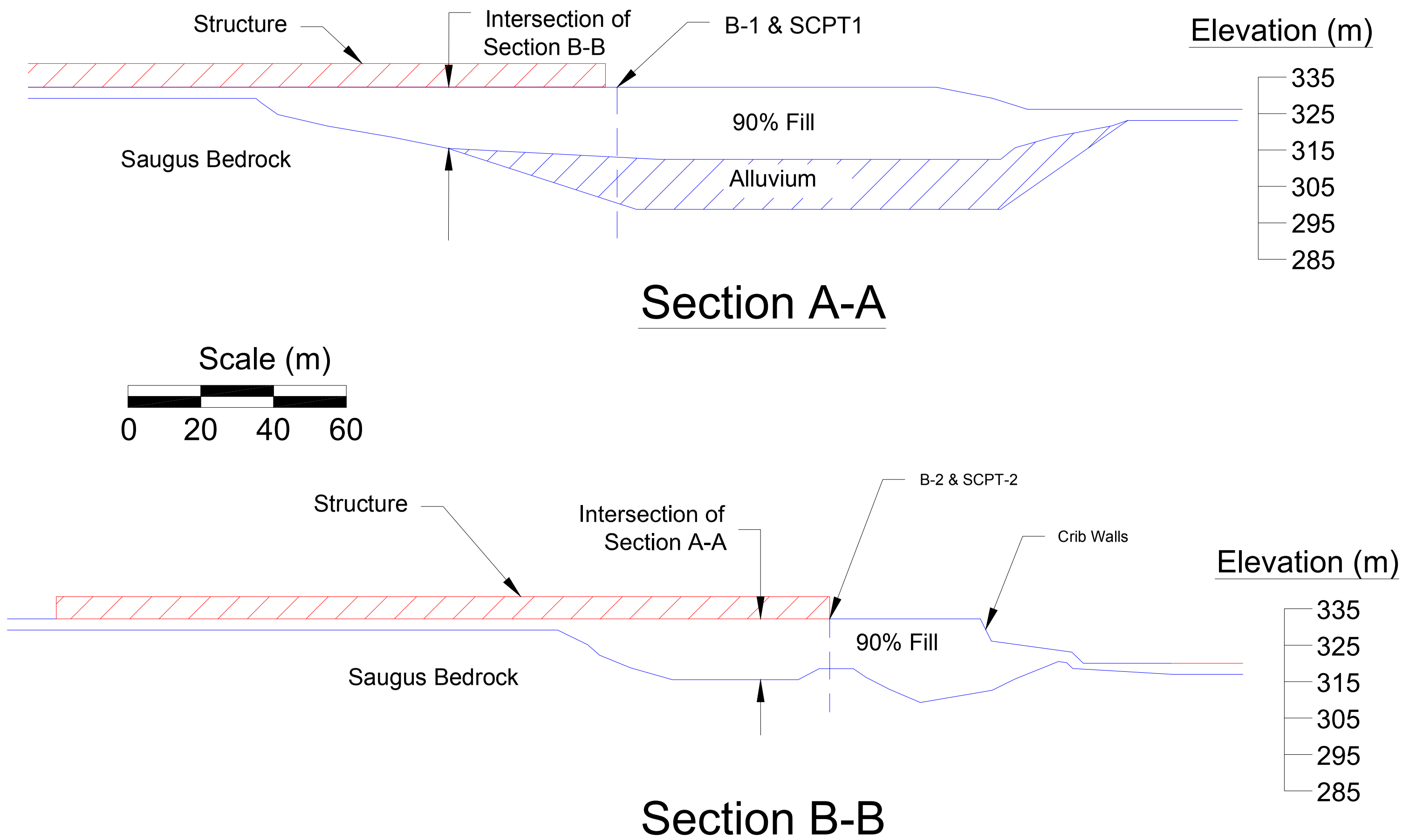

Fig. 3.3. Site A cross sections

Subsurface exploration was performed to verify the conditions depicted on construction documents, to evaluate the shear wave velocities in fill and underlying materials, and to collect samples for laboratory testing. The subsurface exploration program consisted of two seismic cone penetration tests (SCPT) in the fill (SCPT-1 and SCPT-2), and two hollow-stem auger borings, which extended through the fill and into bedrock (B-1 and B-2). Upon completion of drilling, casing was installed in the boreholes and cement-grouted into place to enable seismic velocity testing. The locations of exploration are shown in Figures 3.2(a) and 3.3. Figure 3.2(a) also shows locations of 16 additional borings by Geo-Resources (1994) near the southwest portion of the building. In situ values of shear wave velocity were measured using a downhole technique in the SCPTs and borings. The contractors performing the SCPT work, drilling, and downhole shear wave velocity measurements were Gregg In Situ, Cascade Drilling, and Law/Crandall Inc., respectively. Logs of the SCPT probes and borings are presented in the Appendix.

Soil conditions at the site are consistent with the construction documents in terms of the fill depths. The fill soils consist of sandy silty clays and clayey silty sands with occasional rock fragments. At the base of canyons, the fill soils are underlain by silty sandy clay alluvium, which was encountered to a thickness of about 12 m in B-1. This alluvium was unsaturated at the time of drilling. Underlying the alluvium and fill soils is bedrock consisting of severely weathered silty, sandy claystone belonging to the Saugus Formation. Groundwater was not encountered in any of the CPT holes or borings.

3.2.2 Fill Compaction Conditions

Fill placed at the site was required to have a minimum relative compaction (*RC*) by the Modified Proctor standard (ASTM D1557) of 90%. Water content was not controlled during construction, and cut areas were not overexcavated. Field logs of 1711 tests documenting water content (w), dry density (γ_d), and *RC* were prepared during the construction operations from July 1990 to August 1991. Maximum dry density $(\gamma_d)_{max}$ values used at the time of construction for calculations of *RC* ranged from 1.81 to 2.24 gm/cm^3 (21 different values were reported). A histogram of these values is shown in Figure 3.4. The field logs and $(\gamma_d)_{max}$ values were obtained from the owner of the site. It is noteworthy that the County of Los Angeles did not certify this fill, meaning that the construction of the fill did not meet minimum county requirements.

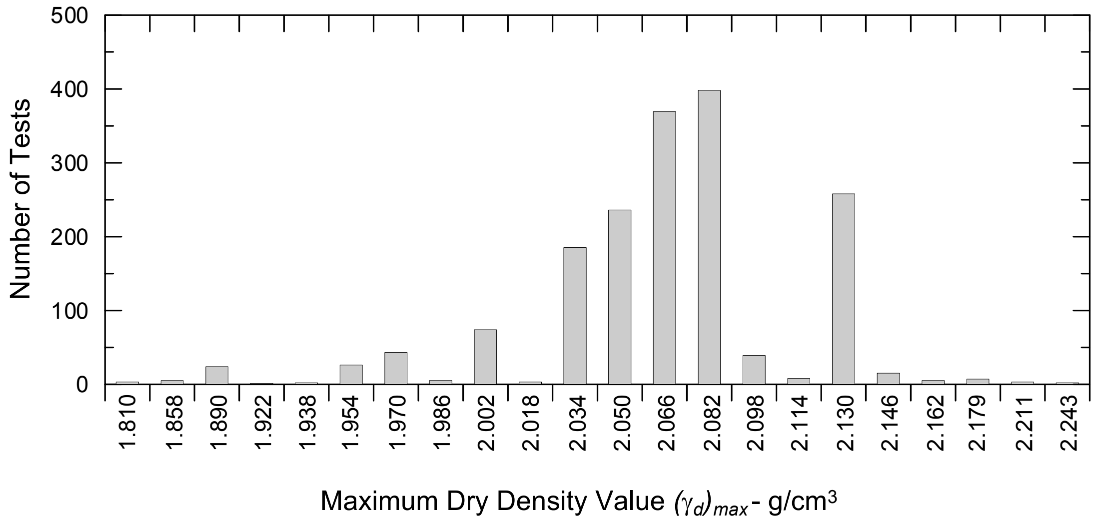

Fig. 3.4. Distribution of maximum dry density values $(\gamma_d)_{max}$ that were used during the construction of fill for Site A

Figures 3.5(a)–(c) show the distribution of *w* and *RC* based on the field logs received from the site owner. These results indicate that almost all of the field compaction tests met the minimum *RC* standard of 90%. Summary statistics of $(\gamma_d)_{max}$, *RC,* and *w* are shown in Table 3.1.

Table 3.1. Summary of statistics for the Site A fill using unadjusted field construction logs

Compaction Variable	Upper Limit	Lower Limit	Mean	Standard Deviation
$(\gamma_d)_{max}$ (g/cm^3)	2.24	1.81	2.07	0.05
RC (%)	105	78	93	2.23
w (%)	24	4	11	2

A total of 23 bulk samples of fill were obtained from borehole cuttings. By obtaining samples in this way, the samples comprise a blend of soils from multiple depths. Because the bulk samples were derived from different depths and two separate drilling locations, as an ensemble they would be expected to be broadly representative of the fill materials at Site A. Modified and Standard Proctor tests (ASTM D1557 and D698, respectively) were performed on nine of the bulk samples and one sample of alluvium, with the results summarized in Table 3.2.

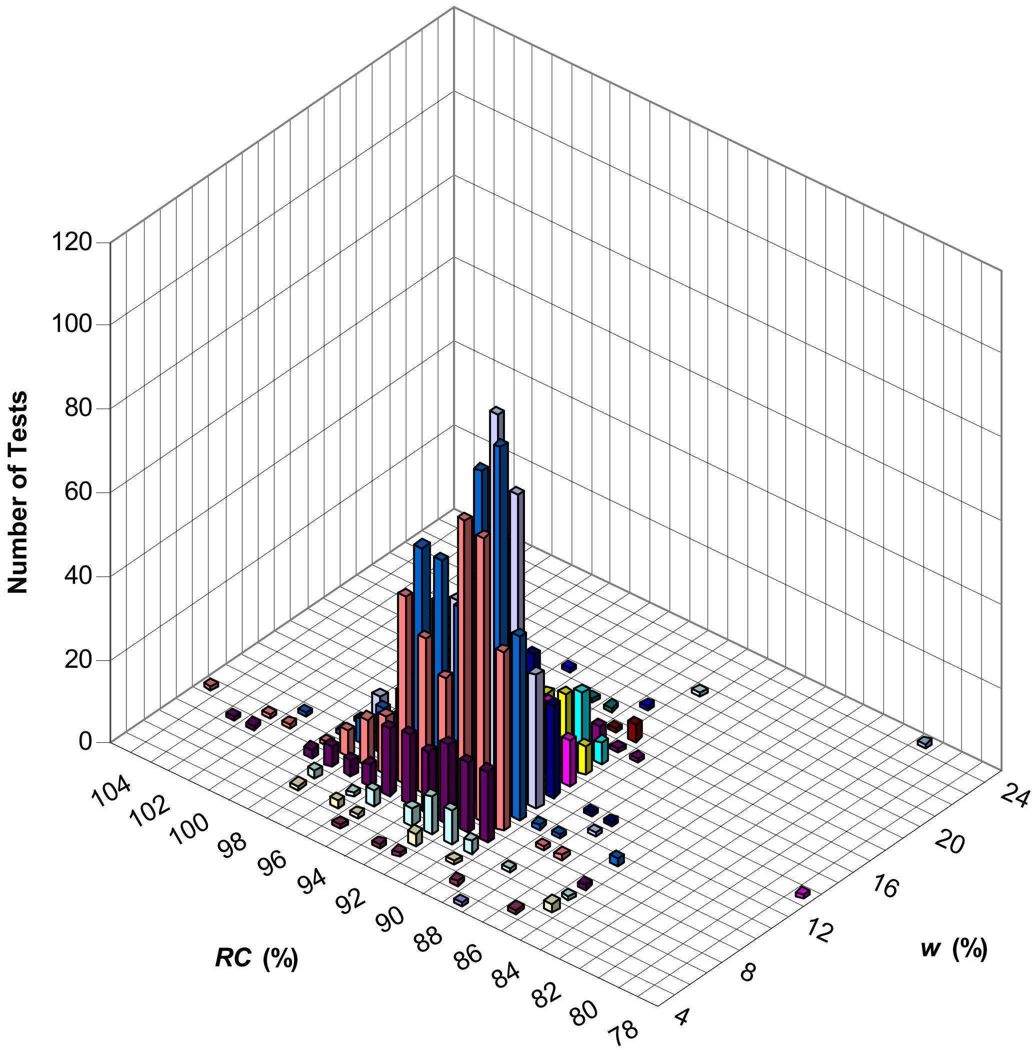

Fig. 3.5(a). Distribution of reported compaction test results for Site A

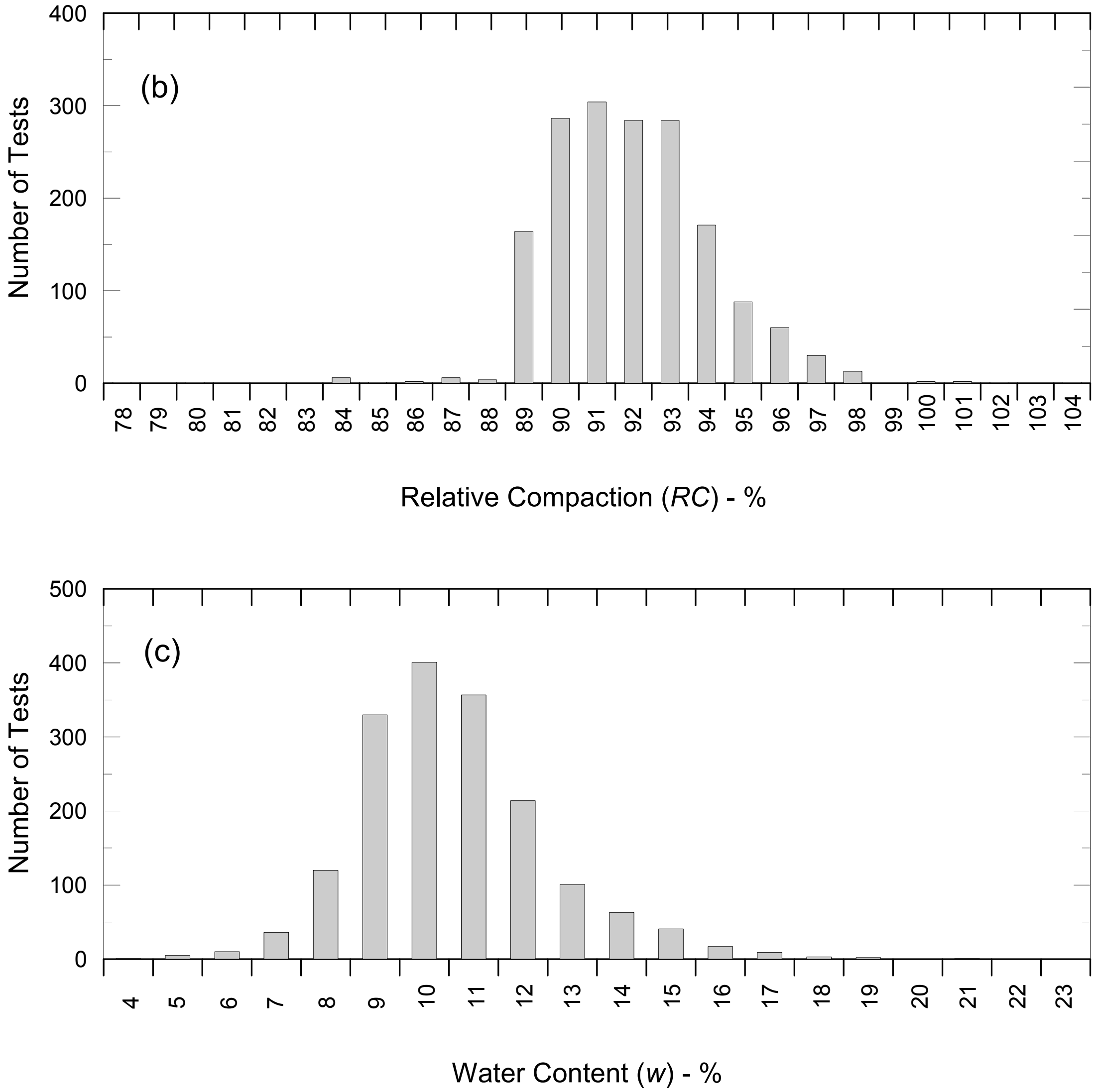

Fig. 3.5 (b)–(c). Distribution of relative compaction (*RC*) and water content (*w*) in fill for Site A, as measured at time of construction

Table 3.2. Summary of compaction test results on bulk samples of fill from Site A

Boring	Depth (m)	Modified Proctor w_{opt} (%)	Modified Proctor $(\gamma_d)_{max}$ (g/cm^3)	Standard Proctor w_{opt} (%)	Standard Proctor $(\gamma_d)_{max}$ (g/cm^3)	Type
B-1	3.1-4.6	8.4	2.20	11.9	2.03	Fill
	9.1-10.7	8.6	2.15	11.6	2.02	Fill
	13.7-15.2	8.4	2.18	11.5	2.01	Fill
	16.8-18.3	7.9	2.17	10.8	2.03	Fill
	19.8-21.3	7.4	2.17	10.0	2.02	Fill
	24.4-25.9	7.5	2.13			Alluv.
B-2	0.0-1.5	8.5	2.18	11.2	2.04	Fill
	4.6-6.1	9.7	2.15	12.4	1.99	Fill
	12.2-13.7	9.3	2.11	13.5	2.02	Fill
	15.2-16.8	9.5	2.16	12.0	2.03	Fill

The compaction curves resulting from this testing were reasonably consistent. As indicated in Table 3.2, values of $(\gamma_d)_{max}$ and optimum water content (w_{opt}) from individual Modified Proctor tests range from $(\gamma_d)_{max}$ = 2.11 to 2.20 g/cm^3 and w_{opt} = 7.4 to 9.7%, respectively. The consistency of these results suggests that a single compaction curve (for a given energy level) may be used. Accordingly, individual compaction points from each of the compaction tests are plotted together in Figure 3.6. A polynomial regression fit through these results was used to develop representative moisture-density curves of the fill soil. Based on the regression, $(\gamma_d)_{max}$ and w_{opt} for the Modified Proctor moisture-density curve for fill are 2.15 g/cm^3 and 8.3%, respectively.

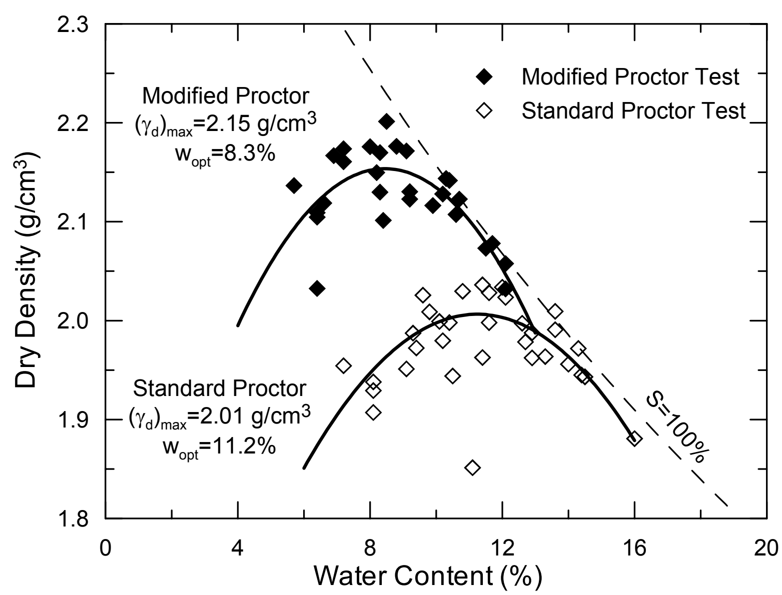

Fig. 3.6. Moisture-density curves for Site A fill evaluated from UCLA samples

An important outcome of the above compaction testing is a significant deviation between our $(\gamma_d)_{max}$ values and those reported in the construction logs. Assuming our values are correct, it appears that the *RC* values reported for this fill in Figures 3.5a–b are too high. Accordingly, we developed modified *RC* values for the fill (RC_m) by assuming that the field-logged γ_d values were correct, and then normalizing these data by $(\gamma_d)_{max}$ = 2.15 g/cm^3 (obtained above). Figure 3.7(a) shows the resulting distribution of RC_m, which ranges from 71–103%, with a mean of 89% and a standard deviation of 3.4%.

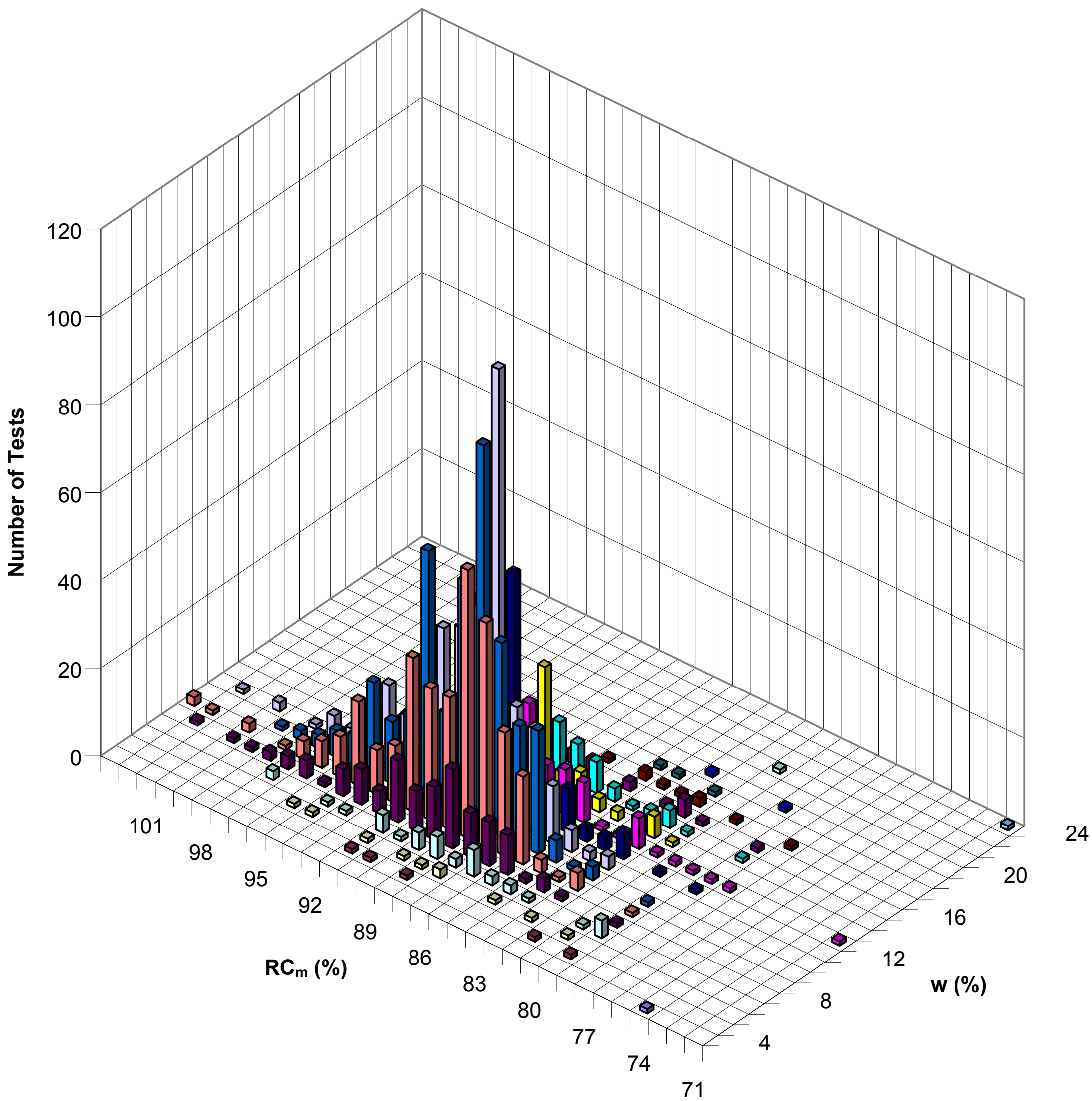

Fig. 3.7(a). Distribution of adjusted field compaction test results for Site A fill soils

Figure 3.7b–c shows the distribution of field test results based on RC_m and S, and indicates that more than half the fill likely has RC below the minimum standard of 90%. Figure 3.8 shows contours of the relative likelihood of field tests having different values of RC_m and w. The likelihood ordinates were compiled by discretizing the RC_m space into 1% intervals and the w space into 1% intervals, calculating the percentage of all tests within each of those bins, and then contouring the resulting data using the *Kriging* geostatistical gridding method (Cressie, 1991). Also shown in Figure 3.8 are Modified and Standard Proctor moisture-density curves and contour lines for constant degree of saturation based on specific gravity, G_s=2.75. A noteworthy aspect of the data in Figure 3.8 is that the mode RC_m is 87.8% and the mode w is 10.5%. Moreover, the majority of the fill soil appears to have been compacted dry of the line of optimums (which occurs at S≈82%). As discussed further in Section 5.3.3, cohesive soils compacted dry of the line of optimums can have a clod structure that is especially vulnerable to hydro- and seismic-compression.

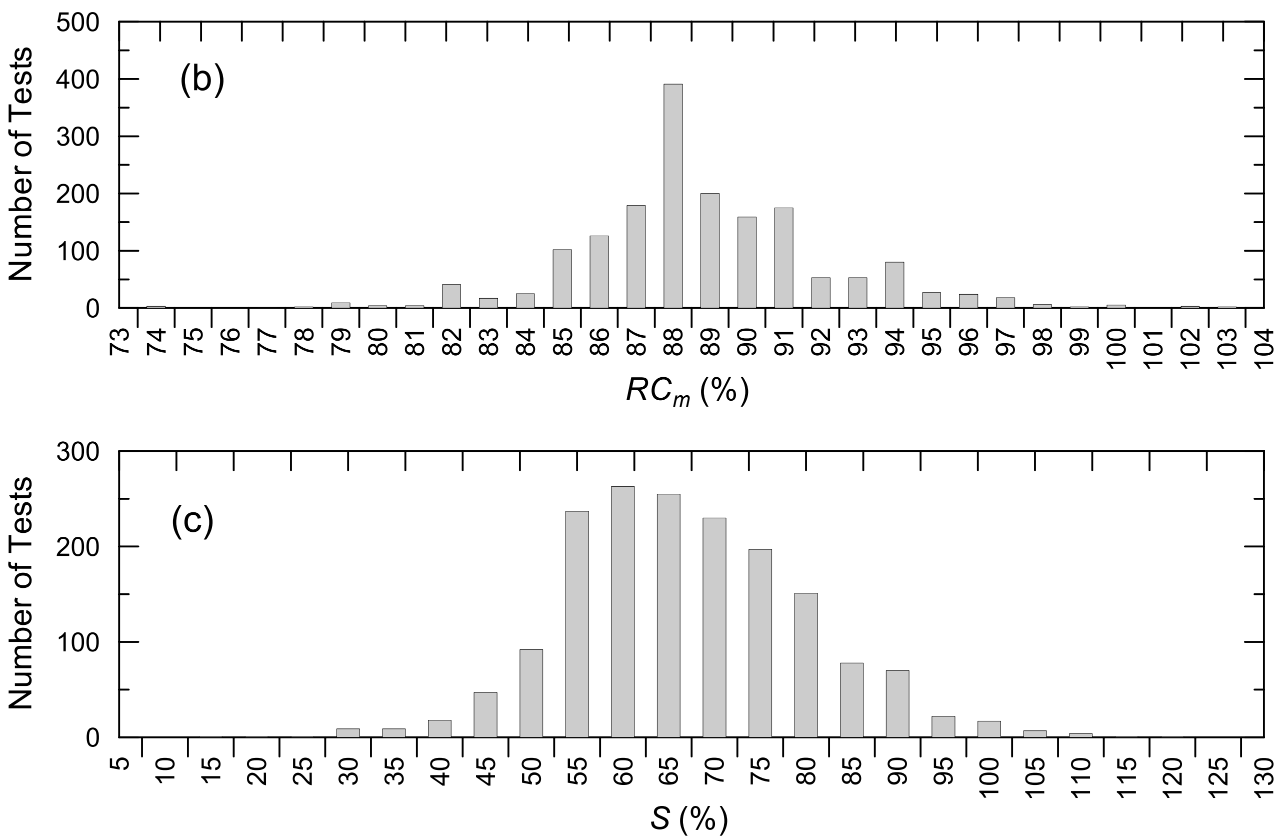

Fig. 3.7(b)–(c). In situ modified relative compaction (RC_m) and saturation (S) for Site A fill soils

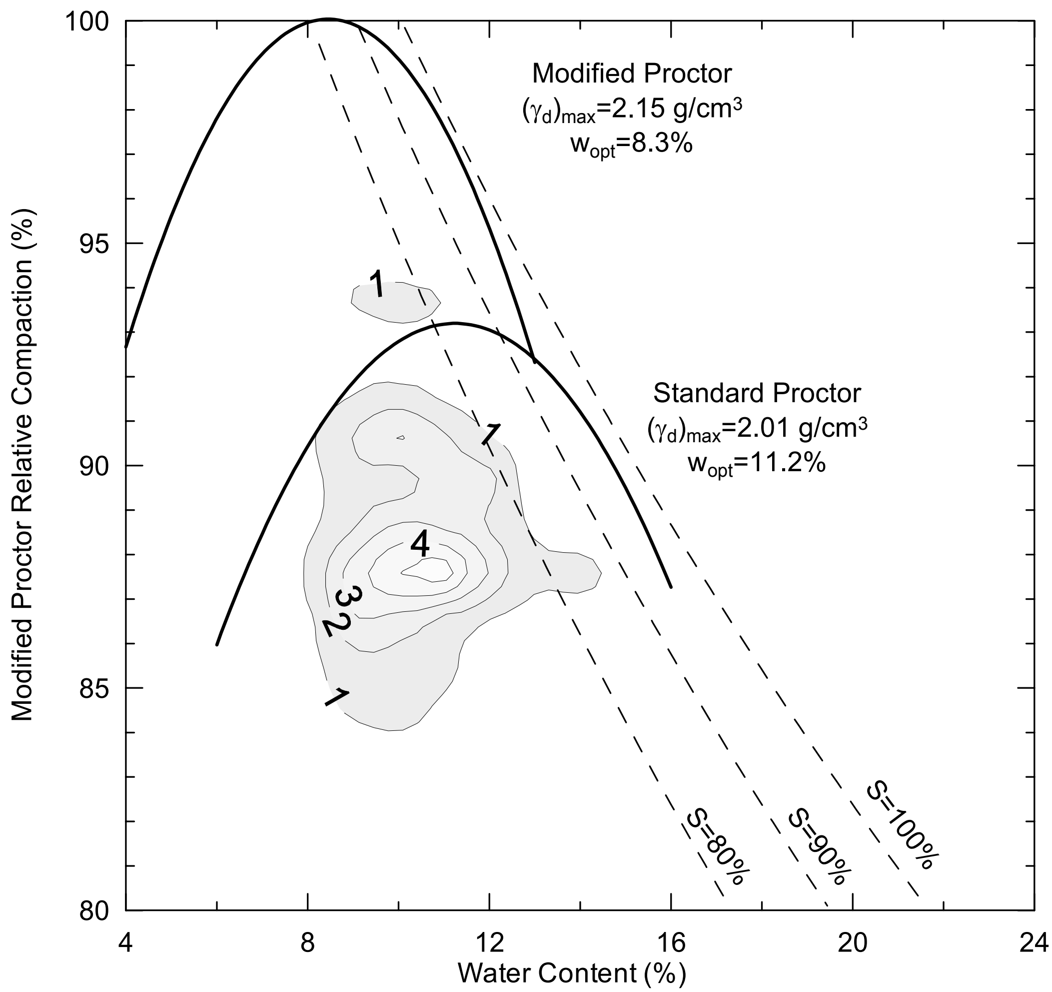

Fig. 3.8. Contours showing relative likelihood of adjusted field compaction test results as a function of *RC_m* and *w* for Site A fill soils

3.2.3 Index Testing

Sieve/hydrometer analyses (ASTM C136 and D422) and Atterberg Limit tests (ASTM D4318) were performed on 25 samples taken from various depths in the fill from Site A. Testing was also performed on four samples retrieved from the alluvium. Results of these tests are reported in Table 3.3. The results for the fill and alluvium soils are similar, and hence are plotted together in Figures 3.9. Figure 3.9(b) shows the mean and mean ± one standard deviation grain-size distribution plots for fill and alluvium soils. All of the tested fill samples were well graded and the fines contents varied from 43 to 58% (average = 52%). Fines contents in alluvium varied from 49 to 69% with an average of 55%. The specific gravity of the fill soils, tested per ASTM D854, was found to be 2.75.

Table 3.3. Summary of index test results on samples from Site A

Boring	Depth (m)	%Clay	%Fines	D_{60} (mm)	D_{10} (mm)	D_{30} (mm)	PI	LL	Cu	Cc	Type
B1	0-1.5	14	45	0.22	n/a	0.019	12	32	n/a	16	Fill
	1.5-3.0	12	43	0.33	n/a	0.033	10	29	n/a	3	Fill
	3.0-4.6	16	47	0.18	n/a	0.017	12	31	n/a	16	Fill
	4.6-6.1	17	53	0.13	n/a	0.01	13	32	n/a	8	Fill
	6.1-7.6	17	54	0.12	n/a	0.013	13	32	n/a	14	Fill
	7.6-9.1	17	44	0.13	n/a	0.01	15	32	n/a	8	Fill
	9.1-10.7	20	53	0.13	n/a	0.009	15	34	n/a	6	Fill
	10.7-12.2	18	55	0.12	n/a	0.0098	15	33	n/a	8	Fill
	12.2-13.7	17	57	0.10	n/a	0.009	16	34	n/a	8	Fill
	13.7-15.2	20	52	0.14	n/a	0.008	13	32	n/a	5	Fill
	15.2-16.8	20	54	0.13	n/a	0.0075	14	33	n/a	4	Fill
	16.8-18.3	20	58	0.09	n/a	0.0095	14	32	n/a	10	Fill
	18.3-19.8	16	46	0.21	n/a	0.019	14	32	n/a	17	Fill
	19.8-21.3	14	43	0.30	n/a	0.032	12	30	n/a	34	Fill
	21.3-22.9	16	49	0.15	n/a	0.015	10	31	n/a	15	Alluv.
	22.9-24.4	16	50	0.14	n/a	0.018	10	31	n/a	23	Alluv.
	24.4-25.9	18	51	0.13	n/a	0.01	12	31	n/a	8	Alluv.
	25.9-27.4	20	69	0.08	n/a	0.008	13	30	n/a	8	Alluv.
B2	0-1.5	14	51	0.15	n/a	0.018	11	31	n/a	2	Fill
	1.5-3.0	13	49	0.17	n/a	0.019	11	31	n/a	2	Fill
	3.0-4.6	17	56	0.10	n/a	0.011	15	35	n/a	12	Fill
	4.6-6.1	14	58	0.09	n/a	0.018	14	33	n/a	4	Fill
	6.1-7.6	15	57	0.09	n/a	0.016	14	33	n/a	28	Fill
	7.6-9.1	-	-	-	-	-	-	-	-	-	Fill
	9.1-10.7	19	54	0.13	n/a	0.0095	13	32	n/a	7	Fill
	10.7-12.2	16	56	0.10	n/a	0.017	14	33	n/a	29	Fill
	12.2-13.7	16	55	0.10	n/a	0.012	14	33	n/a	14	Fill
	13.7-15.2	15	53	0.13	n/a	0.016	14	33	n/a	20	Fill
	15.2-16.8	21	61	0.07	n/a	0.0058	14	34	n/a	5	Fill

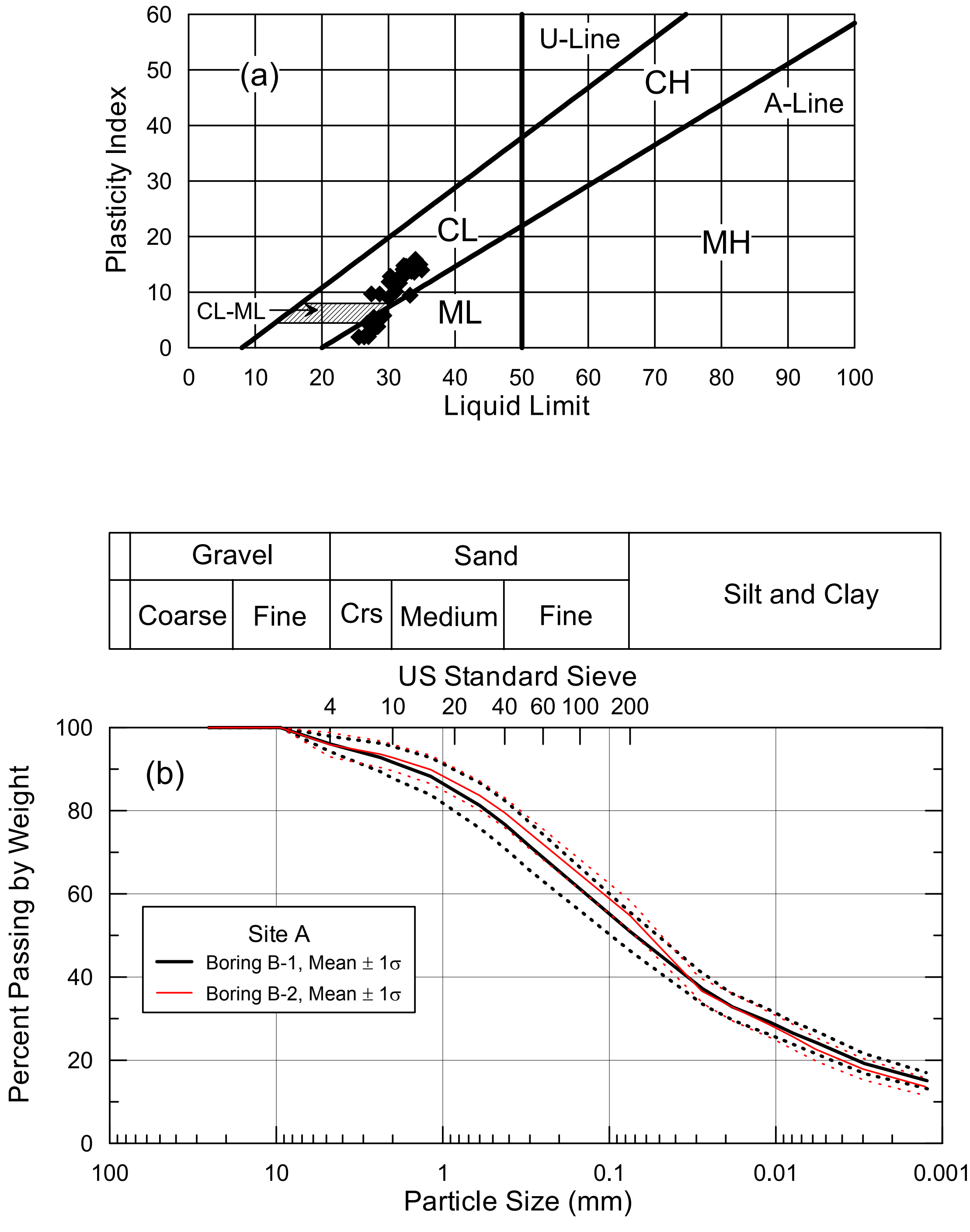

Fig. 3.9. Plots of (a) plasticity data and (b) average grain-size distribution for fill and alluvium soils at Site A

Figure 3.9(a) summarizes the Atterberg Limit test results. The fill and alluvium samples were generally classified as low-plasticity clays (CL), low-plasticity silts (ML), or a clayey/silty sands (SC, SM) according to the Unified Soil Classification System (UCSC). The average Liquid Limit and Plasticity Index for the fill soils was 32 and 13, respectively, and 31 and 11 for the alluvium. These average values correspond to a CL material classification.

3.2.4 Density and Saturation of Alluvial Soils

The dry density and water content of the alluvium are estimated using test data from samples retrieved in test pits and boring logs excavated prior to construction of the fill by a geotechnical consultant to the site owner. Figure 3.10(a) and (b) show histograms for γ_d and w based on reported values from the consultant's report. Equivalent *RC* values of the alluvium are estimated using the $(\gamma_d)_{max}$ value in Table 3.3, which is similar to the values obtained in fill. The degree of saturation (*S*) was also estimated for each sample based on the water content, dry density, and an assumed specific gravity equivalent to that measured for the fill material. Histograms for the estimated values of *RC* and *S* are shown in Figure 3.11(a) and (b), and indicate that the majority of the data falls within a range of *RC* ~ 77 to 85% (average ~ 80%) and *S* ~ 15 to 25%. Actual *RC* values should be slightly higher as a result of contraction induced by the fill overburden and minor wetting. Based on oedometer tests performed by a separate geotechnical consultant, the volume change is estimated to have raised the *RC* to ~ 80 to 87% (average ~ 83-84%). We recognize the approximation associated with assuming that the alluvium, which is a natural soil, can be adequately characterized by an *RC* value, which is associated with soil compaction. In particular, compacted laboratory specimens likely have a different soil fabric from the natural alluvium, and these fabric variations may affect the soil's volume change characteristics. However, these assumptions represent our best approximation of the soil properties given the limited available data on the alluvial soils.

3.2.5 Shear Wave Velocity

As noted in Section 3.1.1, shear wave velocities were measured in the borings and SCPT probes using downhole testing. Individual velocity profile logs are shown in the Appendix. A summary of the shear wave velocity data in the fill, alluvium, and bedrock materials is presented in Figure 3.12.

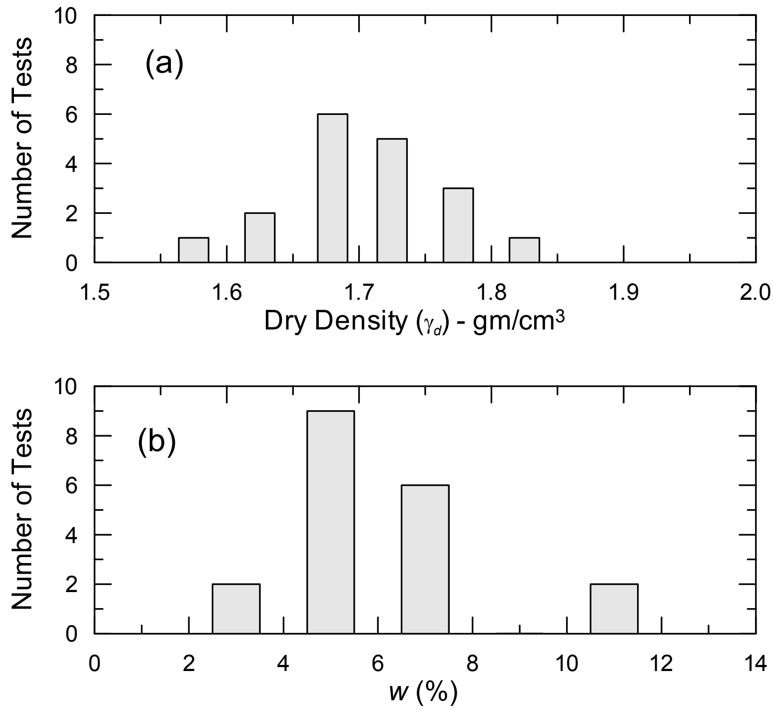

Fig. 3.10(a)–(b). Distribution of dry density (γ_d) and water content (w) in alluvium for Site A, as measured prior to fill construction

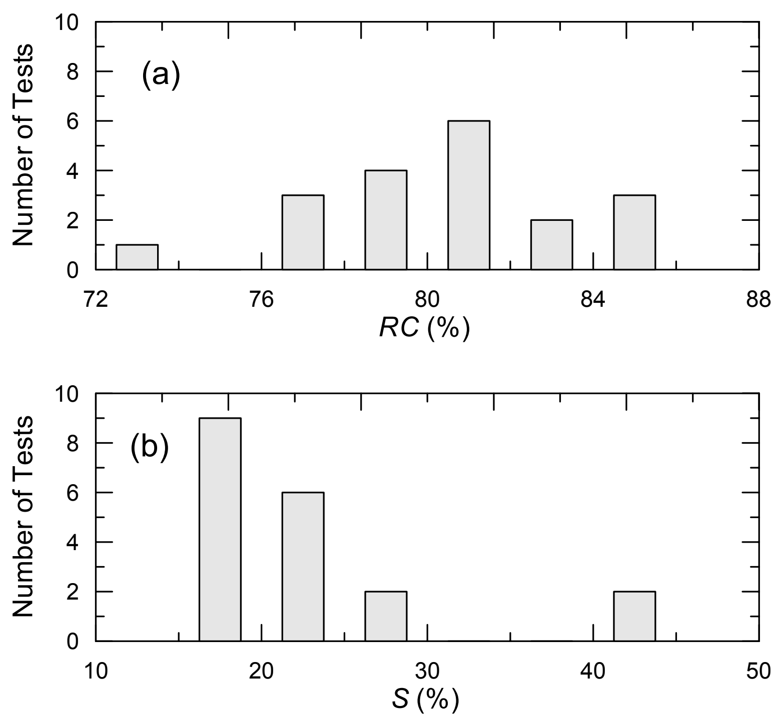

Fig. 3.11(a)–(b). Distribution of estimated relative compaction (RC) and degree of saturation (S) in alluvium at Site A prior to fill construction

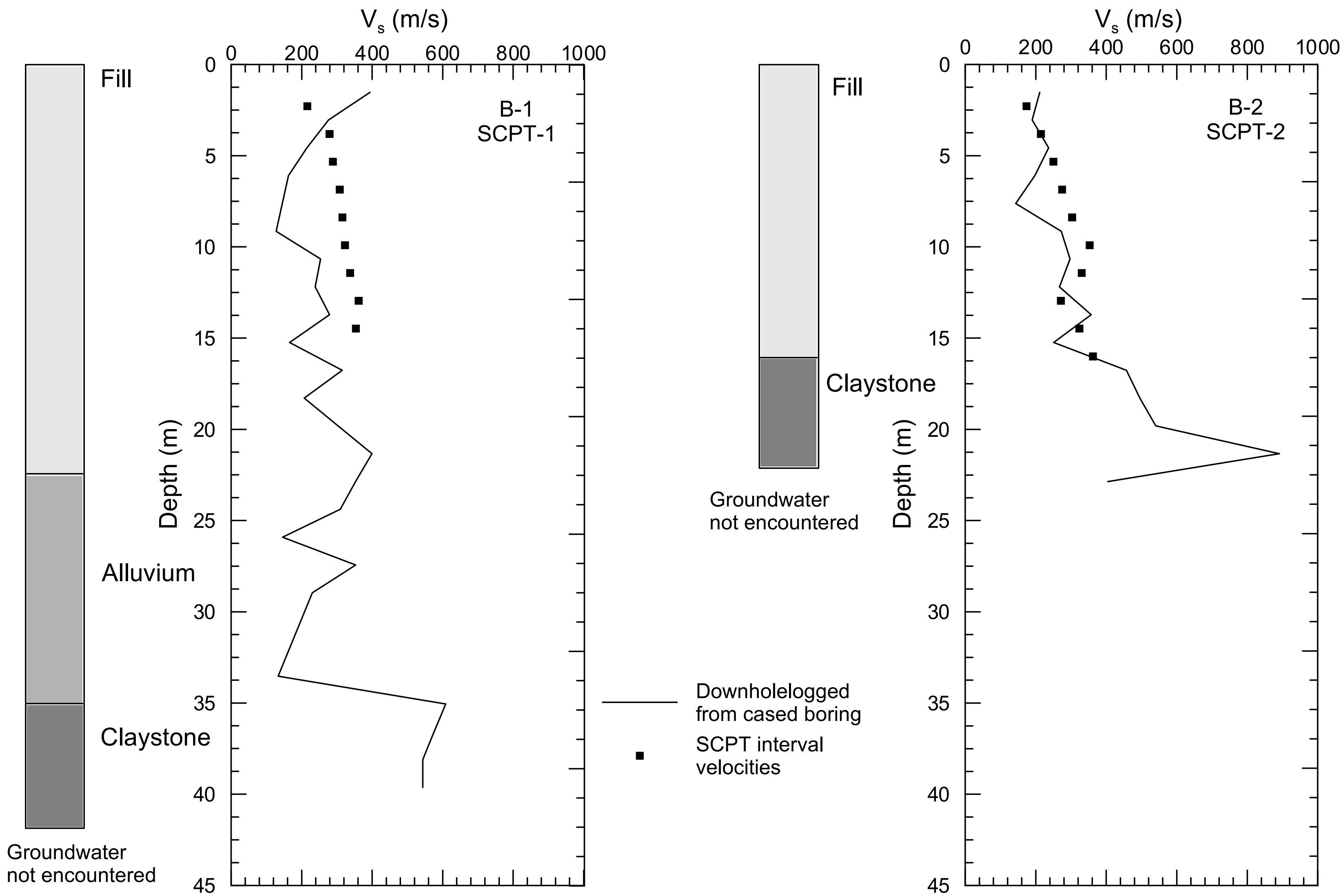

Fig. 3.12. Shear wave velocity profiles measured at Site A

3.3 SITE B CHARACTERISTICS

Site B is located in the Santa Clarita Valley, east of the City of Santa Clarita, and is approximately 7.2 km from the 1994 Northridge earthquake fault rupture plane, based on the fault rupture model by Wald and Heaton (1994).

3.3.1 Stratigraphy

Plan views and cross sections of the 9310 m^2 site are shown in Figures 3.13 and 3.14, respectively. The topographic and depth of fill data are based on as-built construction drawings provided by the project geotechnical engineer. Original topography at the site consisted of several steeply sloping canyons, with a general increase in elevation to the west. The level final grade at the site was realized with cuts into the hillside at the west end of the site, and large fills extending to depths of up to 30.5 m at the east end. All cut areas were overexcavated in order to maintain a minimum depth of fill of about 15 m across developed portions of the site.

Subsurface exploration was performed to verify the conditions depicted on construction documents, to evaluate shear wave velocities in the fill and underlying bedrock materials, and to collect samples for laboratory testing. The subsurface exploration program consisted of three seismic cone penetration tests (SCPTs) in the fill (SCPT-1 to SCPT-3) and one rotary wash boring, which extended through the fill and approximately 33.5 m into bedrock (B-1). The locations of exploration are shown in Figures 3.13 and 3.14. Shear wave velocities were measured using a downhole technique in the SCPTs, and with suspension logging in the borehole. The contractors performing the SPCT work, drilling, and suspension logging were Holguin-Fagan Associates, Pitcher Drilling, and Geo-Vision Inc., respectively. Logs of the SCPT probes and boring are presented in the Appendix.

Soil conditions encountered at the site are consistent with construction documents in terms of the fill depth. The fill soils consist of medium to coarse-grained sands and low-plasticity silts with occasional gravels. The underlying bedrock consists of poorly consolidated and deeply weathered interbedded sandstone and conglomerate belonging to the Saugus Formation. Groundwater was not encountered in any of the CPT holes or the boring.

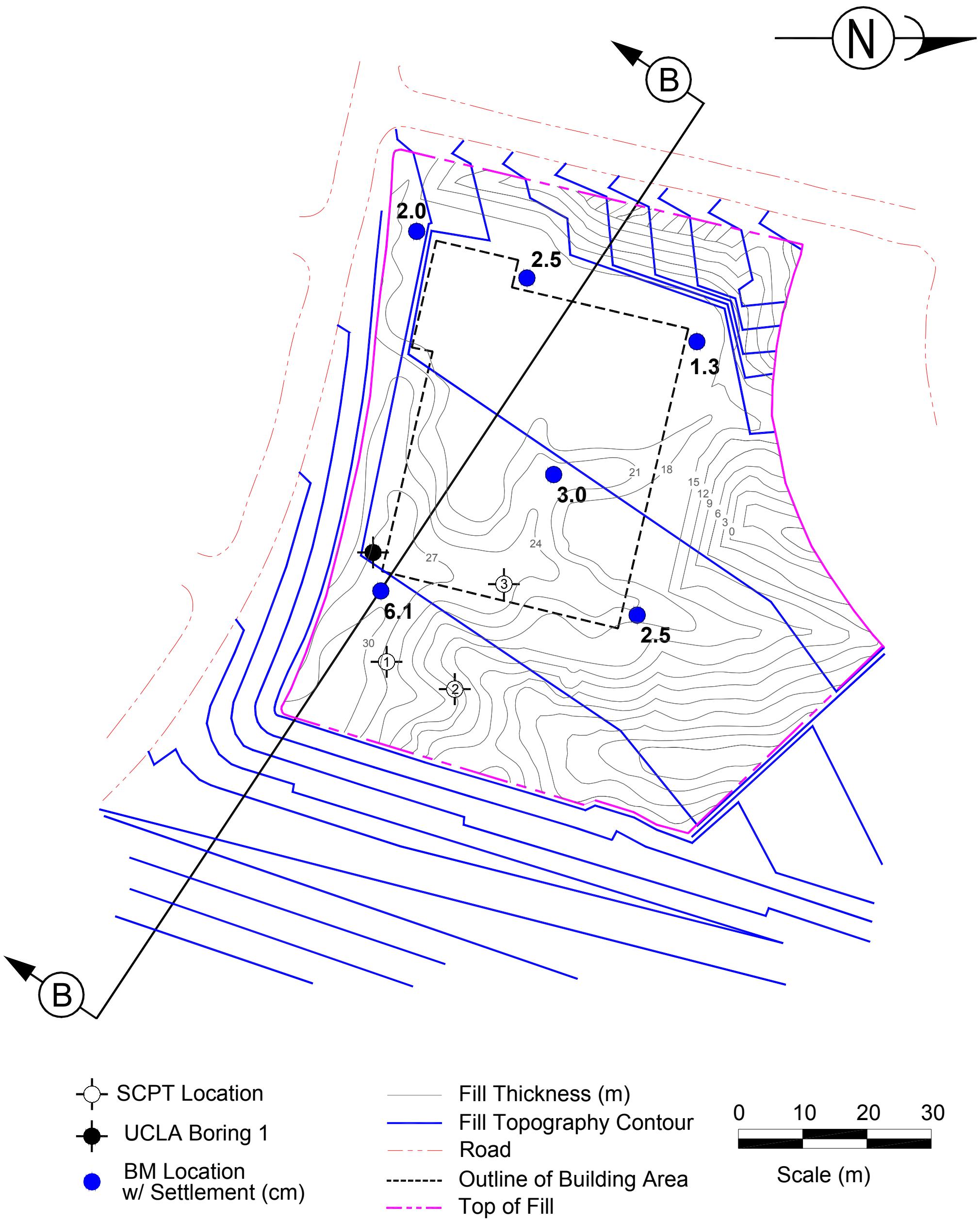

Fig. 3.13. Site B plan view

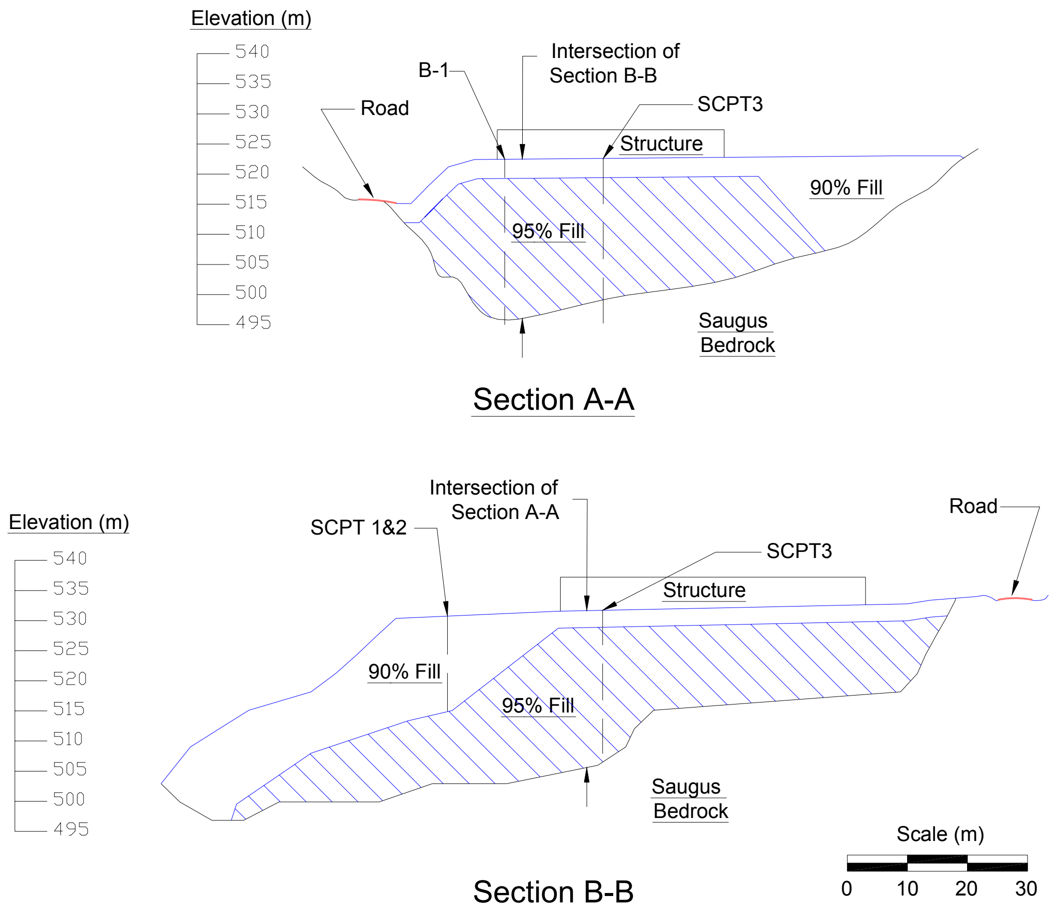

Fig. 3.14. Site B cross sections

3.3.2 Fill Compaction Conditions

In order to minimize potential settlements from hydro-compression, fill placed at the site was required to have as-compacted water contents greater than the optimum water content (w_{opt}) based on the Modified Proctor standard (ASTM D1557). In addition, dual density criteria were employed. The first criterion applied to fills supporting structures and consisted of a minimum relative compaction by Modified Proctor of 95% (RC > 95%), while the second criterion applied to open space areas and consisted of a minimum of 90% RC. In addition, all fill materials at depths > 15 m were subject to the RC > 95% standard, and transitions from the RC > 95% to RC > 90% zones were accomplished with a 2H:1V slope across the top of the RC > 95% zone.

Field tests preformed during construction of the fill between October and November of 1993 document the moisture content (w), dry density (γ_d), and *RC* (Del Yoakum, personal communication). A total of 674 tests were performed in the RC > 90% zone and 506 tests were performed in the RC > 95% zone. Maximum dry density values used at the time of construction for the calculation of *RC* generally ranged from about $(\gamma_d)_{max}$ = 2.00 to 2.14 g/cm^3, with an average of 2.10 (7 different values were reported). A histogram of these values is shown in Figure 3.15. Summary statistics for the distribution of $(\gamma_d)_{max}$, *RC,* and w are shown in Table 3.4.

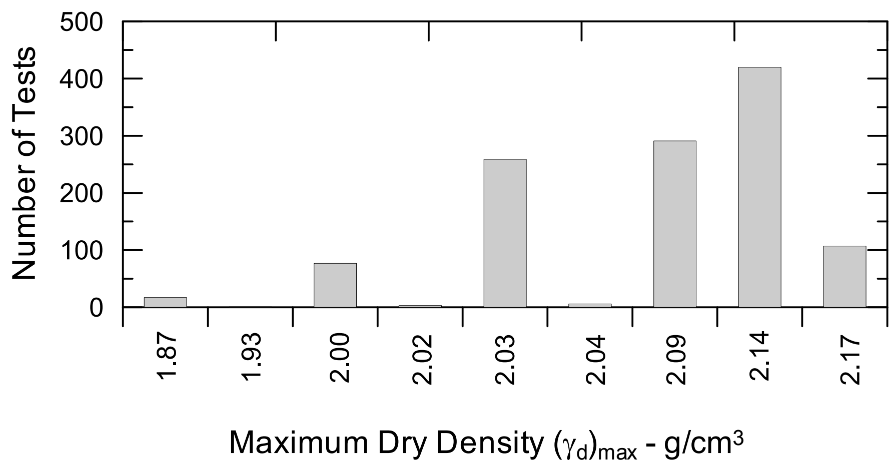

Fig. 3.15. Distribution of maximum dry density values $(\gamma_d)_{max}$ that were used during the construction of fill for Site B

Table 3.4. Summary of statistics for the Site B fill using unadjusted field construction logs

Fill Zone	Compaction Variable	Upper Limit	Lower Limit	Mean	Standard Deviation
RC > 90%	$(\gamma_d)_{max}$ (g/cm^3)	2.17	1.87	2.10	0.06
	RC (%)	94.0	90.0	92.2	1.2
	w (%)	18.0	2.0	12.0	1.6
RC > 95%	$(\gamma_d)_{max}$ (g/cm^3)	2.17	1.87	2.09	0.06
	RC (%)	98.0	95.0	95.6	0.7
	w (%)	19.0	9.0	11.8	1.7

Seven Pitcher tube samples were obtained from Boring B-1. In addition, two bulk samples were retrieved from shallow test pits in fill at various locations around the site. Modified and Standard Proctor compaction tests (ASTM D1557 and D698, respectively) were performed on four reconstituted fill specimens from the Pitcher tubes and one bulk sample with results summarized in Table 3.5. As was the case at Site A, the compaction curves from this testing were reasonably consistent with each other, as indicated in Table 3.5. Accordingly, the data are plotted together in Figure 3.16, and a polynomial regression of the results was used to evaluate representative moisture-density curves for the fill soils.

Table 3.5. Summary of compaction test results on bulk samples of fill from Site B

Sample No.	Boring	Depth (m)	Modified Proctor w_{opt} (%)	Modified Proctor $(\gamma_d)_{max}$ (g/cm^3)	Standard Proctor w_{opt} (%)	Standard Proctor $(\gamma_d)_{max}$ (g/cm^3)
1	B-1	4.6	8.3	2.07	12.0	1.93
2	B-1	7.9	9.0	2.11	10.6	1.94
3	B-1	9.1	8.7	2.11	9.7	1.94
4	B-1	13.7	9.2	2.08	12.4	1.92
5	Bulk	0.0	8.4	2.16	10.7	2.02

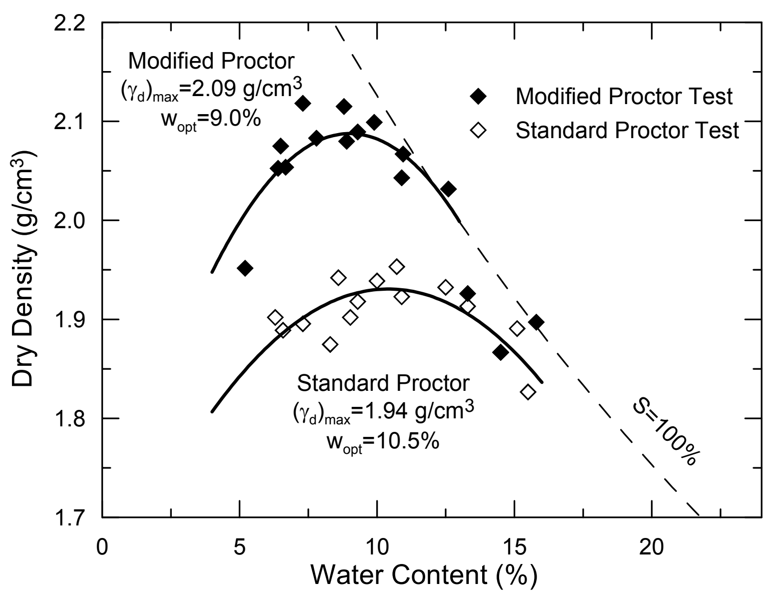

Fig. 3.16. Moisture-density curves for Site B, as evaluated from testing of UCLA samples

The results of our compaction testing are consistent with those obtained at the time of construction. Accordingly, we take the *RC* and *w* values reported by the consultant as representative of the as-compacted condition of the fill. Figures 3.17–3.18 show the resulting distributions of *RC* and *w* for fill in the *RC* > 90% and *RC* > 95% compaction zones, respectively. Table 3.6 summarizes statistics for the compaction conditions at Site B.

Table 3.6. Summary of statistics for Site B fill

	***RC* > 90% zone**		***RC* > 95% zone**	
	***RC* (%)**	***w* (%)**	***RC* (%)**	***w* (%)**
Lower Bound	90.0	9.0	95.0	9.0
Upper Bound	94.0	17.0	98.0	17.0
Mean	92.2	12.0	95.6	11.7
Variance	1.6	2.3	0.5	2.8

Figures 3.17 and 3.18 show that all of the reported tests meet the minimum compaction requirements for the constructed fill. These figures also suggest that the distribution of the dry density data are truncated at the 90% and 95% minimum requirements. It is our judgment that the field test data are likely biased in this regard, meaning that some soil was likely compacted at *RC*s less than the minimum allowable value. We assume that the distribution of *RC* above the minimum value is correct, and use the Kriging geostatistical gridding method (Cressie, 1991) to infer a distribution below the truncation limit. The Kriging gridding method essentially performs this extrapolation based on the trends of the data at higher *RC*. The inferred data distribution was then used to develop "synthetic" data to supplement the actual data, and the combined data set was then used to evaluate the relative likelihood of various *RC* and *w* values in the field. The results were then contoured using the methods described in Section 3.1.2, and are shown in Figures 3.19–3.20. Also shown in Figures 3.19–3.20 are Standard and Modified Proctor moisture-density curves and contour lines for constant degree of saturation based on G_s=2.70. As expected, the mode using the new data set is identical to that of the reported *RC* values (~92-93% in the *RC* > 90% zone, and 95% in the *RC* > 95% zone). Fill in the *RC* > 90% zone spans the line of optimums, whereas fill in the *RC* > 95% zone is generally wet of the line of optimums. Note the significant difference in the position of these compaction data relative to the line of optimums as compared to the data from Site A (Figure 3.8).

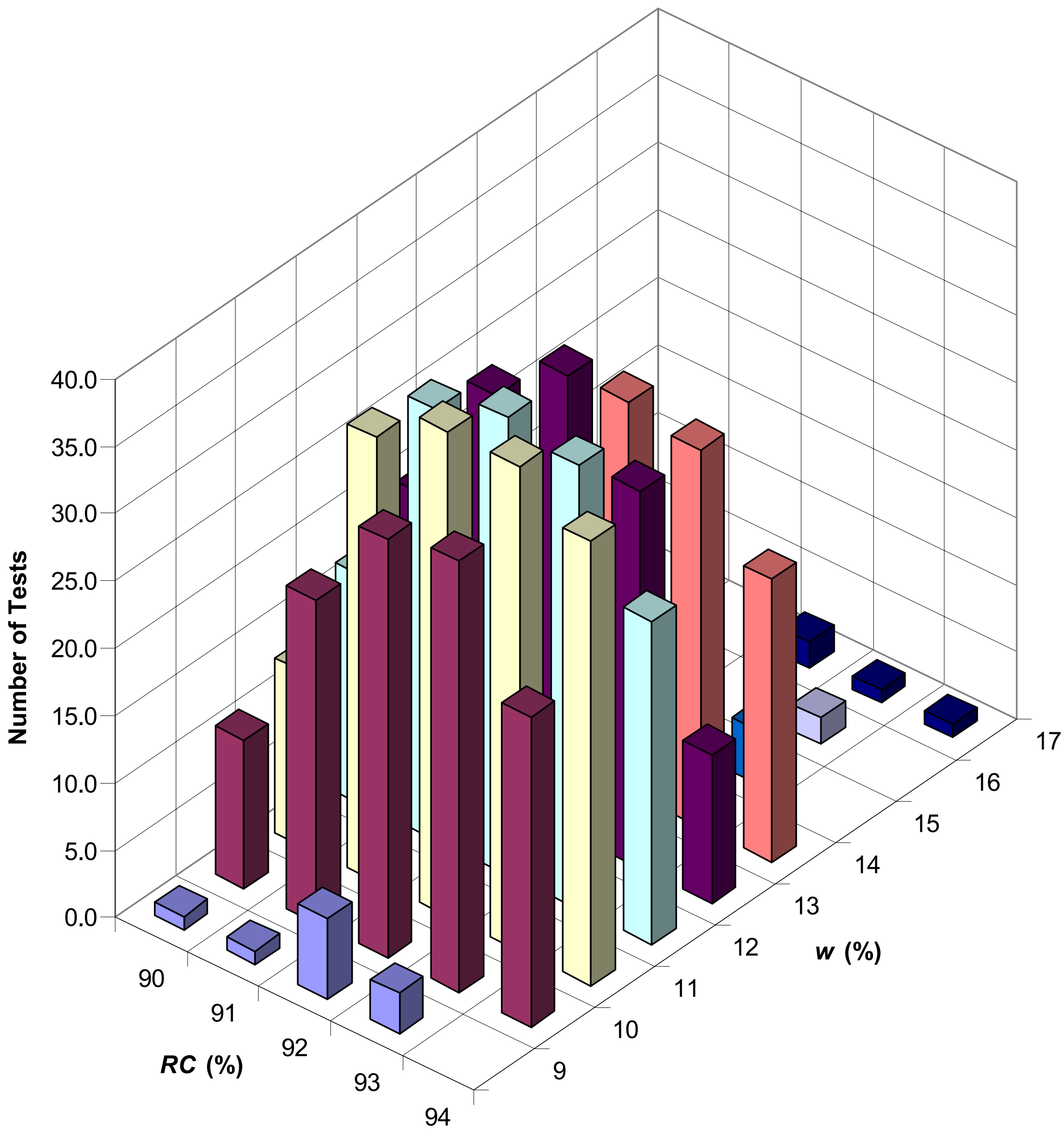

Fig. 3.17(a). Distribution of reported compaction test results in the Site B *RC* > 90% zone

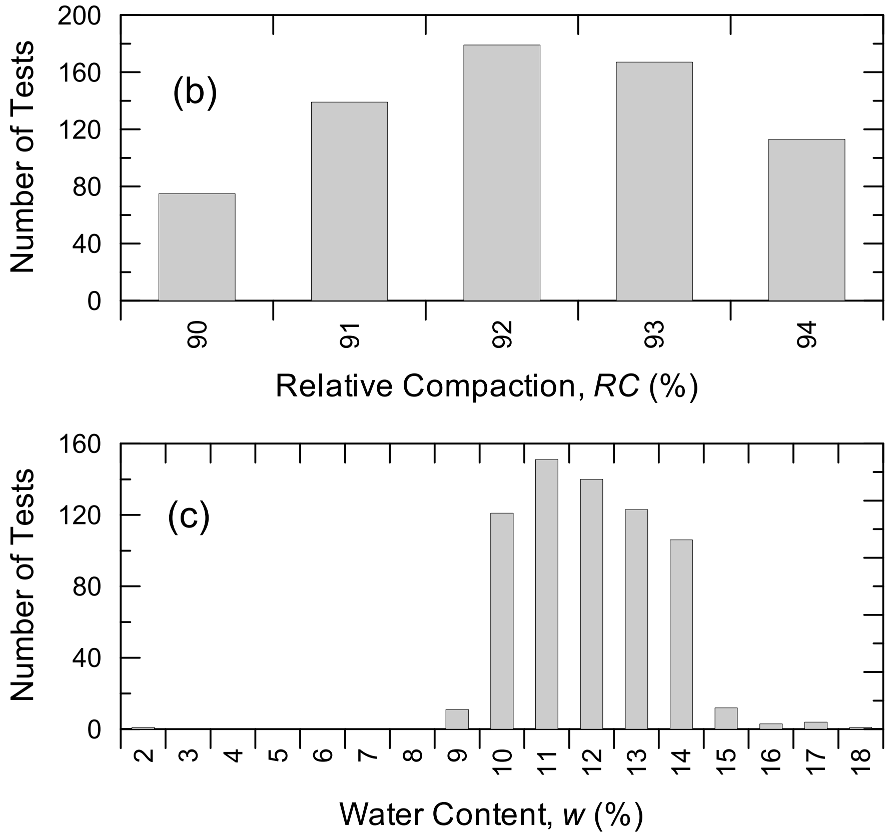

Fig. 3.17(b)–(c). Distribution of relative compaction (*RC*) and water content (*w*) in fill for the Site B *RC* > 90% zone

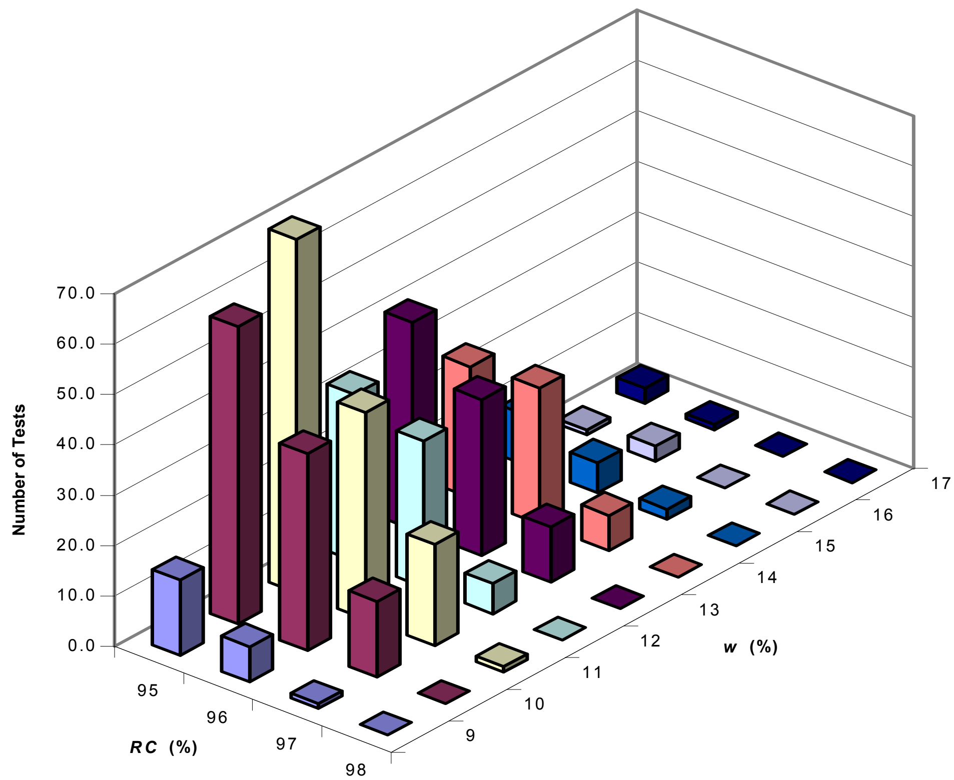

Fig. 3.18(a). Distribution of compaction test results in the Site B *RC* > 95% zone

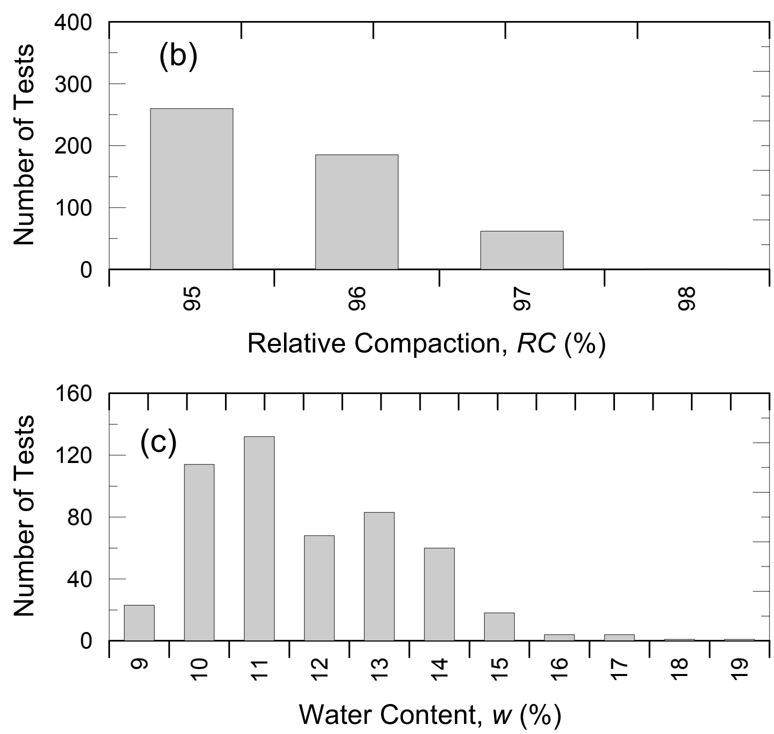

Fig. 3.18(b)–(c). Distribution of relative compaction (*RC*) and water content (*w*) in fill for Site B *RC* > 95% zone

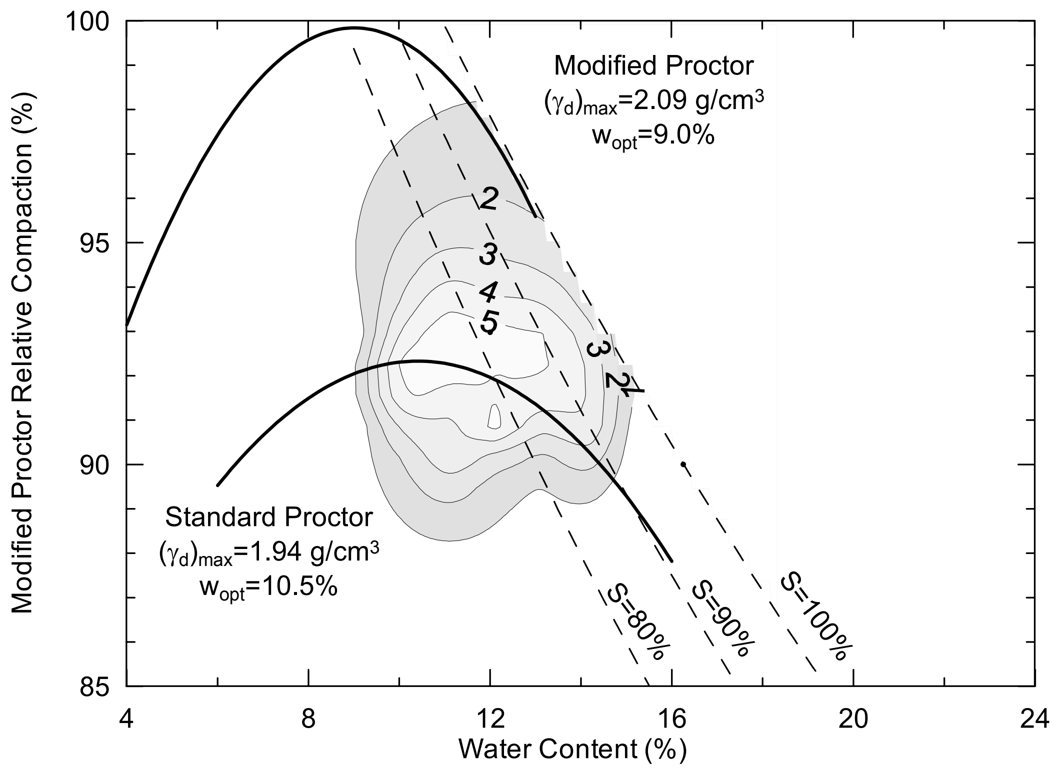

Fig. 3.19. Site B (*RC* > 90% zone) relative likelihood of compaction conditions

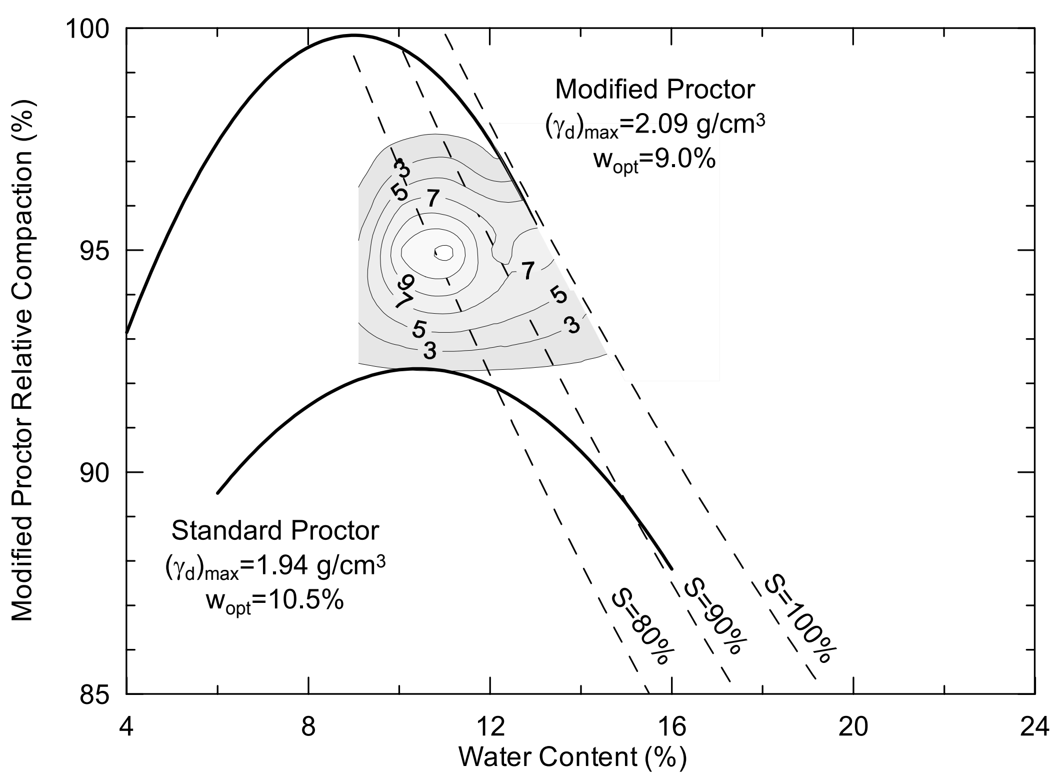

Fig. 3.20. Site B (*RC* > 95% zone) relative likelihood of compaction conditions

3.3.3 Index Testing

Sieve/hydrometer analyses (ASTM C136 and D422) and Atterberg Limit tests (ASTM D4318) were performed on samples taken from various depths in the fill and two bulk samples from test pits. Results of these tests are reported in Table 3.7. Figure 3.21(b) shows the mean and mean ± one standard deviation grain-size distribution plots for fill soils. All of the tested fill samples were well graded ($C_u \geq 6$, as per ASTM D2487), and the fines content varied from 43–61% (average=52%). The specific gravity of the fill soil, tested per ASTM D854, was found to be 2.70.

Table 3.7. Summary of index test results on samples from Site B

Boring	Depth (m)	%Clay	%Fines	D_{60} (mm)	D_{10} (mm)	D_{30} (mm)	PI	LL	Cu	Cc	Type
B1	1.7	8	50	0.14	0.0025	0.031	2	26	56	3	Fill
	3.5	6	44	0.18	0.0044	0.038	2	26	41	2	Fill
	4.4	5	40	0.14	0.0031	0.030	14	35	45	2	Fill
	5.2	5	50	0.15	0.0029	0.024	9	33	52	1	Fill
	6.6	6	52	0.13	0.0045	0.026	6	29	29	1	Fill
	8.2	4	48	0.29	0.0032	0.040	9	30	91	2	Fill
	8.8	10	44	0.17	0.0090	0.020	2	27	19	0	Fill
	10.8	5	45	0.18	0.0050	0.034	2	27	36	1	Fill
	14.5	2	52	0.11	0.0075	0.038	4	27	15	2	Fill
	16	5	45	0.17	0.0050	0.035	5	28	34	1	Fill
	23.2	5	46	0.16	0.0058	0.036	5	27	28	1	Fill
	26.2	8	36	0.27	0.0034	0.046	5	28	79	2	Fill
Bulk 1	0	4	44	0.17	0.0031	0.032	2	27	55	2	Fill
Bulk 2	0	5	46	0.18	0.0040	0.038	4	28	45	2	Fill

Figure 3.21(a) summarizes the Atterberg Limit test results. All of these soil samples were classified as low-plasticity silt (ML) or silty sand (SM) according to the Unified Classification System (UCSC) and the average Liquid Limit and Plasticity Index were 28 and 5, respectively.

3.3.4 Shear Wave Velocity

A summary of the shear wave velocity data in the fill and bedrock materials is presented in Figure 3.22. Velocities in the *RC* > 90% fill were obtained from SCPT-1 to 3 and B-1, whereas only SCPT-3 and B-1 provided velocities in *RC* > 95% fill. Velocities in the Saugus Formation bedrock are based solely on the suspension logging in B-1.

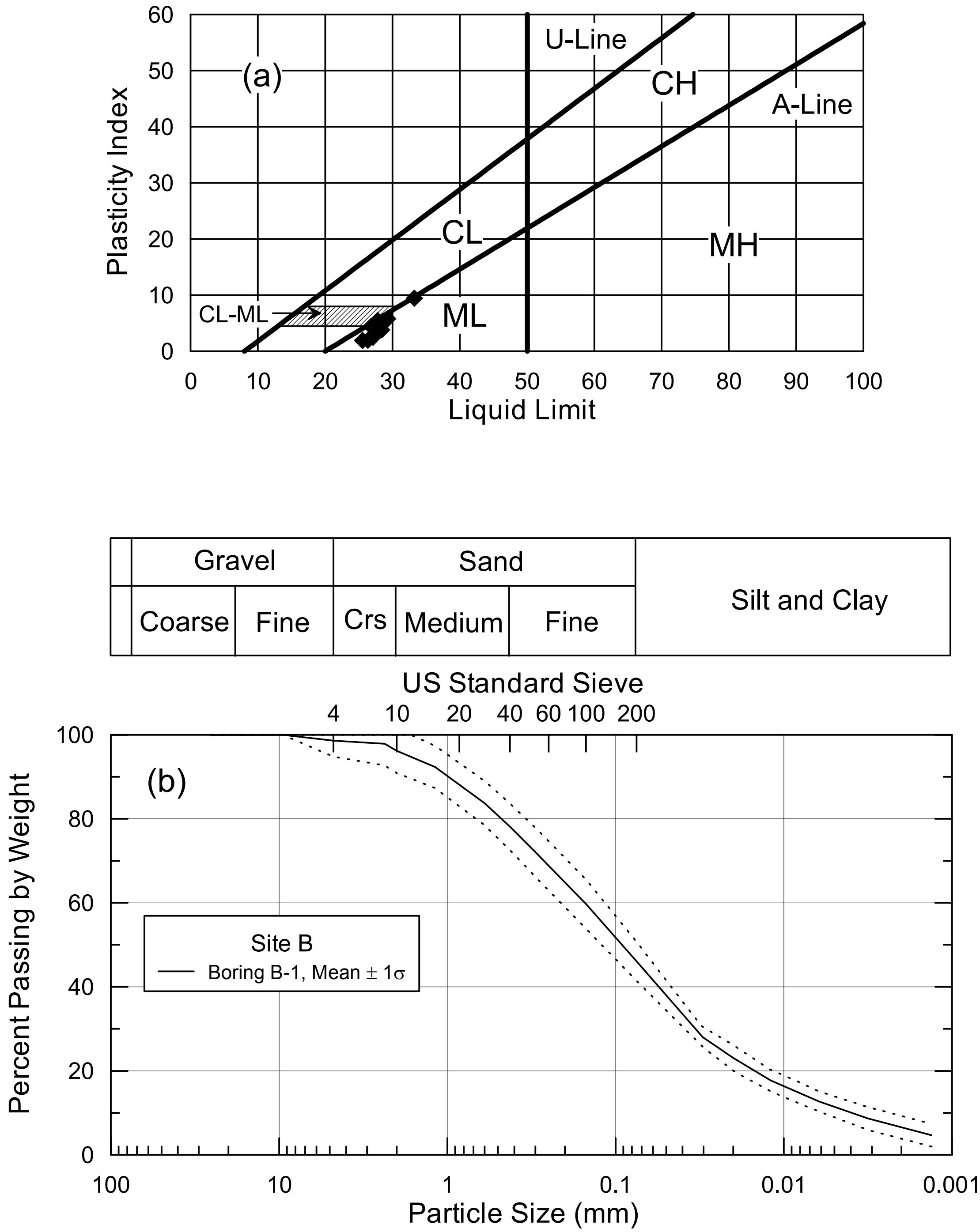

Fig 3.21. Plots of (a) plasticity data and (b) average grain-size distribution for fill soils at Site B

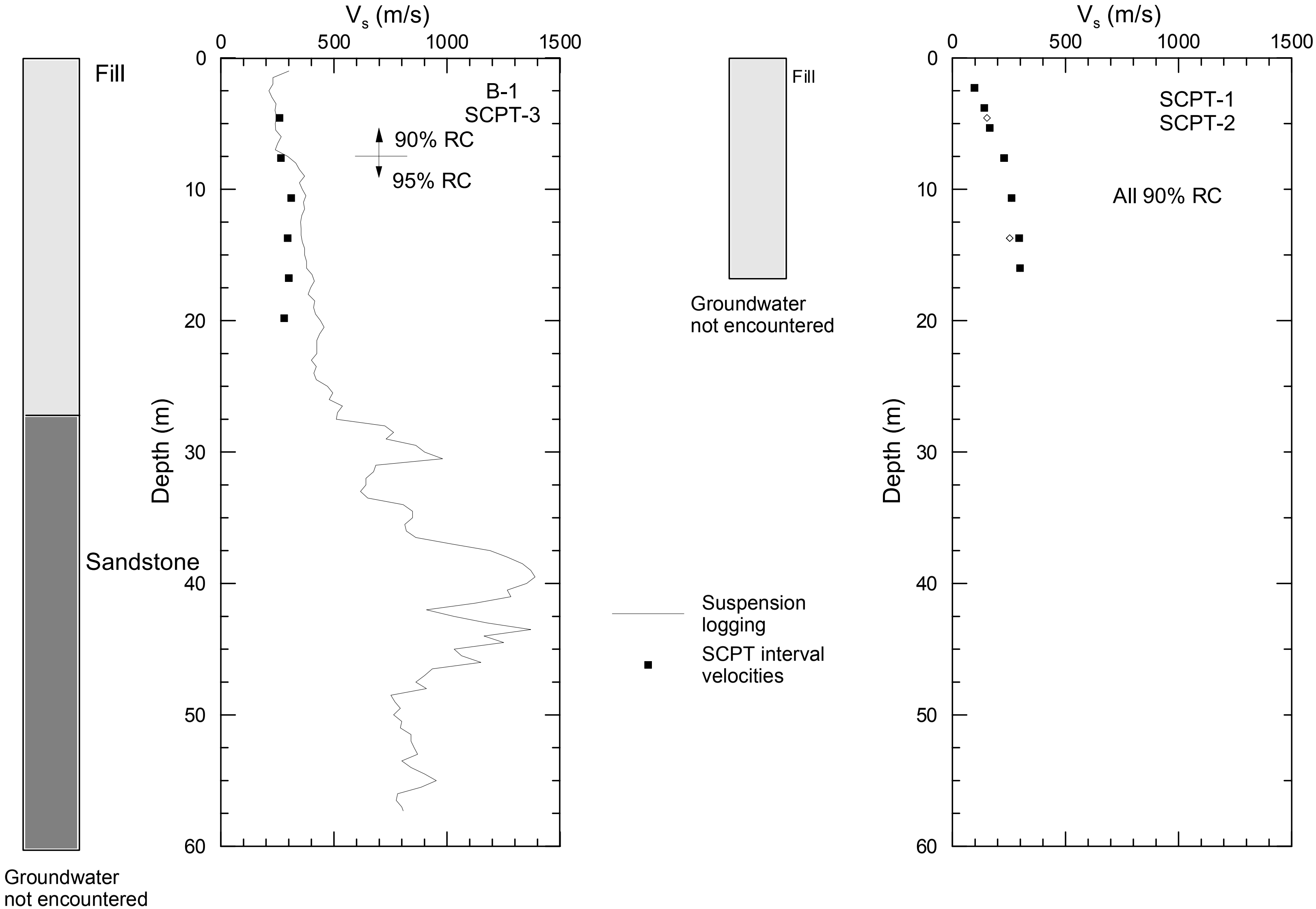

Fig. 3.22. Shear wave velocity profiles from SCPT and suspension logging for Site B

3.4 GROUND DEFORMATIONS RESULTING FROM THE 1994 NORTHRIDGE EARTHQUAKE

3.4.1 Site A

Vertical surface displacements at Site A were established from pre– and post–Northridge earthquake surveys of floor elevations in the building. Horizontal movement survey data are unavailable, but significant horizontal deformations were not evident from floor crack patterns nor from cracking of pavement outside of the building. The pre–earthquake data are from as-built drawings dated October 31, 1991. Elevations on these drawings were based on a post–construction survey by a licensed land surveyor, and reflect elevations after the installation of flooring. Post–earthquake data are based on a survey (made by the same licensed land surveyor) performed on January 25, 1994. Interviews of the surveyor by the authors indicated no change in the flooring material, suggesting that the difference in elevation from these two surveys can be used to estimate floor settlements between the specified dates.

The maximum observed settlement was 21.6 cm at the southwest corner of the building, which is located over about 20.3 m of fill. As shown in Figure 3.2(b), the amount of settlement generally increases with depth of fill, and no appreciable settlement was measured in cut areas.

As approximately 26 months elapsed between the pre– and post–earthquake surveys, it is likely that some of the observed settlements occurred before the earthquake as a result of hydro-compression. Interviews of permanent staff working at Site A indicated no perceptible distress from settlement. These staff report noticing significant settlements only after the earthquake, and as they have no financial interest in the cause of the settlement (i.e., they are not participants in legal actions), their statements are considered unbiased. These observations suggest pre–earthquake settlements were small, but not necessarily zero.

Water content data from Geo-Resources (1991) and from our borings (1998 — see Appendix) are shown in Figure 3.23. These data provide evidence for wetting across the upper ~10–15 m of the site, with near surface water contents rising from ~10% to ~14%, which corresponds to a change in degree-of-saturation from $S \sim 60\%$ to $\sim 80\%$. It does not appear that significant wetting occurred at depths > 15 m. Based on the results of response to wetting tests performed on the fill soils (by Geo-Resources, 1991 and from this study), standard hydro-compression analyses were performed (Coduto, 1994) to estimate settlements associated with the above change in saturation.

The results suggest the 1991 to 1998 settlements were likely in the range of 6 to 20 cm, with a best estimate of 12 cm. The variability in the analysis results is associated with variability in the laboratory response to wetting tests.

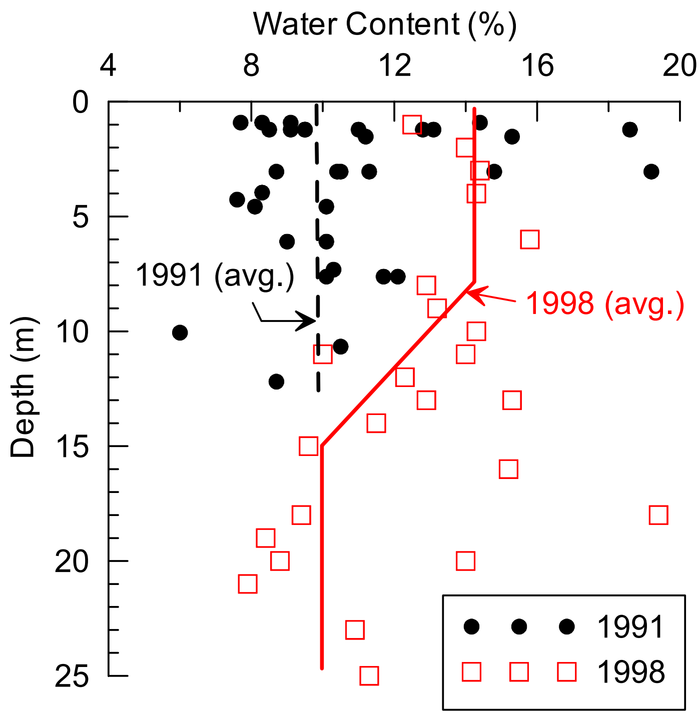

Fig 3.23. Water content data in fill at Site A from October 1991 and March 1998 geotechnical investigations

Because these hydro-compression settlement estimates are based on water content changes between October 1991 and March 1998 at locations near irrigated portions of the building perimeter, we can only speculate as to (1) how much of the hydro-compression settlement occurred by January 1994 (at the time of the earthquake) and (2) how much settlement and water content change occurred at locations within the building envelope.

With respect to the variations in hydro-compression settlement between 1994 and 1998, natural precipitation between 1991 and 1998 at the nearest weather stations averaged 40 cm/year, which is much less than the water likely introduced to the fill near the building perimeter from irrigation of lawns near the building. As the lawn irrigation introduces a consistent rate of infiltration, it would seem reasonable that the fraction of the 1998 settlement that had occurred by 1994 would approximately match the ratio of elapsed times since 1991 (this ratio is about 1/3). By this reasoning, the best estimate of 1994 settlement is approximately 4 cm for portions of the site with ≥ 10 m of fill, and the likely range of settlements for this fill depth is estimated to be 2 to 10 cm (allowing for uncertainty in the 1991-1994 / 1991 – 1998 settlement ratio).

The above settlement calculation is considered appropriate along portions of the building perimeter with adjacent lawns, where most of the samples used for water content testing were obtained. The data are also likely appropriate within the building envelope in canyon areas adjacent to the building perimeter, as subsurface water will tend to naturally migrate to such areas. The above settlement estimates are likely not appropriate in areas that are both within the building envelope and which overlie sloping canyon walls. In these areas, water content changes are likely to be smaller. As a first order estimate, hydro compression settlements in these areas are estimated to be approximately 25-50% of those near irrigated portions of the building perimeter.

3.4.2 Site B

Horizontal and vertical surface displacements at the site are known from pre– and post–Northridge earthquake surveys. The surveys were performed after construction of the fill, but before construction of buildings and other improvements. The surveys were performed on January 14, 1994 and January 21, 1994 by the same surveyor. In these surveys, the position of the fill at a given time was referenced to a rock outcrop adjacent to the site.

Horizontal displacements were negligibly small. The settlement data at six monuments on the fill are shown in Figure 3.13. The maximum observed settlement was 6.1 cm at Monument 3, which is located over about 5.2 m of $RC > 90\%$ fill and 23.5 m of $RC > 95\%$ fill. Other monuments generally were underlain by about 3.0 m of $RC > 90\%$ fill and variable depth of $RC > 95\%$ fill, and experienced 1.3 to 3.0 cm of settlement.

4 Seismic Compression of Sands

4.1 INTRODUCTION

As noted in Chapter 2, ground deformations induced by the 1994 Northridge earthquake in typical fill geometries have been found to be principally associated with volumetric strain in fill, as opposed to permanent shear strain. The term "seismic compression" is used to describe volumetric strain accumulation in unsaturated soil during earthquake shaking. Prior to this study, most of the available information on seismic compression was based on limited laboratory testing of clean sandy soils under simple shear loading conditions. This work was performed in the late 1960s and early 1970s, and was complementary to additional, pioneering studies of soil liquefaction. While the soil liquefaction testing research would ultimately examine a myriad of compositional factors (e.g., gradation, grain-size, and D_R) and environmental factors (e.g., confining stress, presence of static shear stress, stress history/OCR, and ageing), the seismic compression work was considerably more limited in scope.

In this chapter, we review prior work on the seismic compression of sand and summarize the results of sand testing performed in this study. Additional details on the sand testing program performed in this study are presented by Whang (2001).

4.2 PRIOR LABORATORY STUDIES

The pioneering works of Silver and Seed (1971), Youd (1972), Seed and Silver (1972), and Pyke et al. (1975) used laboratory studies to investigate the volumetric strains induced in dry, clean sands undergoing cyclic loading with zero mean (static) shear stress.

Silver and Seed (1971) and Seed and Silver (1972) performed strain-controlled simple shear testing using an NGI-type device on dry quartz sand (Crystal Silica No. 20). The specimens were prepared by dry pluviating a preweighed amount of sand, and then vibrating it to a specified height such that the target density (D_R = 45, 60, and 80%) was achieved. The tests were performed by first applying a specified vertical stress to the specimen (values of σ_v' = 24, 96, and 192 kN/m^2 were used), and then subjecting the specimens to a uniform cyclic shear strain amplitude that varied from γ_c = 0.01 to 0.5%. Continuous readings of vertical deformation were made that enabled vertical strains to be evaluated as a function of the number of strain cycles (N). Figure 4.1 shows a summary of test results at N = 10 cycles of loading for the three relative densities. The vertical strain was seen to increase with cyclic shear strain amplitude, and to decrease with increasing relative density. The vertical strains were found to be negligible below a limiting value of shear strain. Denoted γ_{tv}, this limiting strain has since come to be known as the volumetric threshold shear strain (Vucetic, 1994). Typical values of threshold shear strains for sands are γ_{tv} = 0.01 to 0.03% (Vucetic, 1994).

The dependence of vertical strain on the number of strain cycles was relatively consistent for the suite of test results, as shown in Figure 4.2. These results demonstrate a characteristic feature of seismic compression, which is that a significant fraction of the overall volumetric strain occurs within the first few cycles (e.g., 50% of the volumetric strain at 15 cycles occurs within the first 3 cycles), and relatively little deformation occurs for N > 100. Several suites of tests were performed at different vertical stresses (σ'_v), but vertical strain was found to not be significantly affected by σ'_v.

Youd (1972) investigated seismic compression of Ottawa Sand using simple shear laboratory testing with an NGI-type device. The specimens were prepared by pouring sand into a membrane and in some cases, vibrating the top cap to densify the specimen. Youd performed one subset of tests on specimens that were saturated, consolidated under vertical stresses of σ'_v = 5, 48 and 192 kN/m^2, and then sheared under drained conditions. Volume change was monitored by a water column (equipped with a pressure transducer) that was connected to the specimen. A second subset of tests was performed using air-dry specimens. In both subsets of tests, specimens were generally prepared to relative densities of D_R = 70–80%. For each test, sinusoidal loading was applied at a constant frequency that was varied from test-to-test across the range of f = 0.2 to 1.9 Hz. During an individual test, shear strain amplitudes varied somewhat with time as a result of compliance in the loadcell. Accordingly, applied shear strains were reported as a range rather than as a unique value.

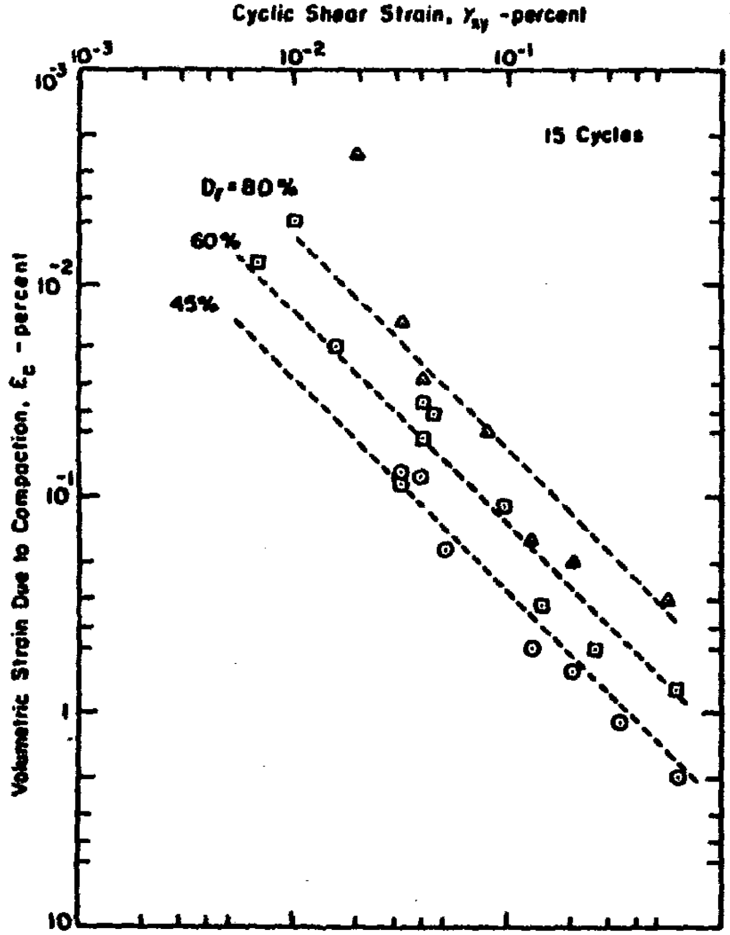

Fig. 4.1. Effect of relative density on settlement of dry sand (Silver and Seed, 1971)

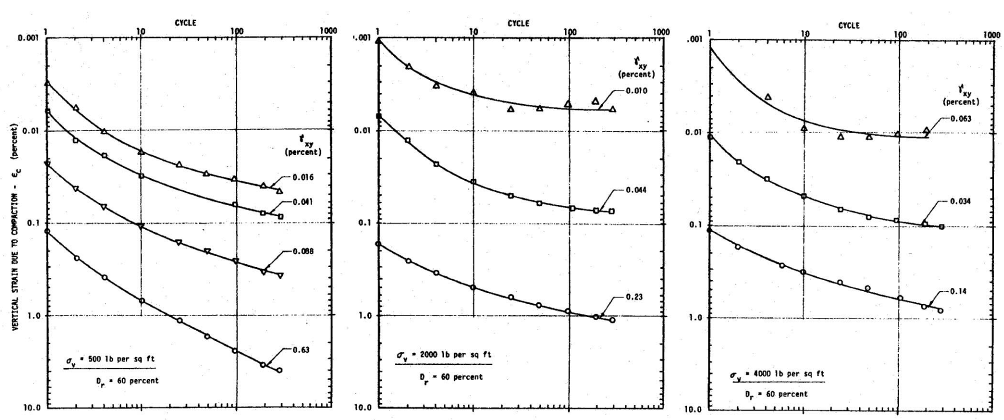

Fig. 4.2. Settlement-number-of-cycles-relationships for D_R = 60% (Silver and Seed, 1971)

The results of selected tests on Ottawa Sand are presented in Figure 4.3, with the Silver and Seed results also indicated for comparison. The Ottawa Sand results confirm the finding of Silver and Seed that vertical strains increase with increasing shear strain, but the vertical strains are systematically higher (by factors of 4 to 6) than those of Silver and Seed for Crystal Silica No. 20 Sand. The reasons for this difference are unknown. The results of Youd's tests investigating saturation and frequency of loading effects revealed no significant influence of either factor.

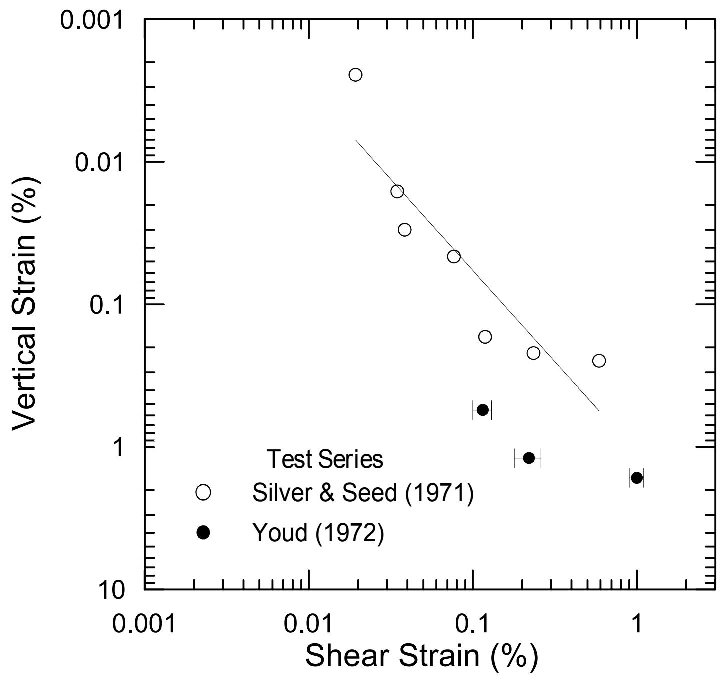

Fig. 4.3. Comparison of vertical strains at 10 cycles for Ottawa Sand at D_R = 80% (Youd, 1971) and Crystal Silica Sand at D_R = 80% (Silver and Seed, 1971)

Pyke et al. (1975) investigated the seismic compression of dry Monterey No. 0 Sand using large-scale specimens tested on a shaking table. The disk-shaped specimens were prepared to

D_R = 40, 60, and 80% by raining sand from a spreader box into a 7.6 cm deep form, temporarily mounted on top of the shaking table. The form was slightly overfilled and the excess sand was removed with a screed. The specimens had sloping lateral boundaries, which were enclosed by a rubber membrane. Vertical stresses were applied by the weight of a steel cap (7.7 kN/m^2) placed on top of the sand and vacuum pressures applied to the specimen. All testing was performed under stress-controlled conditions, and the shear strains that occurred during the tests were not reported.

The intent of the shaking table tests by Pyke et al. (1975) was to evaluate the effect of multi-directional shaking (two horizontal directions and one vertical). The results of uni-directional, bi-directional (two horizontal directions of shaking), and tri-directional (two horizontal and one vertical direction of shaking) are compared in Figure 4.4. Based on the results, Pyke et al. surmised that the settlements caused by the combined horizontal motions are about equal to the sum of the settlements caused by the horizontal stresses acting separately. Since peak accelerations in two horizontal directions are often similar, Pyke et al. recommended that settlements under bi-directional shear generally be taken as about twice those under uni-directional shear. Moreover, as indicated by the results in Figure 4.4, Pyke et al. found that vertical accelerations superimposed on horizontal accelerations could cause an additional increase in the settlements of as much as 50%.

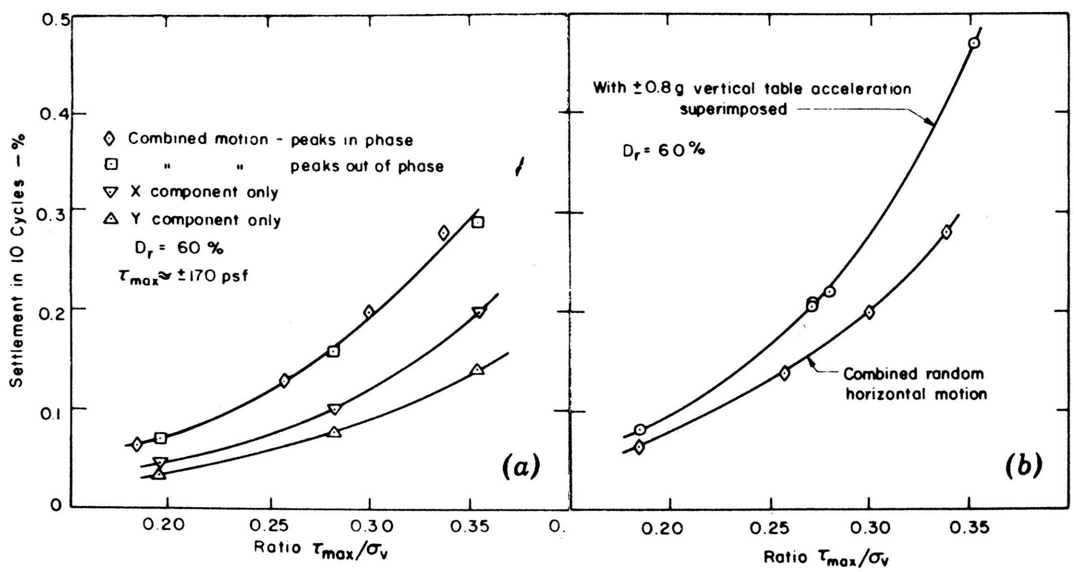

Fig. 4.4. Comparison of settlements of sand from shaking table tests performed (a) under uni-directional and bi-directional stress-controlled loading and (b) under three-directional stress-controlled loading (Pyke et al., 1975)

4.3 LABORATORY TESTING OF CLEAN SANDS IN PRESENT STUDY

4.3.1 Materials Tested

A limited simple shear testing program for clean sandy soils was performed to provide a baseline set of results against which the test results for soils with fines could be compared (this is done in Chapter 5). The cyclic simple shear tests were performed under drained conditions to evaluate the vertical strain accumulation in sand subjected to uniform-amplitude cycles of shear strain. The simple shear apparatus used for soil testing is discussed in detail by Whang (2001). The soils tested included:

1. A uniform fine sand (Crystal Silica No. 30) similar to that tested by Silver and Seed (1971) (denoted as Sand D).
2. Bulk samples of fill soils from field Sites A and B. The sand specimens were created by removing the fines via wet-sieving the soil through a #200 sieve. These materials are denoted Sands A and B.
3. A well-graded, fine sand (denoted as Sand C).

Grain-size distributions for these four sands are shown in Figure 4.5, and index properties are presented in Table 4.1. The maximum and minimum densities and void ratios for each of the sands were determined by the Modified Japanese method and dry tipping, respectively. These techniques are comparable to those in ASTM D4253 and D4254.

Table 4.1. Index properties of tested sands

Sand	e_{max}*	e_{min}*	D_{50} (mm)	c_u**
A	0.693	0.439	0.34	5.0
B	0.931	0.534	0.25	4.9
C	0.825	0.490	0.52	3.0
D	1.042	0.668	0.52	1.5

*e_{max} and e_{min} calculated assuming G_s = 2.7
**C_u = coefficient of uniformity, D_{60}/D_{10}

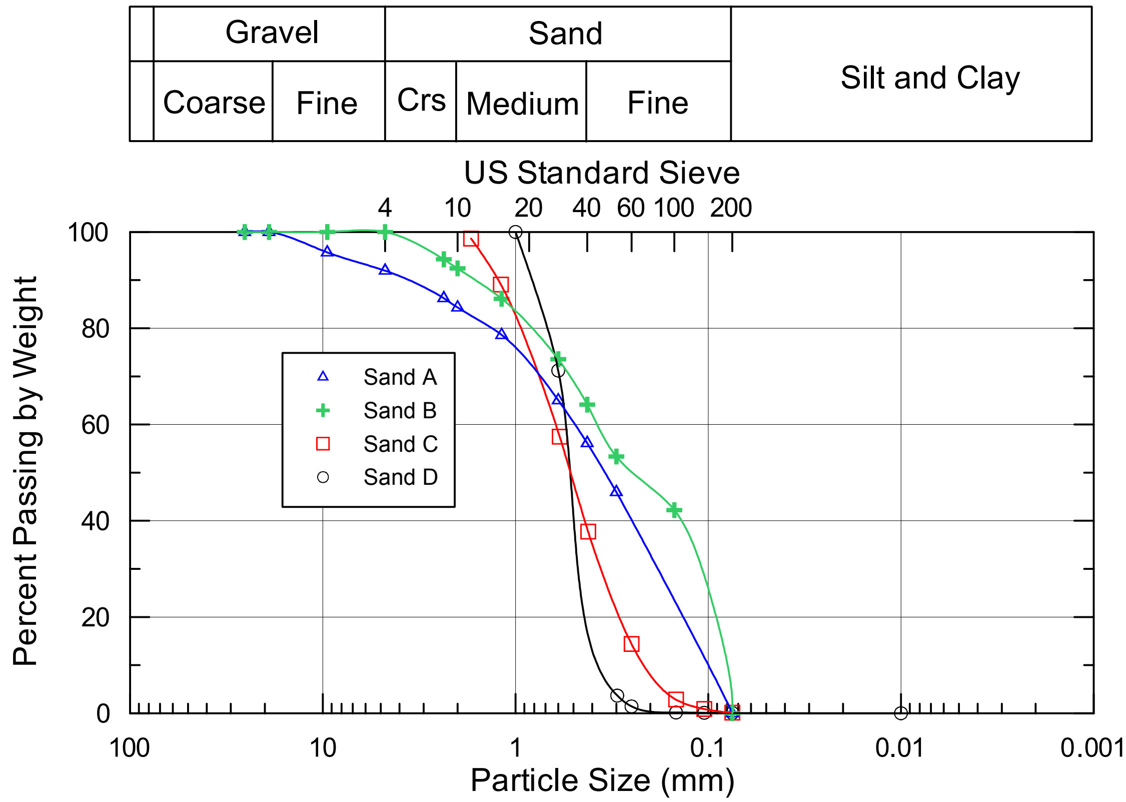

Fig. 4.5. Grain-size distributions of tested sands

4.3.2 Specimen Preparation and Testing Procedures

The specimens were prepared by pouring a preweighed amount of sand into a wire-reinforced membrane premounted on the apparatus bottom cap with a screen at the bottom of a mold. The screen was then pulled up through the specimen to give each specimen essentially the same initial structure. After flattening the specimen and positioning the top cap, a high-frequency (60 Hz) vibrator was placed on the top cap to densify the specimen to a predetermined height that would achieve the appropriate relative density after application of the vertical stress of 101.3 kPa. This specimen preparation procedure is very similar to that performed by Silver and Seed (1971). An isotropic vacuum pressure of 33.8 kPa was applied to the specimen when mounting it into the device to minimize disturbance. This vacuum pressure was removed before application of vertical stress to avoid overconsolidating the specimen.

All tests were performed at σ_v'=101.3 kPa with a sinusoidal loading frequency of 1 Hz. Sinusoidal loading was strain-controlled and the sand specimens were dry. The testing was performed under these conditions in part because of findings of previous research presented in Section 4.2 (i.e., insignificant effects of σ'_v, loading frequency, and $S = 0$ versus $S = 100\%$ on vertical strains from seismic compression).

4.3.3 Test Results

The results of a typical strain-controlled cyclic simple shear test are presented in Figure 4.6 (Crystal Silica Sand, $\gamma = 0.1\%$, $D_R = 60\%$). The shear strain amplitude is seen to be uniform in time, while the shear load amplitude gradually increases over the first few cycles due to strain hardening of the specimen.

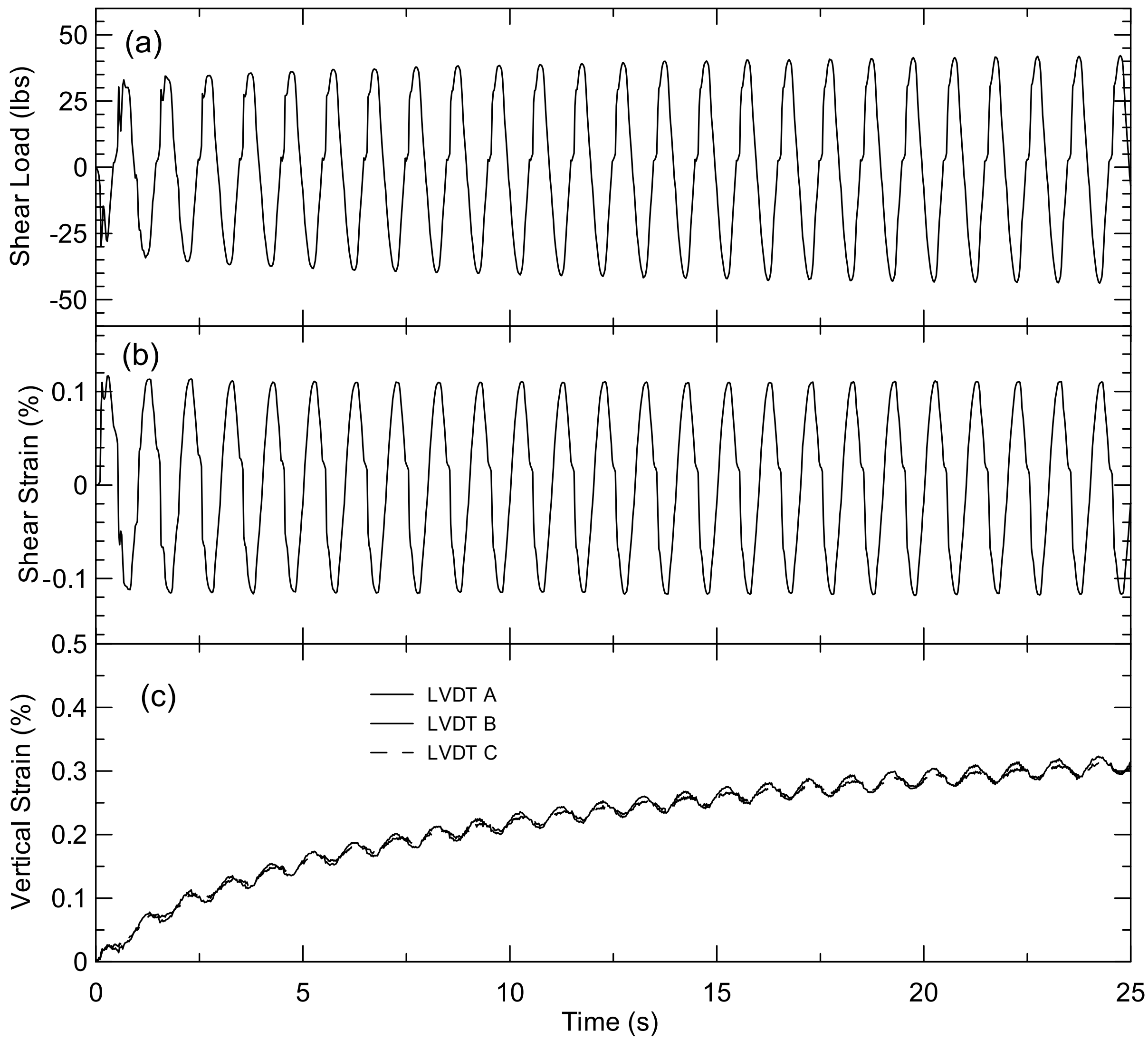

Fig. 4.6. Representative results of a cyclic simple shear test (Sand D, $D_R = 60\%$, $\gamma = 0.1\%$)

The time history of vertical strain has two characteristic features. First, there is a steady, but nonuniform increase of vertical strain with the number of strain cycles, with ~50% of the 25-cycle deformation occurring within the first five cycles, and only ~20% occurring after 15 cycles. Second, superimposed upon the steady increase of vertical strain with time are small amounts of transient contraction and dilation that occur in phase with the shear strain forcing function. For the purpose of this study, the vertical strain at a given number of cycles is taken as a running-average vertical strain (i.e., strains associated with transient contraction and dilation are neglected).

Representative results from this testing program are presented for Sand D in Figure 4.7, which shows a summary of vertical strains at 10 cycles for specimens prepared to D_R = 60% and 80%. As had been found in previous work by Silver and Seed (1971), vertical strain is seen to decrease significantly with increasing relative density, and to increase with increasing shear strain amplitude (γ_c). The volumetric threshold shear strain for these tests was approximately 0.01%, which is consistent with Vucetic's (1994) recommendation of $\gamma_{tv} \approx 0.01–0.03\%$ for clean sands. Test results for the other sands were generally consistent with those for Sand D.

Figure 4.8 shows the normalized vertical strain accumulation [$\varepsilon_v/(\varepsilon_v)_{N=15}$] vs. the number of cycles (N) obtained from tests on Sands A–D. Mean curves are plotted for Sands A–C, while the mean ± one standard deviation is shown for Sand D (for which a relatively large number of test results are available). In general, approximately 50% of the vertical strain at 15 cycles occurs within the first three cycles of loading. This behavior is consistent with the results of Silver and Seed (1971). As shown in Figure 4.8, there do not appear to be significant variations in the N-$\varepsilon_v/(\varepsilon_v)_{N=15}$ curves for the different sand materials, as the curves are generally contained within the range of results for Sand D.

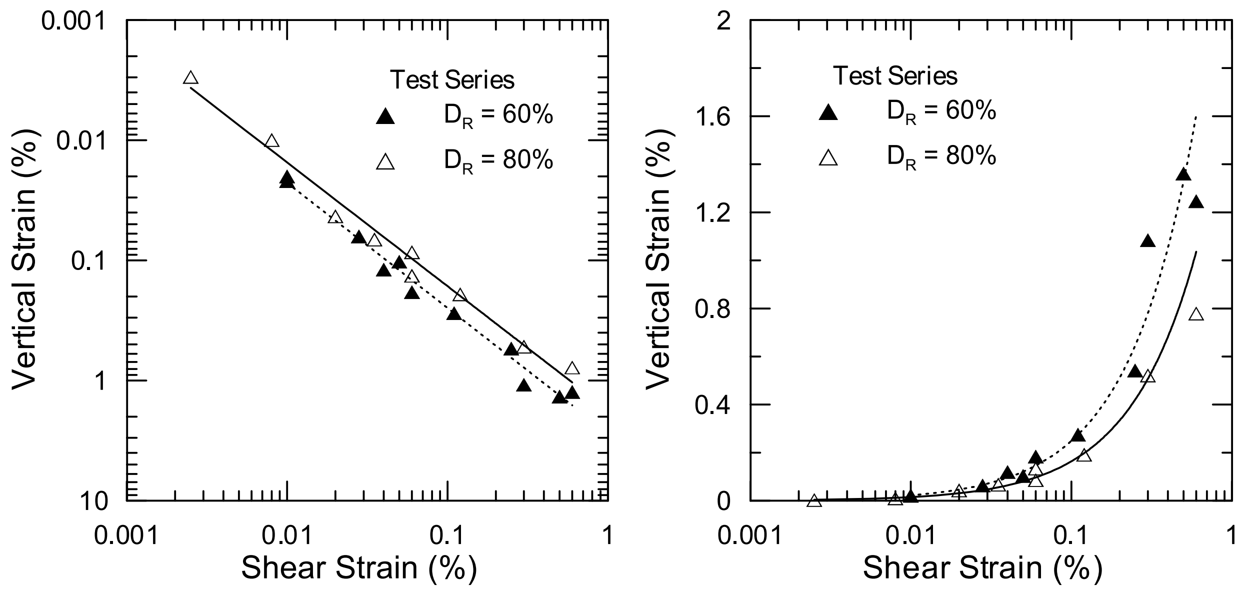

Fig. 4.7. Vertical strain accumulation at 10 cycles for Crystal Silica No. 30 (Sand D)

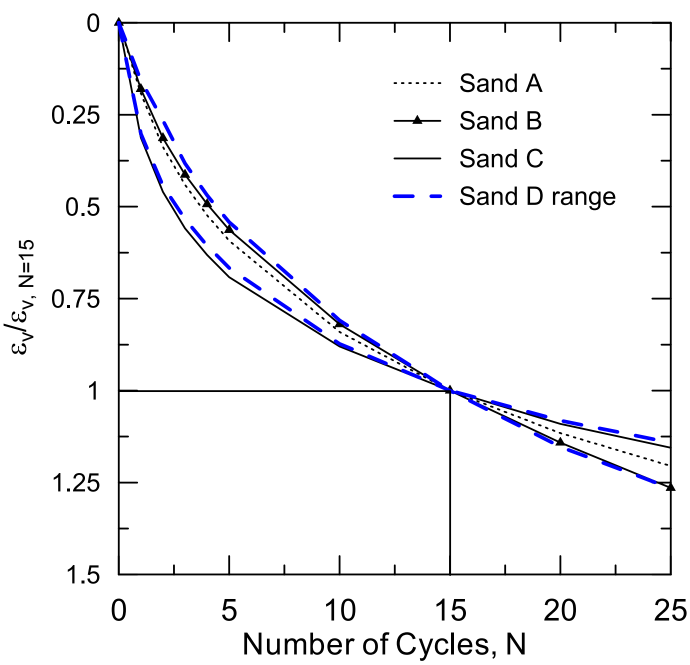

Fig. 4.8. Normalized mean vertical strain vs. number of cycles for all tested sands

4.3.4 Use of Test Results to Establish Protocol for Analysis of Equivalent Number of Uniform Strain Cycles from Accelerograms

The seismic demand placed on soils subject to seismic compression can be quantified by a uniform series of shear strain cycles. This simple representation of earthquake shaking effects facilitates straightforward comparisons between seismic demand and the resistance to seismic compression established from cyclic strain-controlled laboratory tests. A uniform series of strain cycles is described by three parameters:

1. Amplitude: Generally taken as 65% of the peak strain amplitude from an irregular time history of strain.
2. Frequency: Frequency content of strain cycles has been shown to not significantly affect seismic compression in sands (Youd, 1972), but the effect is unknown for plastic soils.
3. Number of Cycles (*N*).

Converting an irregular time history of acceleration to an equivalent number of uniform strain cycles (*N*) involves two steps. First, the acceleration time history is converted to a stress time history, which is coupled with a strain-reduced (equivalent-linear) shear modulus to estimate a shear strain time history. The peak ordinate from this strain time history is used to evaluate amplitude. The second step involves the evaluation of an equivalent number of uniform strain cycles (*N*) from the irregular time history of shear strain.

Procedures for performing the acceleration-to-strain conversion are presented in Section 6.3.2. The evaluation of *N* from an irregular time history is only a function of the relative amplitudes of local minimum and maximum points, i.e., the absolute value of the peak amplitude is not important. Since the phasing of the strain time history is similar to that of the acceleration time history, this evaluation of *N* can be performed using an acceleration time history scaled to a maximum ordinate of unity. In the remainder of this section, we discuss the development of factors used to weight each peak in a normalized accelerogram according to their relative contributions to seismic compression.

Seed et al. (1975) and Liu et al. (2001) demonstrated that the scaling factors used to evaluate *N* are fully dependent on the slope of the relationship between the amplitude of uniform cyclic loading from laboratory testing and the number of cycles required to trigger a particular realization of ground failure. Seed et al. and Liu et al. formulated these relationships for the ground failure mechanism of soil liquefaction, for which the amplitude parameter was cyclic stress ratio. For the problem of seismic compression, the relationship needs to be reformulated such that the ground failure mechanism corresponds to a particular amount of vertical strain from seismic compression and the amplitude parameter is shear strain.

Figure 4.9 shows the relationship between the number of strain cycles (N) and cyclic shear strain amplitude (γ_c) for various amounts of vertical strain (ε_v) in Soils A–D. For a given data set (i.e., soil type and ε_v), a linear regression is performed through the data using the following relationship:

$$\ln(\gamma_c) = a_1 + a_2 \ln(N) \tag{4.1}$$

where a_1 and a_2 are parameters determined by the regression. Parameter a_2 is the slope parameter needed for the derivation of weighting factors. Liu et al. (2001) performed similar regression analyses for the soil liquefaction problem, and found $a_2 \approx$ -0.37 to -0.50. The actual derivation of weight factors from a_2 is presented in Section 6.3.2.

The slopes obtained for different relative densities (D_R) and vertical strain amplitudes for Sand D are shown in Figure 4.10(a). Slope parameter a_2 varies from about -0.3 to -0.5, and appears to increase slightly with ε_v. Parameter a_2 does not appear to vary significantly with D_R. Values of slope parameter a_2 obtained for Sands A–D at a relative density D_R = 60% are presented in Figure 4.10(b). A good representative value for practical application in sandy soils appears to be a_2 =-0.6.

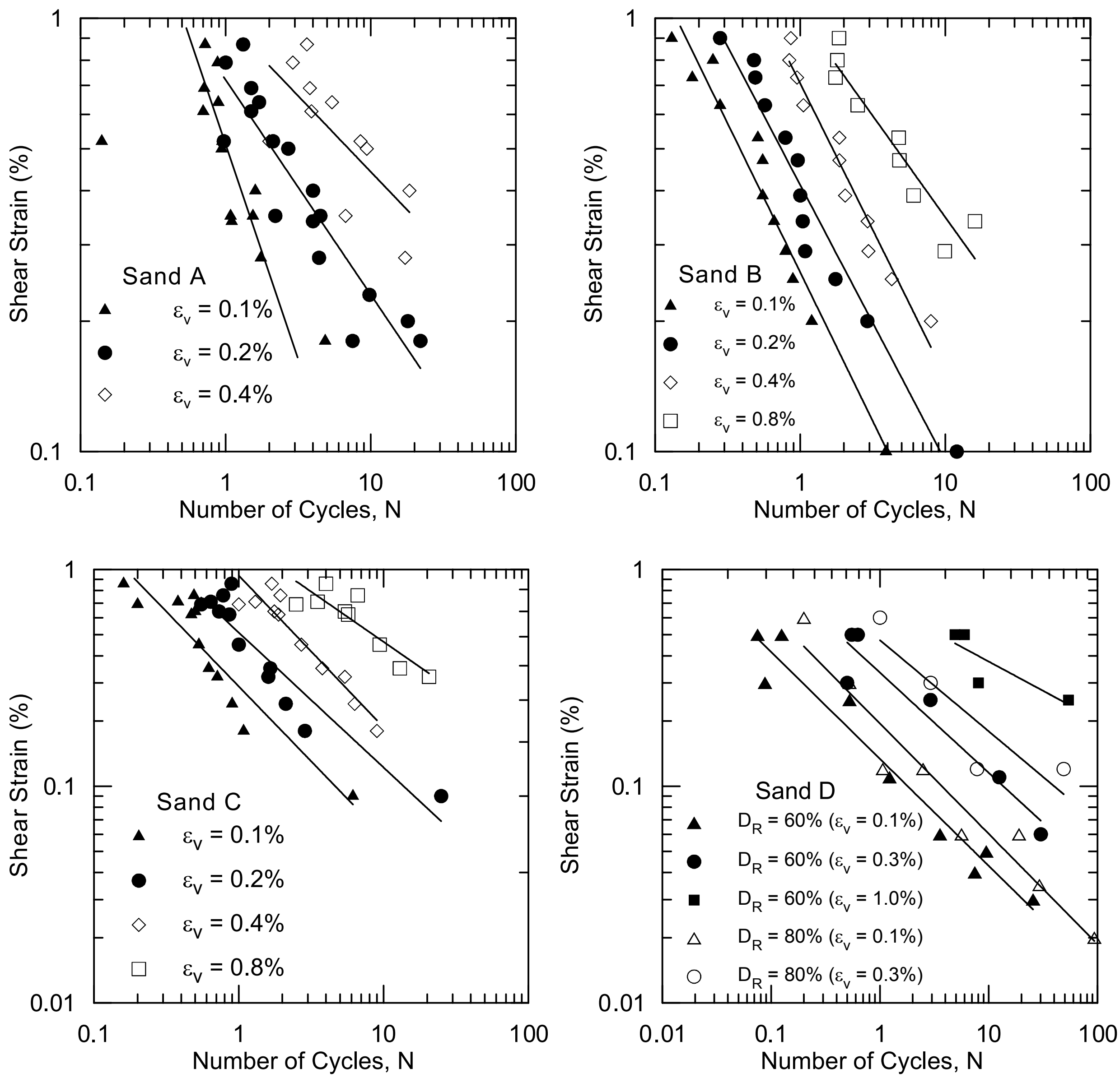

Fig. 4.9. Relationship between shear strain amplitude and number of cycles to cause selected amounts of vertical strain for Sands A–D

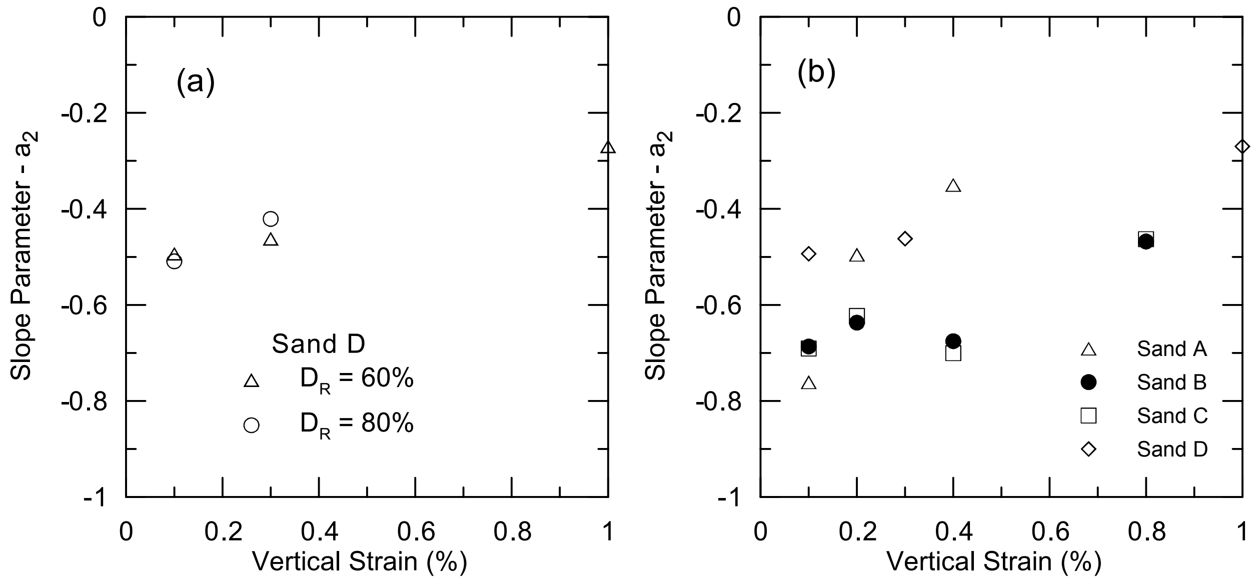

Fig. 4.10. Variation of slope parameter a_2 with (a) D_R and vertical strain for Sand D and (b) vertical strain for Sands A–D for D_R = 60%

5 Seismic Compression of Compacted Fill Soils Containing Fines

5.1 INTRODUCTION

Natural soils used for the construction of compacted fills nearly always contain a fine-grained fraction (i.e., soil grains finer than the #200 sieve opening). It has long been understood that the presence of fines in soil significantly changes ordinary mechanical properties such as shear strength relative to clean sands (e.g., Casagrande, 1932). The presence of fines can be especially important in compacted fill soils where the soil structure is determined by the method of compaction and the formation water content and density (e.g., Seed et al., 1960, Benson and Daniel, 1990). These variations in structure, in turn, are known to affect volume change characteristics such as swell or hydro-compression (e.g., Lawton et al., 1989). Despite the critically important influence of fines on the properties of compacted fills, previous investigations of seismic compression have focused primarily on clean sands. In this chapter, we synthesize previous research on seismic compression of compacted soils with fines, and present the results of seismic compression testing of fill materials from Sites A and B, which contain sufficiently large fines contents that the fines would be expected to control the soil behavior.

5.2 PREVIOUS LABORATORY INVESTIGATIONS OF SEISMIC COMPRESSION IN COMPACTED SOILS CONTAINING FINES

Pyke et al. (1975) performed a limited number of cyclic simple shear tests on a well-graded clayey sand (SC) for back-analysis of settlements that occurred at the Jensen Filtration Plant during the 1971 San Fernando earthquake. Tests were performed on an NGI-type apparatus at one water content (w = 10%) and two Modified Proctor densities (RC = 84.4 and 92%) under cyclic strain-controlled loading (γ_c = 0.1 to 0.4%). The simple shear apparatus used for this testing was the same as that used by Silver and Seed (1971). Figure 5.1 shows the vertical strains obtained by Pyke et al. at 10 cycles of loading along with the Silver and Seed results for sands at D_R = 60% (a reasonable estimate of D_R given the *RC* range of the fine-grained fill soil). These test results indicate that vertical strains for the clayey sand were < 1/3 of the vertical strains in sand at a comparable density. Another important finding from Pyke et al. is the lack of sensitivity of seismic compression to variations in confining stress. As shown in Figure 5.1, Pyke et al. tested the Jensen fill under two vertical stresses (σ_v = 95 and 191 kPa) and found no detectable variation in vertical strain.

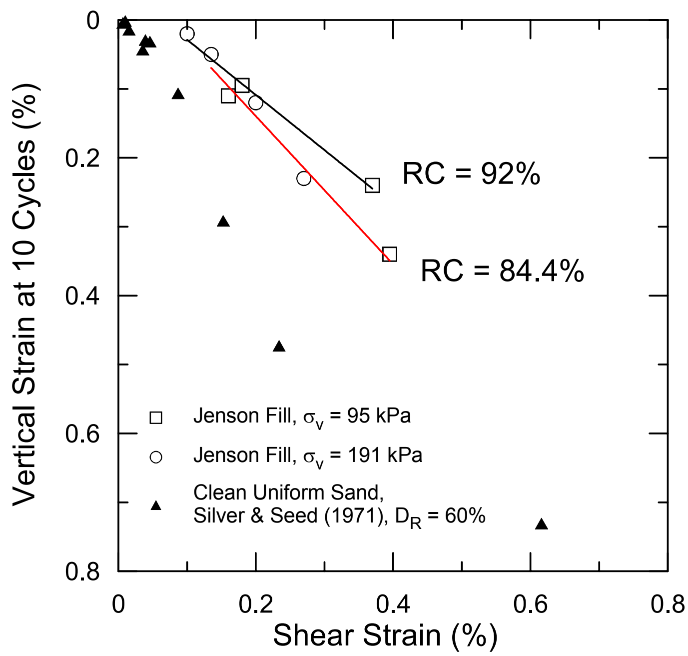

Fig. 5.1. Relationship between shear strain and vertical strain at *N* = 10 cycles for fill material at Jensen Filtration Plant (after Pyke et al., 1975)

Chu and Vucetic (1992) investigated seismic compression of a low-plasticity (PI = 10.5) clay using an NGI-type simple shear device. Figure 5.2 shows the Modified Proctor compaction curve of the low-plasticity clay along with the three testing conditions (*w* = 8.5% and *RC* = 98.8%; *w* = 10.1% and *RC* = 100%; *w* = 14% and *RC* = 94.9%). The reported densities are those present prior to the application of vertical stress, which would be expected to further densify the specimens. Specimens were prepared by (1) mixing water and dry soil which had passed through a No. 4 sieve to the desired water content and curing it for 24 hours, (2) compacting the soil in five layers in a compaction cylinder using a hand tamper, (3) trimming the surplus of soil on the bottom and top specimen surfaces with a straightedge, (4) simultaneously removing the soil specimen from the compaction cylinder and placing it between the bottom and top caps, and (5) sliding the wire-reinforced membrane onto the specimen and securing it with O-rings.

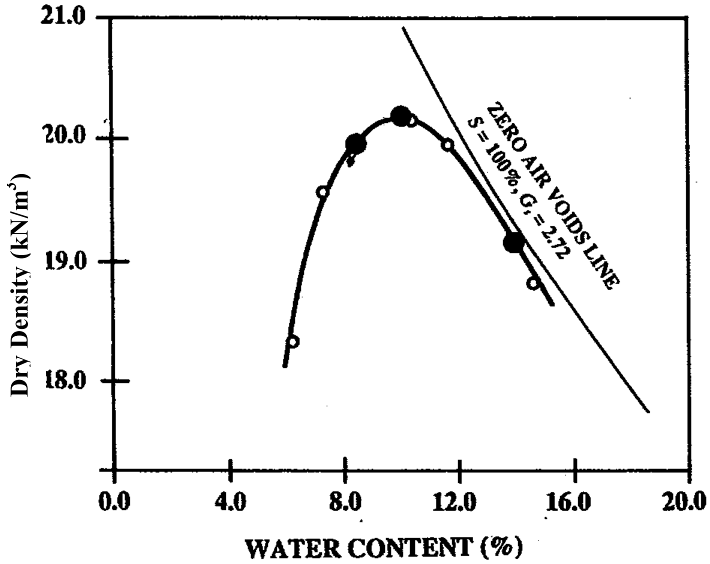

Fig. 5.2. Modified Proctor compaction curve of low-plasticity clay and tested points (Chu and Vucetic, 1992)

After preparation, the specimens were consolidated to σ_v = 550 kN/m^2 in three to four loading increments, and then were subjected to cyclic strain-controlled loading with γ_c = 0.008 to 4.6%. Figure 5.3 shows the variation of vertical strain (ε_v) with γ_c for N = 3, 10 and 40 cycles of loading. From these test results, Chu and Vucetic concluded that (1) for γ_c > 0.1%, ε_v for compacted clay significantly increases with γ_c and N, (2) ε_v for this particular compacted clay does not depend significantly on w for small γ_c, and (3) the volumetric threshold strain, γ_{tv}, of this compacted clay, i.e., the shear strain below which the settlement is negligible, is around 0.1%.

With respect to the second conclusion, it should be noted that specimens at different w in this testing program also had different preconsolidation Modified Proctor *RC*, which ranged from 95% to 100%. Hence, the effect of w was not truly isolated from the effect of *RC* in these tests. Moreover, the *RC* of the tested samples were high, implying an unusually high level of compaction effort. This would be expected to break down macro-structural features such as clods that might have been present at lower densities. Accordingly, the apparent lack of dependence of ε_v on w in this testing may not be applicable to the lower *RC* levels that would typically be encountered in practice.

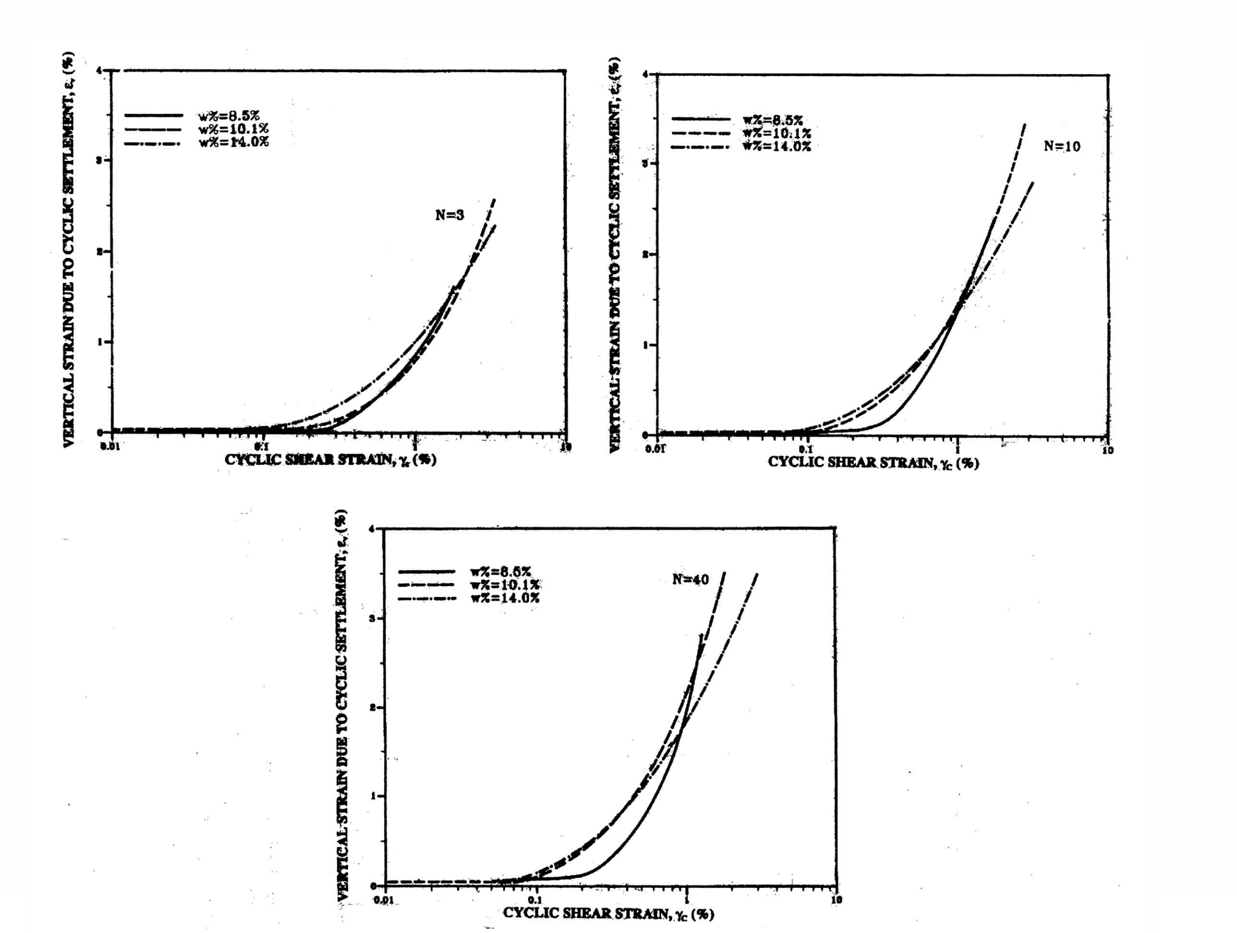

Fig. 5.3. The effect of *w* on settlements of a low-plasticity clay for *N* = 3, 10, and 40 cycles (Chu and Vucetic, 1992)

5.3 TESTING OF SOILS FROM SUBJECT SITES

Cyclic simple shear tests were performed in the present study under drained conditions to evaluate vertical strain accumulation in specimens subjected to strain-controlled, uniform-amplitude cyclic loading. All tests were performed under the same vertical stress of σ_v = 101.3 kPa. A sinusoidal loading frequency of 1 Hz and three different shear strain levels (γ_c = 0.1%, 0.4% and 1.0%) were used in the tests. This section summarizes the results of those tests. Additional details on the testing program and test results are presented by Whang (2001).

5.3.1 Specimen Preparation

Bensen and Daniel (1990) have found that soils with plastic fines tend to have a clod-like structure prior to compaction that is only broken down if the soil is compacted at high water contents or with large compactive energy. In our testing, clod size was controlled by pre-drying the soils and passing them through a No. 4 sieve. It is recognized that this procedure does not match field conditions where the clods would typically be larger. Nonetheless, our use of pre-sieving was motivated by the following considerations:

- The initial clod size at the time of construction in the field is generally not controlled, and is therefore unknown and not reproducible.
- The use of large clods is impractical for cyclic simple shear testing, which is performed on relatively small diameter specimens (i.e., diameter ~ 10 cm).
- A controlled specimen preparation procedure allows for more reproducible test results than if arbitrary precompaction clod sizes were used.

Construction logs indicate that the fill at Sites A and B was compacted using sheepsfoot rollers. These rollers produce a kneading type of compaction that induces large shear strains in the soil. This construction process was simulated by compacting laboratory specimens with a Harvard Miniature-Compactor, which also applies a kneading type of compaction. The complete laboratory specimen preparation procedure consists of:

1. Pre-sieving air-dried soil through a No. 4 sieve,
2. Moisture conditioning the soil to the desired water content,

3. Compacting a preweighed amount of soil into a cylindrical mold in two layers using the Harvard Miniature-Compactor. The pressure applied by the Harvard Mini-Compactor was varied through a pressure regulator to achieve the desired density. Pressures of 10 to 70 psi were applied using 30 tamps per layer.
4. Leveling the top of the specimen to a tolerance of ± 0.01 cm using a straightedge. Holes were filled using the same soil and gentle taps from a rubber hammer.

5.3.2 General Test Results

Strain-controlled cyclic simple shear tests were performed on four different reconstituted soils from Sites A and B. As shown in Figures 5.4 and 5.5, values of formation water content and dry density were chosen to represent the range of in situ conditions reported in Chapter 3.

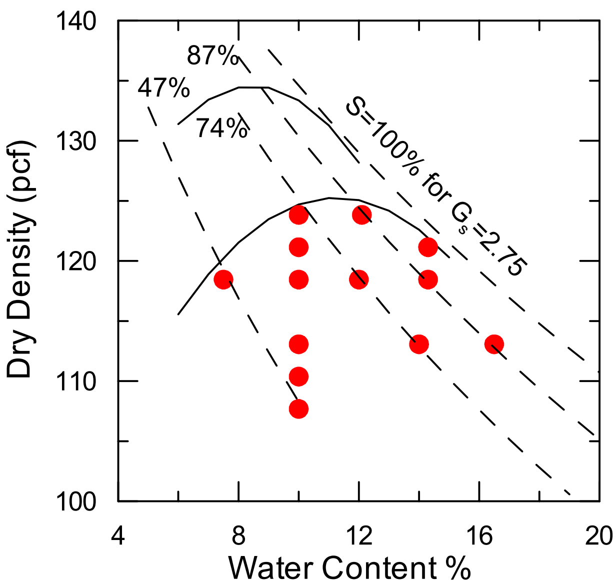

Fig. 5.4. Standard and Modified Proctor compaction curve for Site A soils and compaction points for simple shear tests

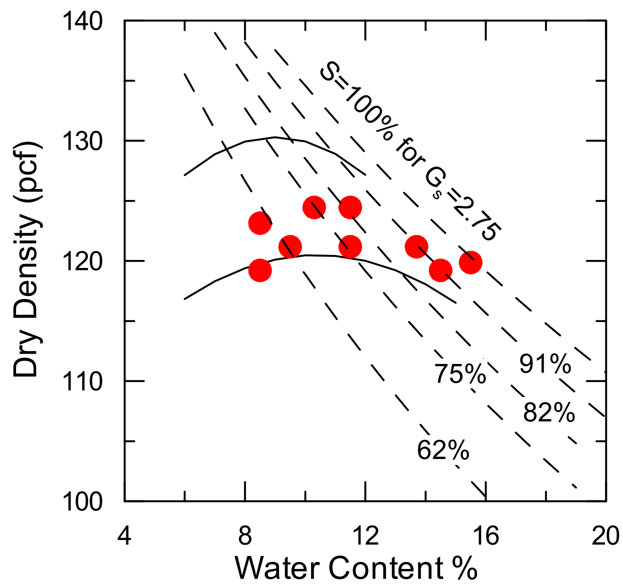

Fig. 5.5. Standard and Modified Proctor compaction curve for Soil B-3 and compaction points for simple shear tests

The results of index tests (Atterberg Limit and hydrometer/sieve analyses) on the tested specimens are reported in Table 5.1 and Figures 5.6–5.7. Soil A-1 is a low-plasticity clay (CL), having 54% fines and PI = 15. Soils B-1 to B-3 are silty or clayey sands (either SM or SC), having 40–48% fines and PI = 2–14. Of the three specimens from Site B, B-3 appears to be the most representative of the typical field conditions, based on the PI values reported in Table 3.7.

Table 5.1. Summary of index properties for Sites A and B soils

Soil	*FC* (%)	PI	LL	USCS	$(\gamma_d)_{max}$ (g/cm^3)[1]	w_{opt} (%)[1]
Site A	43-69	10-16	29-35	SC, CL	2.15-2.24	7.4-9.7
A-1	54	15	33	CL	2.16	8.5
Site B	36-52	2-14	26-35	SM, SC, ML	2.11-2.20	8.3-9.2
B-1	40	14	35	SC	2.10	8.0
B-2	48	9	30	SC	2.08	8.0
B-3	44	2	27	SM	2.10	8.0

[1] Based on modified Proctor compaction tests (ASTM D1557)

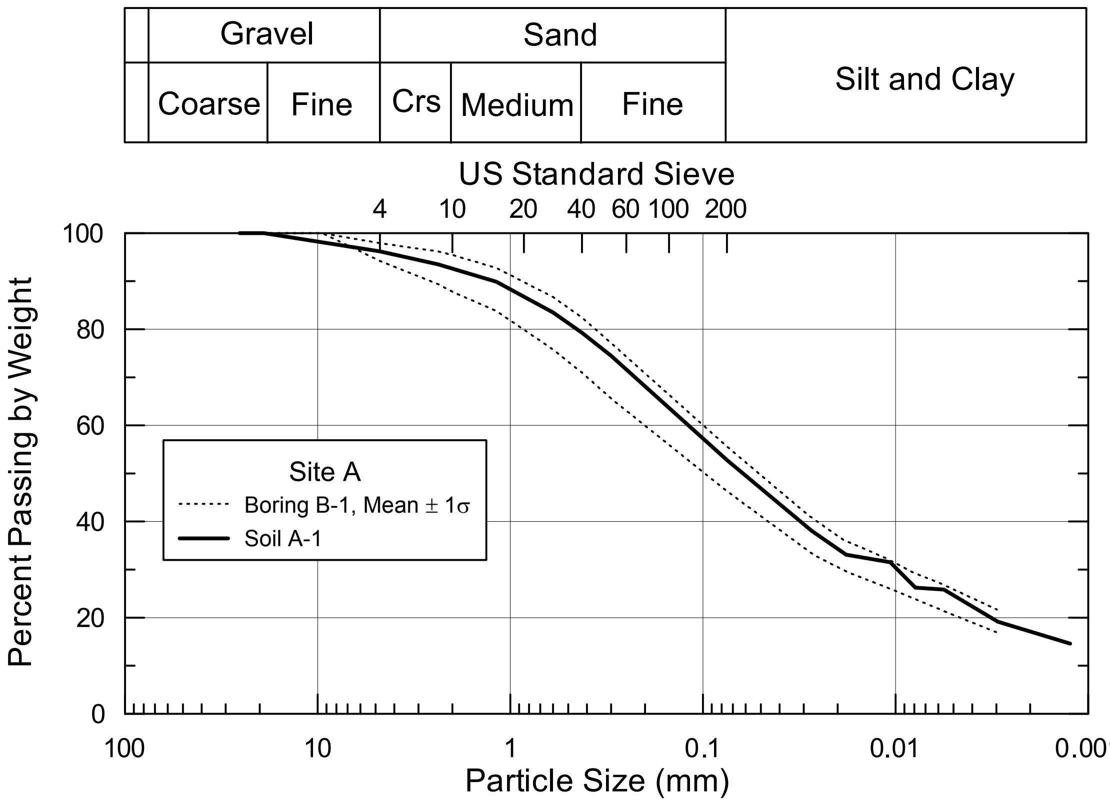

Fig. 5.6. Grain-size distributions of Specimen A-1 along with range of gradation curves for Site A (from Figure 3.9)

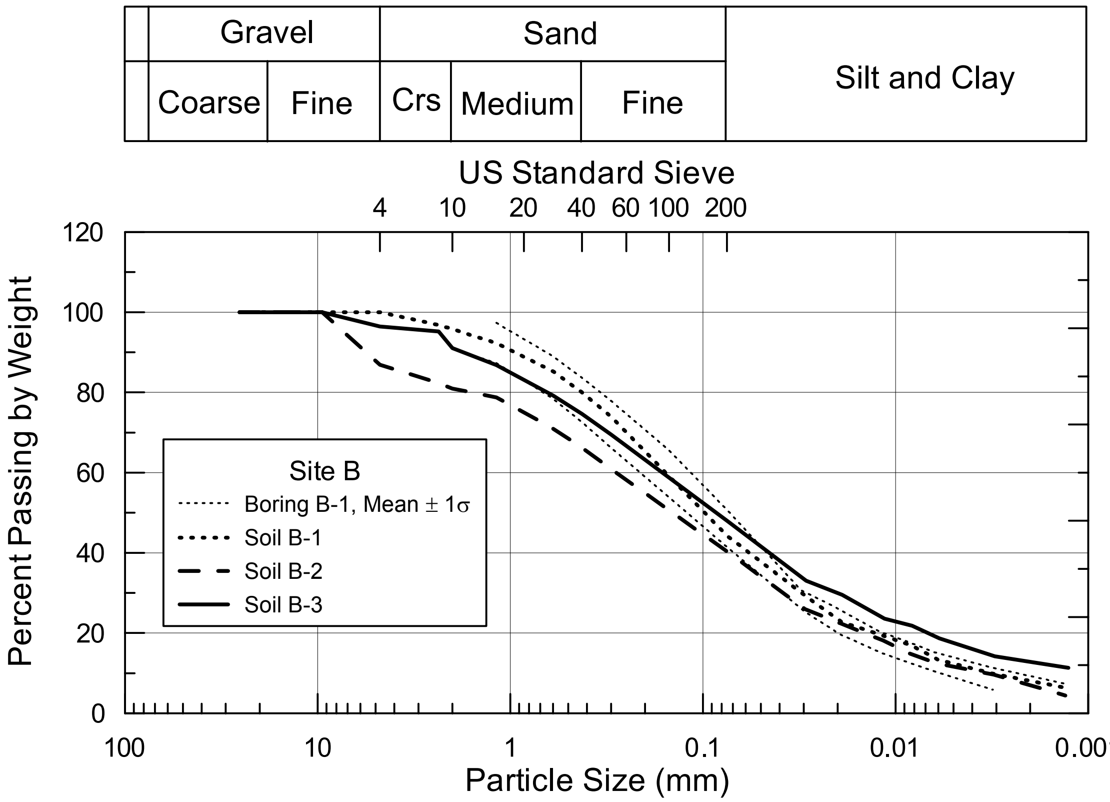

Fig. 5.7. Grain-size distributions of Specimens B-1, B-2, and B-3 along with range of gradation curves for Site B (from Figure 3.21)

The results of a representative cyclic simple shear test are shown in Figure 5.8 [Soil A-1, *RC* = 88% by Modified Proctor standard and *w* = 14.8% (degree of saturation, *S* = 87%)]. A strain hardening effect is evident by the progressive increase in shear load amplitude with time during the initial cycles to achieve a uniform shear strain amplitude. This increase in shear modulus is negligible after about ten cycles.

Results for each sample are presented in the following Sections 5.3.3 to 5.3.5 in terms of the vertical strain associated with *N* = 15 uniform shear strain cycles [$(\varepsilon_v)_{N=15}$]. Section 5.3.6 synthesizes these test results and results for sands presented in Chapter 4 to investigate the effect of fines on seismic compression. Also examined is the variation of ε_v with *N* in Section 5.3.7, and the development of appropriate weighting factors for the evaluation of *N* from accelerograms in Section 5.3.8.

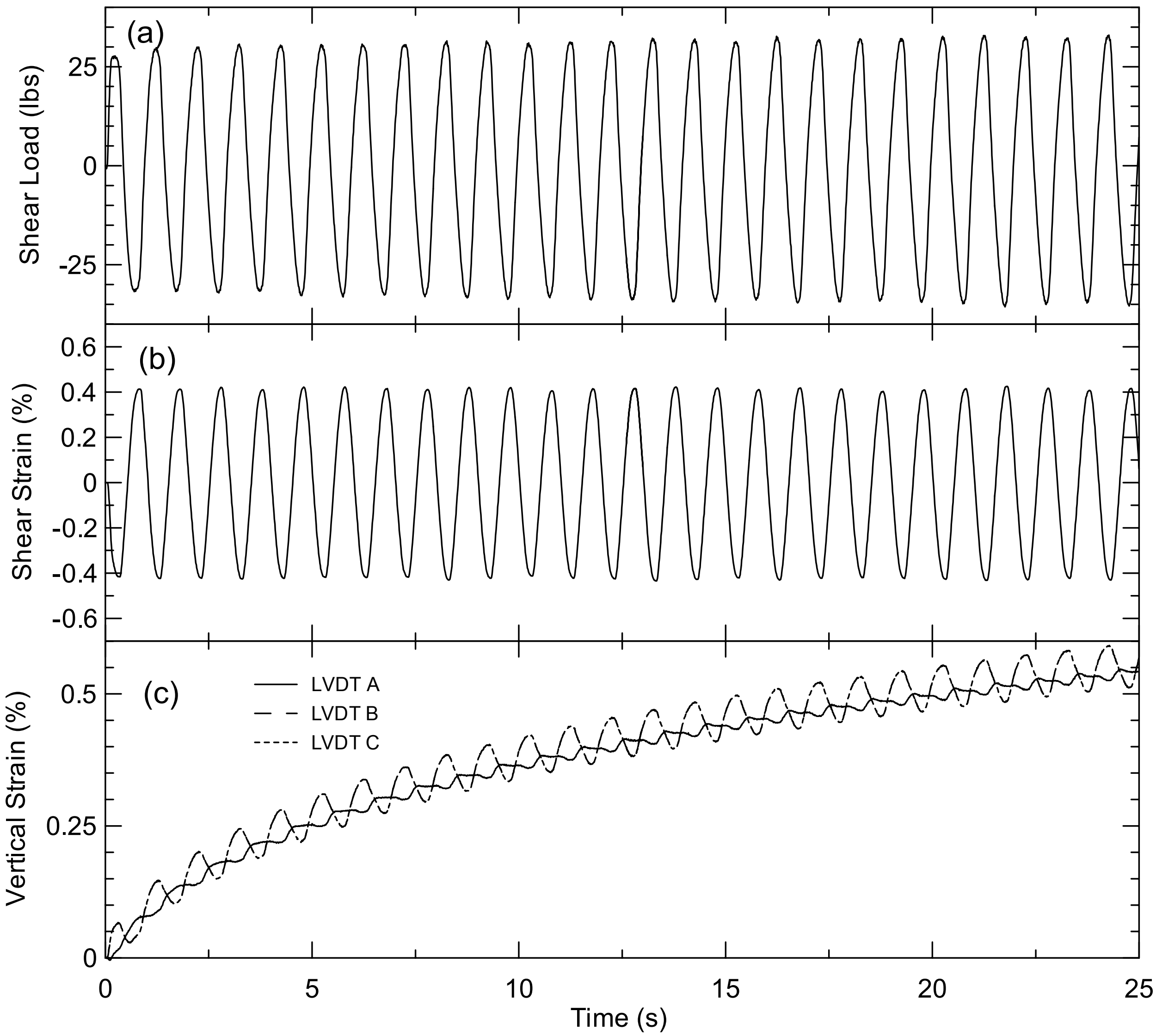

Fig. 5.8. Representative cyclic simple shear test result (Soil A-1, *RC* = 88%, *w* = 14.8%)

5.3.3 Seismic Compression of Soil A-1

Soil A-1 is a low-plasticity clay (Table 5.1). A complete inventory of simple shear tests performed on Soil A-1 is provided by Whang (2001). Each compaction condition (i.e., formation *RC* relative to Modified Proctor standard and *S*) was tested at a minimum of two cyclic shear strain amplitudes (γ_c = 0.4 and 1.0%) and in some cases a third (γ_c = 0.1 %). The test results show that $(\varepsilon_v)_{N=15}$ is strongly dependent on γ_c (as had been previously known), and also demonstrate the dependence of $(\varepsilon_v)_{N=15}$ on both the formation *RC* and *S*.

The effect of relative compaction (*RC*) on the seismic compression of Soil A-1 is illustrated in Figure 5.9, where specimens were prepared to a common $S \approx 74\%$ but different *RC* = 84, 88, and 92%. Values of $(\varepsilon_v)_{N=15}$ decrease with increasing *RC* for all γ_c.

Figure 5.10 illustrates the effect of degree of saturation (*S*) on the seismic compression of Soil A-1. The shaded bands in Figure 5.10 correspond to a given relative compaction (*RC* = 84, 88, and 92%) and variability within the bands is associated with variation in *S*. The results indicate that values of $(\varepsilon_v)_{N=15}$ can decrease significantly with increasing *S* when the relative compaction is moderate (*RC* = 88–92%). The variation of $(\varepsilon_v)_{N=15}$ with *S* for a given *RC* can be as much as a factor of two. Interestingly, values of $(\varepsilon_v)_{N=15}$ do not vary significantly across the range of *S* = 53–87% at low relative compaction ($RC \approx 84\%$).

The effects of *RC* and *S* on $(\varepsilon_v)_{N=15}$ are synthesized in Figures 5.11 and 5.12 for γ_c = 1% and 0.4%, respectively. The contours indicate a decrease of $(\varepsilon_v)_{N=15}$ with increasing *RC* across the full range of *S* and with increasing *S* for moderate to high *RC*. The trends of the contours are similar to those for other soil properties such as as-compacted peak shear strength (Seed et al., 1960) and volume change upon wetting (Lawton et al., 1989). We interpret the observed dependence of $(\varepsilon_v)_{N=15}$ on *S* to be associated with variations in soil structure. Specimens compacted at high *S* with at least a moderate compactive effort are likely to have a relatively homogeneous structure with little to no clods. Specimens compacted at relatively low *S* with moderate compactive effort, are inferred to have a clod structure, and thus interclod void space. Figure 5.13 shows photographs taken of Soil A-1 specimens compacted to a moderate density (*RC* = 88%) and two different degrees of saturation (*S* = 66 and 87%). As expected, the specimen compacted at *S* = 66% appears to have more remnant clods, while the specimen compacted at *S* = 87% shows a more homogeneous soil macrostructure.

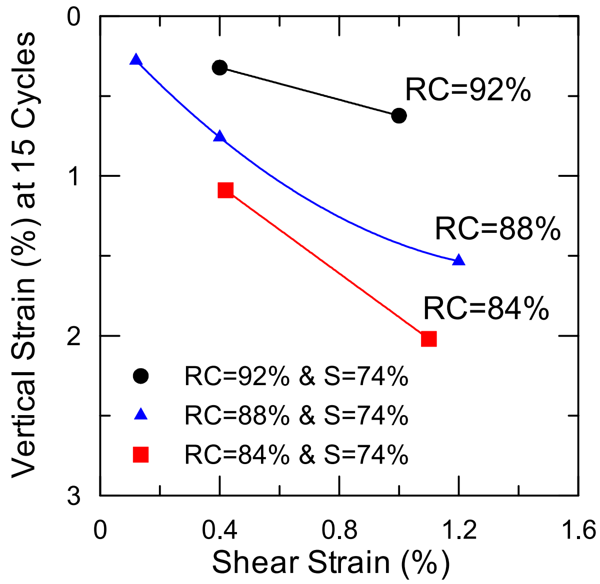

Fig. 5.9. Effects of *RC* on the seismic compression of Soil A-1

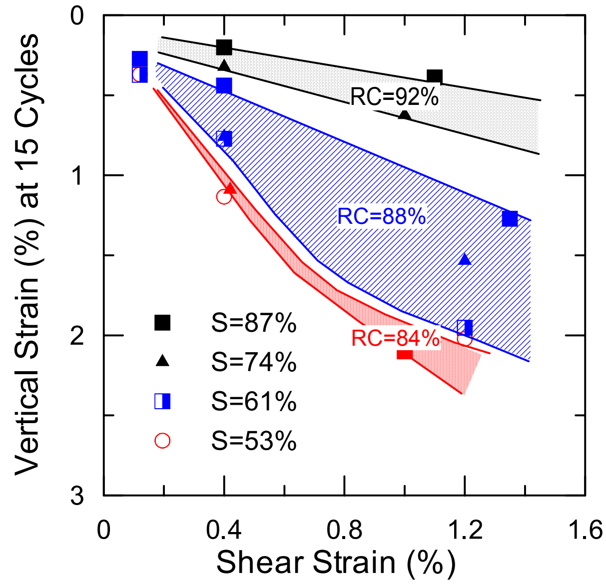

Fig. 5.10. Effects of degree of saturation on the seismic compression of Soil A-1

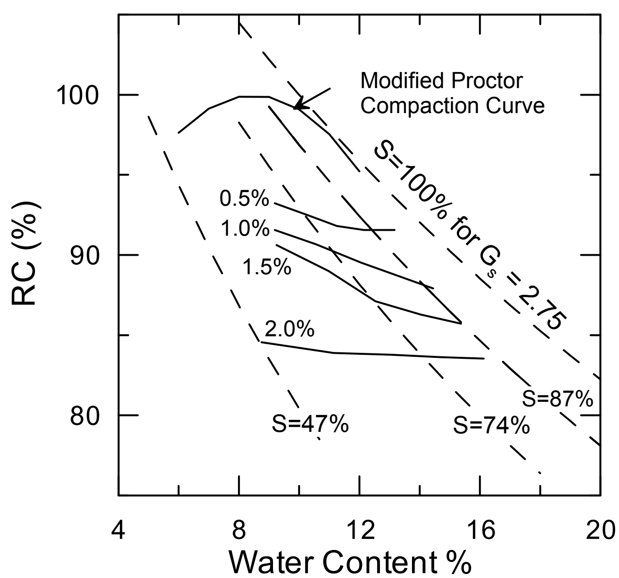

Fig. 5.11. Contours of $(\varepsilon_v)_{N=15}$ for Soil A-1 at $\gamma_c = 1.0\%$

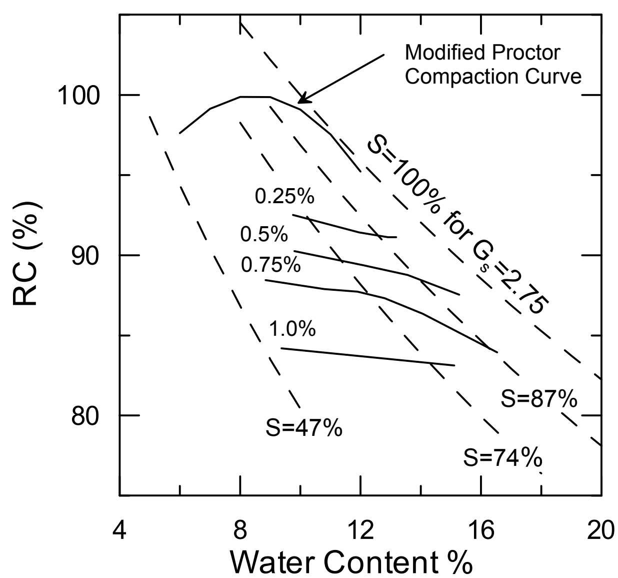

Fig. 5.12. Contours of $(\varepsilon_v)_{N=15}$ for Soil A-1 at $\gamma_c = 0.4\%$

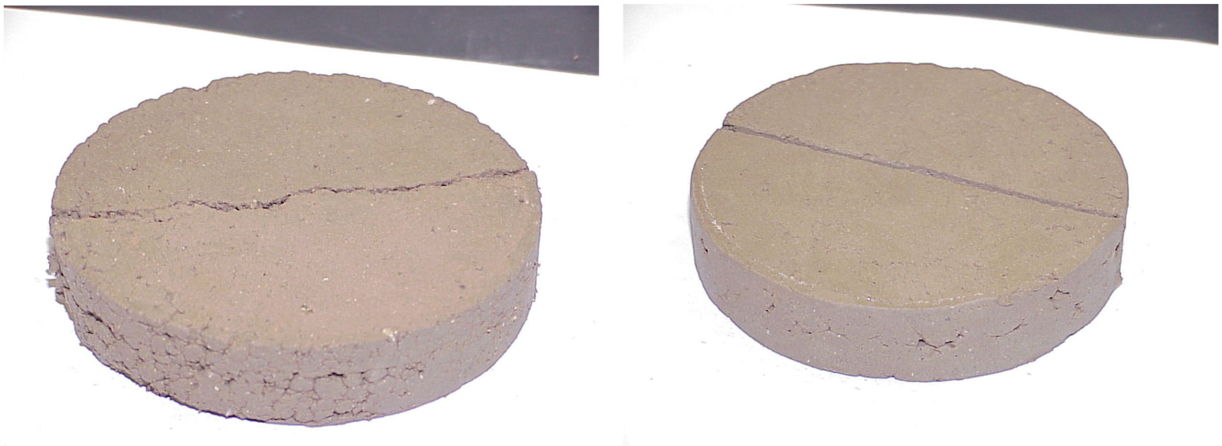

***RC* = 88% and *S* = 66%** ***RC* = 88% and *S* = 87%**

Fig. 5.13. Photographs showing macrostructure of Soil A-1

These postulated variations of soil structure can explain a number of key trends in the test results. For moderate compactive efforts (i.e., *RC* = 88 and 92%), the decrease of $(\varepsilon_v)_{N=15}$ with increasing *S* may result from a corresponding decrease in interclod void space with *S*. At very low compactive efforts (i.e., *RC* = 84%), the compaction process may not break down clods, which would result in a consistent soil structure across a broad range of *S*, and correspondingly consistent values of $(\varepsilon_v)_{N=15}$, as observed. We were not able to prepare specimens of Soil A-1 to very high densities (i.e., *RC* > 92%) with the Harvard compactor, but previous test results by Chu and Vucetic (1992) on a similar material at very high *RC* indicated no significant variation in vertical strain with water content. As noted previously in Section 5.2, this is likely associated with a breakdown of clod structure at high compactive efforts regardless of *S*.

5.3.4 Seismic Compression of Soils B-1 to B-3

Three different reconstituted soils (B-1, B-2, and B-3) were tested from this site. A complete inventory of these tests is provided by Whang (2001). The most extensive testing was performed on Soil B-3, with the objective being to evaluate the effects of formation *RC* and *S* on the seismic compression of this low-plasticity silty sand. Relatively limited testing on Soils B-1 and B-2 enable the effect of *RC* on seismic compression to be evaluated for a given formation water content (*w*).

Figure 5.14 summarizes the variation of $(\varepsilon_v)_{N=15}$ with γ_c for Soil B-3. Values of $(\varepsilon_v)_{N=15}$ are seen to decrease with increasing *RC* (up to the maximum tested value of 95.5%) but there appears to be no significant effect of degree of saturation (*S*). For example, vertical strains were remarkably consistent for *S* = 54 and 91% (clearly on opposite sides of the line of optimums) at a density of *RC* = 90%. These trends are perhaps most clearly illustrated with the contour plots of $(\varepsilon_v)_{N=15}$ shown in Figures 5.15 and 5.16 for shear strain levels γ_c = 1% and 0.4%, respectively.

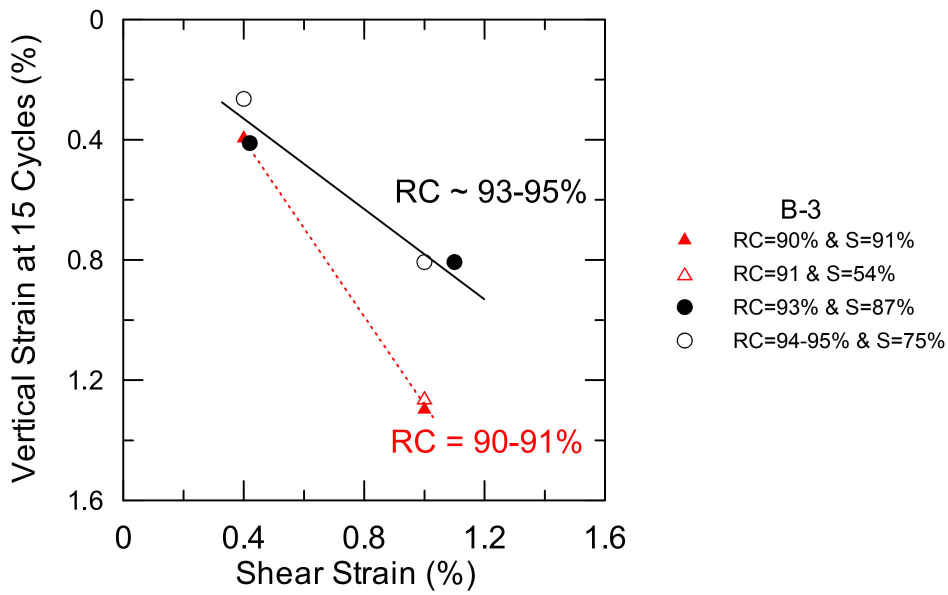

Fig. 5.14. Seismic compression of Soil B-3

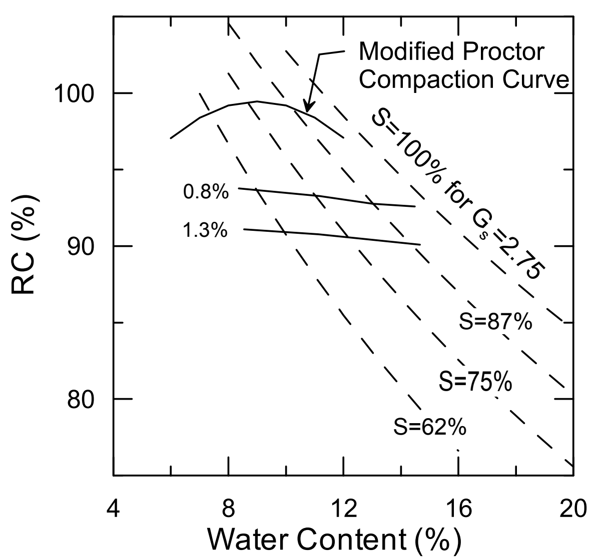

Fig. 5.15. Contours of $(\varepsilon_v)_{N=15}$ for Soil B-3 at γ_c = 1.0%

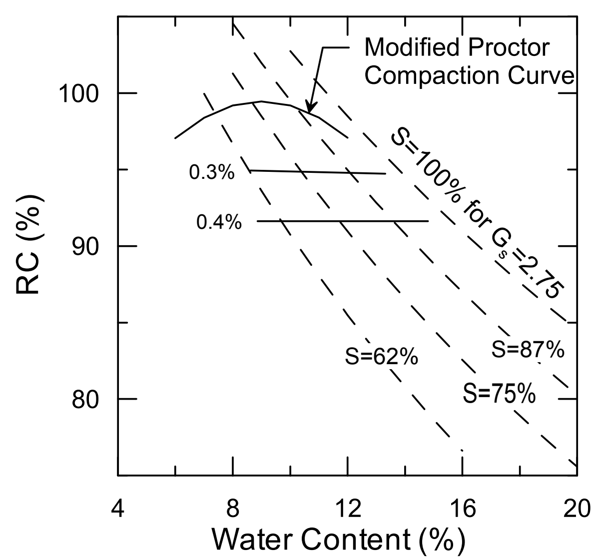

Fig. 5.16 Contours of $(\varepsilon_v)_{N=15}$ for Soil B-3 at γ_c = 0.4%

The lack of dependence of $(\varepsilon_v)_{N=15}$ on S may be associated with the low plasticity (PI = 2) of Soil B-3. Whereas the clays in plastic soils tend to promote the formation of clods, in nonplastic soils such clods are unlikely to be present for any S. If there is no clod formation, then soil structure would not be significantly affected by the formation S, which in turn would result in a lack of dependence of $(\varepsilon_v)_{N=15}$ on S, as observed. The lack of clods in this material is shown in Figure 5.17, where photographs of Soil B-3 specimens compacted at RC = 90% and S = 62 and 87% both show no discernible clod formation.

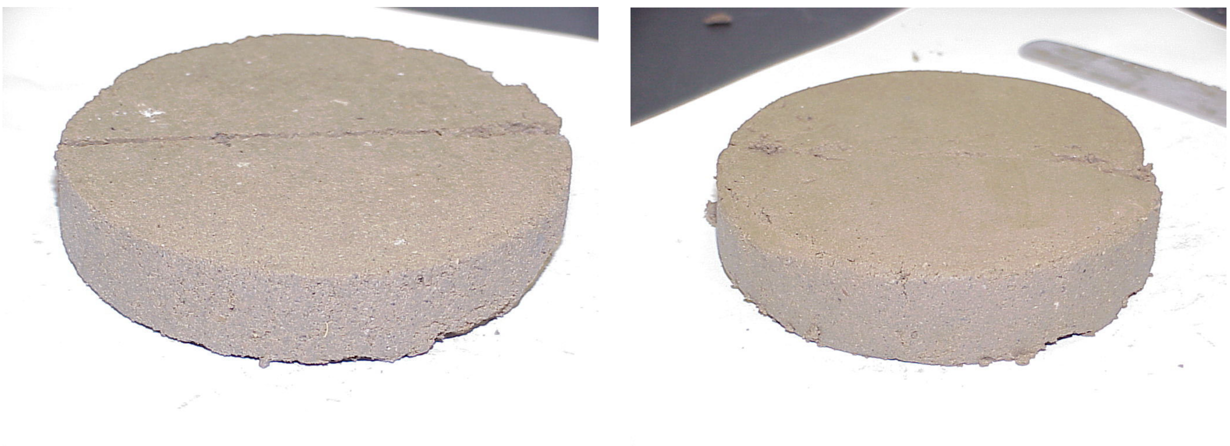

***RC* = 90% and *S* = 62%** **_RC_ = 90% and *S* = 87%**

Fig. 5.17. Photographs showing macrostructure of Soil B-3

Figure 5.18 summarizes the variation of $(\varepsilon_v)_{N=15}$ with γ_c for Soils B-1 and B-2. The trends are consistent with those from Soil A-1, where $(\varepsilon_v)_{N=15}$ increased with increasing γ_c and decreased with increasing RC and S. The tendency of $(\varepsilon_v)_{N=15}$ to decrease with S can be seen by comparing B-1 soil specimens prepared to S = 61 and 81% for $RC \approx$ 90–91%, and S = 74 and 97% for RC = 95.5%. For both RC levels, increasing S decreases $(\varepsilon_v)_{N=15}$ by up to 30%.

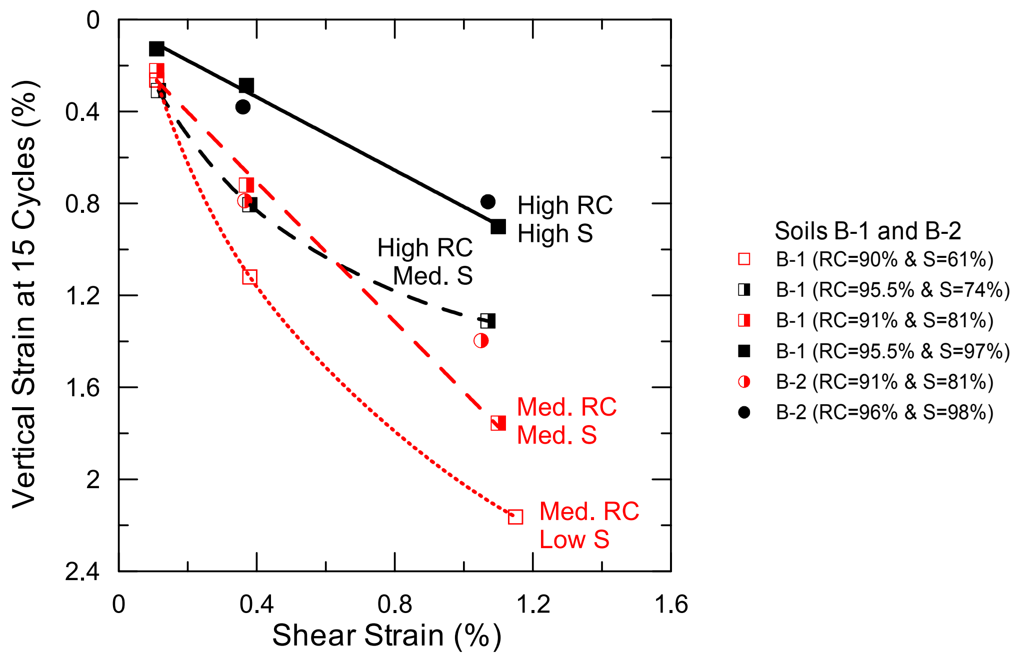

Fig. 5.18. Seismic compression of Soils B-1 and B-2

5.3.5 Volumetric Threshold Strain

The volumetric threshold strain has previously been defined as the cyclic shear strain amplitude above which a significant permanent volume change or a permanent pore-water pressure change may occur in the soil. Vucetic (1994) showed that the volumetric threshold shear strain varies with soil type, and generally increases as the size of the soil particles decreases and the plasticity index increases. Vucetic (1994) compiled existing laboratory test data from numerous researchers and found that the volumetric threshold strain is approximately 0.1% and 0.01% for clays and sands, respectively.

While our testing program did not specifically emphasize obtaining volumetric threshold shear strains, this parameter is needed for a statistical model (discussed subsequently in Section 7.2.3) that we use to relate shear strains to volumetric strains for a given compaction condition. Accordingly, limited tests were performed to constrain the volumetric threshold strain for Soil A-1. Soil A-1 specimens were compacted to RC = 88% and S = 74%, before cyclic shear strains of 0.05% and 0.03% were applied. At both of these shear strain amplitudes, vertical strains greater than 0.02% were observed within the first cycle of loading, suggesting that the volumetric threshold strain had been exceeded. Consequently, the volumetric threshold strain for this material is less than 0.03%. Testing to constrain the threshold strain for Site B soils was not performed because relatively strong shaking at Site B makes the threshold strain parameter unimportant to the analysis of seismic compression (i.e., shear strains are well beyond threshold).

5.3.6 Comparison to Clean Sands

In this section, we compare results for different soils to gain insight into the effect of fines content and fines plasticity on seismic compression. Parameter $(\varepsilon_v)_{N=15}$ is compared for moderately plastic silty clay soil, A-1, and Sands A and D. Similar comparisons are made between a low-plastic silty sand, B-3, and Sands B and D. Sands A and B were manufactured by washing Soils A-1 and B-3, respectively, through a #200 sieve to remove the fine-grained portion of the soil. Presumably, differences in vertical strains between Soil A-1 and Sand A are attributed to the effect of plastic fines. Likewise, differences in test results between Soil B-3 and Sand B allow for a preliminary evaluation of the influence of nearly nonplastic silty fines.

Because relative compaction (*RC*) is used to characterize the density of soils containing significant fines, while relative density (D_R) is used to characterize the density of clean sands, a comparison between the two can only be made with the use of a soil-specific relationship between *RC* and D_R. These relationships were developed by Whang (2001), and the resulting comparison of test results for Sands A and D at an equivalent *RC* = 90–92% to those for moderately plastic Soil A-1 (PI = 15) is shown in Figure 5.19. Whereas the range of $(\varepsilon_v)_{N=15}$ for sands is narrow, the range for Soil A-1 is much broader. Within this broad range of results for Soil A-1, there is a systematic increase in $(\varepsilon_v)_{N=15}$ with decreasing degree of saturation, *S*. Fill specimens compacted at moderate to high degrees of saturation ($S \geq 74\%$) experienced considerably less seismic compression than clean sands. At these saturation levels, the seismic compression susceptibility of Soil A-1 was three to five times smaller than that of Sand A. However, specimens compacted at a low degree of saturation ($S = 66\%$) experienced vertical strains within the range of settlements expected for clean sands.

Based on these results, it appears that the effect of moderately plastic fines on seismic compression behavior is dependent on formation *S*. At moderate to high formation *S*, the clayey fines can significantly decrease the seismic compression susceptibility. In contrast, when compacted at low *S*, the clayey fines do not reduce the seismic compression relative to clean sands.

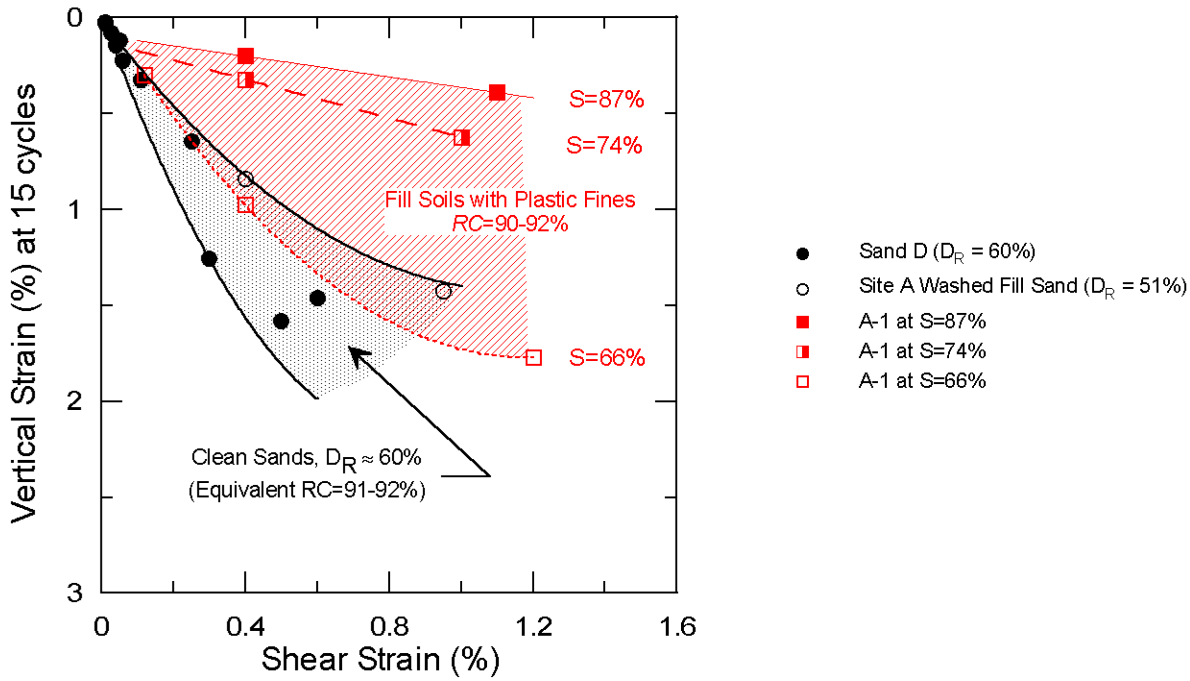

Fig. 5.19. Comparison of vertical strains between Soil A-1 and clean sands at *RC* = 90–92%

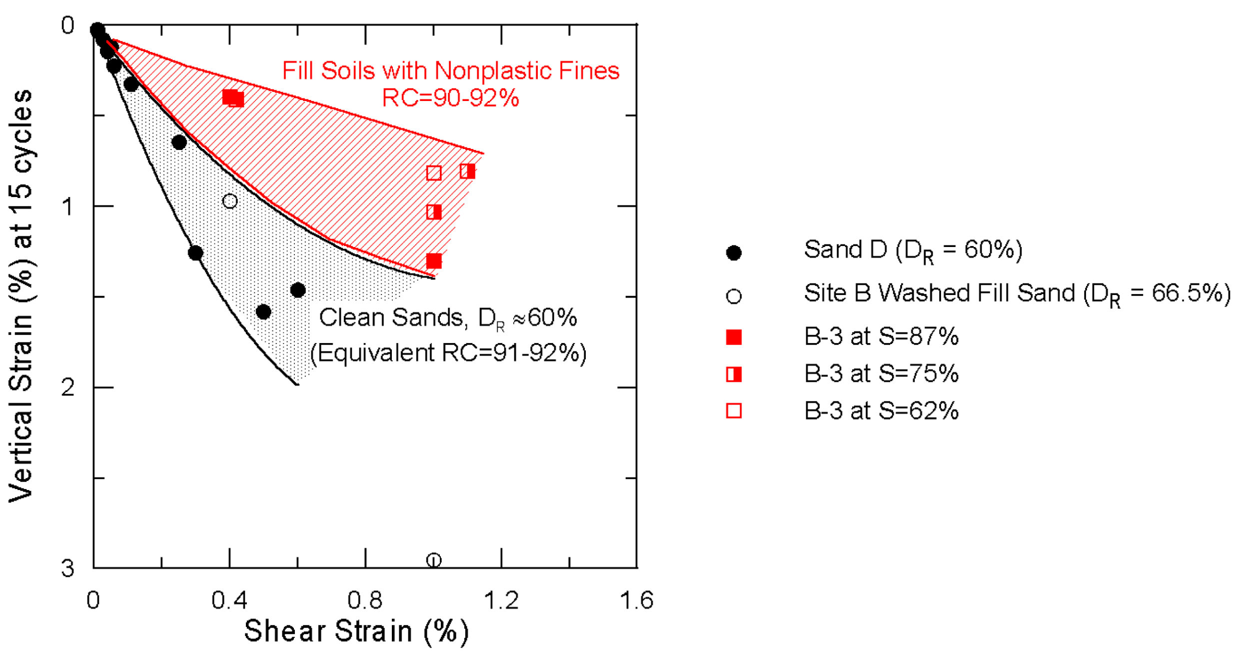

Fig. 5.20. Comparison of vertical strains between Soil B-3 and clean sands at *RC* = 90–92%

The seismic compression behavior of silty sand Soil B-3 (PI = 2) and clean sand are compared in Figure 5.20. Values of $(\varepsilon_v)_{N=15}$ for the silty sand are consistently less than those for Sands B and D. In particular, Soil B-3 specimens experienced vertical strains 2 to 3 times less than Sand B specimens prepared to similar *RC*. There is no systematic variation in $(\varepsilon_v)_{N=15}$ with *S* for Soil B-3 (the apparent adverse influence of *S* in Figure 5.20 can be attributed to variations in *RC* between 90 and 92%).

5.3.7 Variation of Vertical Strain with Number of Cycles

Figure 5.21 shows the mean ± standard deviation range of normalized vertical strains [$\varepsilon_v/(\varepsilon_v)_{N=15}$] versus number of strain cycles (*N*) from tests on Soil A-1. Also shown for comparison is the range for Sand D (presented originally in Figure 4.8). Whang (2001) evaluated $\varepsilon_v/(\varepsilon_v)_{N=15}$ curves for subsets of the data separated into bins of Modified Proctor relative compaction (*RC*), degree of saturation (*S*), and cyclic shear strain amplitude (γ_c), and found that the shape of these curves varies only with *RC*, as shown in Figure 5.21. Specimens compacted to *RC* > 90% experienced relatively more normalized vertical strain in earlier cycles (*N* < 15) and less normalized vertical strain for *N* > 15 than specimens compacted to *RC* < 90%. Specimens of Soil A-1 with *RC* > 90% have $\varepsilon_v/(\varepsilon_v)_{N=15}$ curves that are well approximated by the lower-bound curve for Sand D.

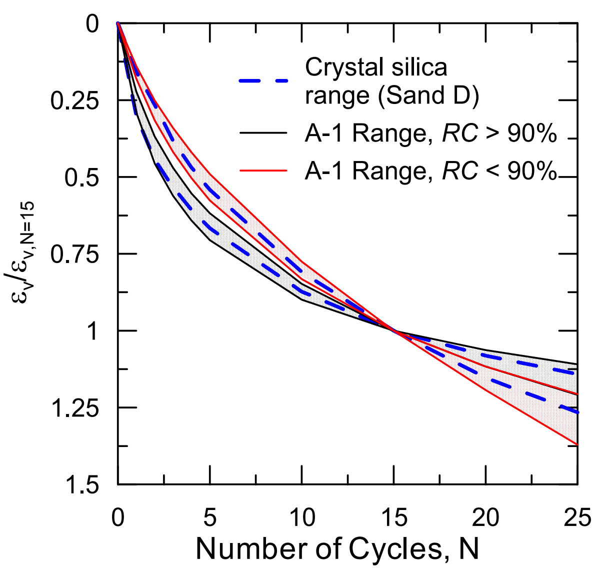

Fig. 5.21. Soil A-1, variation of normalized vertical strain with number of cycles and *RC*

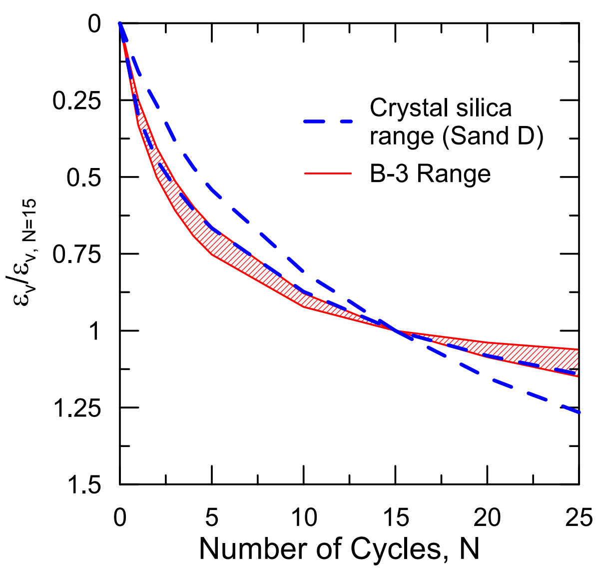

Fig. 5.22. Soil B-3, variation of normalized vertical strain with number of cycles

Figure 5.22 shows the mean ± standard deviation range of $\varepsilon_v/(\varepsilon_v)_{N=15}$ vs. N curves for tests on Soil B-3, along with the Sand D range. Soil B-3 experiences relatively more normalized vertical strain in the earlier cycles (N < 15) than the mean for Sand D, and the $\varepsilon_v/(\varepsilon_v)_{N=15}$ curves are well approximated by the lower-bound curve for Sand D. Whang (2001) investigated the influence of RC, S and γ_c on the Soil B-3 curves, and found no discernible effect. It is noteworthy that the test results for sands also showed no dependence of $\varepsilon_v/(\varepsilon_v)_{N=15}$ curves on D_R.

The results from the sands and Soils A-1 and B-3 suggest that RC is the only compaction condition that significantly affects normalized vertical strain, and this dependence is only present for plastic Soil A-1. Also apparent from the results is significant variability in mean normalized strain curves for different soils, which suggests that unknown soil compositional factors may be important for these relations.

5.3.8 Use of Test Results to Establish Protocol for Analysis of Equivalent Number of Uniform Strain Cycles from Accelerograms

In Section 4.3.4, the process of converting an irregular time history of shear strain to a uniform series of shear strain cycles was described, with specific reference to the problem of seismic compression of clean sands. The key soil property that affects this conversion is the slope of the relationship between the shear strain amplitude from laboratory testing and the number of cycles required to trigger a particular amount of vertical strain (Eq. 4.1). For seismic compression of sands, this slope was found to be approximately $a_2 \approx -0.6$, and showed modest dependence on vertical strain. The laboratory testing of soils with fines was performed for a limited number of shear strain amplitudes, which means that slope parameter a_2 must usually be regressed upon using only 2 to 3 data points. This is not a sufficient number of data points to enable statistically robust evaluation of a_2. Nonetheless, values of a_2 are compiled to see if obvious, significant differences are present between a_2 values for soils with fines and clean sands.

The variations between γ_c and N for various vertical strains are shown in Figure 5.23 for Soils A-1 and B-3. The corresponding slope parameters are plotted as a function of vertical strain in Figure 5.24. The slopes are seen to be slightly steeper for fine-grained soils (a_2 =-0.6 to -0.8) than for clean sands (a_2 =-0.6). There is also a significant variation with vertical strain; a_2 being about -0.8 for ε_v = 0.2% and about -0.6 for ε_v = 0.4%. Slope parameter a_2 was not found to have any consistent variation with Modified Proctor RC or degree of saturation, S.

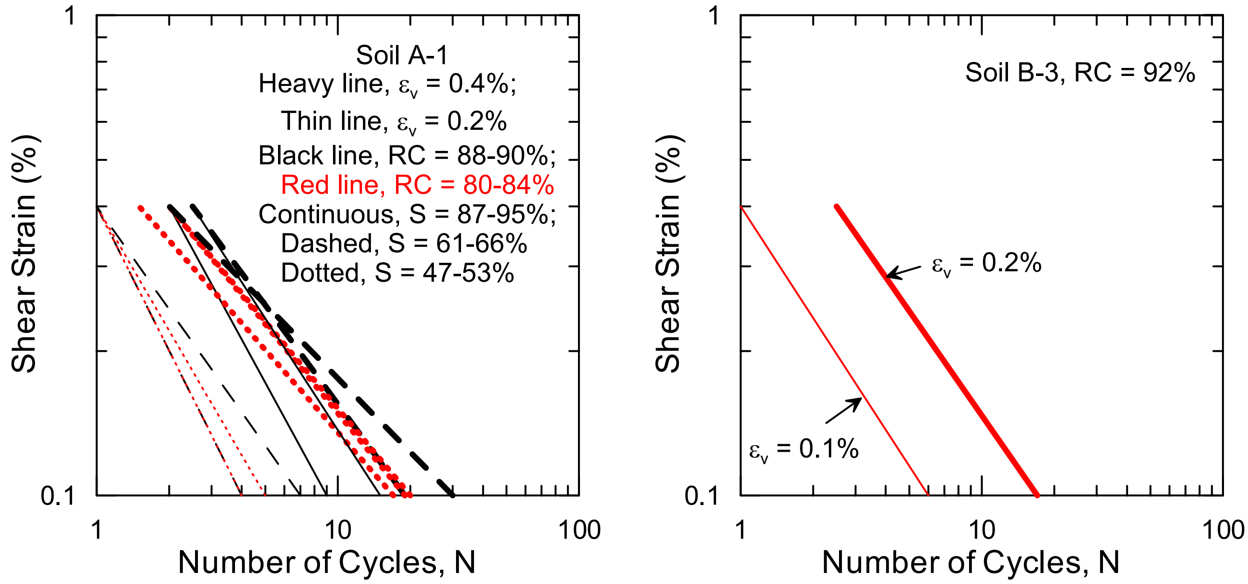

Fig. 5.23. Relationships between shear strain amplitude and number of cycles to cause selected amounts of vertical strain

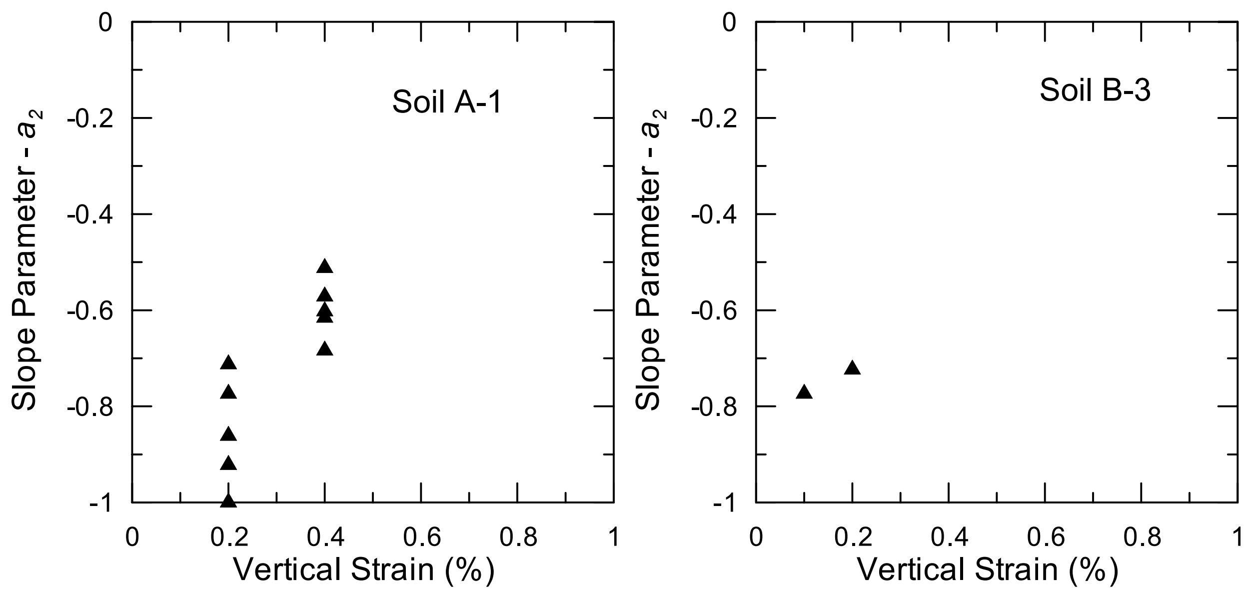

Fig. 5.24. Variation of slope parameter a_2 with vertical strain

A good representative value of a_2 for soils with fines may be –0.7. Unfortunately, there are no existing attenuation models for N derived from N-values determined from weighting factors associated with a_2 < -0.5. However, the evaluation of N for specific time histories recorded near Sites A and B is discussed in Section 6.3.2 using a_2 =-0.7.

6 Ground Motion Characterization

6.1 SELECTION OF TIME HISTORIES

The objective of ground motion characterization for Sites A and B is to develop a suite of time histories representing possible realizations of the ground shaking on rock beneath the sites during the 1994 Northridge earthquake. Three sources of time histories were used: (1) recordings on rock near the sites; (2) deconvolved “rock” motions calculated from recordings at nearby soil sites; and (3) time histories developed from seismological simulations.

The locations of Sites A and B relative to the Northridge fault rupture plane and local strong motion stations are shown in Figure 3.1. An obvious criterion in time history selection is to use stations as close to the subject sites as possible. Strong motion stations within about 10-15 km of the sites include Potrero Canyon (PC), Newhall Fire Station (NFS), Castaic Dam Downstream (CDD), Lake Piru Dam (LPD), Castaic Old Ridge Route (ORR), Lost Canyon (LOS), and Jensen Filtration Plant Generator Building (GEN). A second criterion that is important for time history selection at Sites A and B is possible variations of ground motions with site-source azimuth due to rupture directivity effects. Sites A and B are located north of the rupture plane in the forward rupture directivity region. Of the above-listed strong motion stations, those with epicenter-site azimuths similar to those of Sites A and B are PC, NFS, CDD, LPD, GEN, and ORR. Station ORR is not used herein because of irregular surface topography near the station (the site is located near the crest of a steep ridge). Key information on the remaining sites is provided in Table 6.1, and is discussed in the following sections. Strong motion data for each of these sites were uniformly processed by W.J. Silva of Pacific Engineering and Analysis, and can be obtained from the PEER website (`http://peer.berkeley.edu`). All motions were rotated into their fault-normal and fault-parallel components for use in this study.

Table 6.1. Strong motion stations near Sites A and B that recorded the 1994 Northridge earthquake

Station	Owner	Number	Classification[1]	r (km)[2]
Lake Piru Dam (LPD)	CSMIP	285	B/C1	20.2
Newhall Fire Station (NFS)	CSMIP	24279	C2	7.1
Potrero Canyon (PC)	USC	90056	C2	7.1
Jensen Generator Bldg (GEN)	USGS	655	B	6.2
Castaic Dam Downstream (CDD)	CDWR	-	C2	18.2

[1] Classification scheme from Rodriquez-Marek et al. (2001), B = intact rock, C1 = weathered soft rock, C2 = shallow soil over rock

[2] r = closest distance to Northridge fault rupture plane by Wald and Heaton (1994)

6.1.1 Recordings on Rock

Of the accelerograph stations listed in Table 6.1, the LPD and GEN sites are classified as having rock conditions. Acceleration, velocity, and displacement time histories from the LPD and GEN sites are shown in Figure 6.1.

The LPD station is located approximately 300 m below the left abutment of an embankment dam. Although borehole data from the site are not available, the ground conditions are classified as rock based on observations of outcropping rock near the site observed during field reconnaissance.

The GEN station is located in a single-story structure (Generator Building) at the Jensen Filtration Plant. Ground conditions at the site have been characterized by the ROSRINE program and consist of 3 m of stiff fill overlying Saugus bedrock. A study performed by Crouse and Ramirez (2003) indicates that soil-structure interaction effects were unlikely to have significantly affected the ground motions recorded at the GEN station.

As shown in Figure 6.1, the GEN recording has a large-amplitude pulse in the fault-normal direction that occurs early in the velocity and displacement time histories. This pulse is generally absent in the fault-parallel direction, and the values of peak horizontal velocity (PHV) and displacement (PHD) are correspondingly smaller in the fault-parallel direction (particularly for PHD). These are characteristic features of forward rupture directivity effects (Somerville et al., 1997), which are expected because the subject region is located near the up-dip projection of the fault rupture plane. These rupture directivity features in the waveforms are not evident in the acceleration time histories. These features are also less apparent in the LPD recording, which is further from the source (Table 6.1).

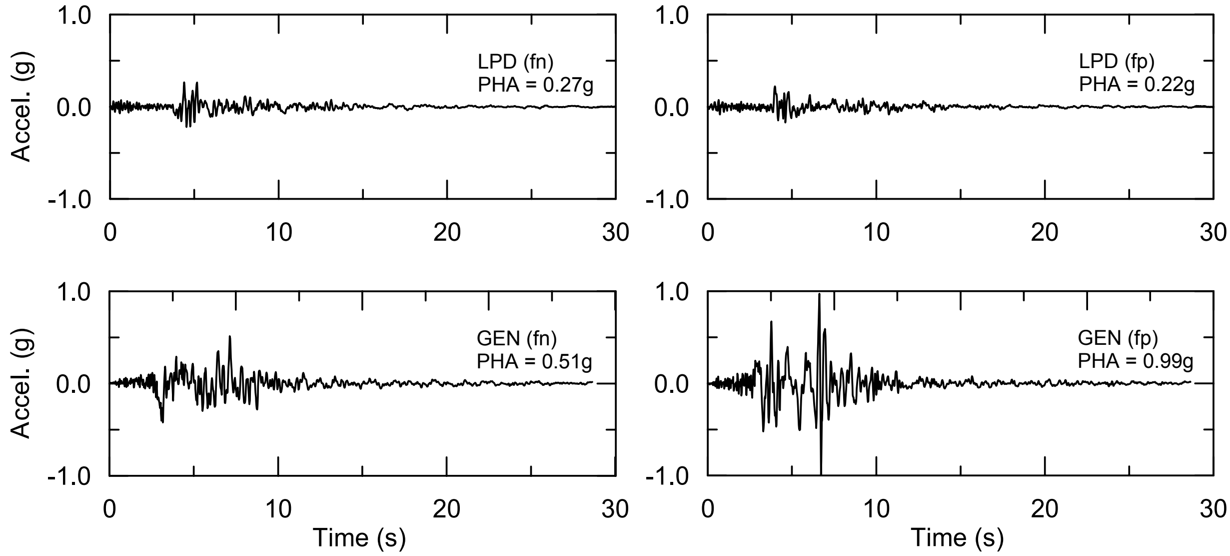

Fig. 6.1(a). Acceleration time histories recorded at strong motion stations on rock near Sites A and B

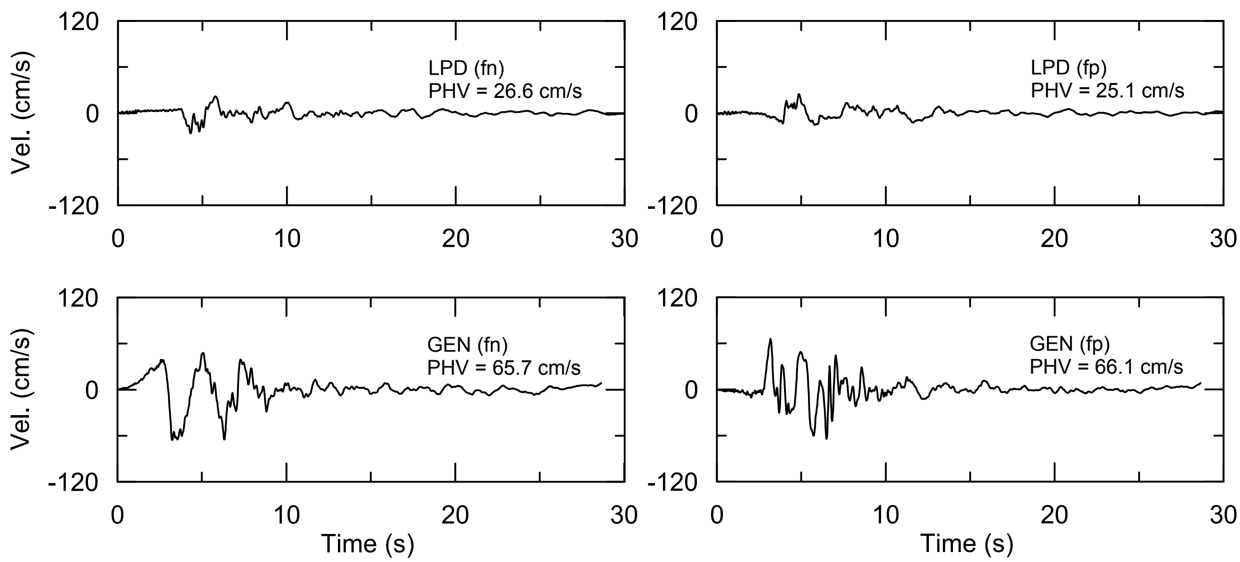

Fig. 6.1(b). Velocity time histories recorded at strong motion stations on rock near Sites A and B

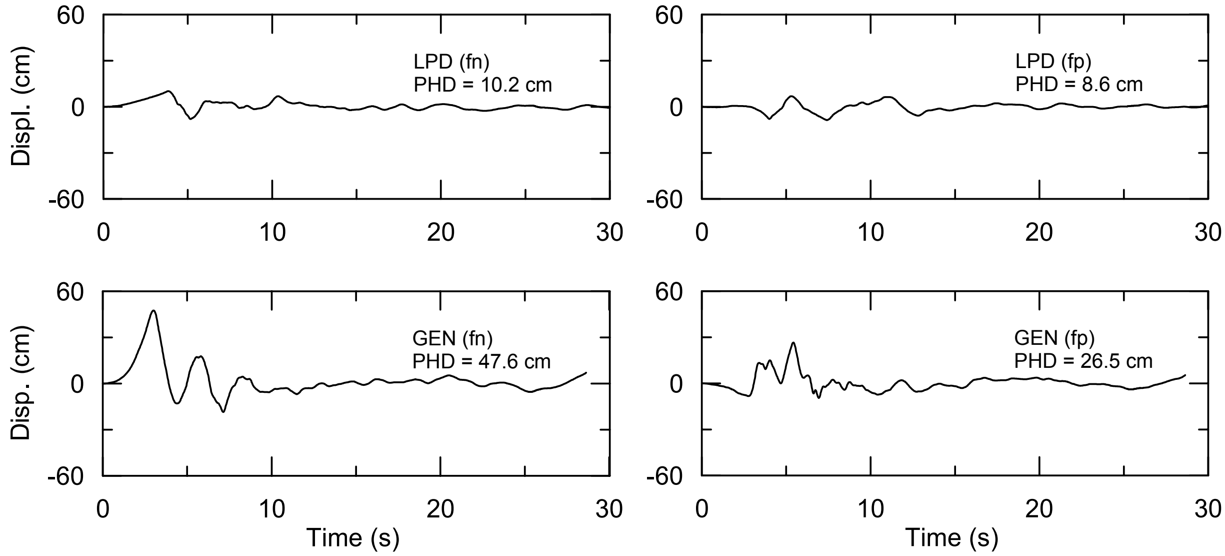

Fig. 6.1(c). Displacement time histories recorded at strong motion stations on rock near Sites A and B

6.1.2 Recordings on Soil

Accelerograph stations NFS, PC, and CDD have a site condition consisting of shallow soil overlying rock. At each of these sites, local borehole data are available from the following sources:

NFS, PC: ROSRINE website (**`http://geoinfo.usc.edu/rosrine/`**)
CDD: Fumal et al. (1982)

NFS is located in a single-story fire station structure on level ground. As shown in Figure 6.2, site conditions consist of about 36 m of alluvial soils overlying Saugus bedrock. The CDD site is located on a fill blanket (approximately 15 m thick) below the toe of Castaic Dam. Soil conditions near this site are shown in Figure 6.3. The PC site is located in a small wooden shack on level ground within Potrero Canyon. As shown in Figure 6.4, site conditions consist of about 19 m of sandy alluvial soils underlain by Saugus bedrock. Liquefaction occurred at a number of locations in the canyon (Stewart et al., 1996), but no surface evidence of liquefaction was observed near the strong motion station during post–earthquake reconnaissance (R. White, *pers. communication*, 2001).

Recorded acceleration, velocity, and displacement time histories from the NFS, CDD, and PC sites are shown in the top three frames of Figures 6.5–6.7. All of the recordings have a large amplitude pulse in the fault-normal direction, which is characteristic of near-fault effects (as discussed previously in Section 6.1.1 for the GEN site).

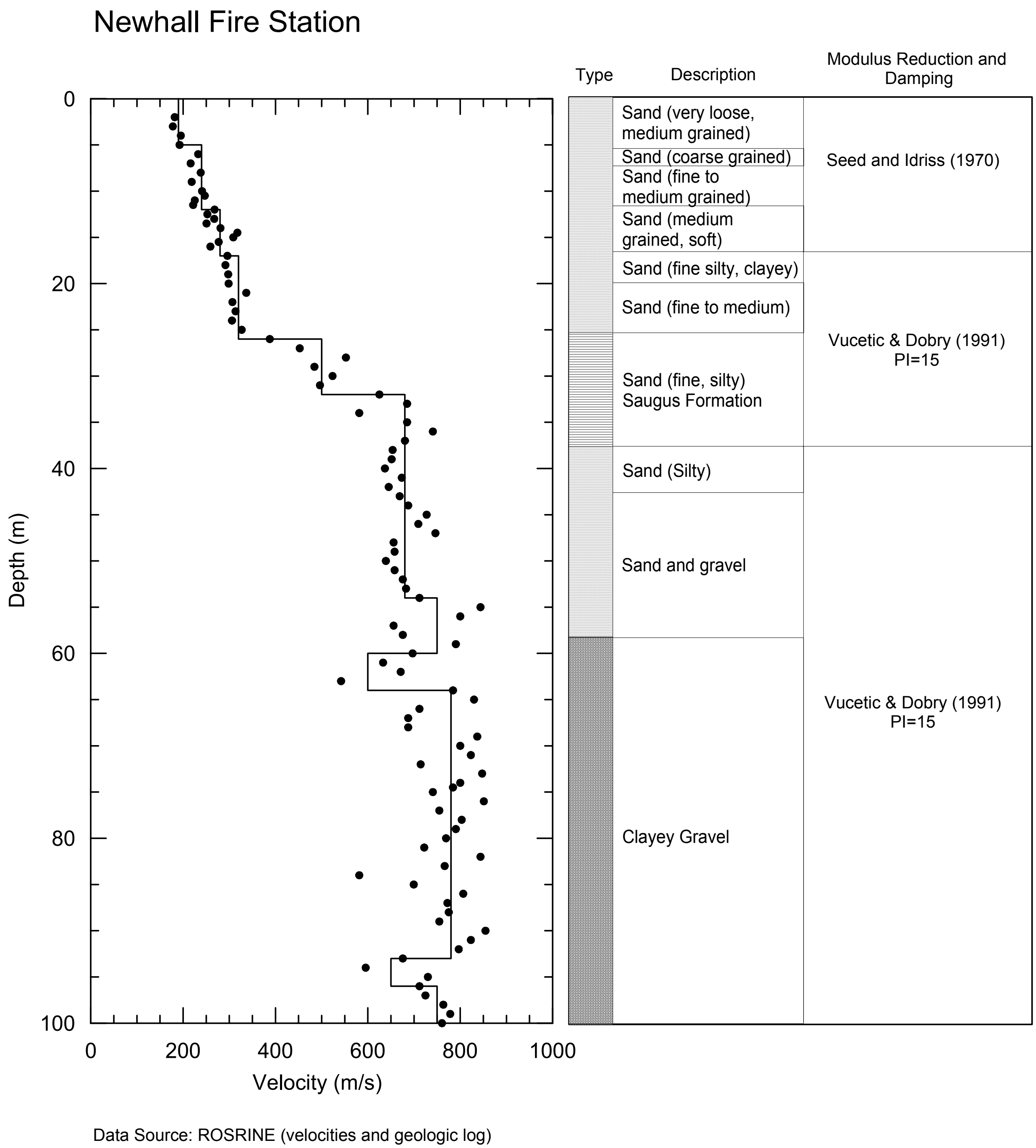

Fig. 6.2. Ground conditions at NFS strong motion accelerograph site (after ROSRINE)

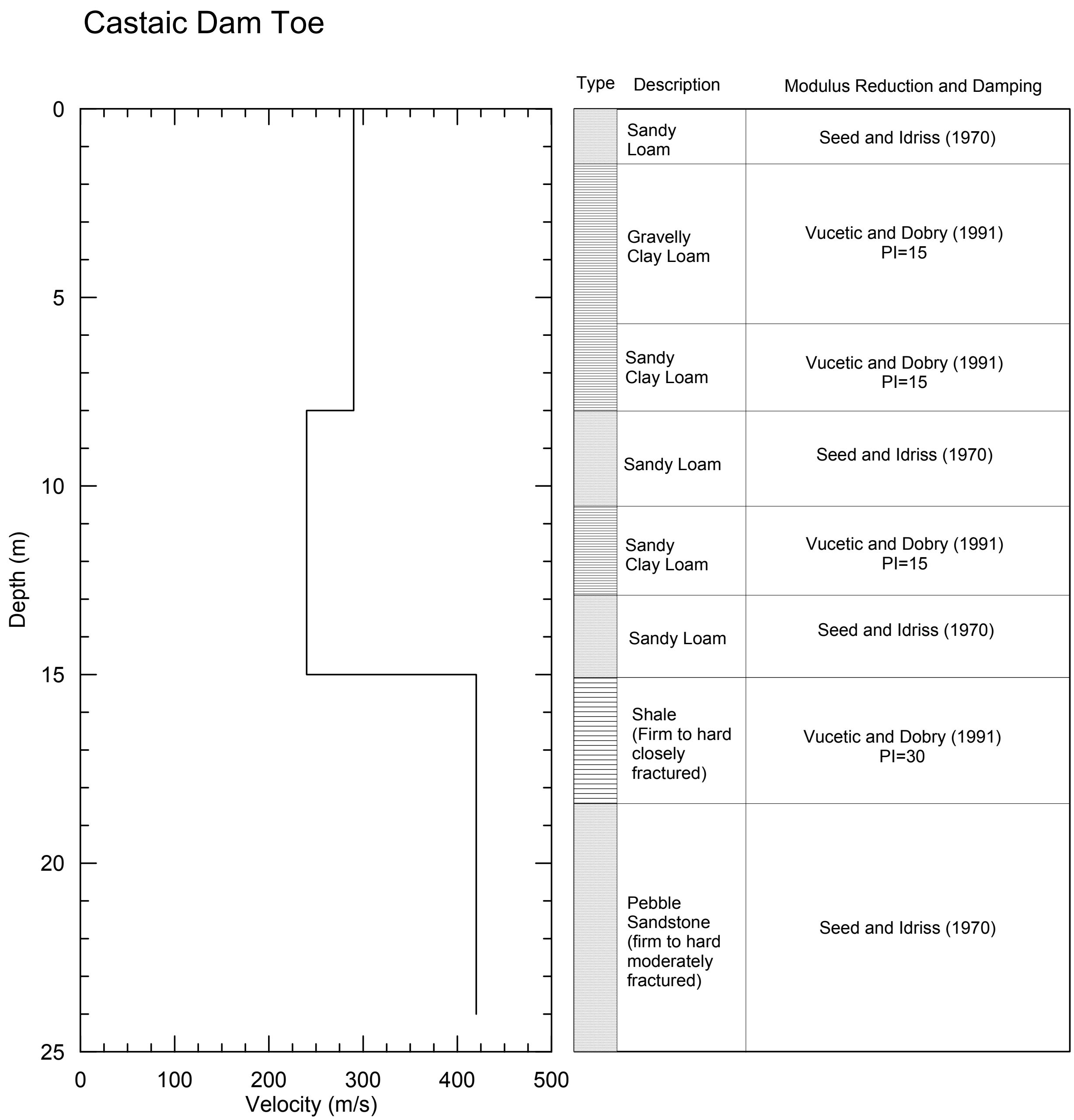

Data Source: Fumal et al., 1982 (velocities and geologic log)
L. F. Harden, Jr. 1998 (personal communication)

Fig. 6.3. Ground conditions at CDD strong motion accelerograph site (after Fumal et al., 1982)

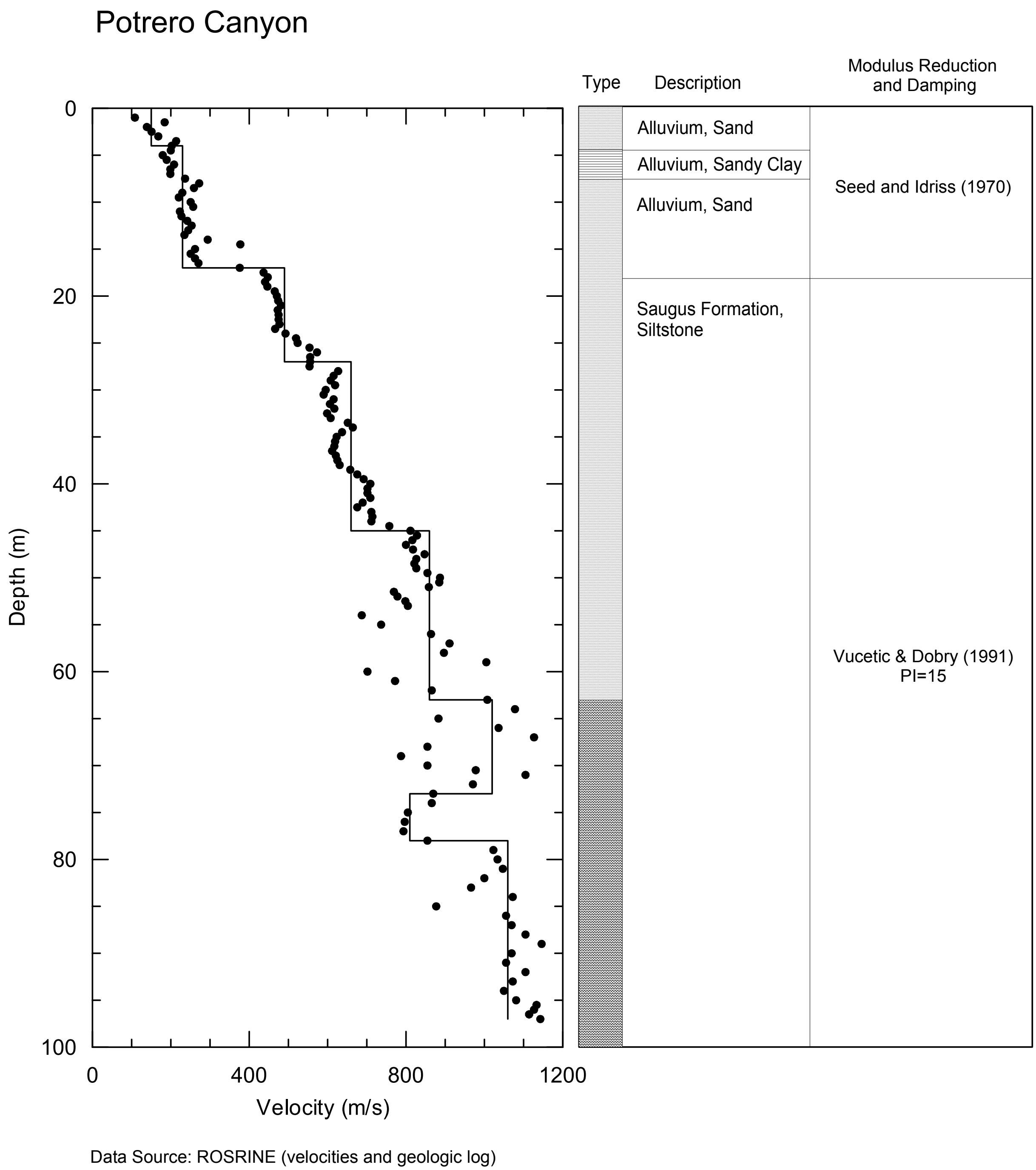

Fig. 6.4. Ground conditions at PC strong motion accelerograph site (after ROSRINE)

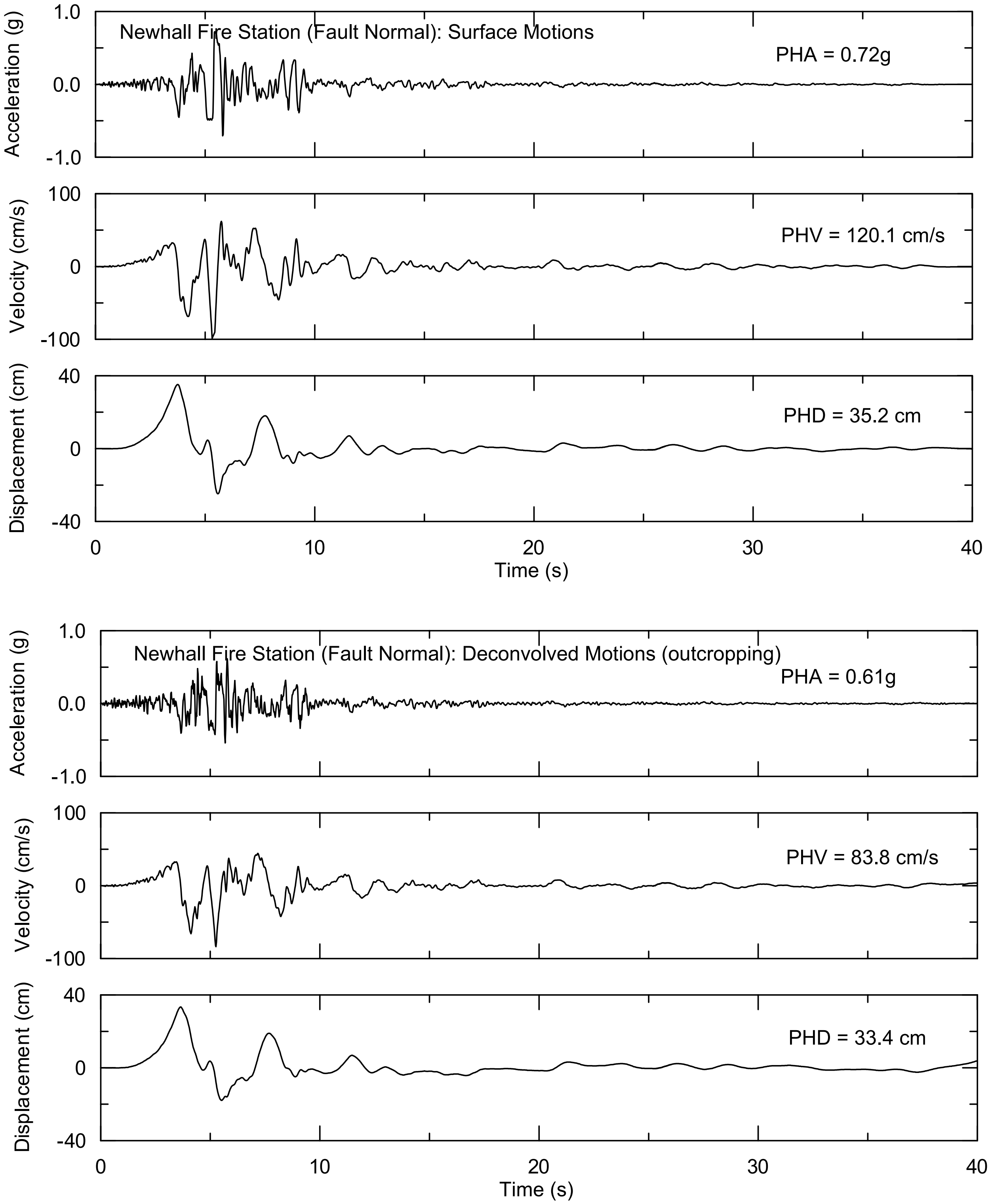

Fig. 6.5(a). Recorded waveform of NFS recording on soil and calculated waveform of deconvolved motion, fault-normal direction

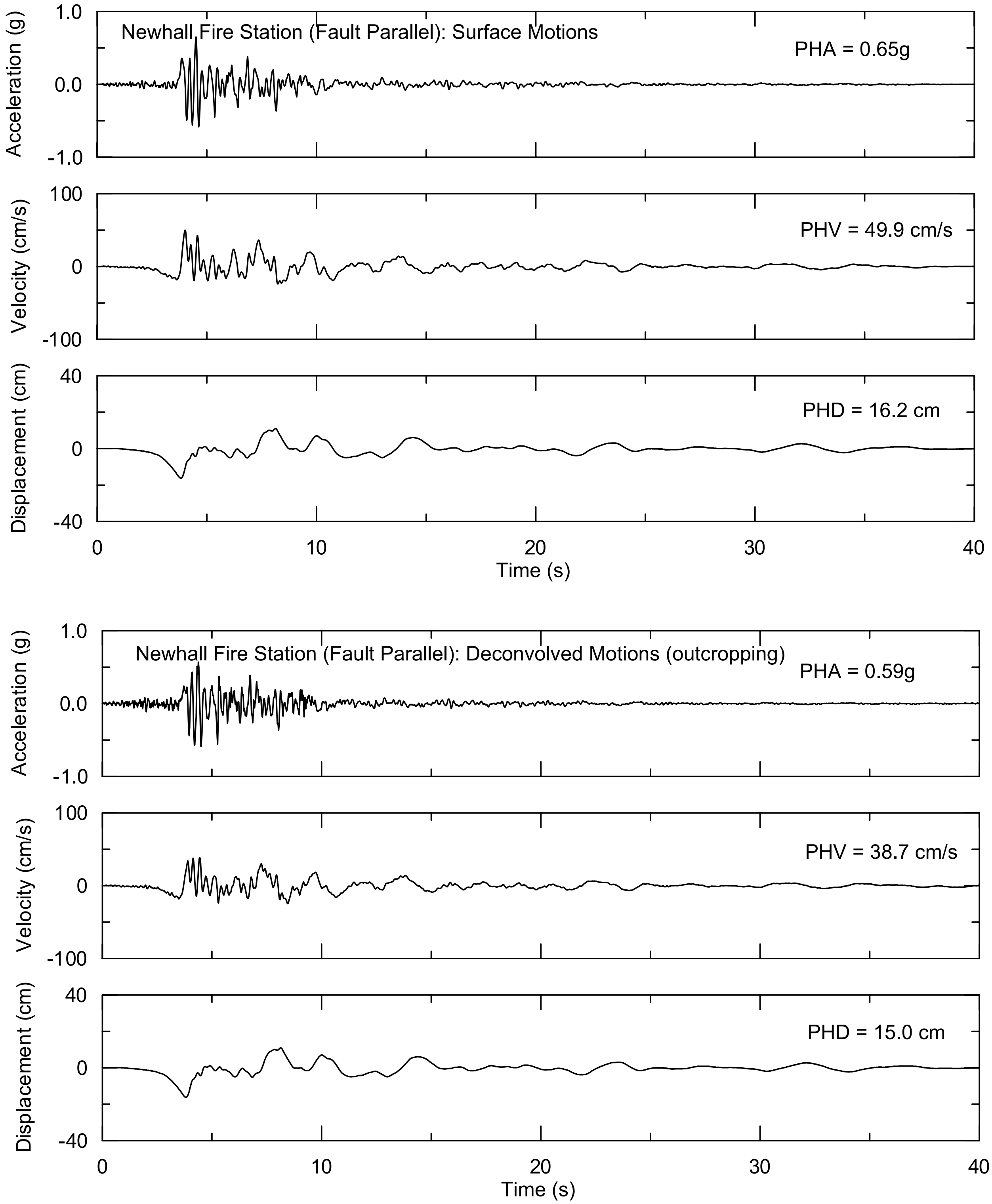

Fig. 6.5(b). Recorded waveform of NFS recording on soil and calculated waveform of deconvolved motion, fault-parallel direction

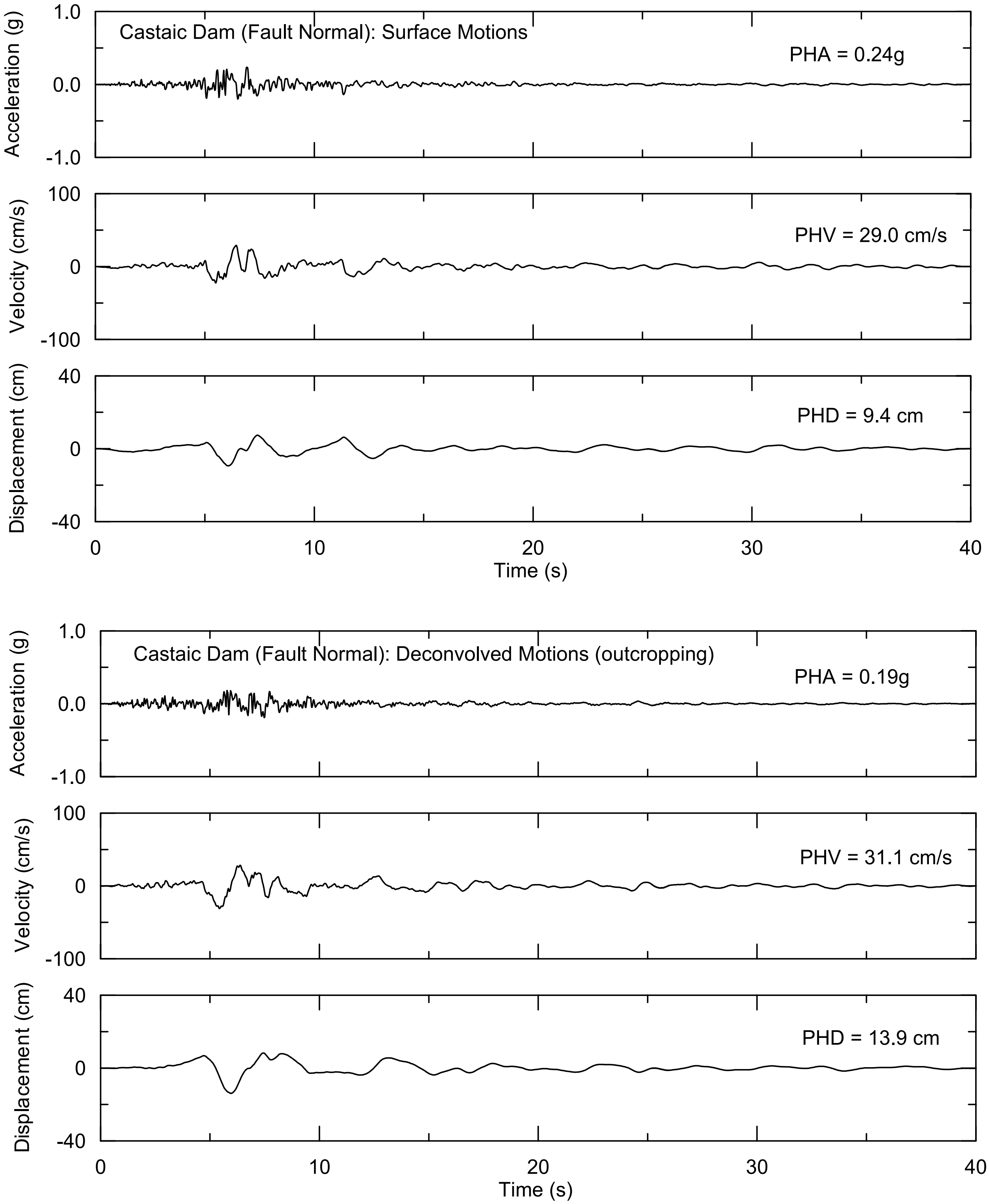

Fig. 6.6(a). Recorded waveform of CDD recording on soil and calculated waveform of deconvolved motion, fault-normal direction

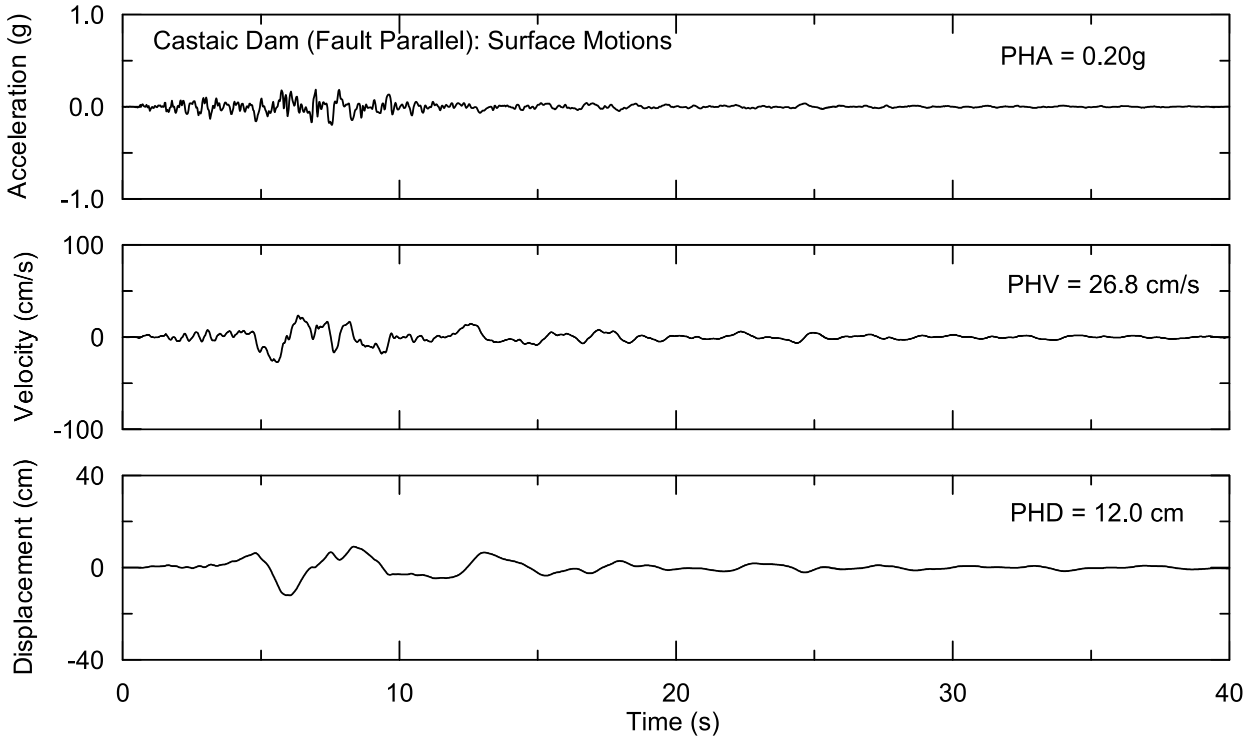

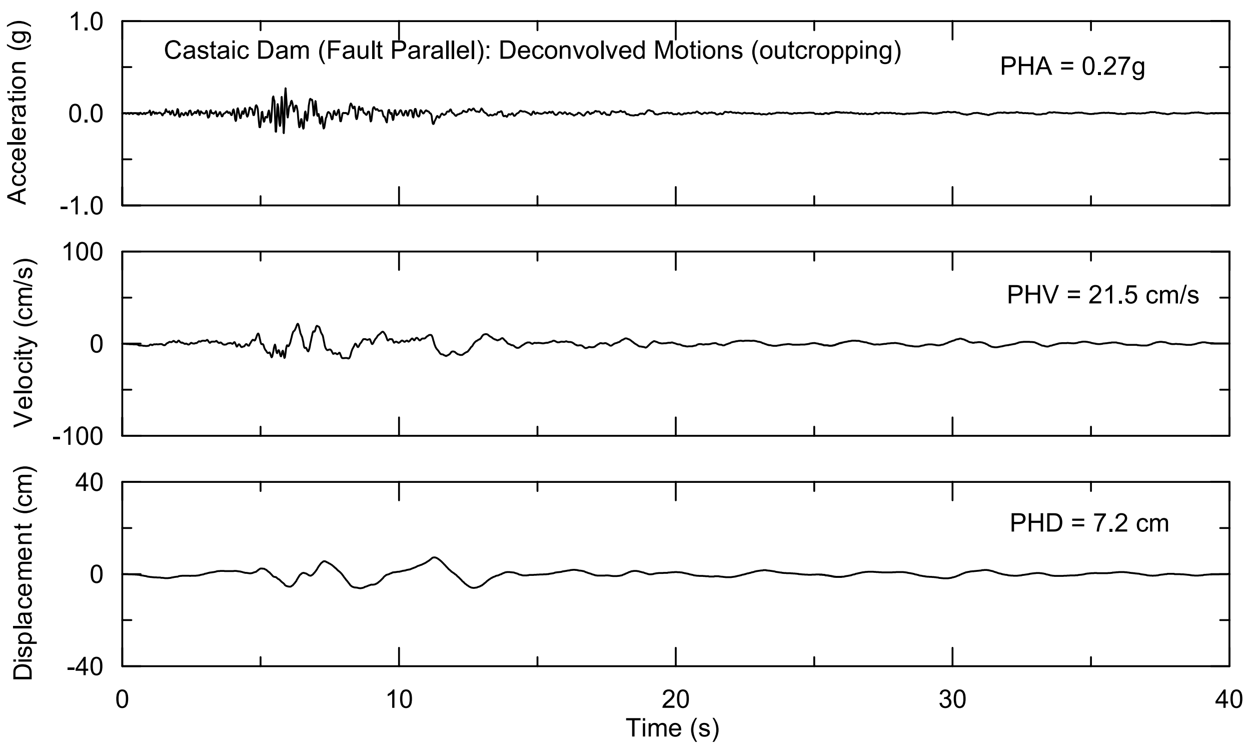

Fig. 6.6(b). Recorded waveform of CDD recording on soil and calculated waveform of deconvolved motion, fault-parallel direction

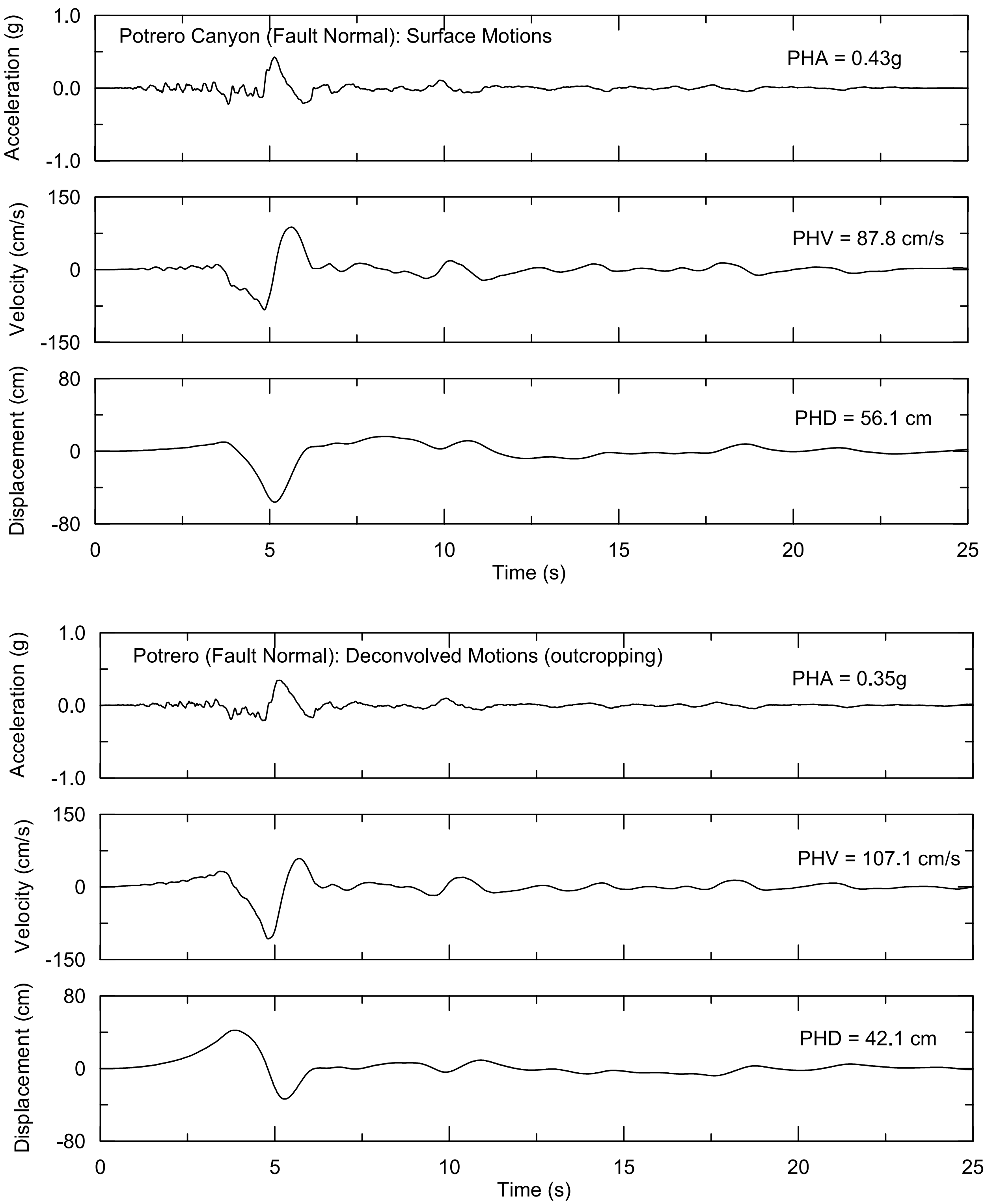

Fig. 6.7(a). Recorded waveform of PC recording on soil and calculated waveform of deconvolved motion, fault-normal direction

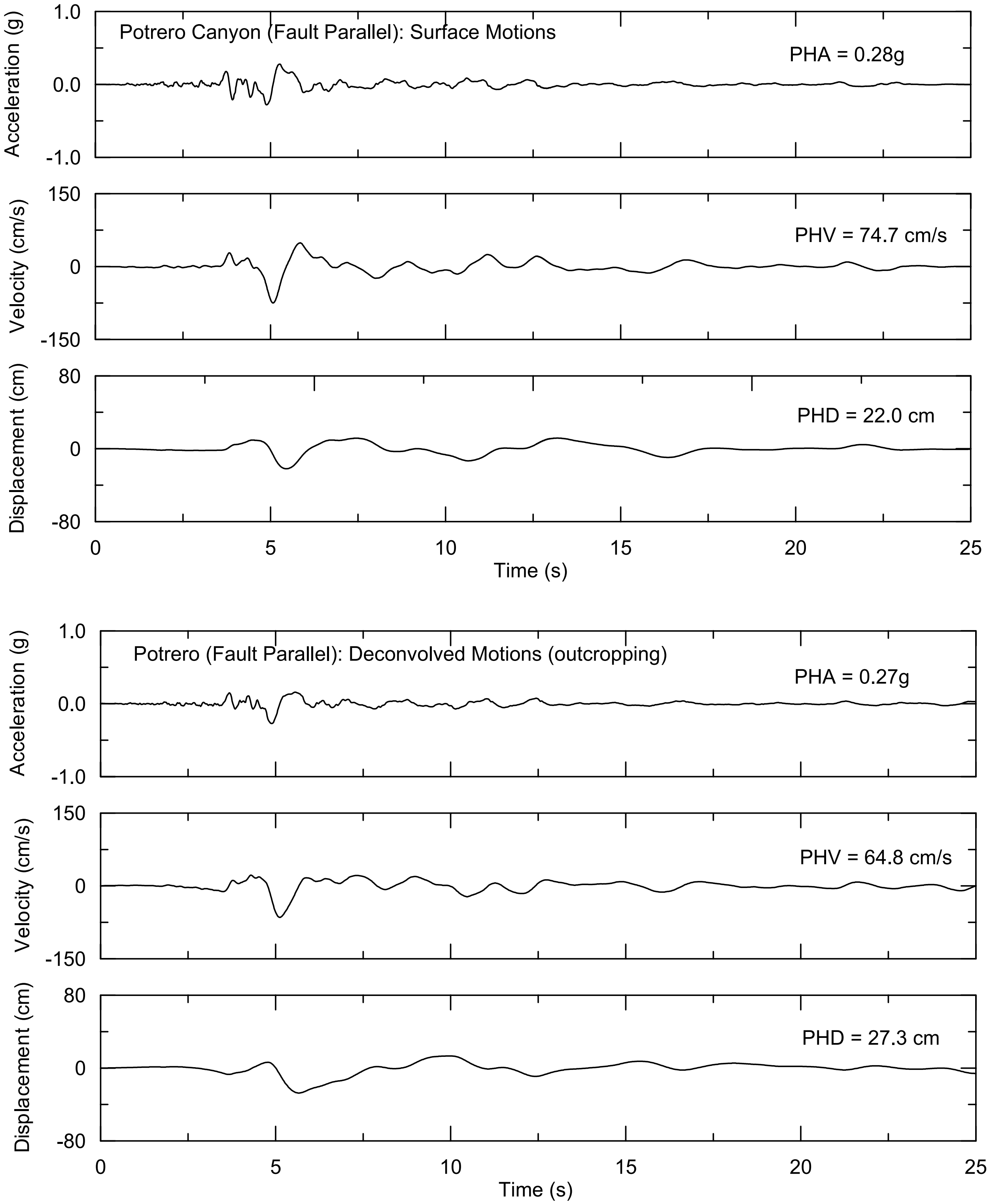

Fig. 6.7(b). Recorded waveform of PC recording on soil and calculated waveform of deconvolved motion, fault-parallel direction

For the NFS, CDD, and PC sites, deconvolution analyses were performed to estimate motions on rock from the soil recordings. These calculations were performed according to the procedure of Silva (1986), which follows:

1. Soil recordings are low-pass filtered with a corner frequency of 15 Hz.
2. Strain-dependent soil properties are calculated using 87% of the recorded amplitude using equivalent linear ground response analyses (SHAKE91, Idriss and Sun, 1991).
3. Rock motions are calculated for an outcropping condition using strain-dependent soil properties from (2) and the full amplitude of the ground surface recordings on soil.

References to the modulus reduction and damping curves used in these analyses are provided in Figures 6.2–6.4. The calculated waveforms for the rock site condition are shown in the bottom three frames of Figures 6.5–6.7. The phasing and shape of the waveforms are shown in the figures to not be significantly effected by the deconvolution process. Values of *PHA*, *PHV*, and *PHD* are generally changed < 30%.

6.1.3 Time Histories from Simulation

A stochastic finite source model of the Northridge earthquake developed by W. J. Silva was used to develop synthetic waveforms for Sites A and B. General features of this method of simulation are described in Silva et al. (1990). The time histories developed by this method are not direction-dependent. The time histories are shown in Figure 6.8.

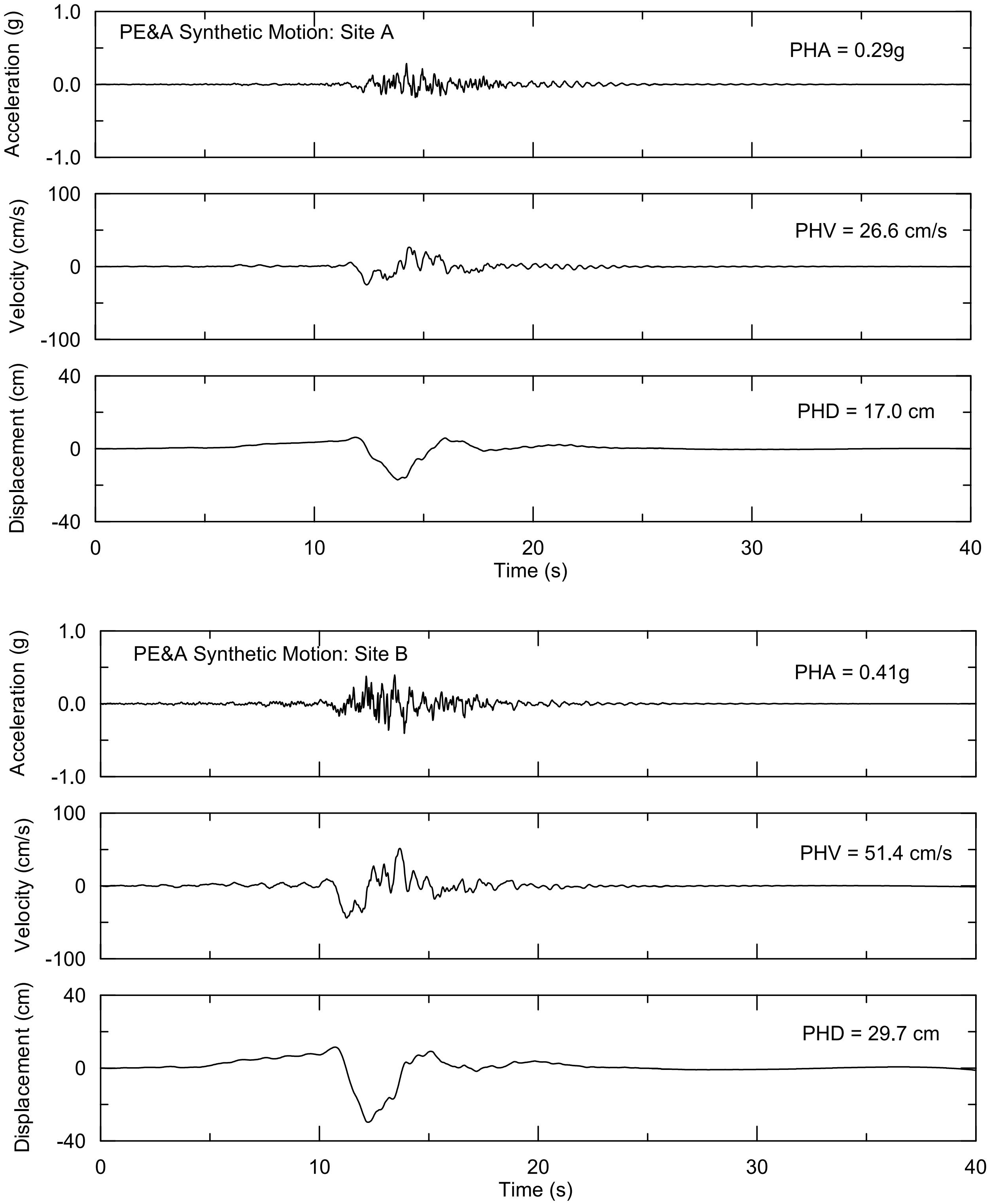

Fig. 6.8. Waveforms for motions at Sites A and B derived from stochastic finite fault simulation procedure

6.2 SCALING OF TIME HISTORIES

As indicated in Table 6.1, the strong motion stations near Sites A and B have different site-source distances than are present at Sites A or B (for which r = 12.2 and 7.2 km, respectively). Accordingly, the recorded (or deconvolved) time histories are scaled to provide estimates of the time histories at Sites A and B. Empirical attenuation relationships for spectral acceleration predict distance-scaling that is a function of spectral period, T. The scaling factor for a given period can be taken as the ratio of the *predicted* spectral acceleration on rock at the subject site [$S_{a,site}(T)$] to the *predicted* spectral acceleration at the strong motion accelerograph [$S_{a,SMA}(T)$]:

$$SF(T) = \frac{S_{a,site}(T)}{S_{a,SMA}(T)} \tag{6.1}$$

where the term "predicted" refers to the calculated median spectral acceleration from an attenuation relationship. Justification for the use of this method of distance scaling is provided in Figure 6.9 by comparing recorded spectral accelerations for stations north of the Northridge fault rupture to predictions from the Abrahamson and Silva (1997), Sadigh et al. (1997), and Idriss (1994) attenuation relationships. The distance scaling provided by all three relations is seen to be similar to the general trend of the data for T = 0–0.3 s. We select the Abrahamson and Silva (1997) relation to define $SF(T)$ because of its ability to incorporate hanging wall effects into the scale factors. However, as shown in Figure 6.9, all three relations predict similar amounts of distance scaling.

Since $SF(T)$ values are only weakly dependent on period, we use a single SF value which is an average of $SF(T)$ over the period range T = 0–0.3 s. The use of the short-period range for scaling was motivated by the relatively large sensitivity of the computed shear strains to peak acceleration (as shown subsequently). Scaling factors derived in this way for each recording are presented in Table 6.2. Motions with scale factors that deviate significantly from one are given a lower weight in the response analyses, as described in Chapter 7.

Table 6.2. Factors used to scale recorded motions to provide estimates of the ground motion amplitude at Sites A and B

Site	CDD	LPD	NFS	GEN	PC
A	1.46	1.62	0.65	0.48	0.65
B	2.24	2.48	0.99	0.74	0.99

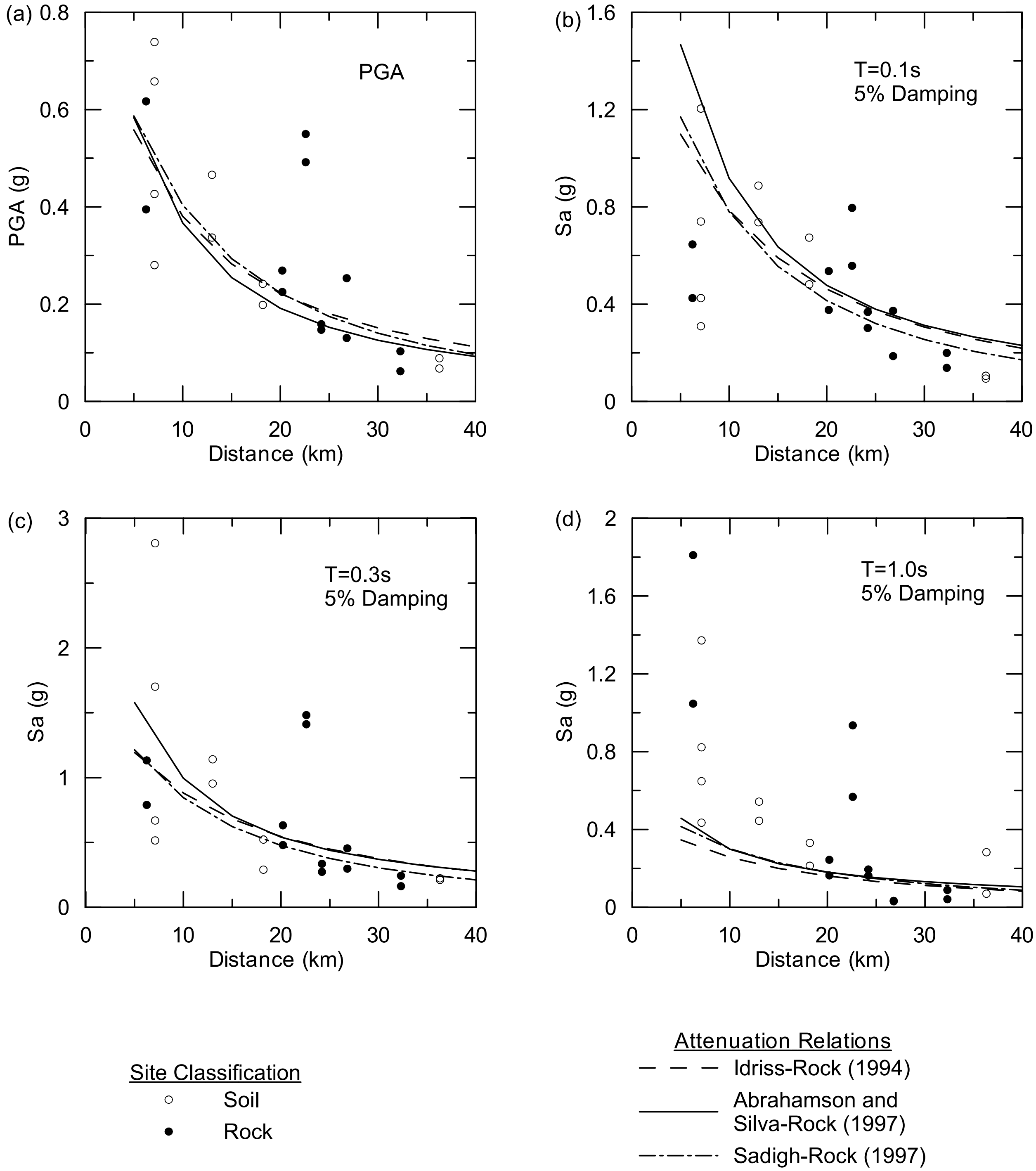

Fig. 6.9. Strong motion data for stations north of the Northridge fault rupture plane and median predictions from attenuation relations for rock sites

6.3 COMPARISON OF SELECTED MOTIONS

The time histories recorded at the NFS, LPD, GEN, CDD, and PC stations were rotated into their fault-normal and fault-parallel directions, and were scaled according to the procedures described in Section 6.2. These scaled motions are the time histories used in the ground response calculations described in Chapter 7. In this section we compare the ground motion intensity measures associated with these time histories.

6.3.1 Response Spectra

Response spectral accelerations at 5% damping for the fault-normal and fault-parallel directions are compared in Figure 6.10. Also shown in these figures is the predicted spectra at the site based on the Abrahamson and Silva (1997) attenuation relation for rock sites adjusted for rupture directivity using the Somerville et al. (1997) model and Northridge event terms (provided by N. Abrahamson, *pers. communication*). The spectra for motions LPD, CDD, and NFS are reasonably consistent with one another and with the median attenuation prediction. The PC and PEA spectra have relatively low spectral ordinates at low periods (T < 0.5–1.0 s), but more pronounced long-period energy content. The GEN motion has low ordinates in the fault-normal direction and high ordinates in the fault-parallel direction.

6.3.2 Equivalent Number of Uniform Strain Cycles

An equivalent number of uniform amplitude loading cycles can be calculated from an orthogonal pair of horizontal acceleration time histories once an appropriate set of scaling factors has been developed for the problem under consideration. In the previous work of Liu et al. (2001), the demand parameter under consideration was shear stress, and weight factors were developed for soil liquefaction. For our purpose, the demand parameter is shear strain, and the weight factors need to be appropriate to the problem of seismic compression. The two horizontal components of shaking are combined using a vector sum normalization scheme described by Liu et al. (2001).

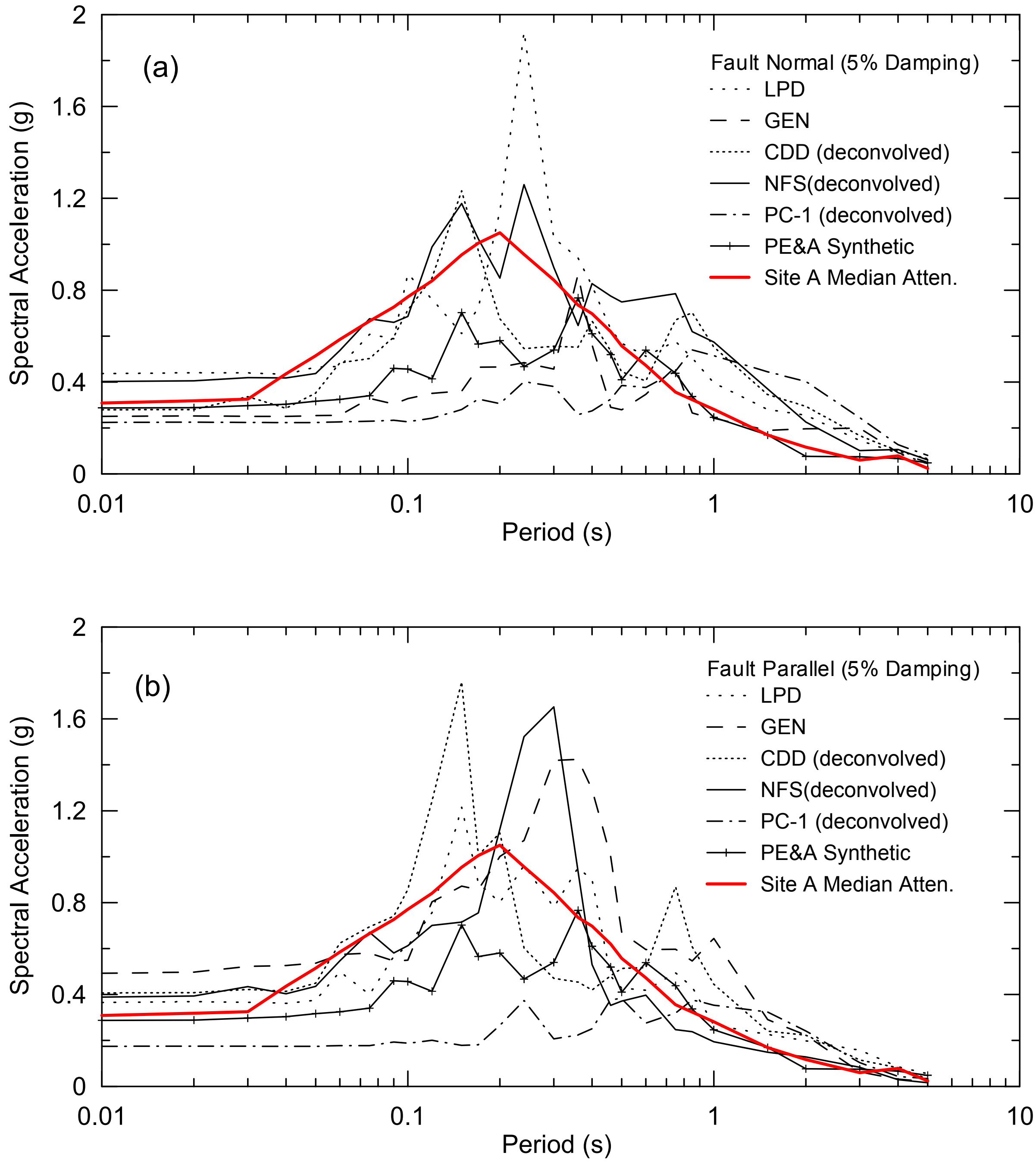

Fig. 6.10(a). Acceleration response spectra at 5% damping for scaled ground motion time histories used for ground response analyses at Site A

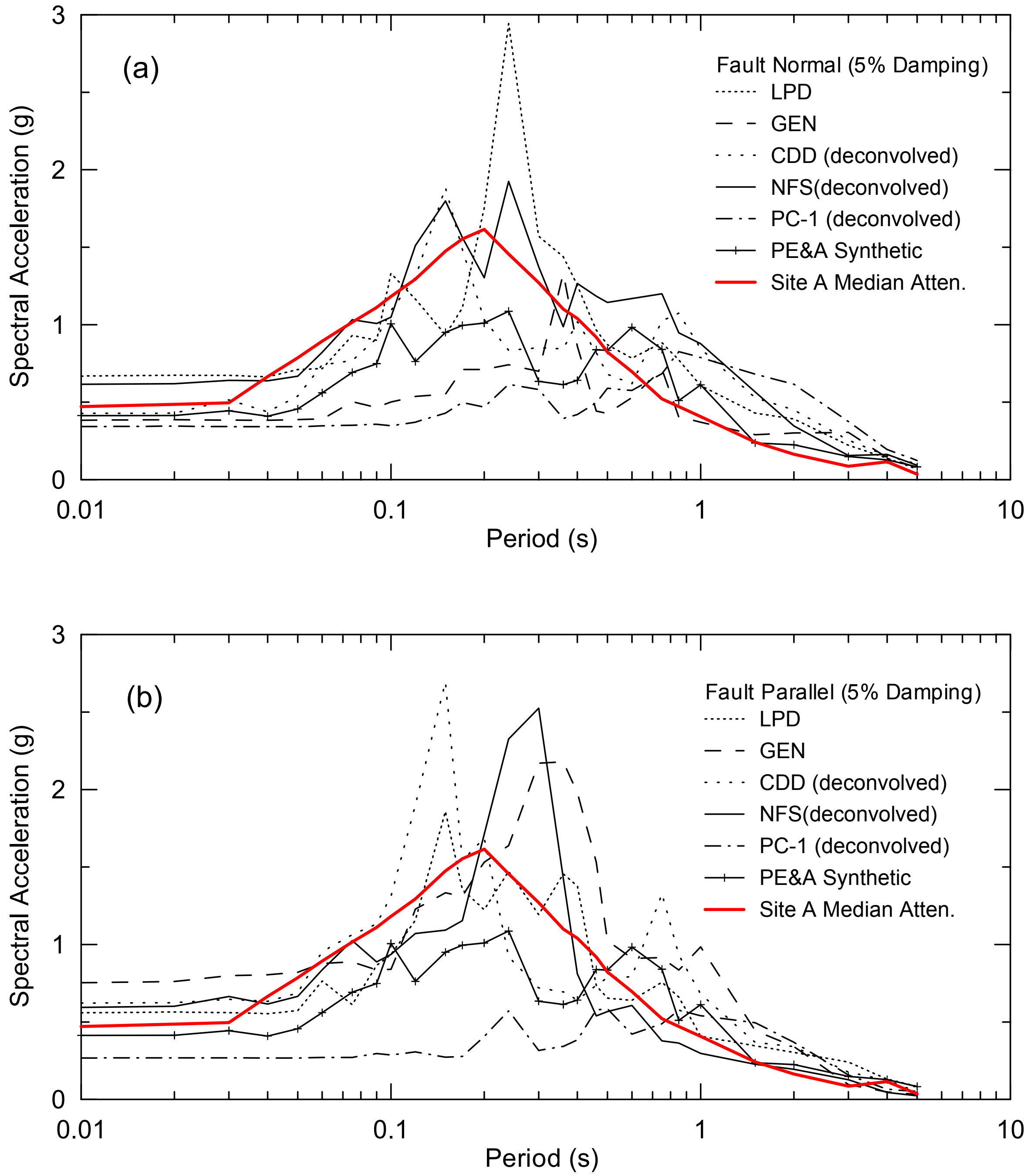

Fig. 6.10(b). Acceleration response spectra at 5% damping for scaled ground motion time histories used for ground response analyses at Site B

Laboratory test results presented in Section 5.3.8 provide the data from which weight factors for the evaluation of N can be derived. As shown in Figure 5.23, these data relate the cyclic shear strain amplitude (γ_c) required to produce a particular amount of volumetric strain (ε_v) to N. As shown in Figure 5.24, the data were found to have a slope in log-log space of $a_2 \approx -0.7$ (in natural logarithmic units).

The weight factors are derived by recognizing that each point on a given curve in Figure 5.23 is equivalent (all induce the specified volumetric strain). Accordingly, the relative damage potential of single pulses with different amplitudes is the ratio of the N-values corresponding to those amplitudes along the curve. If a strain amplitude of 65% of the peak ($0.65\gamma_{pk}$) is taken as a "standard," then the weighting factor for amplitude i (WF_i) can be defined as:

$$WF_i = \frac{N_{0.65}}{N_i} \tag{6.2}$$

where i = 0–1.0, and N_i and $N_{0.65}$ = values of N at amplitude i and amplitude 0.65, respectively. Using Eq. 6.2 and a representative slope for the curves in Figures 5.23–5.24 of a_2 = -0.7, weight factors appropriate to the seismic compression of fill soils from Sites A and B were derived using the following expression:

$$WF_i = \exp\left[\frac{1}{a_2}\cdot\left(\ln(0.65) - \ln(i)\right)\right] \tag{6.3}$$

These weight factors are listed in Table 6.3.

The weight factors in Table 6.3 were used to derive N values for each of the selected time histories. These N values are listed in Table 6.4. The values for N indicated in Table 6.4 are approximately 1.7 times larger than those computed by Liu et al. (2001), who used a different set of weighting curves appropriate to the problem of soil liquefaction. There is significant variability in the N values among the various recordings, with two motions close to the source (i.e., PC and GEN) having particularly low N values.

Table 6.3. Derived weighting factors for calculation of number of cycles for Fills A and B

$i=\gamma_c/\gamma_{c,N=1}$	N_i	WF_i
0.10	26.8	0.069
0.15	15	0.123
0.20	10	0.186
0.25	7.2	0.255
0.30	5.6	0.331
0.35	4.5	0.413
0.40	3.7	0.500
0.45	3.1	0.591
0.50	2.7	0.687
0.55	2.3	0.788
0.60	2.1	0.892
0.65	1.9	1.000
0.70	1.7	1.112
0.75	1.5	1.227
0.80	1.4	1.345
0.85	1.3	1.467
0.90	1.2	1.592
0.95	1.1	1.720
1.00	1	1.850

Table 6.4. Characteristic of input time histories for response analyses

				As Recorded				Scaled for Site A				Scaled for Site B			
Recording	Duration (s)[1]	N^2	T_m (s)[3]	PHA (g)	PHV (cm/s)	PHD (cm)	$I_{a,max}$ (cm/s)	PHA (g)	PHV (cm/s)	PHD (cm)	$I_{a,max}$ (cm/s)	PHA (g)	PHV (cm/s)	PHD (cm)	$I_{a,max}$ (cm/s)
CDD(fn)	5.3	18.1	0.74	0.19	31.1	13.9	64.3	0.28	45.4	20.2	137.2	0.43	69.6	31.0	322.9
CDD(fp)	3.6		0.59	0.27	21.5	7.2	60.9	0.40	31.4	10.6	129.9	0.61	48.2	16.2	305.8
LPD(fn)	5.3	16.3	0.57	0.27	26.6	10.2	62.3	0.43	43.0	16.5	163.6	0.66	65.9	25.3	383.4
LPD(fp)	6.7		0.61	0.22	25.1	8.6	44.0	0.36	40.6	13.9	115.4	0.55	62.1	21.3	270.5
NFS(fn)	3.2	19.9	0.60	0.61	83.8	33.4	429.8	0.40	54.5	21.7	181.6	0.61	83.0	33.0	421.2
NFS(fp)	2.9		0.37	0.59	38.7	15.0	344.5	0.38	25.1	9.7	145.6	0.58	38.3	14.8	337.7
GEN(fn)	4.2	10.2	0.87	0.51	65.7	47.6	263.1	0.25	31.8	23.0	61.6	0.38	48.6	35.2	144.1
GEN(fp)	3.6		0.53	0.99	66.1	26.5	708.1	0.48	32.0	12.8	165.9	0.74	48.9	19.7	388.0
PC(fn)	1.7	6.1	1.73	0.35	107.1	42.1	128.8	0.22	69.4	27.3	54.0	0.34	106.1	41.7	126.4
PC(fp)	4.0		1.39	0.27	64.8	27.3	70.7	0.17	41.9	17.7	29.6	0.27	64.1	27.1	69.3
PE&A-A	3.5	10.8	0.53	-	-	-	-	0.29	26.6	17.0	61.3	-	-	-	-
PE&A-B	3.1	14.5	0.58	-	-	-	-	-	-	-	-	0.41	51.4	29.7	168.7

1. Duration calculated from Husid plot as time between 0.05 and 0.75 normalized Arias intensity
2. Calculated as vector sum normalization of both horizontal components
3. T_m derived from Fourier spectral amplitudes as defined by Rathje et al. (1998)

6.3.3 Other Intensity Measures

Ground motion intensity measures other than spectral acceleration and N are compared in Table 6.4. The parameters of significant duration, mean period, and N are not dependent on scaling. Notable features of the data in Table 6.4 include significantly larger PHV and PHD for the fault-normal time histories than for the fault-parallel time histories. As expected, the level of shaking anticipated for Site B is considerably stronger than that for Site A because Site B is closer to the fault.

7 Back-Analyses of Settlements from Seismic Compression

7.1 INTRODUCTION

In this chapter, we perform back-analyses of seismic compression-induced settlements at Sites A and B from the 1994 Northridge earthquake. The general objectives of this work are to identify whether seismic compression analyses can explain the observed ground displacements and to characterize the variability of calculated settlements associated with parametric variability.

Our analysis procedure de-couples the ground response calculation (used to evaluate the spatial distribution of shear strain amplitude) from the analysis of volumetric strain. The ground response calculations are performed using 1-D and 2-D representations of the site geometry and equivalent-linear modeling of dynamic soil behavior [programs SHAKE91, Idriss and Sun (1991) and QUAD4M, Hudson et al. (1994), respectively]. Shear strain amplitudes resulting from these calculations are used with material-specific relationships developed from laboratory tests (described in Chapter 5) to estimate volumetric strains. The volumetric strains are then integrated across the fill height to estimate the settlement due to seismic compression.

In addition to seismic compression, ground movements from permanent shear deformations in soil were also considered. However, using strength parameters estimated from penetration resistance data, yield coefficients were found to exceed the maximum horizontal equivalent acceleration within slide mass geometries that could have realistically influenced the observed ground displacements. Accordingly, permanent shear deformations in the compacted fill slopes were unlikely to have influenced the observed settlements, and are not discussed further.

Most of the parameters used in the seismic compression/settlement analyses have natural scatter or are not known precisely due to potential measurement/estimation errors. We attempt to quantify the variability of these parameters, and incorporate this variability into our calculations of settlement. This is performed with a logic tree approach in which parameter spaces are discretized and weighted, and all possible combinations of parameters are compiled to evaluate the variability of calculated shear strains, volumetric strains, and settlement. These calculated response quantities are represented by statistical distributions that are referred to as "weighted frequency functions." The calculated settlements from the weighted frequency functions are then compared to estimated settlements from the field surveys described in Section 3.4.

7.2 METHODOLOGY

7.2.1 Variability and Uncertainty in Seismic Compression Analysis

Estimates of seismic compression-induced settlements are dependent on the form of the analytical model (including simplifying assumptions associated with the model) and uncertainty in the values of parameters used within the model. We refer to the range of estimated settlements as "variability," which is affected by "epistemic uncertainty" and "aleatory uncertainty." The total variability associated with estimating seismic compression is portioned into "modeling variability" and "parametric variability," each having components of epistemic and aleatory uncertainty. Table 7.1 outlines the four components of total variability in the context of seismic compression analysis.

Table 7.1. Contributions to total variability in seismic compression settlement estimates (after Roblee et al. 1996)

	Modeling Variability	**Parametric Variability**
Epistemic Uncertainty	<u>Modeling Epistemic Uncertainty:</u> Variability resulting from model assumptions, simplifications and /or fixed parameter values. *Can be reduced by adjusting or "calibrating" model to better fit observed settlement, or by using more sophisticated model.*	<u>Parametric Epistemic Uncertainty:</u> Variability resulting from incomplete data for parameter characterization. *Can be reduced by the collection of additional information, which better constrains parameters.*
Aleatory Uncertainty	<u>Modeling Aleatory Uncertainty:</u> Variability resulting from discrepancies between model and actual complex physical processes. *Cannot be reduced for a given model form.*	<u>Parametric Aleatory Uncertainty:</u> Variability in predicted settlement resulting from natural dispersion of model parameters. *Cannot be reduced by collection of additional information.*

Modeling variability can be thought of as the difference between the observed settlement and the settlement calculated from a model if the model parameters are known precisely. The calculation of shear strains in soil using a linear and a nonlinear soil model can be used to illustrate the relationship between modeling epistemic and aleatory uncertainty. If a linear model were used, the nonlinear response of the actual soil deposit would contribute to the modeling variability due to the difference between the actual response and the model's estimated response. This type of model will have large aleatory uncertainty because the model prediction is based on the soil behaving linear-elastically when in fact the soil behaves nonlinearly. Examination of the scatter as a function of a parameter might indicate that a systematic trend, or bias, exists within the scatter. This bias can be viewed as the epistemic uncertainty, and can be accounted for by correcting the linear-soil model to eliminate any trends, thus leaving a reduced level of aleatory uncertainty in the model prediction. An alternative way to remove the parameter-dependent bias would be to adopt a new model that accounts for the nonlinear response. This would lead to a reduction in the epistemic uncertainty, but would also introduce additional parametric variability by the addition of new model parameters to simulate the nonlinear response. Using a model that accounts for the nonlinear site response should improve the accuracy of the prediction, but may not reduce the total variability.

Parametric variability can be thought of as the sensitivity of model predictions to a viable range of values for model input parameters. With this in mind, the parametric epistemic uncertainty could be reduced by using site-specific models instead of generic models, or by using generic models that are well defined and are functions of a number of parameters. The parametric aleatory uncertainty is associated with the portion of the response variability that results from measurement errors, natural spatial variations in the soil profile, or the natural spatial variability of earthquake ground motions.

7.2.2 Models Used for Seismic Compression Analysis: Seismic Demand

As noted previously, our procedure for analysis of seismic compression involves first evaluating peak shear strains (γ_{pk}) in fill, and then calculating volumetric strains (ε_v) from effective shear strain $\gamma_{eff} = 0.65\gamma_{pk}$ and the equivalent number of uniform strain cycles (N). Models for the evaluation of ε_v are discussed in the following section. Here we focus on models used to evaluate seismic demand, as represented by shear strain amplitude γ_{pk} and number of cycles (N).

We utilize two approaches to evaluate γ_{pk}. The first approach consists of 2-D ground response analysis using the program QUAD4M (Hudson et. al, 1994), which employs a time domain solution of the equations of motion and equivalent linear dynamic soil modeling. Peak shear strains are calculated for each fill element. The second approach is similar to the first, except that the peak shear strains (γ_{pk}) are evaluated from 1-D equivalent linear ground response analysis with the program SHAKE91 (Idriss and Sun, 1991). As noted previously, the peak shear strains calculated by either the 1-D or 2-D analysis approach are converted to γ_{eff} by taking 65% of the peak values for the purpose of calculating volumetric strains.

Figures 7.1 and 7.2 show the finite element meshes that are used to represent the analyzed cross sections for Sites A and B in the 2-D analyses. The locations of soil columns used in the 1-D analysis are also shown in Figures 7.1 and 7.2, and have the same element layering as the finite element mesh. The number of elements and nodes in the respective 2-D meshes are as follows:

	Section A-A'	**Section B-B'**
Site A	5408 nodes, 5238 elements	4041 notes, 3895 elements
Site B	1734 nodes, 1636 elements	3156 notes, 3035 elements

The mesh element heights were selected to be smaller than one tenth of the wavelengths associated with 10 Hz vertically propagating waves, which should maintain good computational accuracy at these wavelengths. In order to minimize boundary effects, the 2-D meshes were extended laterally a distance of approximately eight times the height of the soil column beyond the crest and base of the slope.

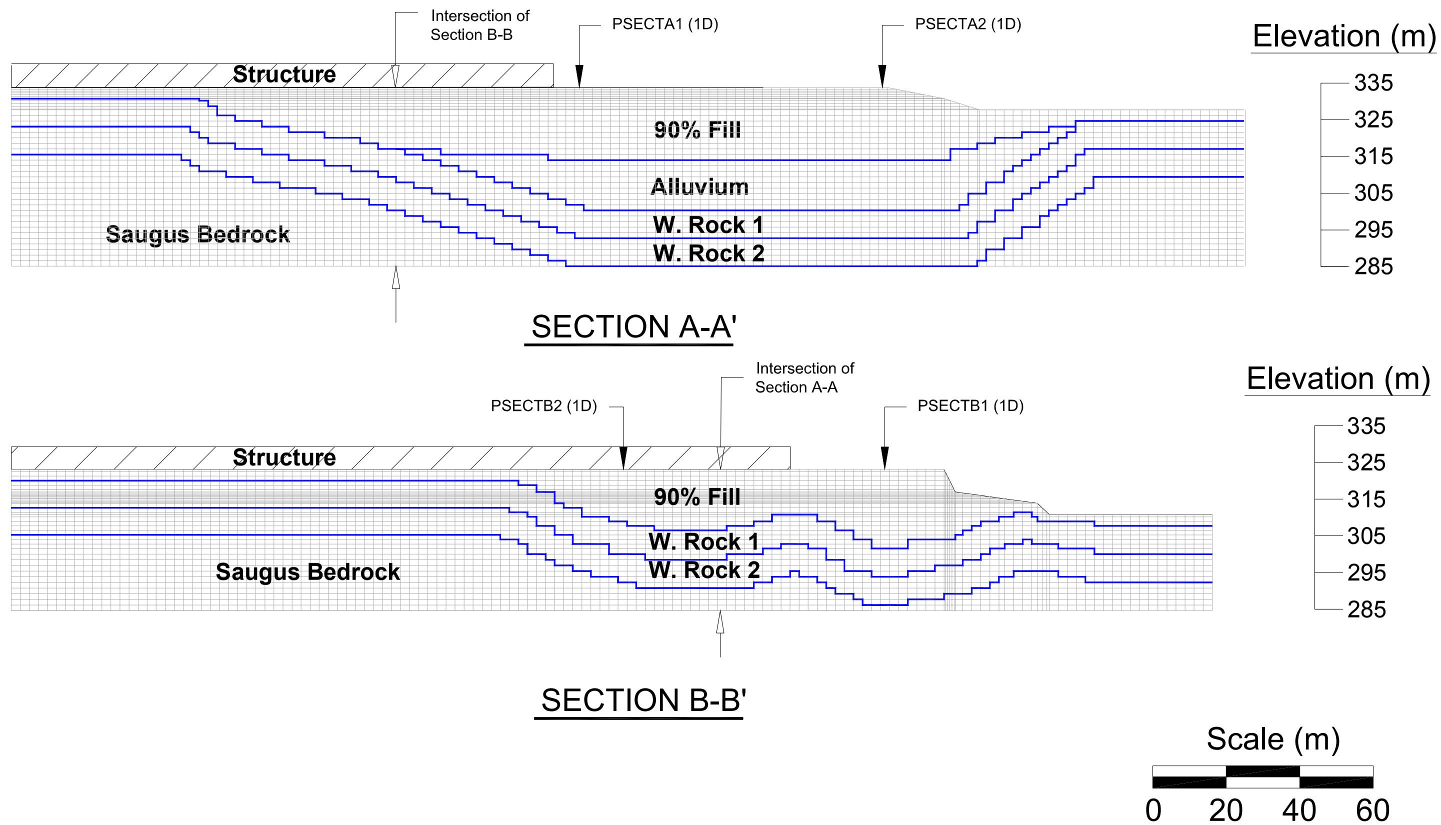

Fig. 7.1. Finite element meshes used for analysis of Site A

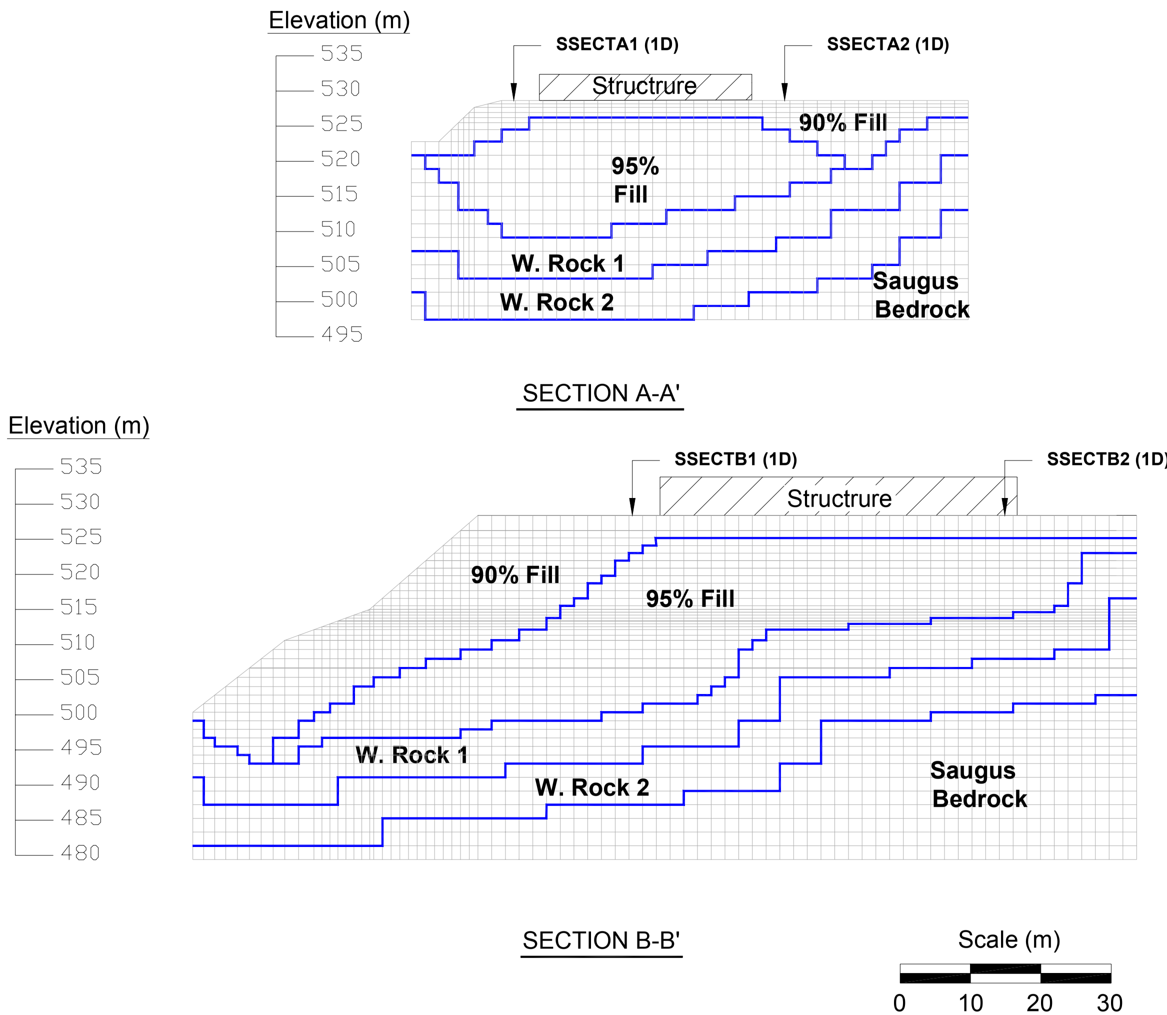

Fig. 7.2. Finite element meshes used for analysis of Site B

7.2.3 Models Used for Seismic Compression Analysis: Volumetric Strain

Models for the evaluation of ε_v are site specific and consist of the following:

- Volumetric strain at 15 cycles of loading [$(\varepsilon_v)_{N=15}$] versus cyclic shear strain (γ_c) relations, developed from the data presented in Chapter 5.
- The variation of normalized volumetric strain [$C_N=\varepsilon_v/(\varepsilon_v)_{N=15}$] with number of cycles (N), developed from the data presented in Chapter 5.
- Protocols used to evaluate the equivalent number of uniform strain cycles (N) from a given accelerogram. These protocols are based on the relationship between normalized shear strain ($\gamma_c/\gamma_{c,N=1}$) and N, which was developed in Section 6.3.2.

The seismic demand parameter γ_{eff} is assumed equal to γ_c, which allows the demand to be linked to the volumetric strain models. Analysis of ground settlement begins with the evaluation of $(\varepsilon_v)_{N=15}$ at representative locations throughout the fill. The relationship between $(\varepsilon_v)_{N=15}$ and $\gamma_{eff}=\gamma_c$ depends on the compaction condition of the fill, as represented by relative compaction RC (using the Modified Proctor energy standard) and formation degree of saturation, S. A correction for multi-directional shaking effects is then made by multiplying $(\varepsilon_v)_{N=15}$ by two per the recommendations of Pyke et al., 1975 [i.e., the actual 15-cycle volumetric strain is taken as $2\times(\varepsilon_v)_{N=15}$]. This volumetric strain is then adjusted by factor C_N, which accounts for $N\neq 15$. Thus, the volumetric strain at a point is taken as $C_N\times 2\times(\varepsilon_v)_{N=15}$. These corrected volumetric strains are then integrated over the fill column height to estimate settlement from seismic compression.

Our use of material-specific models for seismic compression analysis is intended to optimize accuracy and minimize parametric epistemic uncertainty. However, significant parametric aleatory uncertainty exists in these models as a result of the underlying aleatory uncertainty in RC and S as well as the general limitations of volumetric strain estimation from laboratory testing.

(a) Form of Volumetric Strain Models

Statistical models were developed to describe the relationship between shear strain and volumetric strain for fill soils at Sites A and B, based on the results of cyclic simple shear testing presented in Chapter 5. Model parameters are related to basic soil characteristics such as the formation Modified Proctor relative compaction and the degree of saturation, as well as soil index properties (percent fines, plasticity, etc). It is important to note that these models were developed strictly for the soils tested in this research and may not be applicable for other soils.

As illustrated in Figure 7.3, the functional form of the statistical model consists of two adjoining parabolas, and is herein termed the double parabola model. The first parabola applies for $\gamma_{tv} \leq \gamma \leq 0.1\%$, and is described by the following equation:

$$\varepsilon_v(\%) = a_1\gamma^2 + b_1\lambda + c_1 \tag{7.1}$$

where γ is in percent, and γ_{tv} is the volumetric threshold shear strain (i.e., the shear strain below which volumetric strains are negligible). The second parabola applies to $\gamma \geq 0.1\%$ and is described by:

$$\varepsilon_v(\%) = a_2\gamma^2 + b_2\lambda + c_2 \tag{7.2}$$

where, γ is again in percent. The parabolas are constrained such that their ordinates and slopes match at $\gamma = 0.1\%$.

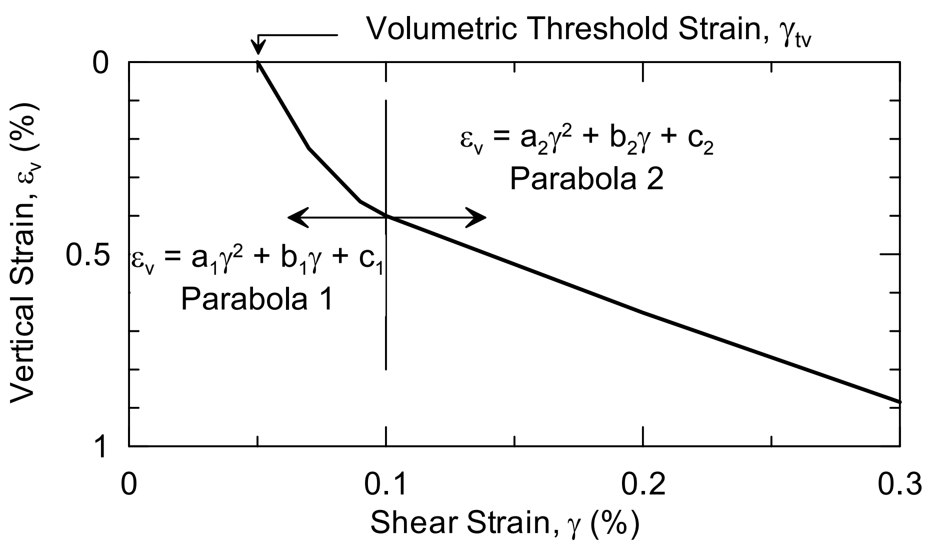

Fig. 7.3. Double parabola model

The shape of the shear strain-volumetric strain relationship for $\gamma_{tv} < \gamma < 0.1\%$ is not known for soils containing significant fines (only limited laboratory tests on fill soils were performed using $\gamma < 0.1\%$). The parabolic shape was used to accommodate three constraints for this curve: (1) $\varepsilon_v = 0$ at $\gamma = \gamma_{tv}$, (2) specified ε_v at $\gamma = 0.1\%$, (3) specified slope at $\gamma = 0.1\%$.

For a given soil, the parabolas were defined by the following constraints and model parameters:

1. A value for volumetric threshold strain, γ_{tv}, is assumed. We take γ_{tv} = 0.01% based on a review of published data (e.g., Vucetic 1994), and the small strain testing discussed in Section 5.3.5, which suggested γ_{tv} < 0.03%.
2. Vertical strain compatibility between the two parabolas was enforced at γ = 0.1%.
3. Slope compatibility between the two parabolas was enforced at γ = 0.1%.
4. The vertical strains at γ_c = 0.1% and 1.0%, [ε_v (0.1%) and ε_v (1.0%)].
5. The slope in linear-linear space of the γ_c-$(\varepsilon_v)_{N=15}$ relationship, denoted *e*.

The model parameters *e*, ε_v *(0.1%)* and ε_v *(1.0%)* are soil specific and are functions of *RC* and *S*. Remaining parameters to be determined analytically are a_1, b_1, c_1, a_2, b_2, c_2, *f* and ε_v *(0.4%)*. Parameter *f* is the intercept of the best-fit line through the γ_c-$(\varepsilon_v)_{N=15}$ data at large shear strains (γ ≥ 0.4%), while parameter ε_v (0.4%) is the vertical strain at γ = 0.4%. All the parameters to be determined have general solutions for a given γ_{tv}, and can be described for γ_{tv} = 0.01% as follows:

$$a_1 = 4\, a_2 + 20\, b_2 - 400\, \varepsilon_v\, (0.1\%) \tag{7.3}$$

$$b_1 = -0.6\, a_2 - 3\, b_2 + 80\, \varepsilon_v\, (0.1\%) \tag{7.4}$$

$$c_1 = 0.02\, a_2 + 0.1\, b_2 - 3\, \varepsilon_v\, (0.1\%) \tag{7.5}$$

$$a_2 = 1.851851851\, \varepsilon_v\, (1.0\%) + 3.703703704\, \varepsilon_v\, (0.1\%) - 5.555556\, \varepsilon_v\, (0.4\%) \tag{7.6}$$

$$b_2 = -0.9259259259\, \varepsilon_v\, (1.0\%) - 5.185185185\, \varepsilon_v\, (0.1\%) + 6.111111\, \varepsilon_v\, (0.4\%) \tag{7.7}$$

$$c_2 = 0.07407407407\, \varepsilon_v\, (1.0\%) + 1.481481481\, \varepsilon_v\, (0.1\%) - 0.555556\, \varepsilon_v\, (0.4\%) \tag{7.8}$$

$$f = \varepsilon_v\, (1.0\%) - e \tag{7.9}$$

$$\varepsilon_v\, (0.4\%) = 0.4\, e + f \tag{7.10}$$

Similar relationships can be derived for other values of γ_{tv}.

(b) Site A

Regression analyses for model parameters ε_v *(1%)* and *e* were performed on test results from Soil A-1. Figure 7.4 shows the regression of the parameter *e* against *RC*, the results of which can be expressed numerically as:

$$e = -0.1228\ RC\ (\%) + 11.812 \tag{7.11}$$

Figure 7.5 shows ε_v (1%) plotted against saturation for various relative compaction levels. The slope of the line for ε_v (1%) versus saturation was fixed at –0.02, independent of the relative compaction level, while the coefficient c_1 varied with *RC* as follows:

$$\varepsilon_v\ (1\%) = -0.02\ S\ (\%) + c_1 \tag{7.12}$$

$$c_1 = -0.175\ RC\ (\%) + 18.233 \tag{7.13}$$

The data in Figure 7.6 relate ε_v (0.1%) to ε_v (1.0%). From these data, ε_v (0.1%) is seen to be about 20% of ε_v (1.0%). This relationship is independent of *RC* and *S*.

Using these parameters, the double parabola model can accurately reproduce the shear strain-volumetric strain relationships for Soil A-1 for $45\% < S < 90\%$ and $84\% \leq RC \leq 92\%$. Figure 7.7 shows the computed values for $S = 74\%$ along with actual laboratory test results. This model is nearly a perfect match at $S = 74\%$. Similar results were found at other degrees-of-saturation.

(c) Soil B-3

Since the seismic compression susceptibility of Soil B-3 did not vary significantly with saturation level, the model parameters *e* and ε_v *(1%)* were regressed only against *RC*. Figure 7.8 shows the regression of *e* (slope parameter) vs. *RC*, which can be described numerically as:

$$e = 0.046726\ RC(\%)^2 - 8.770536\ RC(\%) + 412.284524 \tag{7.14}$$

Figure 7.9 shows the regression of ε_v *(1%)* vs. *RC*, which was found to be:

$$\varepsilon_v\ (1\%) = 0.029643\ RC\ (\%)^2 - 5.578786\ RC\ (\%) + 263.2857 \tag{7.15}$$

As shown in Figure 7.10, ε_v *(0.1%)* was found to be approximately 0.18% independent of *RC*.

The double parabola model for Soil B-3 is calibrated for *RC*=90-95%, and is independent of *S*. Figure 7.11 shows the shear strain-volumetric strain curves computed using the model parameters from Eqs. 7.14-7.15. Also plotted in this figure are the laboratory test results for Soil B-3. The double parabola model appears to capture the laboratory data reasonably well.

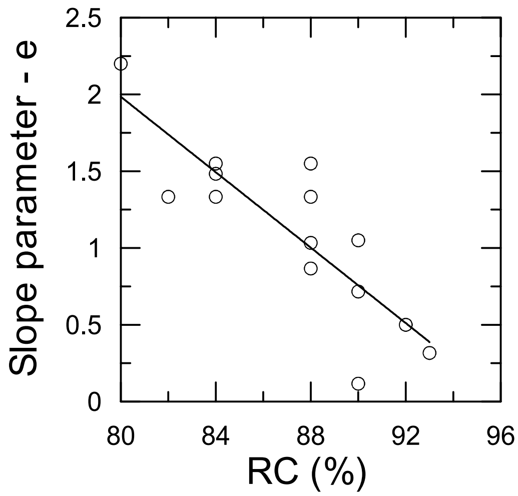

Fig. 7.4. Relationship between *e* and *RC* for Soil A-1

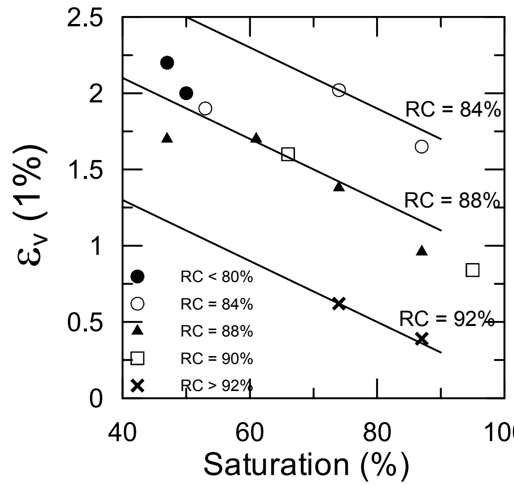

Fig. 7.5. Relationship between ε_v (1%) and degree of saturation for Soil A-1

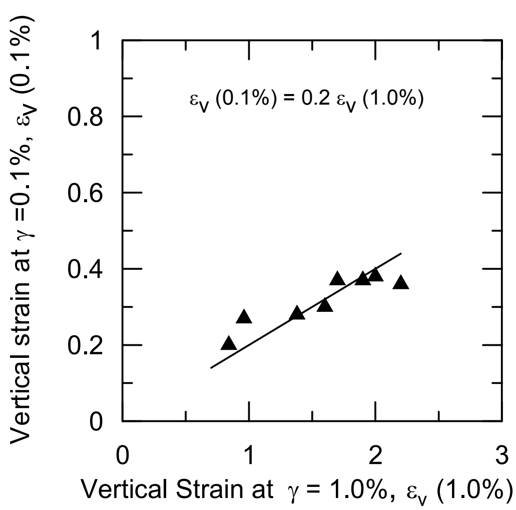

Fig. 7.6. Relationship between ε_v (0.1%) and ε_v (1.0%) for Soil A-1

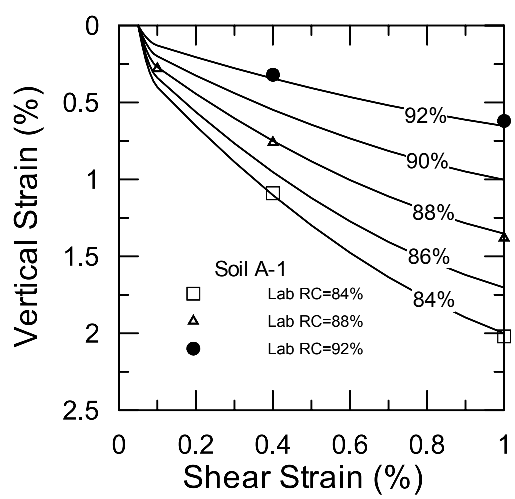

Fig. 7.7. Double parabola model for Soil A-1 at *S*=74%

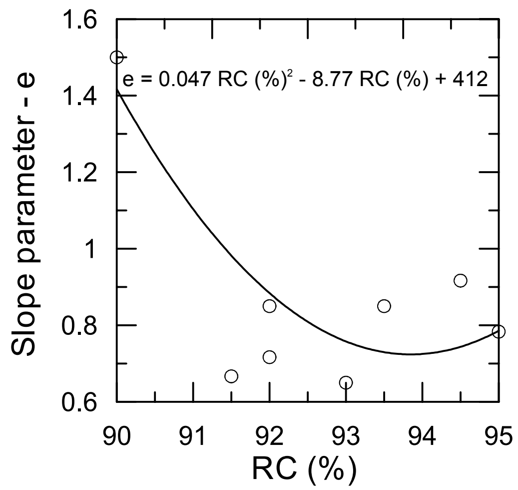

Fig. 7.8. Relationship between *e* and *RC* for Soil B-3

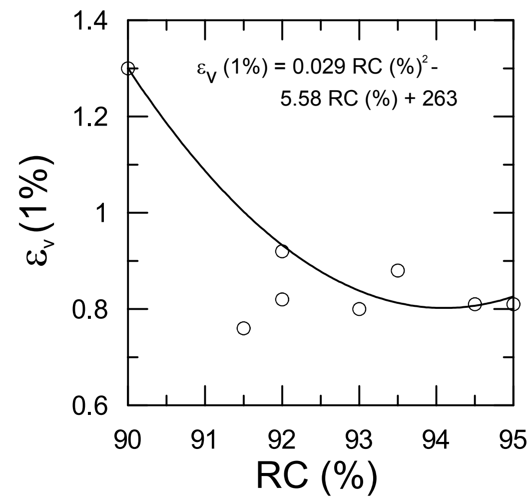

Fig. 7.9. Relationship between ε_v (1.0%) and *RC* for Soil B-3

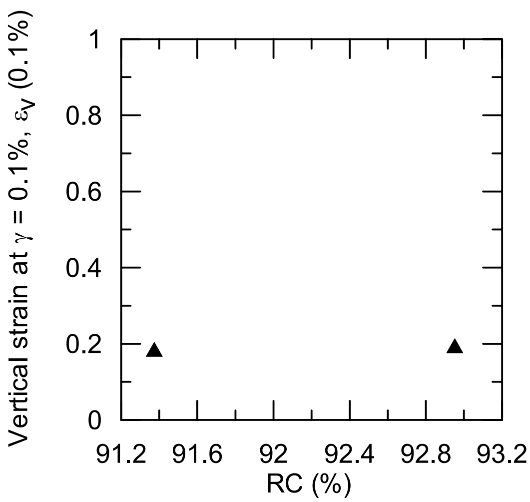

Fig. 7.10. Relationship between ε_v (0.1%) and *RC* for Soil B-3

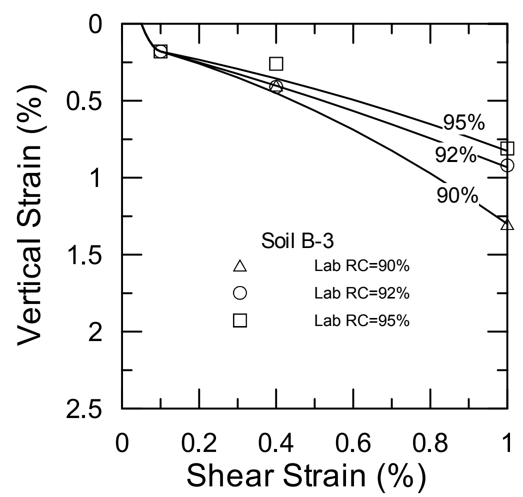

Fig. 7.11. Double parabola model for Soil B-3

(d) Normalized Volumetric Strain Models

The mean normalized volumetric strain models discussed in Section 5.3.7 are used to obtain correction factors C_N for $N \neq 15$. Figure 7.12 shows the C_N models used for Sites A and B. Neglected in these models for C_N are variations with RC, which have a negligible effect on the calculated settlements.

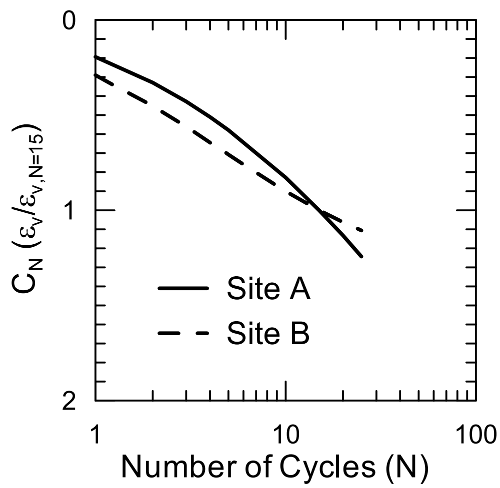

Fig. 7.12. Models for normalized volumetric strain vs. *N* for Sites A and B soils

7.2.4 Model Parameters

Parameters/quantities required to implement the seismic demand and volumetric strain models described in the previous sections include modulus reduction (G/G_{max}) and damping curves (β), profiles of shear wave velocity (V_s), ground motion time histories, and compaction condition of fill soils (RC and S). Uncertainties associated with the estimation of these parameters are propagated through the overall analysis procedure using a logic tree approach, which is illustrated in Figure 7.13. The logic tree approach allows the use of alternative realizations of model parameters, each of which is assigned a weight, which is interpreted as the relative likelihood of that realization being correct. The weighting factors for all possible realizations of a parameter sum to unity. Each calculated response quantity corresponds to a unique combination of parameter realizations (i.e., a path through the logic tree), and the weight belonging to that response quantity is the product of all the weights in the path. The sum of weights for all response quantity realizations is unity.

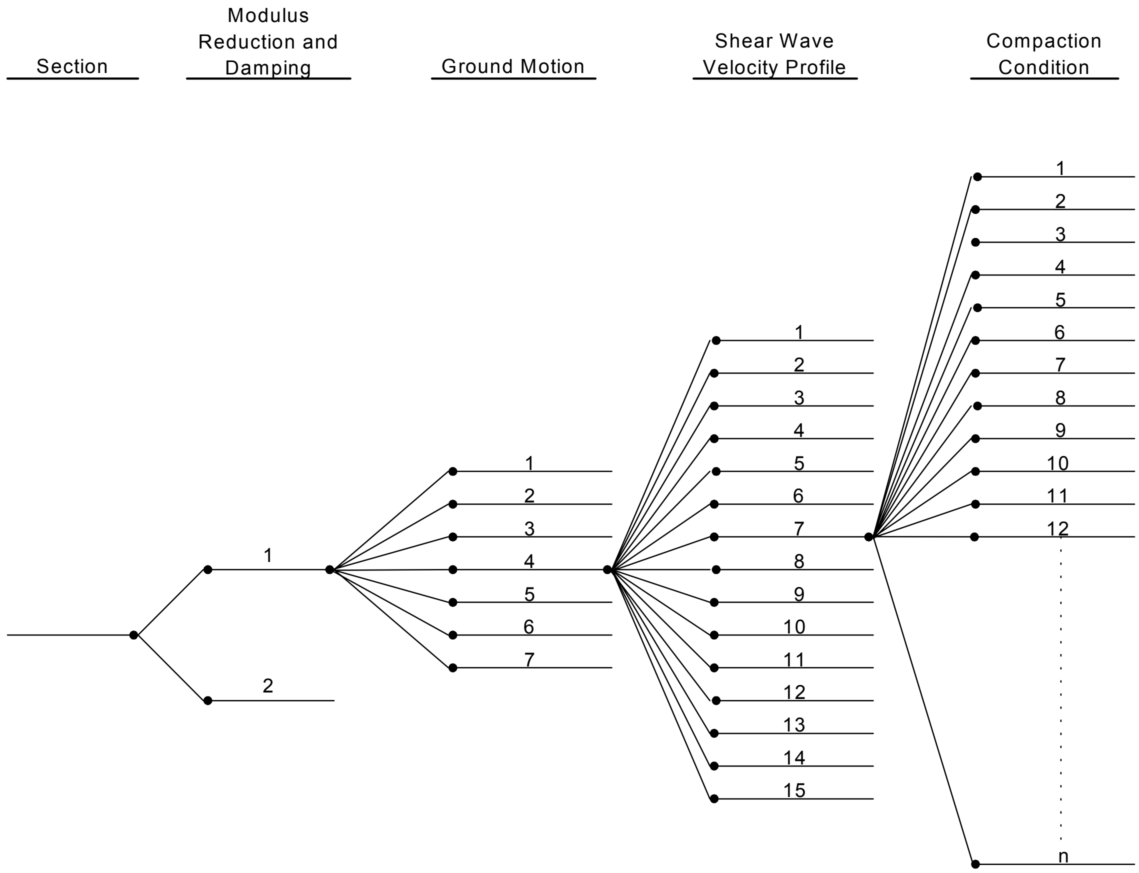

Fig. 7.13. Logic tree used for seismic compression analysis

The following equation is used to determine the weight (w_i) of a given parameter based on its relative likelihood of occurring (L_i) and the sum of all of the relative likelihoods in a parameter set.

$$w_i = \frac{L_i}{\sum_{i=1}^{n} L_i} \tag{7.16}$$

7.3 ESTIMATION OF PARAMETER VALUES AND WEIGHTS

7.3.1 Modulus Reduction and Damping Curves

No testing was performed on the fill soils from Sites A and B to determine material-specific curves for the variation with shear strain of shear modulus reduction and damping. These curves are required input for equivalent-linear ground response calculations. Two published sets of curves were selected based upon the fill soils' index properties. The two curves are intended to bound the parameter space where the site-specific curves are expected to lie. One of these curve sets is the upper-bound modulus reduction curve and lower-bound damping curve for sand published by Seed and Idriss, 1970 (referred to as the "sand" curve). The other curve set is the PI = 15 clay curve published by Vucetic and Dobry, 1991 (referred to as the "clay" curve). Both curves sets are plotted in Figure 7.14. Note that the two curve sets are similar to each other. Equal weights ($w_i=0.5$) are assigned to each curve set for the analysis.

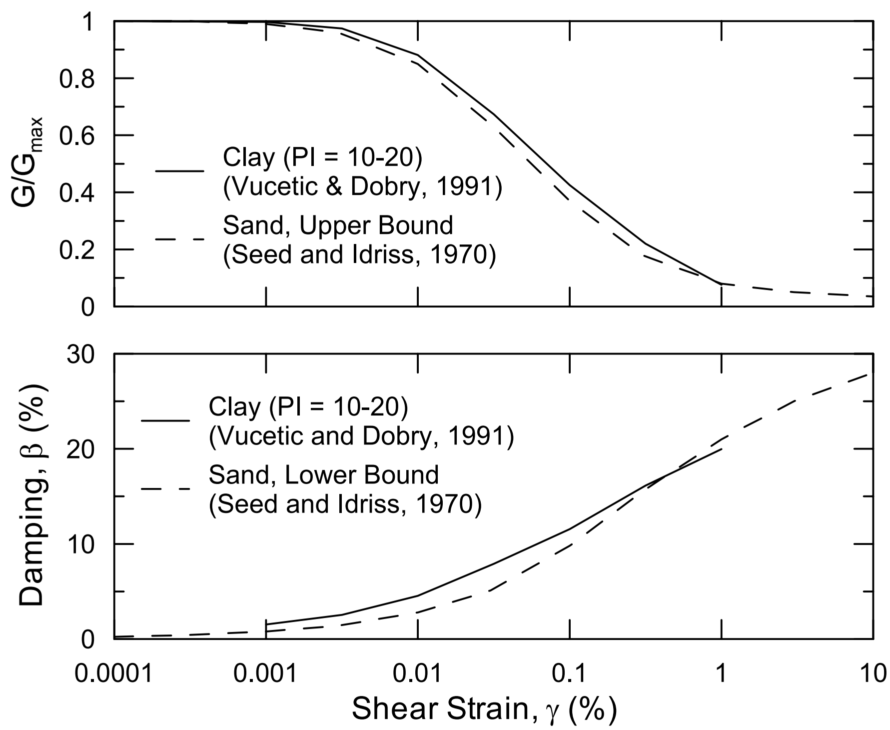

Fig. 7.14. Modulus reduction and damping curves used for Sites A and B fill soils

Underlying most of the fill materials at both Sites A and B are weathered rock and rock belonging to the Saugus Formation. Modulus reduction and damping for the weathered Saugus bedrock were modeled with the Seed and Idriss (1970) sand curves. Relatively intact bedrock materials at depth are modeled with the rock curves published by Schnabel (1973). The other material that enters the analysis is sandy clay alluvium underlying a portion of the Site A fill. This material was modeled with the Seed and Idriss (1970) sand curves.

7.3.2 Ground Motions

In Chapter 6, we selected suites of ground motion time histories for each site. Each selected ground motion time history is intended to represent a possible realization of the shaking at the site during the Northridge earthquake for a soft rock site condition. As discussed in Section 6.2, recorded time histories had to be scaled for use at the sites because of nonequal site-source distances. If we denote the amount of scaling as *SF*, we can say that the quality of an empirical recording for a site decreases as *SF* departs increasingly from unity (because the site-source distances become increasingly disparate and all selected recordings have site-source azimuths similar to those for the fill sites). This concept is used to construct relative likelihoods for individual ground motions (L_{gm}) with respect to a fill site as follows:

$$L_{gm\,i}(SF_i) = \begin{pmatrix} = SF_i \;\; if \;\; SF_i \leq 1 \\ = 1/SF_i \;\; if \;\; SF_i > 1 \end{pmatrix} \tag{7.17}$$

The L_{gm} for synthetic time histories are arbitrarily taken to be one half of the value from the least likely of the recorded time histories. Weight factors for individual ground motions are directly proportional to the relative likelihood values; the weights are simply normalized so that they sum to unity. The results for Sites A and B are shown in Table 7.2.

Table 7.2. Ground motion weights for Sites A and B

Record	Site A	Site B
CDD(fn)	0.106	0.060
CDD(fp)	0.106	0.060
LPD(fn)	0.095	0.054
LPD(fp)	0.095	0.054
NFS(fn)	0.100	0.132
NFS(fp)	0.100	0.132
GEN(fn)	0.074	0.099
GEN(fp)	0.074	0.099
PC(fn)	0.100	0.132
PC(fp)	0.100	0.132
PE&A-A	0.048	-
PE&A-B	-	0.048

7.3.3 Shear Wave Velocity Profiles

Shear wave velocities were measured in situ at Sites A and B. The measurement procedures and results were presented in Chapter 3 (Figures 3.12 and 3.22). In Figures 7.15 and 7.16, these data are shown along with our best-estimate velocity profiles, which are indicated with solid lines denoted as “median, λ” in the legend. The dashed velocity profiles denoted in the legend as “$\lambda \pm 2\sigma_{lnV}$” or “$\lambda \pm 1\sigma_{lnV}$” span the expected range of variability as a function of depth, and correspond to the stated number of standard deviations above and below the median based on a lognormal distribution. Variations of $\pm 1\sigma_{lnV}$ were used in rock, as compared to $\pm 2\sigma_{lnV}$ in soil, because larger variability in rock velocities is generally inconsistent with the observed variability of field measurements. The standard deviation values used to establish these limits were taken from an empirical model by Toro et al. (1997).

The Toro et al. model is based on 176 velocity profiles from the Savannah River site, and is a statistical model for randomized velocity profiles that consists of three parts, (1) a submodel describing the random stratigraphy at a site; (2) a median velocity profile; and (3) a submodel that describes the deviations of the velocity in each layer from the median and its correlation with the velocity in the layer above. We neglect the random stratigraphy feature of the model (since the stratigraphy for Sites A and B are well known), take as the median the median profiles shown in Figures 7.15–7.16, and use the Toro et al. model to describe the expected variation of velocity dispersion with depth.

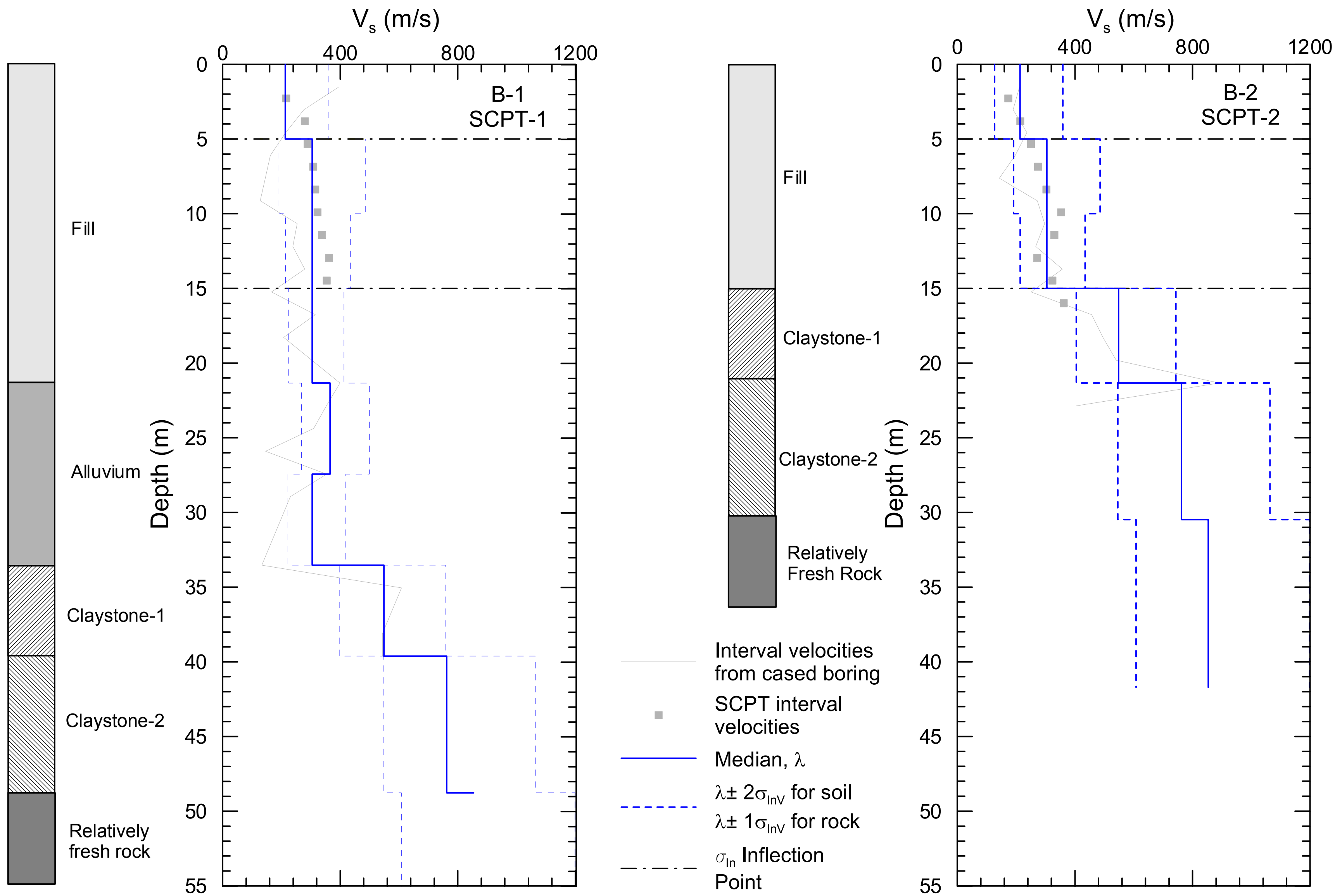

Fig. 7.15. Idealized median, lower-bound, and upper-bound shear wave velocity profile for Site A

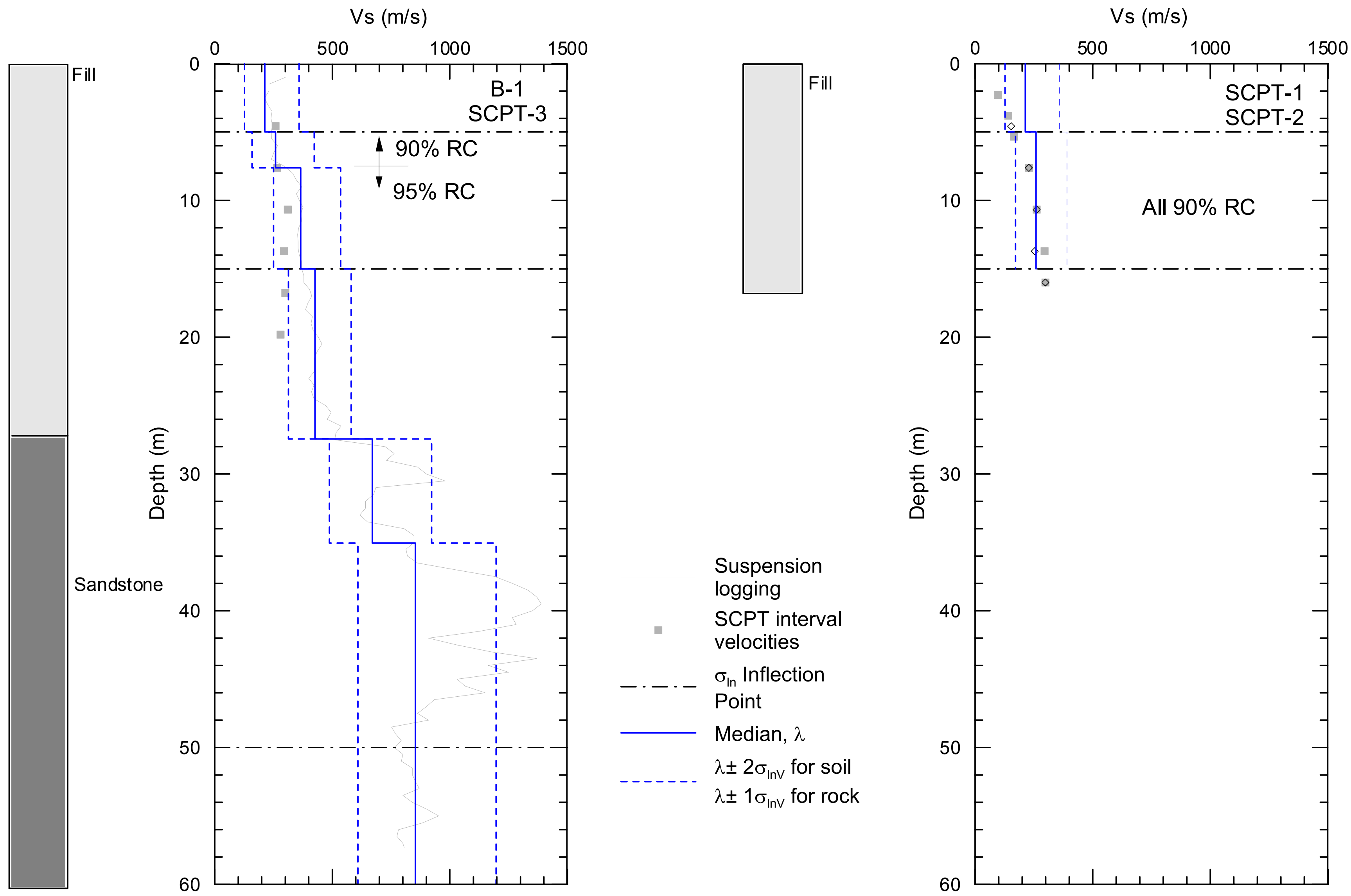

Fig. 7.16. Idealized median, lower-bound, and upper-bound shear wave velocity profile for Site B

Toro et al. found shear wave velocities within a given layer, for a given depth range, to be lognormally distributed with a standard deviation that is a function of depth [σ_{lnV} *(z)*]. The normalized residual of a particular shear wave data point is denoted as

$$Z_i = \frac{\ln(V_i) - \ln[Vmedian(h_i)]}{\sigma_{\ln V}} \tag{7.18}$$

The correlation among subsequent layers is given by a first-order auto-regression model conditioned on the distribution of *Z* in a layer *i*, which in turn is conditioned on *Z* in layers 1, 2 … *i*-1. The mean and standard deviation of Z_i is expressed as

$$mean(Z_i \mid Z_1, Z_2, ...Z_{i-1}) = mean(Z_i \mid Z_{i-1}) = \rho\, Z_{i-1} \tag{7.19}$$

$$\sigma(Z_i \mid Z_1, Z_2, ...Z_{i-1}) = \sigma(Z_i \mid Z_{i-1}) = \sqrt{(1-\rho^2)} \tag{7.20}$$

where ρ is the serial auto-correlation coefficient of *Z*, and is a represented as a function of depth defined by

$$\rho(h) = \begin{cases} \rho_{200}\left[\dfrac{h+h_0}{200+h_0}\right]^b & for\ h \le 200\ m \\ \rho_{200} & for\ h > 200\ m \end{cases} \tag{7.21}$$

The parameters σ_{lnV}, ρ_{200}, h_0, and *b* were determined from the method of maximum-likelihood, and are classified as either generic (broad geographic region) or site specific. Figure 7.17 shows the variation with depth of σ_{lnV} and ρ for both site types. As noted previously, the resulting dispersion of velocity for Sites A and B is represented by the spread between dashed lines shown in Figures 7.15–7.16, which corresponds to ±1-2σ_{lnV} about the median.

Fifteen random shear wave velocity profiles in fill were generated for each of Sites A and B based on the above statistical velocity models. The velocity profile realizations are not randomly distributed across the parameter space, but rather tend to be clustered near the median in accordance with the lognormal distribution. Constraints were placed on the generation of these random shear wave velocity profiles by disallowing realizations of velocity beyond the ±2σ_{lnV} limits for soil and ±1σ_{lnV} for rock. These constraints were added to disallow physically unreasonable realizations of velocity profiles. Velocity profiles were formulated using the above procedures at the borehole locations, and were applied across the sites in accordance with the site stratigraphy (i.e., velocity within a layer was assumed to not vary with lateral position).

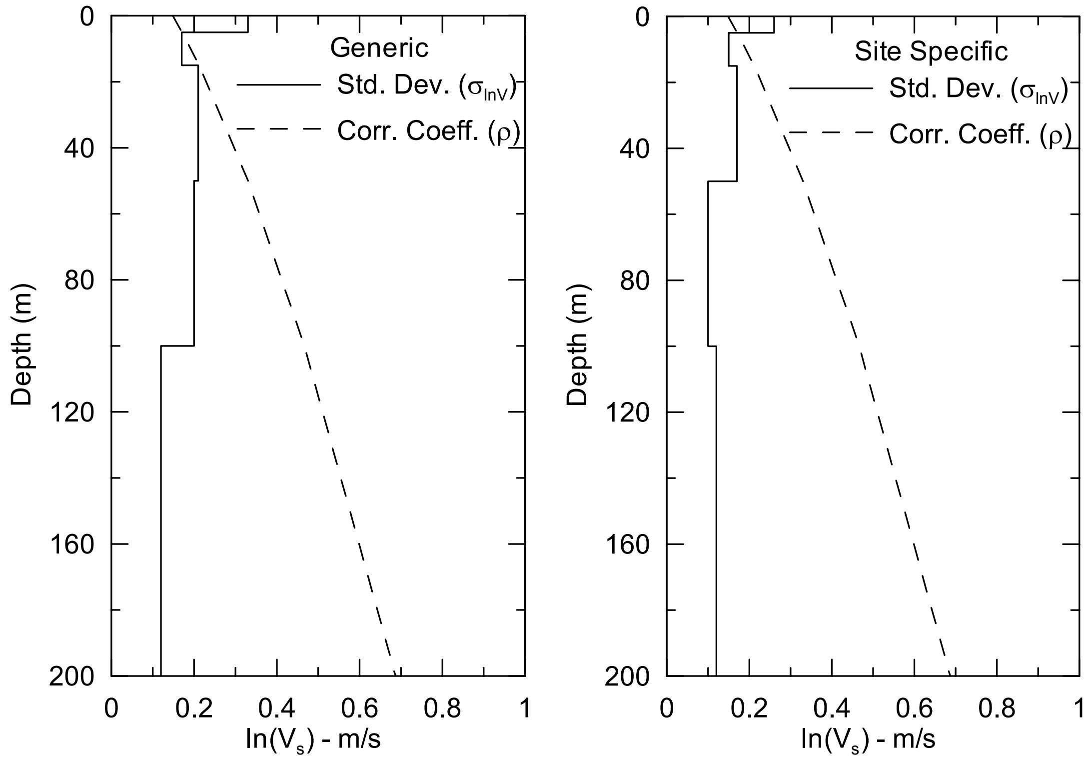

Fig. 7.17. Variation of standard deviation and correlation coefficient with depth for generic and site-specific site profiles (Toro et al. 1997)

Figure 7.18 shows the random shear wave velocity realizations along with the median and the upper/lower-bound limiting velocities. The likelihood value associated with each profile being the "actual" is constant, hence equal weight is assigned to each profile. Tables 7.3 and 7.4 show the layer shear wave velocity values and their respective weights.

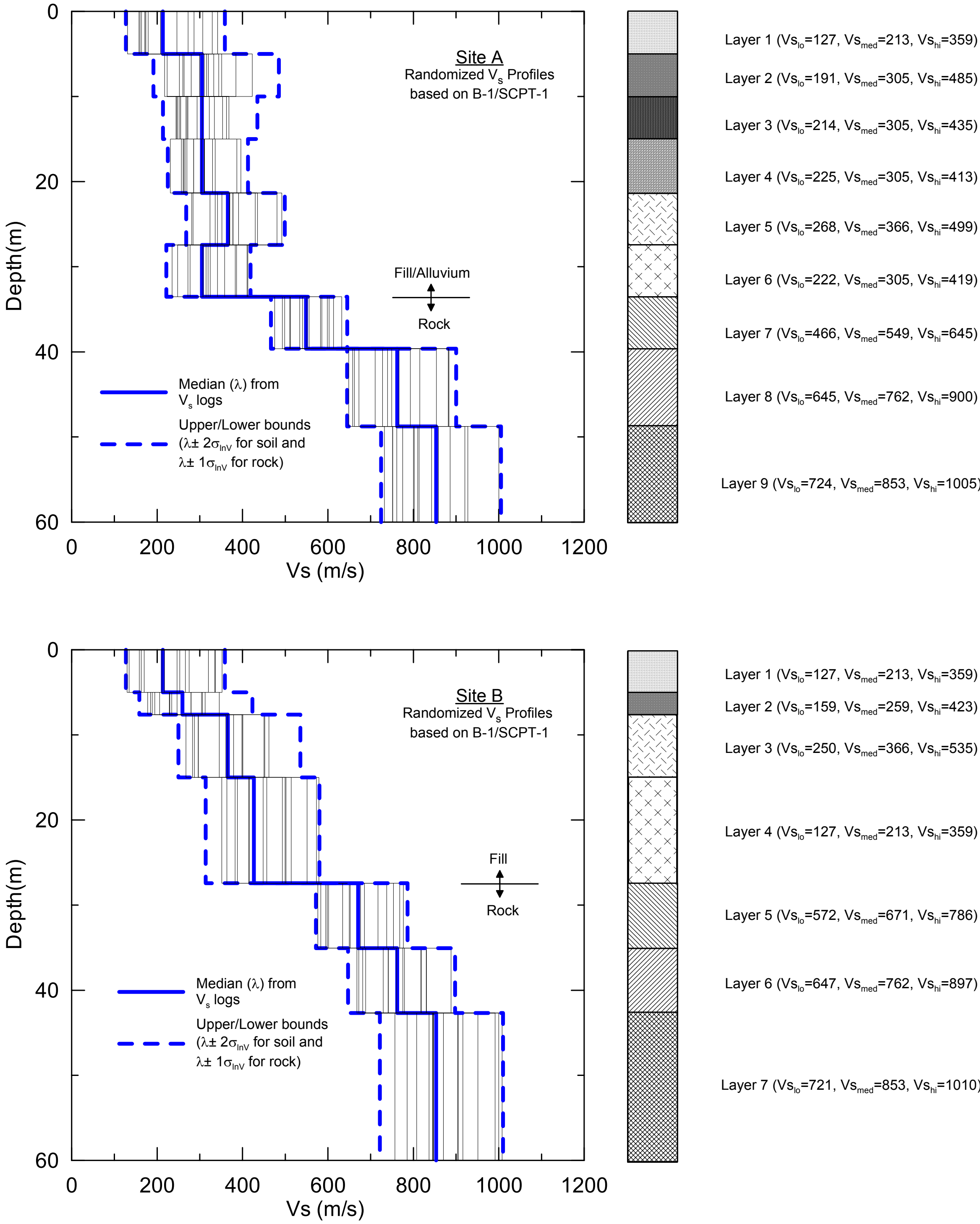

Fig. 7.18. Random shear wave velocity profiles for Sites A and B

Table 7.3. Random shear wave velocity profiles and associated weights for Site A

Simulation No.	Layer No. 1 -Fill (m/s)	2-Fill (m/s)	3-Fill (m/s)	4-Fill (m/s)	5-Qa (m/s)	6-Qa (m/s)	7-Rock (m/s)	8-Rock (m/s)	9-Rock (m/s)	Weight
1	329	299	270	257	435	341	541	657	810	0.067
2	286	223	322	285	369	386	511	883	1000	0.067
3	173	280	246	263	378	319	632	882	921	0.067
4	208	261	362	231	370	324	583	766	775	0.067
5	307	310	306	330	481	307	493	673	761	0.067
6	171	344	244	336	324	358	499	793	751	0.067
7	342	218	268	270	430	277	603	749	813	0.067
8	158	385	249	387	341	413	512	649	859	0.067
9	164	333	272	261	492	308	534	815	928	0.067
10	246	351	255	310	391	272	586	728	752	0.067
11	160	252	294	304	352	235	599	740	802	0.067
12	272	263	353	286	336	411	551	662	886	0.067
13	179	423	253	396	284	383	556	854	800	0.067
14	131	320	368	311	281	315	476	883	843	0.067
15	173	316	334	266	377	248	613	711	732	0.067

Table 7.4. Random shear wave velocity profiles and associated weights for Site B

Simulation No.	Layer No. 1-Fill (m/s)	2-Fill (m/s)	3-Fill (m/s)	4-Fill (m/s)	5-Rock (m/s)	6-Rock (m/s)	7-Rock (m/s)	Weight
1	335	178	450	363	768	730	846	0.067
2	217	313	462	448	583	776	757	0.067
3	336	188	365	457	738	830	847	0.067
4	275	229	401	573	598	688	1008	0.067
5	170	279	399	414	634	888	905	0.067
6	211	247	346	493	652	761	916	0.067
7	247	194	399	352	777	672	837	0.067
8	352	184	268	499	685	819	845	0.067
9	253	206	361	514	650	741	785	0.067
10	320	230	297	416	676	681	904	0.067
11	130	346	296	502	717	668	1000	0.067
12	134	304	379	579	753	831	808	0.067
13	163	306	288	551	576	779	951	0.067
14	266	234	452	383	601	741	870	0.067
15	158	279	283	388	595	817	992	0.067

7.3.4 Compaction Conditions

Compaction conditions for the fill soils at Sites A and B were weighted according to the likelihood contours developed in Chapter 3 (Figures 3.8, 3.19–3.20). Figure 7.19 shows contours depicting the likelihood of compaction conditions at Site A, along with a series of discrete Modified Proctor *RC* and *w* coordinates used to discretize the compaction space for likelihoods greater than 1%. Figures 7.20–7.21 present similar information for Site B in the 90% and 95% relative compaction zones, respectively. Also shown in Figures 7.19–7.21 are the boundaries of the parameter space for which the volumetric strain models developed in Section 7.2.3 are valid. Note that there are cases where the discretized compaction space extends beyond the boundaries of the volumetric strain models. This occurs in parameter *RC* at Site A and Site B (95% zone only), with some field *RC* values exceeding the upper-bound model *RC*. This occurs because it was not possible to achieve very high *RC* values in laboratory specimens using the Harvard compactor (Sections 5.3.3–5.3.4). For points with *RC* exceeding the model upper-bound, volumetric strains were calculated using the upper-bound model *RC*. In effect, this adds the relative likelihoods for points with *RC* beyond the upper-bound model *RC* to the relative likelihoods at the boundaries for the corresponding *w*. While this biases our settlement calculations, the effect is minor because of the small settlement contributions at these high *RC* values.

The logic tree for each site has a branch for each of the compaction coordinates in Figures 7.19–7.21. For the purpose of volumetric strain analyses, the effective compaction condition of the alluvium at Site A is fixed at 84% *RC*. This *RC* value is the minimum allowable with the volumetric strain model for Soil A-1, and is very near the estimated mean *RC* for the alluvial soils (83-84%, see Section 3.2.4). Recall that the volumetric strain model at these low *RC* values is not sensitive to *S*. For Site B the tree is expanded to account for all possible combinations of compaction coordinates for the two distinct compaction zones (i.e., the 90% *RC* and 95% *RC* zones). Since the volumetric strain model for Site B is not dependent on *S*, the likelihoods for a given *RC* and *w* are summed with respect to *w*. Tables 7.5 and 7.6 show the weights associated with the compaction conditions for Sites A and B, respectively.

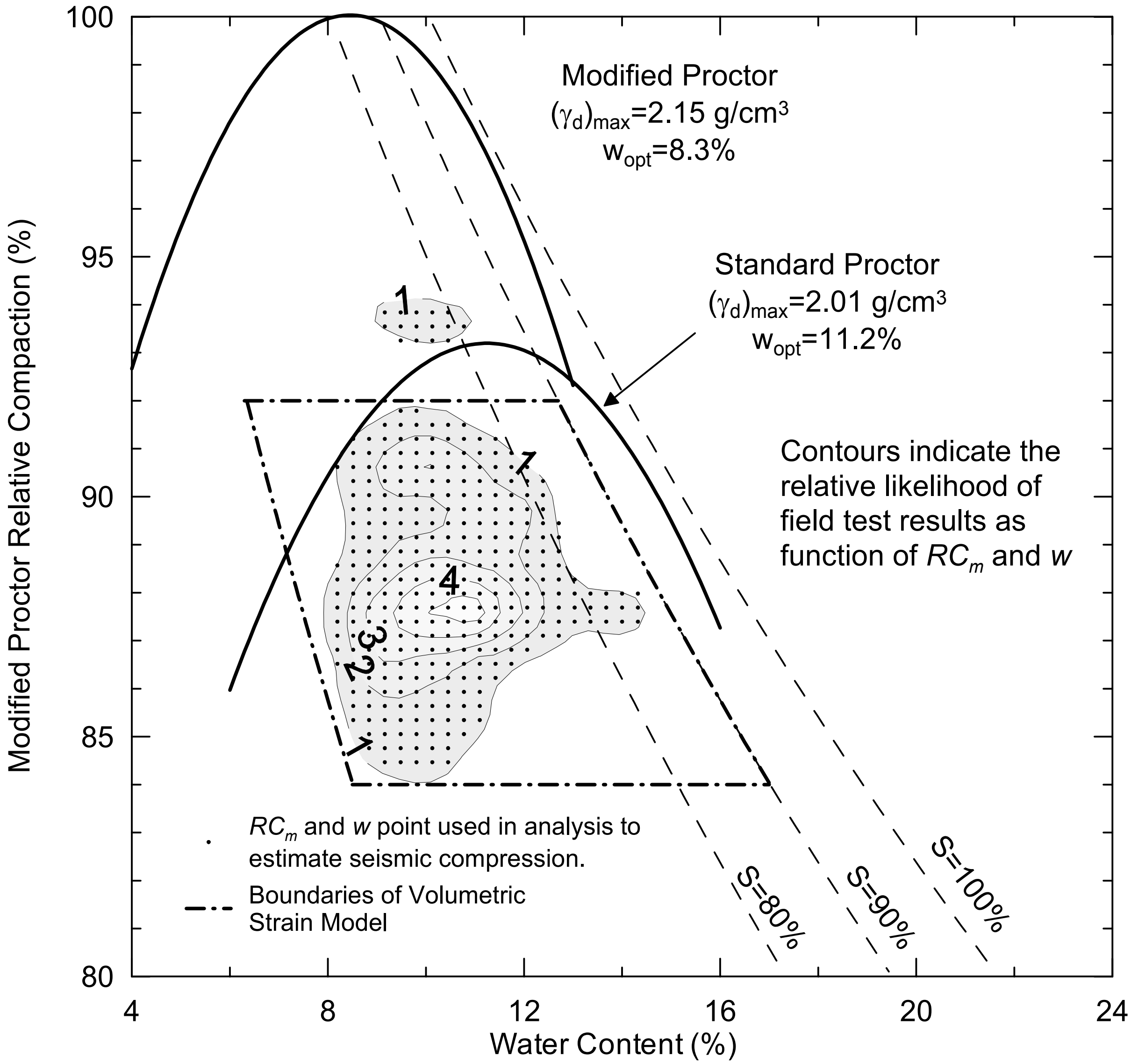

Fig. 7.19. Site A relative likelihood of compaction condition points used in estimation of seismic compression

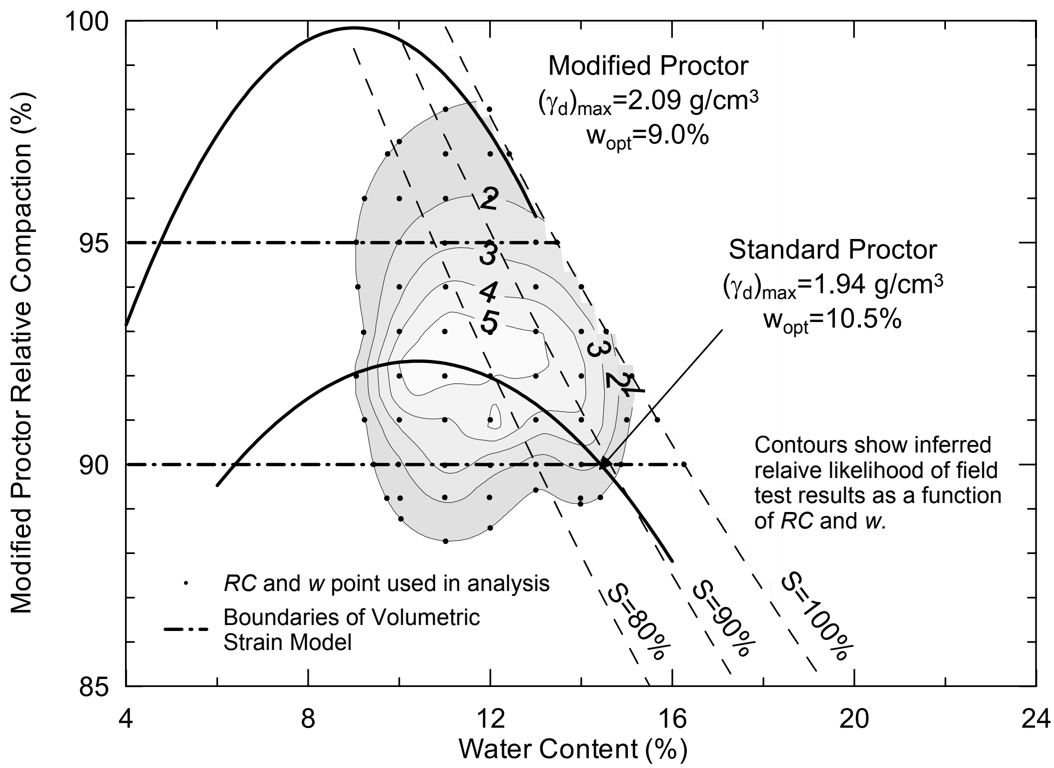

Fig. 7.20. Site B (90% RC Zone) relative likelihood of compaction conditions

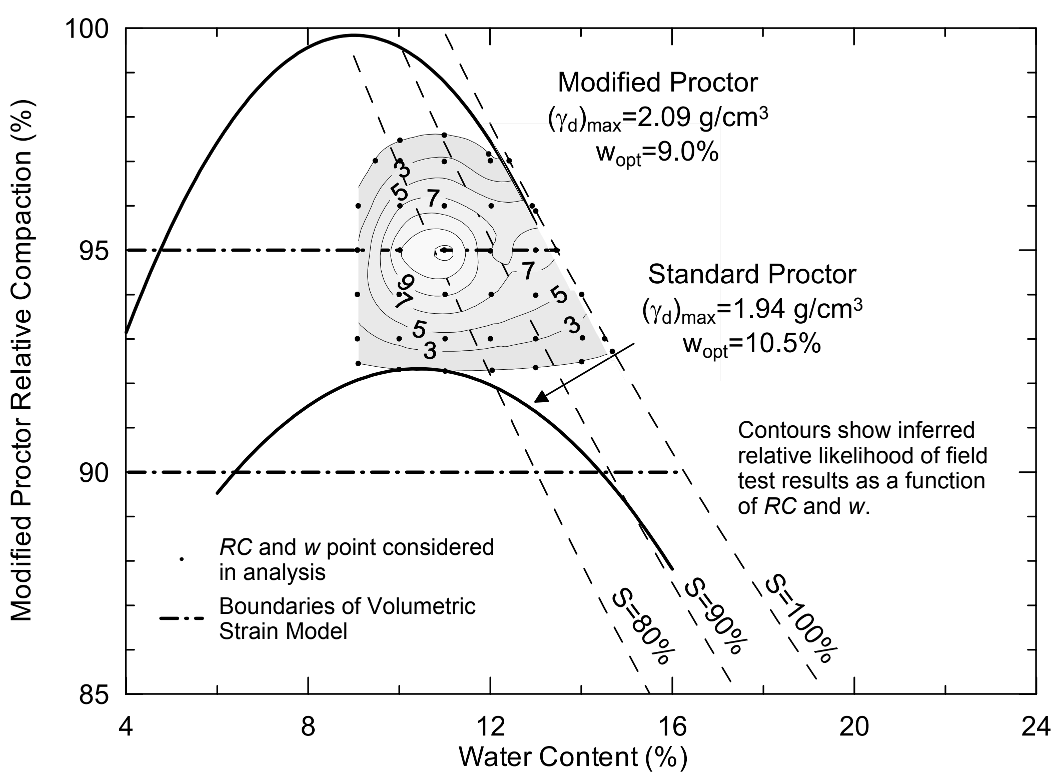

Fig. 7.21. Site B (95% RC Zone) relative likelihood of compaction conditions

Table 7.5. Compaction conditions and weights used for the analysis of Site A

Cond. No.	RC (%)	w (%)	Wt	Cond. No.	RC (%)	w (%)	Wt	Cond. No.	RC (%)	w (%)	Wt	Cond. No.	RC (%)	w (%)	Wt	Cond. No.	RC (%)	w (%)	Wt	Cond. No.	RC (%)	w (%)	Wt	Cond. No.	RC (%)	w (%)	Wt
1	84.8	8.2	0.0015	48	86.5	8.8	0.0033	95	87.4	9.5	0.0016	142	88.3	10.1	0.007	189	89.2	10.5	0.0028	236	90	11.1	0.0032	283	91.2	12.1	0.0029
2	84.8	8.2	0.0017	49	86.5	8.8	0.0034	96	87.7	9.5	0.0021	143	88.3	10.1	0.0073	190	89.2	10.5	0.0035	237	90	11.1	0.0034	284	91.2	12.1	0.0034
3	84.8	8.2	0.0019	50	86.5	8.8	0.0031	97	87.7	9.5	0.0033	144	88.3	10.1	0.0075	191	89.2	10.5	0.0039	238	90	11.1	0.0035	285	91.2	12.1	0.004
4	84.8	8.2	0.0018	51	86.5	8.8	0.0029	98	87.7	9.5	0.0045	145	88.3	10.1	0.0073	192	89.2	10.5	0.0042	239	90	11.1	0.0035	286	91.2	12.1	0.0041
5	84.8	8.2	0.0015	52	86.5	8.8	0.0026	99	87.7	9.5	0.0054	146	88.3	10.1	0.0062	193	89.2	10.5	0.0042	240	90	11.4	0.0034	287	91.2	12.1	0.0035
6	85.1	8.2	0.0016	53	86.5	8.8	0.0023	100	87.7	9.5	0.0059	147	88.3	10.1	0.0051	194	89.2	10.5	0.004	241	90	11.4	0.0023	288	91.2	12.4	0.003
7	85.1	8.2	0.0019	54	86.5	9.2	0.0019	101	87.7	9.5	0.0064	148	88.3	10.1	0.0041	195	89.2	10.8	0.0038	242	90.3	11.4	0.0019	289	91.2	12.4	0.0026
8	85.1	8.2	0.002	55	86.5	9.2	0.0016	102	87.7	9.5	0.0067	149	88.3	10.1	0.0031	196	89.2	10.8	0.0037	243	90.3	11.4	0.0025	290	91.2	12.4	0.0021
9	85.1	8.2	0.0023	56	86.8	9.2	0.0015	103	87.7	9.5	0.0068	150	88.3	10.1	0.0023	197	89.2	10.8	0.0033	244	90.3	11.4	0.0028	291	91.2	12.4	0.0016
10	85.1	8.5	0.0023	57	86.8	9.2	0.0025	104	87.7	9.5	0.007	151	88.3	10.1	0.0018	198	89.2	10.8	0.0027	245	90.3	11.4	0.003	292	91.5	12.4	0.0015
11	85.1	8.5	0.0018	58	86.8	9.2	0.0035	105	87.7	9.5	0.0067	152	88.3	10.1	0.0017	199	89.2	10.8	0.0022	246	90.3	11.4	0.0029	293	91.5	12.4	0.0019
12	85.4	8.5	0.0018	59	86.8	9.2	0.004	106	87.7	9.5	0.0056	153	88.3	10.1	0.0017	200	89.2	10.8	0.0017	247	90.3	11.4	0.003	294	91.5	12.4	0.0024
13	85.4	8.5	0.0021	60	86.8	9.2	0.004	107	87.7	9.5	0.0046	154	88.3	10.1	0.0018	201	89.5	10.8	0.0017	248	90.3	11.4	0.0032	295	91.5	12.4	0.0028
14	85.4	8.5	0.0022	61	86.8	9.2	0.0037	108	87.7	9.5	0.0036	155	88.3	10.1	0.0015	202	89.5	10.8	0.0022	249	90.3	11.4	0.0033	296	91.5	12.4	0.0031
15	85.4	8.5	0.0024	62	86.8	9.2	0.0034	109	87.7	9.5	0.0028	156	88.6	10.1	0.0018	203	89.5	10.8	0.0026	250	90.3	11.4	0.0033	297	91.5	12.4	0.0031
16	85.4	8.5	0.0023	63	86.8	9.2	0.0031	110	87.7	9.8	0.0021	157	88.6	10.1	0.0026	204	89.5	10.8	0.0029	251	90.3	11.4	0.0033	298	91.5	12.4	0.0028
17	85.4	8.5	0.002	64	86.8	9.2	0.0026	111	87.7	9.8	0.0017	158	88.6	10.1	0.0034	205	89.5	10.8	0.0031	252	90.3	11.4	0.0031	299	91.5	12.4	0.0023
18	85.4	8.5	0.0017	65	86.8	9.2	0.0021	112	87.7	9.8	0.0016	159	88.6	10.1	0.0042	206	89.5	10.8	0.0033	253	90.3	11.4	0.0028	300	91.5	12.7	0.0019
19	85.6	8.5	0.0016	66	86.8	9.2	0.0019	113	87.7	9.8	0.0017	160	88.6	10.1	0.005	207	89.5	10.8	0.0035	254	90.3	11.4	0.0021	301	91.5	12.7	0.0015
20	85.6	8.5	0.0019	67	86.8	9.2	0.0015	114	87.7	9.8	0.0017	161	88.6	10.1	0.0057	208	89.5	10.8	0.0036	255	90.6	11.4	0.002	302	91.8	12.7	0.0017
21	85.6	8.5	0.0022	68	87.1	9.2	0.0017	115	87.7	9.8	0.0015	162	88.6	10.1	0.0061	209	89.5	10.8	0.0035	256	90.6	11.4	0.0026	303	91.8	12.7	0.002
22	85.6	8.5	0.0024	69	87.1	9.2	0.0028	116	88	9.8	0.0021	163	88.6	10.1	0.0063	210	89.5	10.8	0.0035	257	90.6	11.4	0.0031	304	91.8	12.7	0.0022
23	85.6	8.5	0.0024	70	87.1	9.2	0.004	117	88	9.8	0.0033	164	88.6	10.1	0.0063	211	89.5	10.8	0.0033	258	90.6	11.7	0.0034	305	91.8	12.7	0.0021
24	85.6	8.5	0.0023	71	87.1	9.2	0.0046	118	88	9.8	0.0046	165	88.6	10.1	0.0059	212	89.5	10.8	0.0029	259	90.6	11.7	0.0037	306	91.8	12.7	0.002
25	85.6	8.5	0.0021	72	87.1	9.2	0.0046	119	88	9.8	0.0055	166	88.6	10.1	0.0053	213	89.5	10.8	0.0023	260	90.6	11.7	0.0038	307	91.8	12.7	0.0016
26	85.6	8.5	0.0019	73	87.1	9.2	0.0044	120	88	9.8	0.0061	167	88.6	10.5	0.0044	214	89.5	10.8	0.0016	261	90.6	11.7	0.0036	308	92.1	12.7	0.0015
27	85.6	8.5	0.0016	74	87.1	9.2	0.0042	121	88	9.8	0.0069	168	88.6	10.5	0.0036	215	89.7	10.8	0.0017	262	90.6	11.7	0.0035	309	92.1	13	0.0015
28	85.9	8.5	0.0017	75	87.1	9.2	0.0041	122	88	9.8	0.0074	169	88.6	10.5	0.0028	216	89.7	10.8	0.0022	263	90.6	11.7	0.0033	310	93.6	13	0.0015
29	85.9	8.5	0.0022	76	87.1	9.2	0.0036	123	88	9.8	0.0075	170	88.6	10.5	0.0021	217	89.7	10.8	0.0025	264	90.6	11.7	0.003	311	93.6	13	0.0016
30	85.9	8.5	0.0025	77	87.1	9.2	0.003	124	88	9.8	0.0081	171	88.6	10.5	0.0016	218	89.7	10.8	0.0026	265	90.6	11.7	0.0026	312	93.6	13	0.0016
31	85.9	8.8	0.0026	78	87.1	9.2	0.0028	125	88	9.8	0.0081	172	88.9	10.5	0.0015	219	89.7	11.1	0.0025	266	90.6	11.7	0.0022	313	93.6	13.4	0.0015
32	85.9	8.8	0.0024	79	87.1	9.2	0.0023	126	88	9.8	0.0064	173	88.9	10.5	0.0021	220	89.7	11.1	0.0026	267	90.6	11.7	0.0016	314	93.8	13.4	0.0016
33	85.9	8.8	0.0023	80	87.1	9.2	0.0017	127	88	9.8	0.0052	174	88.9	10.5	0.0027	221	89.7	11.1	0.003	268	90.9	11.7	0.0015	315	93.8	13.4	0.0016
34	85.9	8.8	0.0022	81	87.4	9.5	0.002	128	88	9.8	0.0043	175	88.9	10.5	0.0034	222	89.7	11.1	0.0033	269	90.9	11.7	0.002	316	93.8	13.7	0.0017
35	85.9	8.8	0.0021	82	87.4	9.5	0.0031	129	88	9.8	0.0031	176	88.9	10.5	0.0042	223	89.7	11.1	0.0034	270	90.9	11.7	0.0027	317	93.8	13.7	0.0017
36	85.9	8.8	0.0019	83	87.4	9.5	0.0042	130	88	9.8	0.0023	177	88.9	10.5	0.0048	224	89.7	11.1	0.0035	271	90.9	11.7	0.0032	318	93.8	13.7	0.0016
37	86.2	8.8	0.0019	84	87.4	9.5	0.005	131	88	9.8	0.0018	178	88.9	10.5	0.0052	225	89.7	11.1	0.0035	272	90.9	11.7	0.0037	319	93.8	14	0.0016
38	86.2	8.8	0.0025	85	87.4	9.5	0.0053	132	88	9.8	0.0017	179	88.9	10.5	0.0052	226	89.7	11.1	0.0032	273	90.9	11.7	0.0043	320	94.1	14	0.0015
39	86.2	8.8	0.0028	86	87.4	9.5	0.0055	133	88	9.8	0.0019	180	88.9	10.5	0.0049	227	89.7	11.1	0.0024	274	90.9	12.1	0.0045	321	94.1	14	0.0016
40	86.2	8.8	0.0029	87	87.4	9.5	0.0055	134	88	9.8	0.0023	181	88.9	10.5	0.0045	228	89.7	11.1	0.0015	275	90.9	12.1	0.0039	322	94.1	14.3	0.0016
41	86.2	8.8	0.0027	88	87.4	9.5	0.0055	135	88	9.8	0.0017	182	88.9	10.5	0.0043	229	90	11.1	0.0018	276	90.9	12.1	0.0034	323	94.1	14.3	0.0016
42	86.2	8.8	0.0025	89	87.4	9.5	0.0052	136	88.3	9.8	0.002	183	88.9	10.5	0.0037	230	90	11.1	0.0023	277	90.9	12.1	0.0031	324	94.1	14.3	0.0015
43	86.2	8.8	0.0024	90	87.4	9.5	0.0048	137	88.3	9.8	0.003	184	88.9	10.5	0.0029	231	90	11.1	0.0027	278	90.9	12.1	0.0026				
44	86.2	8.8	0.0022	91	87.4	9.5	0.0042	138	88.3	9.8	0.0041	185	88.9	10.5	0.0024	232	90	11.1	0.0026	279	90.9	12.1	0.0021				
45	86.2	8.8	0.0019	92	87.4	9.5	0.0034	139	88.3	10.1	0.005	186	88.9	10.5	0.0018	233	90	11.1	0.0023	280	90.9	12.1	0.0016				
46	86.5	8.8	0.0022	93	87.4	9.5	0.0027	140	88.3	10.1	0.0058	187	89.2	10.5	0.0018	234	90	11.1	0.0023	281	91.2	12.1	0.0018				
47	86.5	8.8	0.0029	94	87.4	9.5	0.0021	141	88.3	10.1	0.0065	188	89.2	10.5	0.0023	235	90	11.1	0.0029	282	91.2	12.1	0.0024				

Table 7.6. Compaction conditions and weights used in the analysis of Site B

Cond.	90 % RC Zone		95% RC zone		
No.	RC (%)	w (%)	RC (%)	w (%)	Weight
1	90	n/a	92	n/a	0.0034
2	90	n/a	93	n/a	0.0310
3	90	n/a	94	n/a	0.0542
4	90	n/a	95	n/a	0.0426
5	91	n/a	92	n/a	0.0033
6	91	n/a	93	n/a	0.0297
7	91	n/a	94	n/a	0.0519
8	91	n/a	95	n/a	0.0408
9	92	n/a	92	n/a	0.0084
10	92	n/a	93	n/a	0.0757
11	92	n/a	94	n/a	0.1325
12	92	n/a	95	n/a	0.1041
13	93	n/a	92	n/a	0.0040
14	93	n/a	93	n/a	0.0357
15	93	n/a	94	n/a	0.0624
16	93	n/a	95	n/a	0.0490
17	94	n/a	92	n/a	0.0054
18	94	n/a	93	n/a	0.0485
19	94	n/a	94	n/a	0.0849
20	94	n/a	95	n/a	0.0667
21	95	n/a	92	n/a	0.0017
22	95	n/a	93	n/a	0.0156
23	95	n/a	94	n/a	0.0272
24	95	n/a	95	n/a	0.0214

7.4 ANALYSIS RESULTS

7.4.1 Statistical Distributions of Response Quantities

(a) Overview

Analysis of the settlements resulting from seismic compression was performed using the procedures outlined in Sections 7.2.2 and 7.2.3. We begin by evaluating peak shear strains within the fill mass (γ_{pk}) through the use of 1-D and 2-D ground response analyses. We then evaluate volumetric strains (ε_v), which are integrated across the thickness of the fill section to estimate settlement. We also compile calculated peak horizontal accelerations (*PHA*) across the fill surface as well as the *PHA* amplification (ratio of calculated output *PHA* to input). Effective shear strains, settlement, and *PHA* amplification are termed *response quantities* for the purpose of the subsequent discussion.

A large amount of parametric aleatory and epistemic uncertainty exists in the various inputs into the analyses, which include the ground motion time histories, shear wave velocity (V_s) profiles, compaction conditions, and modulus reduction and damping curves. Because of this uncertainty, numerous estimates of response quantities can be made at Sites A and B. We refer to a given set of input quantities for the analysis as an *input vector*, which for settlement consists of a single time history, a single V_s profile, a single compaction condition (i.e., a value of *RC* and *w*), and a particular set of modulus reduction and damping curves. Note that a subset of the input vector is needed for the evaluation of shear strain, *PHA*, and *PHA* amplification (the compaction condition element is not needed). Corresponding to each input vector is a single realization of the response quantity to which a weight is assigned based on the product of the weights associated with each element of the input vector.

(b) Weighted Frequency Function

Since the weight (or likelihood) of each realization of a response quantity is known, a weighted frequency function (*WFF*) for the response quantity can be constructed. The *WFF*, which is analogous to a probability mass function or normalized frequency, is constructed by subdividing the numerical domain of the response quantity into bins, and for each bin summing the weights associated with all realizations of the response quantity. The number of bins is determined from the following equation:

$$k = 1 + 3.3 \times \log_{10}(m) \tag{7.22}$$

where k is the number of bins and m is the number of observations (i.e., the number of realizations of the response quantity), and the bin size is found by dividing the range of observations by k (Benjamin and Cornell, 1970, page 8).

(c) Construction of Theoretical Models

Once the *WFF* is constructed, four theoretical models are compared to the *WFF* in order to identify a suitable model to represent the response quantity. The normal, lognormal, shifted-lognormal, and Type II Extreme Value theoretical distributions are considered as candidate model types, since they are asymptotic in nature and are often used to represent variables that are a consequence of many other factors whose individual behaviors are poorly understood. Parameters for these assumed distributions are estimated from *the method of moments* utilizing *point estimation* calculated from the sample data (Benjamin and Cornell, 1970, page 372).

The *point estimations* made from the sample data are the weighted mean, the weighted variance, and the skewness coefficient which are defined for variable X by the following equations:

$$m_X = E(X) = \sum_{all\ x_i} x_i\ w(x_i) \qquad \text{Weighted mean} \tag{7.23}$$

$$s_x^{\ 2} = VAR(X) = \sum_{all\ x_i} w(x_i)\,(x_i - m_x)^2 \qquad \text{Weighted variance} \tag{7.24}$$

$$g_i = \frac{E(X - m_x)^3}{s_x^{\ 3}} = \frac{\sum_{all\ x_i} (x_i - m_x)^3\ w(x_i)}{s_x^{\ 3}} \qquad \text{Skewness coefficient} \tag{7.25}$$

where $x_1, x_2, \ldots, x_i$ are the calculated response quantities and $w(x_1), w(x_2), \ldots, w(x_i)$ are the associated weights. As shown below, the *point estimates* are easily related to the assumed distribution parameters by *the method of moments*.

The Normal and Lognormal Distribution

The normal and lognormal distributions are among the most common distributions for fitting sample data to asymptotic functions. The probability density functions for the normal and lognormal distributions are as follows:

$$f_X(x) = \frac{1}{\sigma\sqrt{2\pi}} \exp\left[-\frac{1}{2}\left(\frac{x-\mu}{\sigma}\right)^2\right] \quad -\infty < x < \infty \qquad \text{Normal} \qquad (7.26)$$

$$f_X(x) = \frac{1}{x\sigma_{\ln x}\sqrt{2\pi}} \exp\left[-\frac{1}{2}\left(\frac{\ln(x)-\lambda_{\ln}}{\sigma_{\ln x}}\right)^2\right] \quad 0 \le x < \infty \qquad \text{Lognormal} \qquad (7.27)$$

where μ and λ_{ln} represent the means of the respective distributions, while σ and σ_{lnx} represent the standard deviations. The weighted mean and variance are directly related to the moments of the normal distribution as follows:

$$\mu_x = E(x) \approx m_x \qquad \text{Normal mean/median} \qquad (7.28)$$

$$\sigma_x^{\ 2} = VAR(x) \approx s_x^{\ 2} \qquad \text{Normal variance} \qquad (7.29)$$

and are related to the lognormal distribution by the following equations:

$$\lambda_{\ln x} = E[\ln(x)] \approx \ln(m_x) - \tfrac{1}{2}\sigma_{\ln x}^2 \qquad \text{Lognormal mean/median} \qquad (7.30)$$

$$\sigma_{\ln x}^{\ 2} = VAR[\ln(x)] \approx \ln\left(1 + \frac{s_x^{\ 2}}{m_x^{\ 2}}\right) \qquad \text{Lognormal variance} \qquad (7.31)$$

where m_x and s_x are the weighted mean and standard deviation from Eqs. 7.23–7.25. In subsequent notation, λ_{lnx} and λ are used to represent the mean in natural log units (which equals the median) and the median in arithmetic units, respectively [i.e., $\lambda=\exp(\lambda_{lnx})$].

The Shifted Lognormal Distribution

The shifted lognormal distribution was selected as a candidate probability density function (PDF) because it is easily fitted and capable of reflecting an observed shift and skew in the data. The PDF of the shifted lognormal distribution functions is as follows:

$$f_X(x) = \frac{1}{(x-a)\sigma_{\ln Y}\sqrt{2\pi}} \exp\left[-\frac{1}{2}\left(\frac{\ln(x-a)-\lambda_{\ln Y}}{\sigma_{\ln Y}}\right)^2\right] \quad x \ge a \qquad (7.32)$$

where σ_{lnY} is the standard deviation of the natural logarithm of Y=X-a, λ_{lnY} is the mean/median of ln(Y), and a represents the shift parameter.

Since the standard deviation and skewness coefficient of Y equal those of X, which are in turn estimated by the corresponding sample moments, we can solve the following skewness equation for the mean of Y (μ_Y) (Benjamin and Cornell, 1970, page 484):

$$\gamma_1 = 3\frac{\sigma_Y}{\mu_Y} + \left(\frac{\sigma_Y}{\mu_Y}\right)^3 \qquad \text{Skewness} \tag{7.33}$$

where μ_Y and σ_Y represent the mean and standard deviation of Y (not ln$Y$) and γ_1 = skewness. Rearranging Eq. 7.33 and substituting s_Y and g_1 for the σ_Y and γ_1, respectively, yields,

$$\mu_Y{}^3 - \frac{s_Y{}^3}{g_1} - \frac{3s_Y\mu_Y^2}{g_1} = 0 \tag{7.34}$$

which can be solved by trial and error to estimate μ_Y. The median of the natural log of Y (λ_{lnY}) and variance of the natural log of Y ($\sigma_{lnY}{}^2$) can be estimated using Eqs. 7.30 and 7.31, and the shift parameter a is given in the following equation.

$$a = \mu_X - \mu_Y = m_x - \mu_Y \tag{7.35}$$

Type II Extreme Value Distribution

The Extreme Value Distribution represents the distribution of the largest or smallest values of a parameter of interest. It has been applied to quantities for which the maximum realization is of engineering interest, such as flood levels, wind loads, or earthquake magnitudes.

We use a Type II extreme value distribution, which represents a distribution limited to the largest value of many independent, identically distributed random variables. Our rationale for consideration of this distribution is that the *WFF* of some response quantities may be controlled by a few large realizations of underlying parameters (e.g., settlements being controlled by few parameter combinations that lead to large shear strains). The underlying variables are assumed to occupy the range (0 – +∞), and to have an exponentially decaying right tail. The asymptotic density distribution of Y, the largest of many X_i, is (Benjamin and Cornell, 1970, page 279)

$$f_Y(y) = \frac{k}{u}\left(\frac{u}{y}\right)^{k+1} e^{\left(-u/y\right)^k} \qquad for \quad y \geq 0 \tag{7.36}$$

where u is a location parameter (mode) and k is a scale parameter. The mean (μ_Y) and the variance (σ_Y^2) are defined by the following equations:

$$\mu_Y = u\Gamma\left(1-\frac{1}{k}\right) \approx m_X \quad k>1 \qquad \text{Type II Mean} \qquad (7.37)$$

$$\sigma_Y^{\ 2} = u^2\left[\Gamma\left(1-\frac{2}{k}\right) - \Gamma^2\left(1-\frac{1}{k}\right)\right] \approx s_X^{\ 2} \quad k>2 \qquad \text{Type II Variance} \qquad (7.38)$$

where Γ refers to the gamma function (Benjamin and Cornell, 1970, page 246). The coefficient of variation (δ_Y) can be evaluated as

$$\delta_Y^{\ 2} = \left[\frac{\Gamma\left(1-\frac{2}{k}\right)}{\Gamma^2\left(1-\frac{1}{k}\right)} - 1\right] \approx \left(\frac{s_X}{m_X}\right)^2 k>1 \qquad (7.39)$$

Eq. 7.39 can be used iteratively to find parameter k if δ_Y is known from the data.

(d) Testing the Validity of the Assumed Models

The ability of an assumed model to describe the distribution of a data set can be evaluated statistically by goodness-of-fit tests. Two such tests that are commonly used are the *Chi-squared* and *Kolmogorov-Smirnov* (*K-S*) tests, both of which are used to accept or reject a candidate model for the data set's probability density function (PDF).

Chi-square Test for Distribution

The Chi-square goodness-of-fit test is applied to binned data, and quantifies the error between the observed frequencies $n_1, n_2,...,n_k$ of k values (or k intervals) of the variant with the corresponding frequencies $e_1, e_2,...,e_k$ for a candidate theoretical distribution. The cumulative error (E) is compared to the cumulative probability of a Chi-square distribution with ($f=k-1$) degrees of freedom by the following inequality (Ang and Tang, 1975, page 274):

$$E = \sum_{i=1}^{k} \frac{(n_i - e_i)^2}{e_i} < c_{1-\alpha,f} \qquad (7.40)$$

where $c_{1-\alpha,f}$ is the value of the appropriate Chi-square distribution for degree of freedom f at the cumulative probability ($1-\alpha$). The assumed model is acceptable at significance level α if $E < c_{1-\alpha,f}$.

The expected frequency (e_i) in interval k is computed as

$$e_i = N \cdot p_i \tag{7.41}$$

where N is the total sample size and p_i is the probability for that interval based on the assumed model. The observed frequency (n_i) is computed by

$$n_i = N \cdot w_i \tag{7.42}$$

where w_i is the weighted frequency, or likelihood, in interval k.

It has been suggested by Mann and Wald (1942) and others that the interval ranges should be determined from the assumed distribution with equal probability among all intervals k. The equal-interval probability is taken as *1/k* where k is determined from Eq. 7.22. The *w's* for the assumed distribution in the interval k are found by the same method used to construct the *WFF* diagrams, which were described in Section 7.4.1(b).

Figure 7.22 illustrates the difference between the construction of *WFF* diagrams used in Section 7.4.1(b) and the model-dependent *WFF* diagrams with equal interval probability used for the Chi-square goodness-of-fit test based on random data. Table 7.7 shows the bin intervals (boundaries) for the *WFF* and for the theoretical distributions with equal interval probability.

Table 7.7. Example of intervals used for frequency diagrams in the Chi-square test. Interval widths are equal for *WFF* and variable for theoretical distributions to maintain consistent probabilities for each interval

WFF Diagram Distribution		Normal Distribution		Lognormal Distribution		Shifted-Lognormal Distribution		Type II Extreme Value Distribution	
Upper	Lower	Upper	Lower	Upper	Lower	Upper	Lower	Upper	Lower
1.48	1.00	-0.10	-∞	1.02	0.00	0.88	0.00	1.62	0.00
1.96	1.48	0.80	-0.10	1.36	1.02	1.28	0.88	1.81	1.62
2.43	1.96	1.28	0.80	1.59	1.36	1.53	1.28	1.94	1.81
2.91	2.43	1.61	1.28	1.76	1.59	1.72	1.53	2.04	1.94
3.39	2.91	1.87	1.61	1.91	1.76	1.89	1.72	2.13	2.04
3.87	3.39	2.09	1.87	2.05	1.91	2.04	1.89	2.21	2.13
4.35	3.87	2.29	2.09	2.18	2.05	2.19	2.04	2.30	2.21
4.83	4.35	2.47	2.29	2.32	2.18	2.33	2.19	2.38	2.30
5.30	4.83	2.65	2.47	2.45	2.32	2.47	2.33	2.47	2.38
5.78	5.30	2.82	2.65	2.58	2.45	2.61	2.47	2.55	2.47
5.78	6.26	2.98	2.82	2.72	2.58	2.76	2.61	2.65	2.55
6.26	6.74	3.15	2.98	2.87	2.72	2.91	2.76	2.75	2.65
6.74	7.22	3.32	3.15	3.03	2.87	3.07	2.91	2.87	2.75
7.22	7.70	3.49	3.32	3.20	3.03	3.25	3.07	2.99	2.87
7.70	8.17	3.67	3.49	3.40	3.20	3.44	3.25	3.14	2.99
8.17	8.65	3.87	3.67	3.62	3.40	3.66	3.44	3.32	3.14
8.65	9.13	4.09	3.87	3.88	3.62	3.92	3.66	3.54	3.32
9.13	9.61	4.34	4.09	4.20	3.88	4.24	3.92	3.83	3.54
9.61	10.09	4.65	4.34	4.64	4.20	4.67	4.24	4.27	3.83
10.09	10.57	5.10	4.65	5.36	4.64	5.35	4.67	5.06	4.27
		6.08	5.10	7.34	5.36	7.17	5.35	8.00	5.06
		∞	6.08	∞	7.34	∞	7.17	∞	8.00

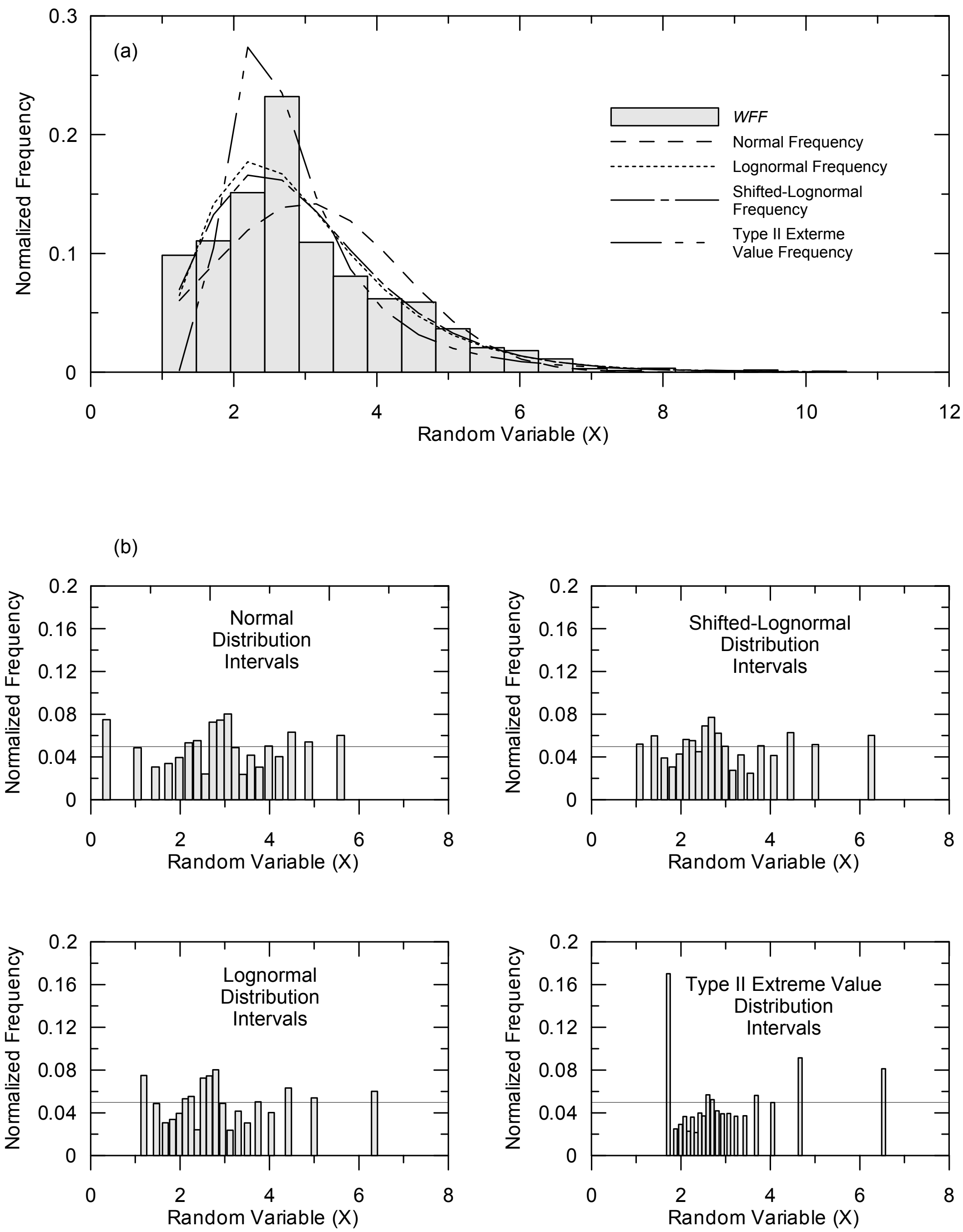

Fig. 7.22. Schematic comparison between empirical normalized frequency distribution based on equal intervals (a) vs. empirical normalized frequency distributions based on equal probability intervals of variable width from theoretical distributions models (b).

Kolmogorov-Smirnov Test for Distribution

The Kolmogorov-Smirnov (*K-S*) distribution test begins with a comparison between the experimental cumulative frequency and an assumed theoretical cumulative distribution function. If the discrepancy is large with respect to what is normally expected for a given sample size, the model is rejected. A step-wise cumulative frequency function (S_n) is developed from a weighted data set as follows:

$$S_n(x) = \begin{cases} 0 & x < x_1 \\ \sum_i w_i & x_i \le x < x_{i+1} \\ 1 & x \ge x_n \end{cases} \tag{7.43}$$

where $w_1, w_2, \ldots, w_n$ are the values of the weighted frequency for the realizations $x_1, x_2, \ldots x_n$. Figure 7.23 shows a schematic comparison between values of $S_n(x)$ and a proposed theoretical cumulative distribution function $F(x)$. The maximum difference between $S_n(x)$ and $F(x)$ over the entire range of X is a measure of discrepancy between the assumed model and the observed data. This maximum difference is denoted by

$$D_n = \max_x \left| F(x) - S_n(x) \right| \tag{7.44}$$

Theoretically, D_n is a random variable whose distribution depends on the total number of events (n) in $F(x)$. For a specified significance level α, the *K-S* test compares D_n with a critical value D_n^α, which is defined by

$$P(D_n \le D_n^\alpha) = 1 - \alpha \tag{7.45}$$

If the observed D_n is less than D_n^α, then the proposed model is said to be acceptable at the specified significance level α; otherwise, the assumed model would be rejected.

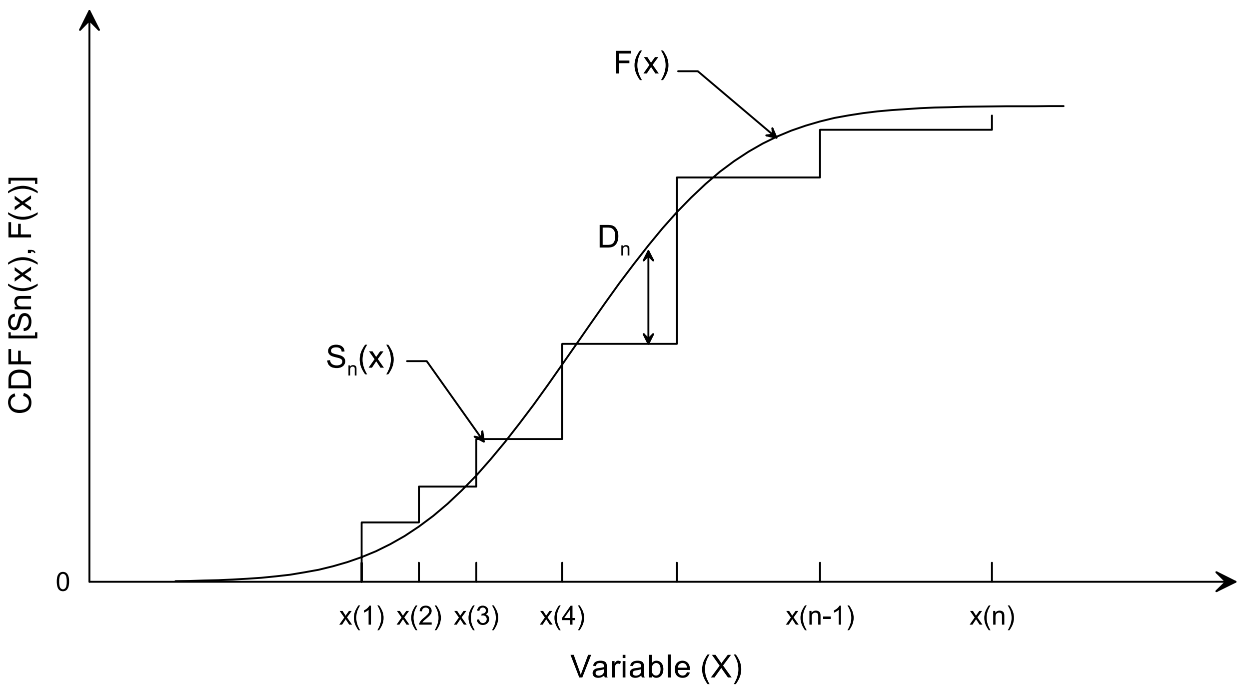

Fig. 7.23. Schematic comparison between empirical cumulative frequency vs. theoretical distribution function for *K-S* test (after Ang and Tang, 1975)

Protocol for Selection of Optimum Theoretical Distribution and Parameters

Goodness-of-fit tests are not specifically designed to discriminate among two or more distributions or to help choose from among several contending distributions. Their purpose is to determine if a given distribution can be used to represent a data set. Nonetheless, these tests do offer a means by which to quantify the relative errors between alternative theoretical cumulative distribution functions and the experimental cumulative frequency, and hence we used these tests to identify the most appropriate theoretical models for various response quantities.

The identification of the optimal theoretical model for a response quantity involves comparing the goodness-of-fit test results for the four theoretical models. Both the Chi-square and *K-S* goodness-of-fit tests rely on the choice of the significance level (α) to determine the reference level of acceptance. We select a maximum value of $\alpha = 5\%$ (a common but arbitrary value) to indicate an acceptable fit between a model and data set.

Using the Chi-square test, a theoretical model is chosen to represent a response quantity if that model exhibits the smallest E value and that E value is also less than $c_{1-\alpha,f}$. Using the *K-S* test, a model is chosen if it has the smallest D_n value and that D_n value is also less than D_n^{α}.

Many such Chi-square or *K-S* tests could be performed for calculated response quantities at different locations at a given site. The final choice of the theoretical PDF for a particular response quantity is made by identifying the distribution most frequently found to be optimized at the locations considered at Sites A and B. Once a theoretical distribution is chosen to represent the data, then the descriptive parameters for the distribution (e.g., median, standard deviation) can be estimated as described in Section 7.4.1(c).

7.4.2 Analysis Results for Maximum Shear Strain at Sites A and B

(a) Identification of Optimum Theoretical Model for Distribution of Shear Strain

Locations within the fill sections at Sites A and B where shear strains are compiled for testing of the statistical distributions are shown in Figures 7.24–7.25. For these locations, shown in Table 7.8 are point estimates of shear strain calculated using Eqs. 7.23–7.25. The weighted frequency functions (*WFF*s) and the candidate theoretical cumulative distribution functions for each location are plotted by Smith (2002). Results of the *K-S* and Chi-square goodness-of-fit tests are given in Tables 7.9 and 7.10, respectively.

Table 7.8. Point estimates of peak shear strain at selected locations, Sites A and B

Site	Analysis Type	Location	Depth (m)	Weighted Average	Standard Deviation	Coeff. of Variation	Skewness Coeff.
A	2-D	Psecta1	2.7	0.096	0.082	0.859	3.016
		Psecta2	29.7	0.135	0.111	0.826	2.543
		Psectb1	7.5	0.079	0.075	0.955	2.364
		Psectb2	7.2	0.057	0.039	0.691	1.331
	1-D	Psecta1	2.7	0.057	0.065	1.143	3.208
		Psecta2	29.7	0.26	0.219	0.84	2.034
		Psectb1	7.5	0.064	0.053	0.835	2.334
		Psectb2	7.2	0.075	0.074	0.984	2.233
B	2-D	Ssecta1	23.2	0.047	0.026	0.56	1.957
		Ssecta2	2.6	0.212	0.378	1.787	3.038
		Ssectb1	18.6	0.069	0.037	0.535	1.553
		Ssectb2	10.5	0.042	0.027	0.648	1.343
	1-D	Ssecta1	23.2	0.114	0.083	0.726	1.952
		Ssecta2	2.6	0.162	0.241	1.492	2.482
		Ssectb1	18.6	0.088	0.063	0.714	1.716
		Ssectb2	10.5	0.131	0.123	0.941	1.912

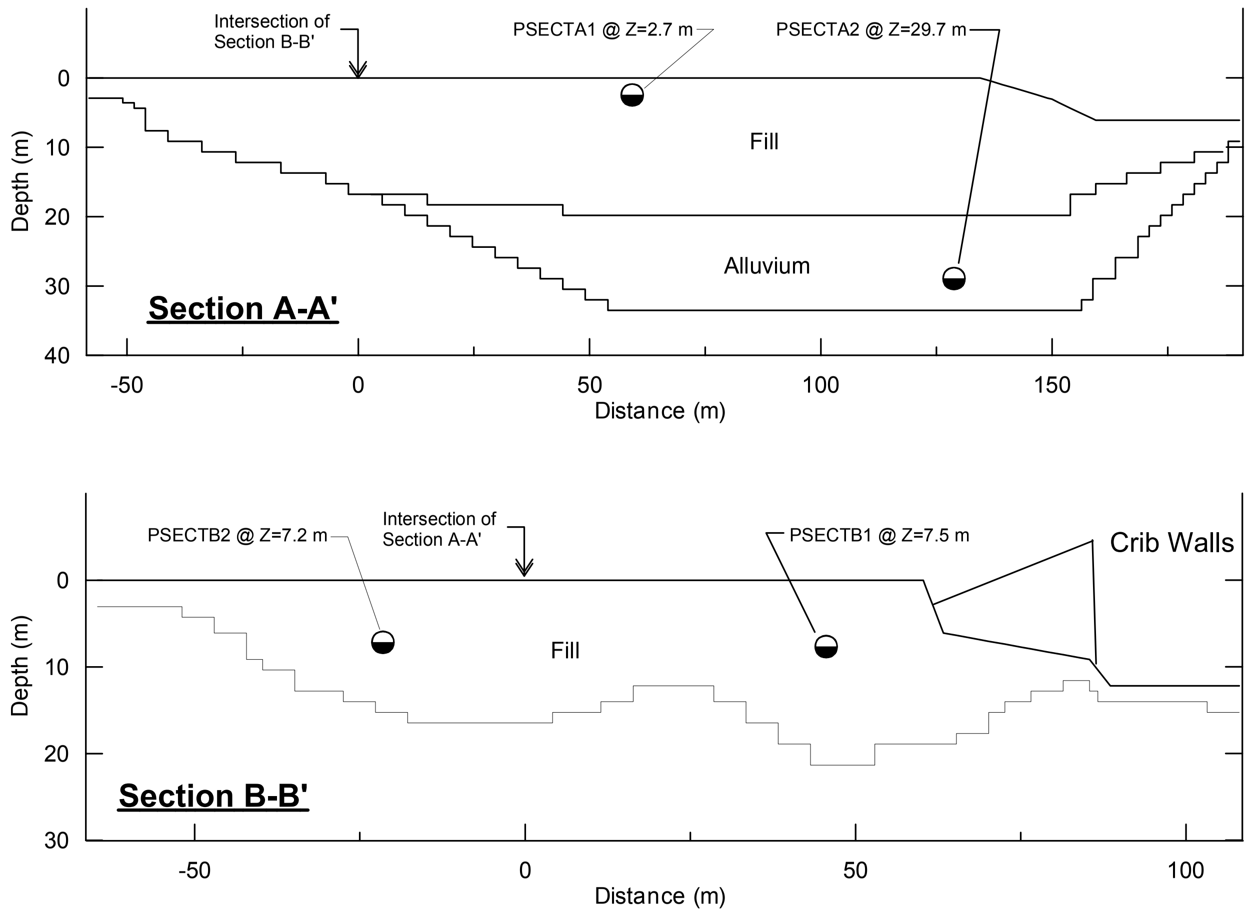

Fig. 7.24. Location of shear strain distribution theoretical model goodness-of-fit tests for Site A

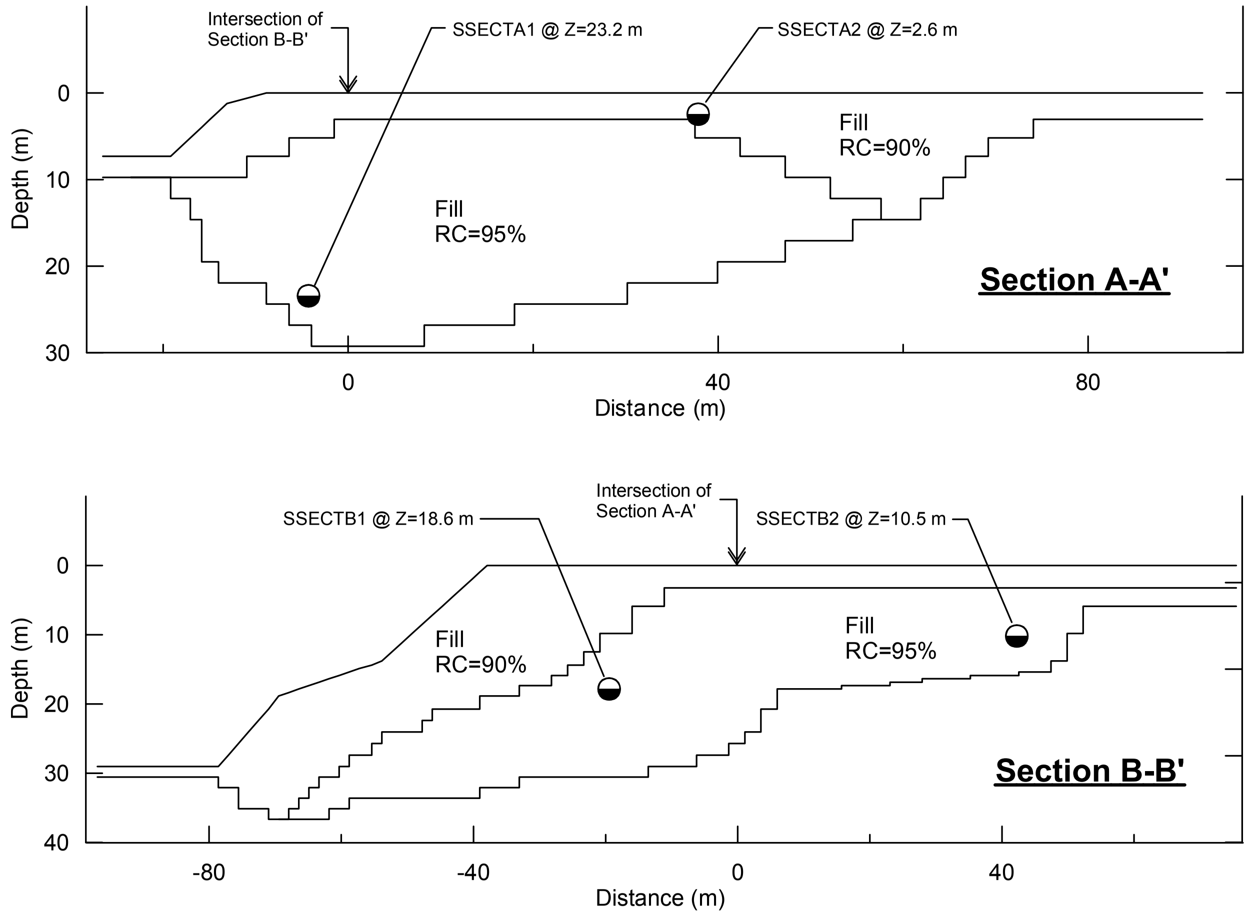

Fig. 7.25. Location of shear strain distribution theoretical model goodness-of-fit tests for Site B

Table 7.9. *K-S* test results for peak shear strain distribution

Site	Analysis Type	Location	Depth (m)	Distribution Model D_n Values: Normal	Log-normal	Shift. Log-normal	Type II	D_n^α Reference Value	Best Fit*
A	2-D	psecta1	2.7	0.148	0.033	0.029	0.218	0.075	Log
		psecta2	29.7	0.179	0.048	0.080	0.188	0.075	Log
		psectb1	7.5	0.188	0.063	0.100	0.277	0.075	Log
		psectb2	7.2	0.137	0.077	0.077	0.233	0.075	Null
	1-D	psecta1	2.7	0.209	0.077	0.119	0.326	0.075	Null
		psecta2	29.7	0.157	0.063	0.082	0.259	0.075	Log
		psectb1	7.5	0.201	0.058	0.080	0.175	0.075	Log
		psectb2	7.2	0.193	0.082	0.126	0.275	0.075	Log
B	2-D	ssecta1	23.2	0.130	0.033	0.033	0.127	0.075	Log
		ssecta2	2.6	0.288	0.182	0.320	0.536	0.075	Null
		ssectb1	18.6	0.126	0.060	0.062	0.145	0.075	Shift
		ssectb2	10.5	0.128	0.072	0.055	0.209	0.075	Log
	1-D	ssecta1	23.2	0.143	0.055	0.061	0.224	0.075	Log
		ssecta2	2.6	0.261	0.214	0.255	0.510	0.075	Null
		ssectb1	18.6	0.154	0.065	0.070	0.227	0.075	Log
		ssectb2	10.5	0.175	0.096	0.113	0.283	0.075	Null

* A "Null" value indicates that no distribution model passed the *K-S* test.

Table 7.10. Chi-square test results for peak shear strain distribution

Site	Analysis Type	Location	Depth (m)	Distribution Model E Values: Normal	Log-normal	Shift. Log-normal	Type II	$c_{1-\alpha,f}$ Reference Value	Best Fit
A	2-D	psecta1	2.7	161	20	18	344	370	Log
		psecta2	29.7	248	28	49	264	370	Log
		psectb1	7.5	303	40	78	507	370	Log
		psectb2	7.2	149	23	55	398	370	Log
	1-D	psecta1	2.7	341	36	103	3321	370	Log
		psecta2	29.7	240	22	66	540	370	Log
		psectb1	7.5	244	31	60	250	370	Log
		psectb2	7.2	361	32	113	521	370	Log
B	2-D	ssecta1	23.2	125	34	38	125	370	Log
		ssecta2	2.6	1087	123	539	3866	370	Log
		ssectb1	18.6	136	26	48	146	370	Log
		ssectb2	10.5	134	32	43	346	370	Log
	1-D	ssecta1	23.2	193	33	54	389	370	Log
		ssecta2	2.6	1065	166	491	1919	370	Log
		ssectb1	18.6	185	41	55	383	370	Log
		ssectb2	10.5	256	41	105	603	370	Log

Tables 7.9 and 7.10 indicate that the theoretical model that most frequently provides the best fit to the *WFF* is the lognormal distribution model. Accordingly, median (λ) and standard deviation (σ_{ln}) values of peak shear strain were calculated for this distribution, which are presented in Table 7.11.

Table 7.11. Median and standard deviation parameter estimates of peak shear strain at selected locations, Sites A and B

Site	Analysis Type	Location	Depth (m)	Median (λ) - %	Std. Dev. (σ_{ln})
A	2-D	Psecta1	2.7	0.073	0.744
		Psecta2	29.7	0.104	0.721
		Psectb1	7.5	0.057	0.805
		Psectb2	7.2	0.047	0.625
	1-D	Psecta1	2.7	0.038	0.914
		Psecta2	29.7	0.199	0.731
		Psectb1	7.5	0.049	0.727
		Psectb2	7.2	0.054	0.823
B	2-D	Ssecta1	23.2	0.041	0.522
		Ssecta2	2.6	0.103	1.197
		Ssectb1	18.6	0.061	0.501
		Ssectb2	10.5	0.035	0.592
	1-D	Ssecta1	23.2	0.092	0.650
		Ssecta2	2.6	0.090	1.082
		Ssectb1	18.6	0.071	0.642
		Ssectb2	10.5	0.095	0.796

(b) Interpretation of Trends in the Shear Strain Results

Shown in Figures 7.26–7.27 are profiles with depth of median (λ) and median ± one standard deviation ($\lambda \pm 1\sigma_{ln}$) shear strains calculated by 2-D analyses at Sites A and B along with 1-D median profiles (λ). The calculated shear strains are greater than typical threshold strains for silty sands (0.01 to 0.05%; Vucetic, 1994), suggesting that nearly the full depth of fill likely contributed to the observed settlements.

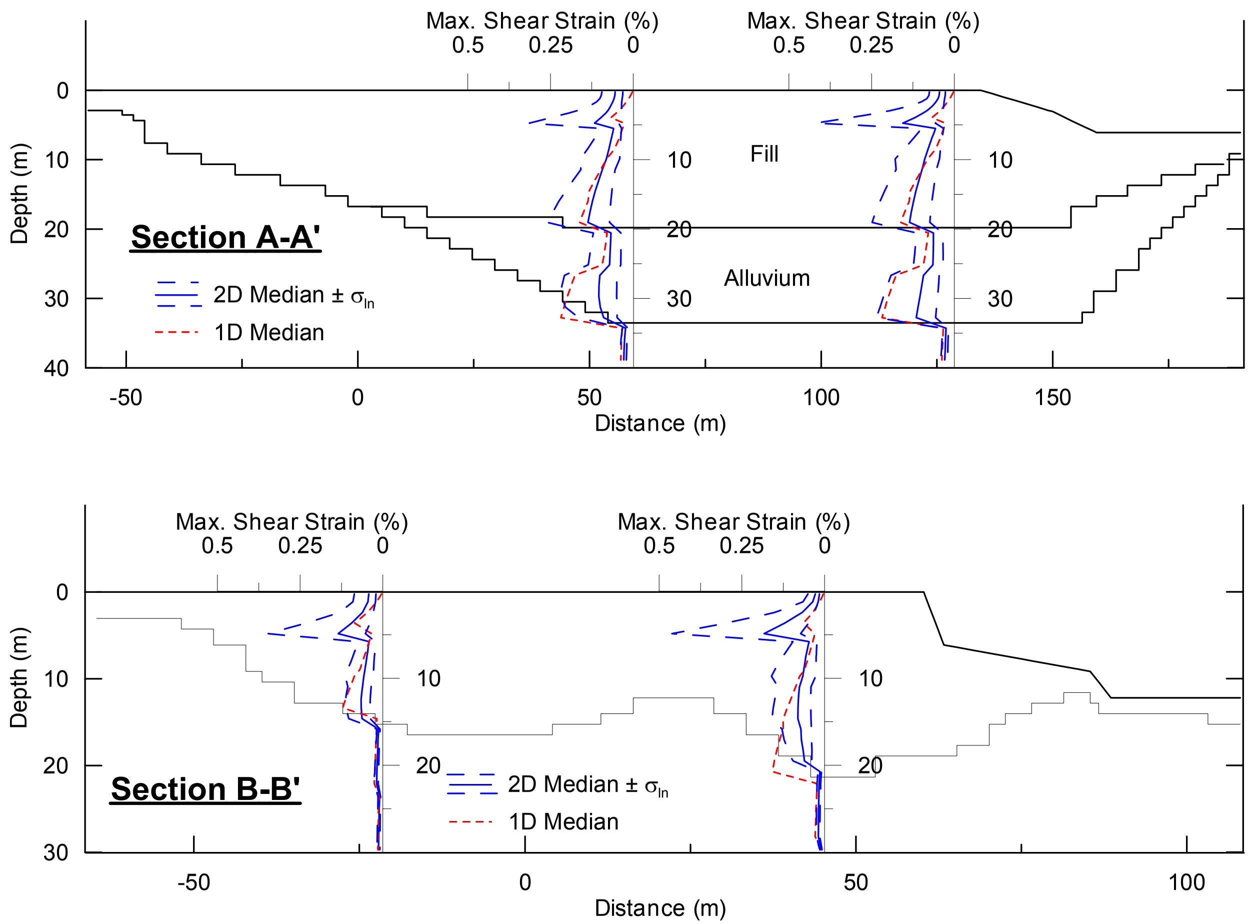

Fig. 7.26. Profiles of peak shear strain with depth at Site A

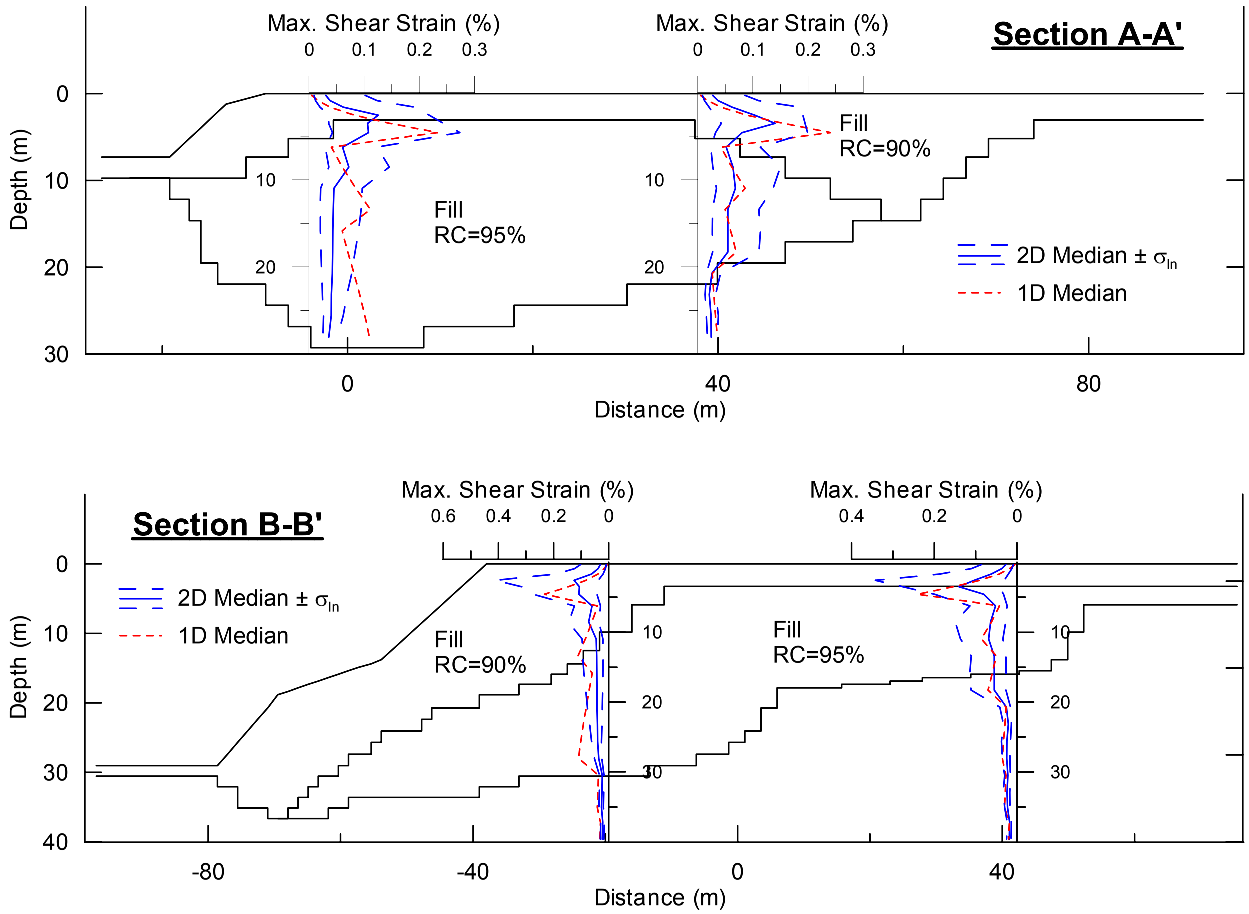

Fig. 7.27. **Profiles of peak shear strain with depth at Site B**

As expected, shear strains generally increase with depth near the surface of the fills, and change sharply at impedance contrasts. The largest shear strains within the profiles most often occur above impedance contrasts within the upper 10 m of fill, but in some nearly 1-D profiles may occur at depth above fill/alluvium or fill/bedrock interfaces. Note that nonzero shear strains are calculated at the surface of the fill in the 2-D analyses. No evidence has been found to suggest that this is a computational error in the QUAD4M program. Rather, these strains may be attributed to the influence of nonzero static shear stresses on the time domain solution of dynamic soil response in areas behind a sloping ground surface.

Overall comparisons of the 1-D and 2-D analysis results in Figures 7.26–7.27 and Table 7.11 reveal three trends: (1) for horizontally layered soils behind a slope face (Site A), median shear strains from the 2-D analyses exceed those from 1-D analyses to depths corresponding roughly with the base-of-slope elevation; (2) the presence of a sloping impedance contrast (i.e., bedrock-soil, or adjacent fill layers) provides additional lateral restraint to the overlying, softer layer, which reduces 2-D strains relative to 1-D strains (e.g., locations near surface at Site B, base of fill at Sites A and B); and (3) the 2-D strains have smaller dispersion (as measured by σ_{ln}) than do 1-D strains.

Many sources of parametric uncertainty affect the width of the shear strain distributions presented in Figures 7.26–7.27. The relative significance of various factors, and the conditions that lead to unusually large or small shear strain realizations, are discussed in Chapter 8.

7.4.3 Analysis Results for Volumetric Strains at Sites A and B

(a) Identification of Optimum Theoretical Model for Distribution of Volumetric Strain

The locations within the fill sections where volumetric strains are compiled for testing of statistical distributions are the same as those used for shear strains, and are shown in Figures 7.24 and 7.25. Table 7.12 shows for these locations the point estimates of volumetric strain calculated using Eqs. 7.23–7.25. Weighted frequency functions (*WFFs*) and candidate theoretical cumulative distribution functions for volumetric strains are plotted by Smith (2002). Results of the *K-S* and Chi-square goodness-of-fit tests are given in Tables 7.13 and 7.14, respectively.

Table 7.12. Point estimations of volumetric strain at selected locations, Sites A and B

Site	Analysis Type	Location	Depth (m)	Weighted Avg. (%)	Std. Dev. (%)	Coeff. of Variation	Skewness Coeff.
A	2-D	Psecta1	2.7	0.339	0.319	0.941	2.305
		Psecta2	29.7	0.844	0.727	0.862	2.282
		Psectb1	7.5	0.269	0.293	1.090	1.985
		Psectb2	7.2	0.196	0.186	0.949	1.310
	1-D	Psecta1	2.7	0.184	0.261	1.415	2.857
		Psecta2	29.7	1.500	1.117	0.745	1.412
		Psectb1	7.5	0.216	0.225	1.042	2.024
		Psectb2	7.2	0.256	0.295	1.152	2.031
B	2-D	Ssecta1	23.2	0.112	0.078	0.692	0.743
		Ssecta2	2.6	0.380	0.525	1.382	2.595
		Ssectb1	18.6	0.179	0.097	0.543	0.350
		Ssectb2	10.5	0.100	0.092	0.922	0.858
	1-D	Ssecta1	23.2	0.253	0.135	0.535	0.561
		Ssecta2	2.6	0.298	0.332	1.112	1.494
		Ssectb1	18.6	0.211	0.127	0.602	0.395
		Ssectb2	10.5	0.244	0.165	0.677	0.524

Table 7.13. *K-S* Test results for volumetric strain distribution

Site	Analysis Type	Location	Depth (m)	Distribution Model D_n Values				D_n^α Reference Value	Best Fit*
				Normal	Log-normal	Shift. Log-normal	Type II		
A	2-D	psecta1	2.7	0.113	0.112	0.029	0.265	0.004	Null
		psecta2	29.7	0.322	0.448	0.415	0.503	0.004	Null
		psectb1	7.5	0.151	0.128	0.085	0.337	0.004	Null
		psectb2	7.2	0.121	0.151	0.067	0.325	0.004	Null
	1-D	psecta1	2.7	0.169	0.254	0.079	0.440	0.004	Null
		psecta2	29.7	0.745	0.806	0.764	0.856	0.004	Null
		psectb1	7.5	0.162	0.105	0.067	0.288	0.004	Null
		psectb2	7.2	0.174	0.135	0.096	0.349	0.004	Null
B	2-D	ssecta1	23.2	0.117	0.107	0.076	0.217	0.015	Null
		ssecta2	2.6	0.206	0.180	0.077	0.390	0.015	Null
		ssectb1	18.6	0.079	0.106	0.075	0.220	0.015	Null
		ssectb2	10.5	0.137	0.215	0.103	0.328	0.015	Null
	1-D	ssecta1	23.2	0.062	0.107	0.050	0.200	0.015	Null
		ssecta2	2.6	0.171	0.237	0.105	0.405	0.015	Null
		ssectb1	18.6	0.095	0.120	0.077	0.245	0.015	Null
		ssectb2	10.5	0.082	0.165	0.079	0.274	0.015	Null

* A "Null" value indicates that no distribution model passed the *K-S* test.

Table 7.14. Chi-square test results for volumetric strain distribution

Site	Analysis Type	Location	Depth (m)	Distribution Model E Values: Normal	Log-normal	Shift. Log-normal	Type II	$c_{1-\alpha,f}$ Reference Value	Best Fit
A	2-D	psecta1	2.7	44223	53839	9864	319843	44223	Shifted
		psecta2	29.7	75760	13236	20936	211513	75760	Shifted
		psectb1	7.5	112097	70419	24220	507043	112097	Shifted
		psectb2	7.2	62288	98735	37031	487012	62288	Shifted
	1-D	psecta1	2.7	312709	275598	258467	864556	312709	Null
		psecta2	29.7	83336	14559	23029	232664	83336	Log
		psectb1	7.5	72468	47288	15188	372964	72468	Shifted
		psectb2	7.2	106483	69054	34035	550746	106483	Shifted
B	2-D	ssecta1	23.2	3615	3949	1673	14150	3615	Shifted
		ssecta2	2.6	15611	8615	8166	40938	15611	Shifted
		ssectb1	18.6	2219	3013	2006	14468	2219	Shifted
		ssectb2	10.5	8556	11954	5470	30381	8556	Shifted
	1-D	ssecta1	23.2	1996	3315	1348	13348	1996	Shifted
		ssecta2	2.6	10532	14672	6989	47629	10532	Shifted
		ssectb1	18.6	1996	4055	1634	18772	1996	Shifted
		ssectb2	10.5	4107	9099	3511	22054	4107	Shifted

* A "Null" value indicates that no distribution model passed the *K-S* test.

Qualitative evaluation of the *WFF*s in Figures B.17–B.32 indicates that many distributions have a peak near the origin and decay relatively smoothly with increasing volumetric strain (e.g., PSECTA1), while others display a more nearly lognormal shape (PSECTA2). The "lumping" of the distributions near zero volumetric strain occurs because many shear strain realizations produce zero or nearly zero volumetric strains based on the models presented in Section 7.2.3.

Not surprisingly, Table 7.13 indicates that none of the candidate theoretical distributions passed the *K-S* goodness-of-fit test. Comparisons of the minimum error (D_n) among the distributions for a given section indicate that the shifted-lognormal distribution is the best fit of the volumetric *WFFs*, although even that fit is generally poor.

Somewhat surprisingly, the shifted lognormal, lognormal, and normal distributions often pass the Chi-square test (see Table 7.14), with the shifted lognormal distribution generally providing the best fit to the *WFF*. As shown in Figures B.17–B.32, the shifted lognormal distributions are approximately equivalent to the normal distributions due to the shifted lognormal distribution trying to match the positive skewness of the data sets. However, we do not choose to represent the data with the shifted lognormal distribution because (1) the fit of the data to the model is poor from a qualitative point of view; (2) difficulties were encountered in estimating the median (λ) and standard deviation (σ_{ln}) for this distribution; and (3) the simpler normal distribution represents the data nearly as well as the shifted lognormal distribution. Given all of the above, we choose to describe the distribution of the volumetric strain results with the point estimates of weighted mean (m) and weighted standard deviation (s). These quantities happen to correspond to the statistical moments of a theoretical normal distribution, although it should be emphasized that the data are not normal. The m and s values are presented in Table 7.12.

(b) Interpretation of Trends in the Volumetric Strain Results

Figures 7.28–7.35 show the distributions with depth of the weighted mean ($m_{\varepsilon v}$) and weighted mean ± one standard deviation ($m_{\varepsilon v} \pm s_{\varepsilon v}$) volumetric and shear strains calculated from the 1-D and 2-D analyses for Sites A and B. For reasons discussed above, the $m_{\varepsilon v}$ and $s_{\varepsilon v}$ values for volumetric strain are point estimates of the data in arithmetic units (based purely on the statistics with no assumption of an underlying model), whereas the λ and σ_{ln} values for shear strain are based on a lognormal distribution. In the volumetric strain case, $m_{\varepsilon v}$ -$s_{\varepsilon v}$ profiles are truncated at zero if necessary.

As with the shear strain distributions, volumetric strains generally increase with depth near the surface of the fills, and change sharply at impedance contrasts. The largest volumetric strains generally occur at shallow impedance contrasts or at the base-of-fill. The differences between volumetric strains calculated in 1-D versus 2-D analyses are very similar to those discussed previously for shear strains in Section 7.4.2.

The dispersion of the volumetric strains is affected by the dispersion of the shear strains and the parametric uncertainty in compaction condition. Interestingly, the coefficients of variation (COV) of the shear and volumetric strains are only modestly different, suggesting that the dispersion in shear strains drives the uncertainty in volumetric strains.

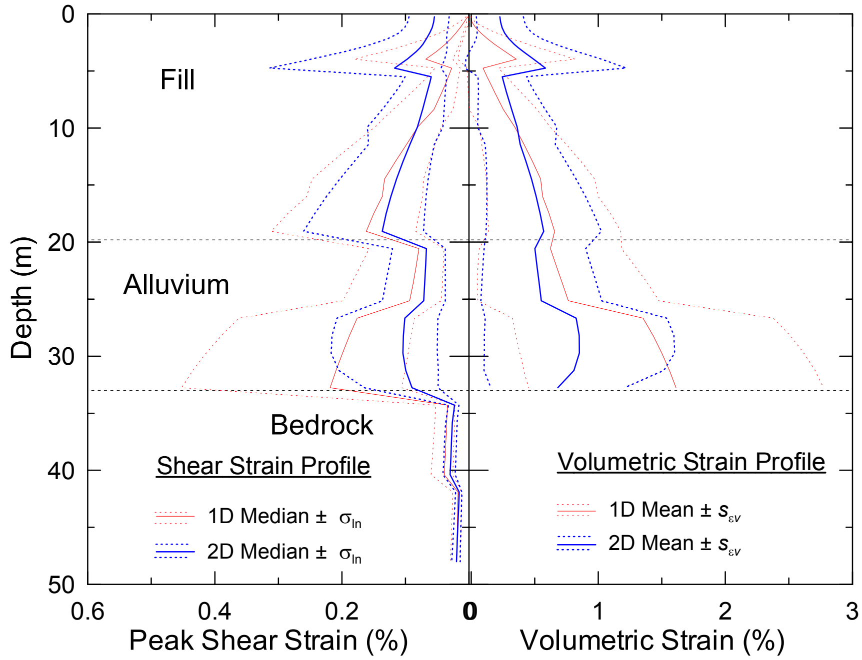

Fig. 7.28. Site A, PSECTA1 shear and volumetric strain profiles from 1-D and 2-D analyses (using lognormal distribution and point estimates, respectively)

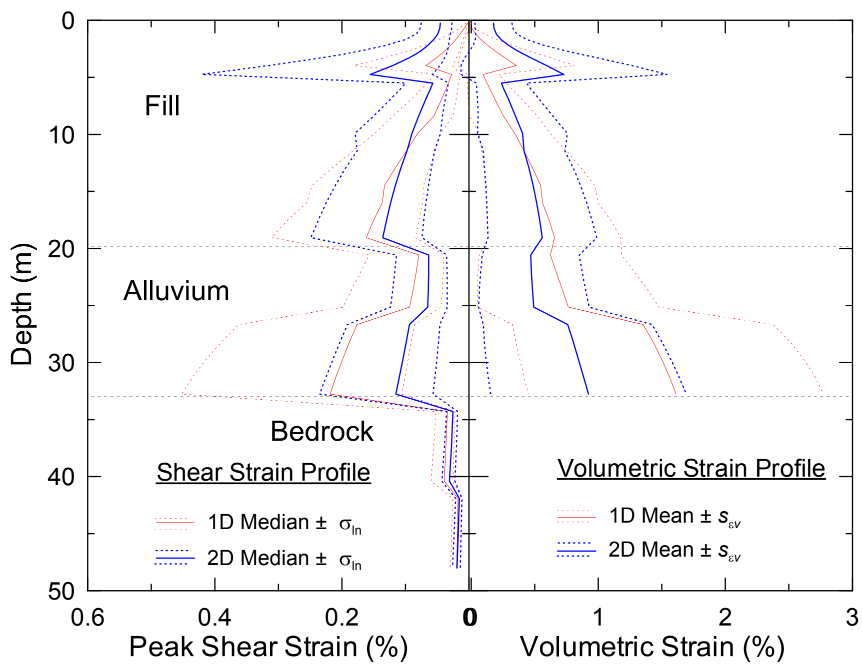

Fig. 7.29. Site A, PSECTA2 shear and volumetric strain profiles from 1-D and 2-D analyses (using lognormal distribution and point estimates, respectively)

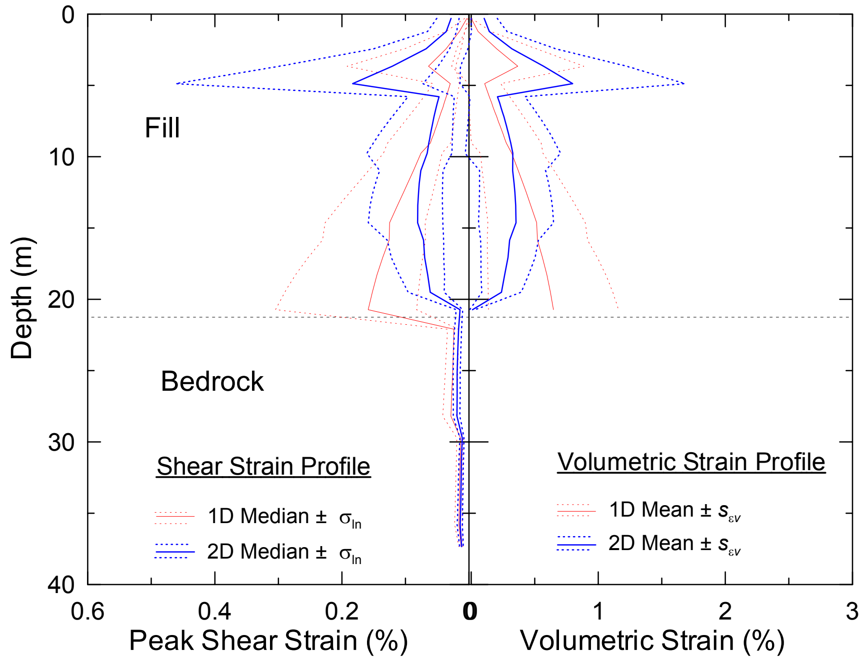

Fig. 7.30. Site A, PSECTB1 shear and volumetric strain profiles from 1-D and 2-D analyses (using lognormal distribution and point estimates, respectively)

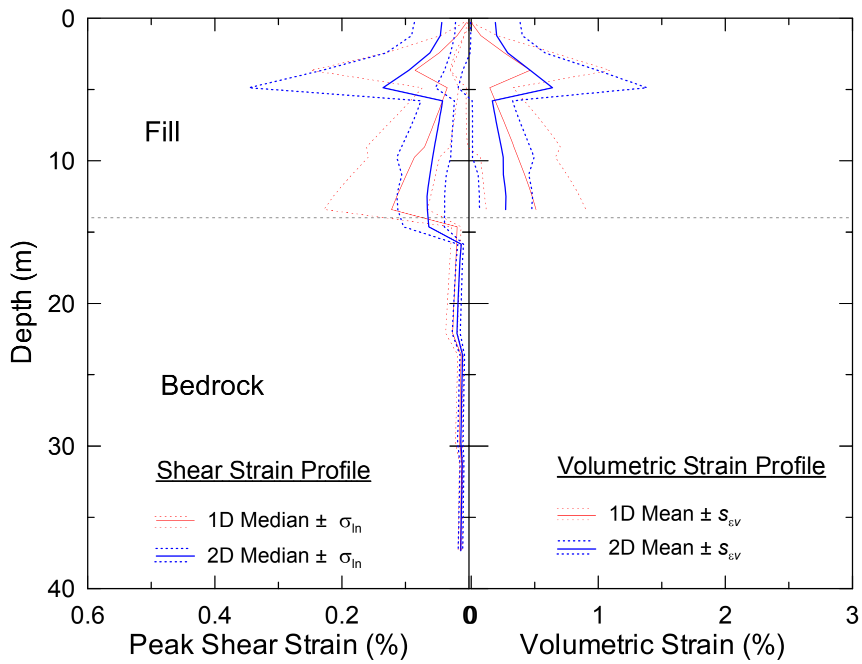

Fig. 7.31. Site A, PSECTB2 shear and volumetric strain profiles from 1-D and 2-D analyses (using lognormal distribution and point estimates, respectively)

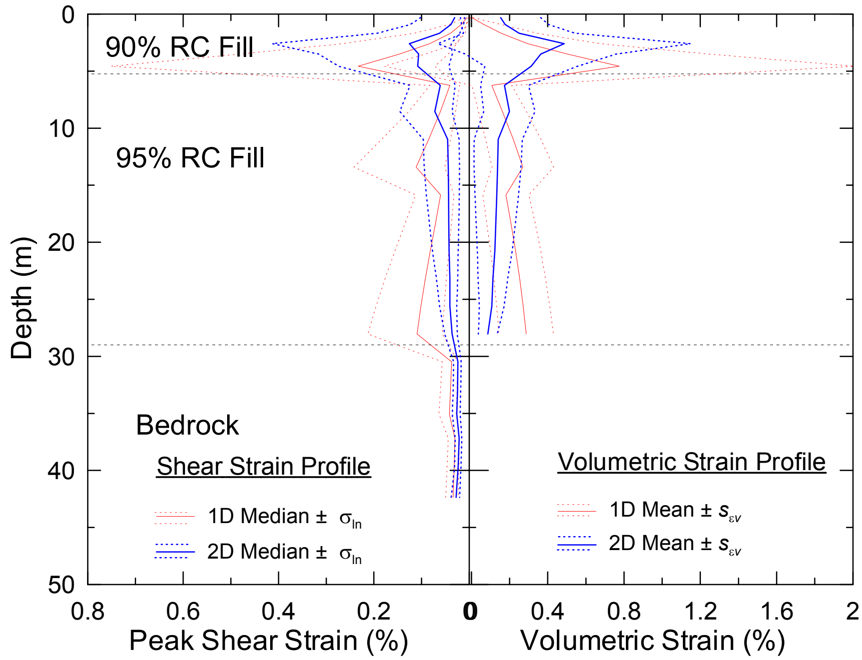

Fig. 7.32. Site B, SSECTA1 shear and volumetric strain profiles from 1-D and 2-D analyses (using lognormal distribution and point estimates, respectively)

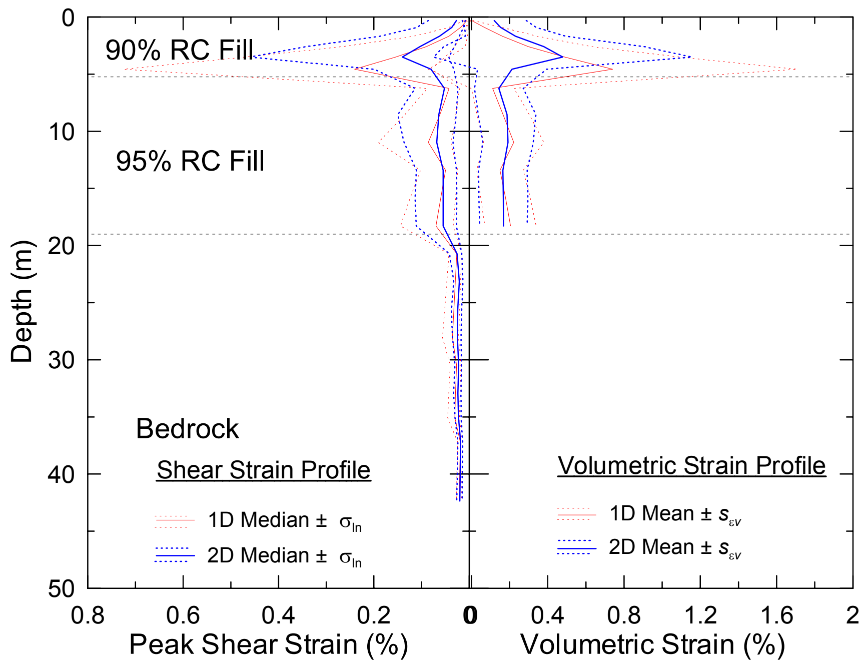

Fig. 7.33. Site B, SSECTA2 shear and volumetric strain profiles from 1-D and 2-D analyses (using lognormal distribution and point estimates, respectively)

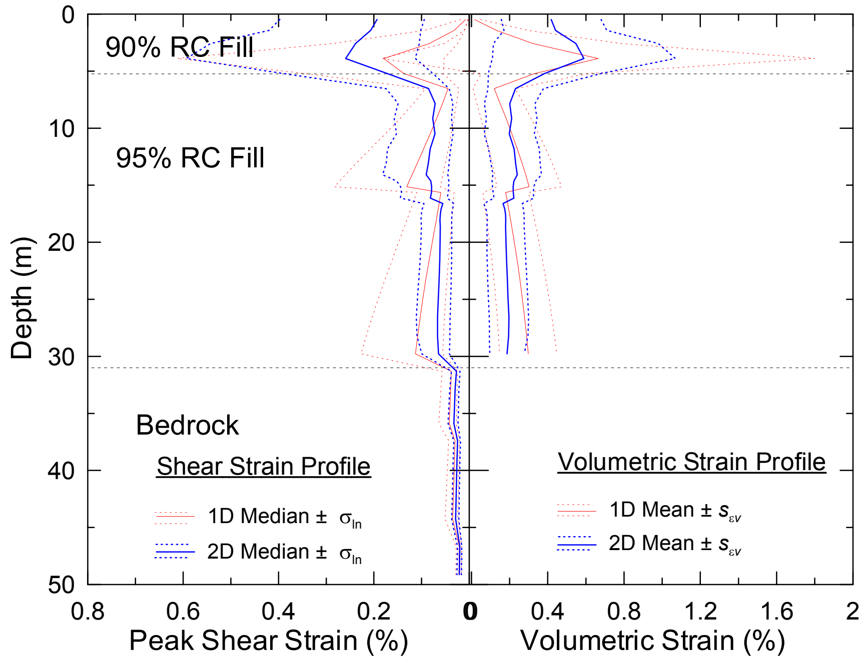

Fig. 7.34. Site B, SSECTB1 shear and volumetric strain profiles from 1-D and 2-D analyses (using lognormal distribution and point estimates, respectively)

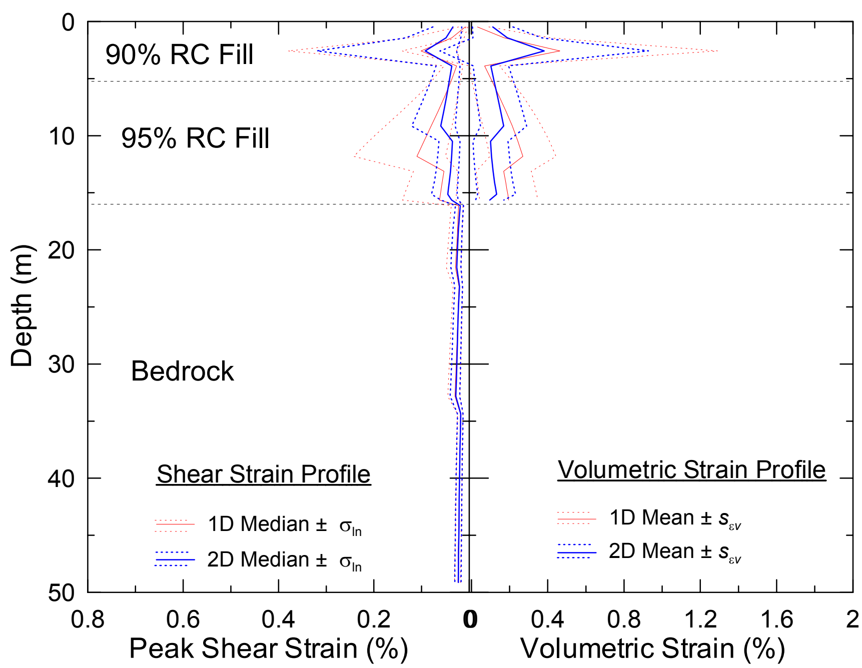

Fig. 7.35. Site B, SSECTB2 shear and volumetric strain profiles from 1-D and 2-D analyses (using lognormal distribution and point estimates, respectively)

7.4.4 Comparison of Predicted and Observed Settlements

Shown in Figures 7.36–7.39 are the estimated / observed settlements along Sections A-A and B-B at Sites A and B (originally presented in Section 3.4) along with settlements calculated from 2-D and 1-D analyses. The Site A settlements shown in Figures 7.36–7.37 are the difference between the settlements evaluated from the 1991 and 1994 surveys and the estimated settlements from hydro-compression over this time interval (see Section 3.4.1 for details). The × symbols in the figures indicate the best estimate of seismically induced settlement, whereas the vertical lines drawn through the settlement values reflect the variability in the estimated hydro-compression settlements. The Site B settlements shown in Figures 7.38–7.39 are the directly measured values.

The calculated settlement quantities are presented as weighted mean (m_Δ) and mean ± one standard deviation ($m_\Delta \pm s_\Delta$) values in arithmetic units. This mimics the above presentation of results for volumetric strain, which is related to settlement through simple integration over soil depth. Settlement predictions derived from the 2-D ground response analyses are presented as continuous curves, whereas 1-D predictions are shown by discrete symbols. The field settlements are compared to calculated settlements in Table 7.15 for the selected locations discussed in previous sections (i.e., the horizontal locations along the sections represented by the PSECT and SSECT points shown in Figures 7.24–7.25).

Table 7.15. Calculated and estimated / observed field settlements at Sites A and B

	1D Analyses			2D Analyses			
Location	Weighted Average (cm)	Standard Deviation (cm)	Coeff. Of Variation	Weighted Average (cm)	Standard Deviation (cm)	Coeff. Of Variation	Field Sett. (cm)
PSECTA1	23.2	18.9	0.81	17.3	11.0	0.64	16-21[1]
PSECTA2	23.2	18.9	0.81	17.4	11.0	0.64	*
PSECTB1	7.8	6.8	0.87	6.5	4.6	0.71	*
PSECTB2	4.3	4.4	1.03	4.2	3.3	0.79	6
SSECTA1	7.0	5.8	0.83	4.3	2.8	0.65	5.3
SSECTA2	4.2	4.0	0.97	3.7	2.4	0.64	2.3
SSECTB1	7.5	5.9	0.78	8.5	3.9	0.45	6.1
SSECTB2	2.9	3.0	1.02	2.2	1.5	0.67	1.5

*Settlement for this section could not be reasonably estimated.
[1]Settlement at this location estimated based on nearby measurements (at edge of building).

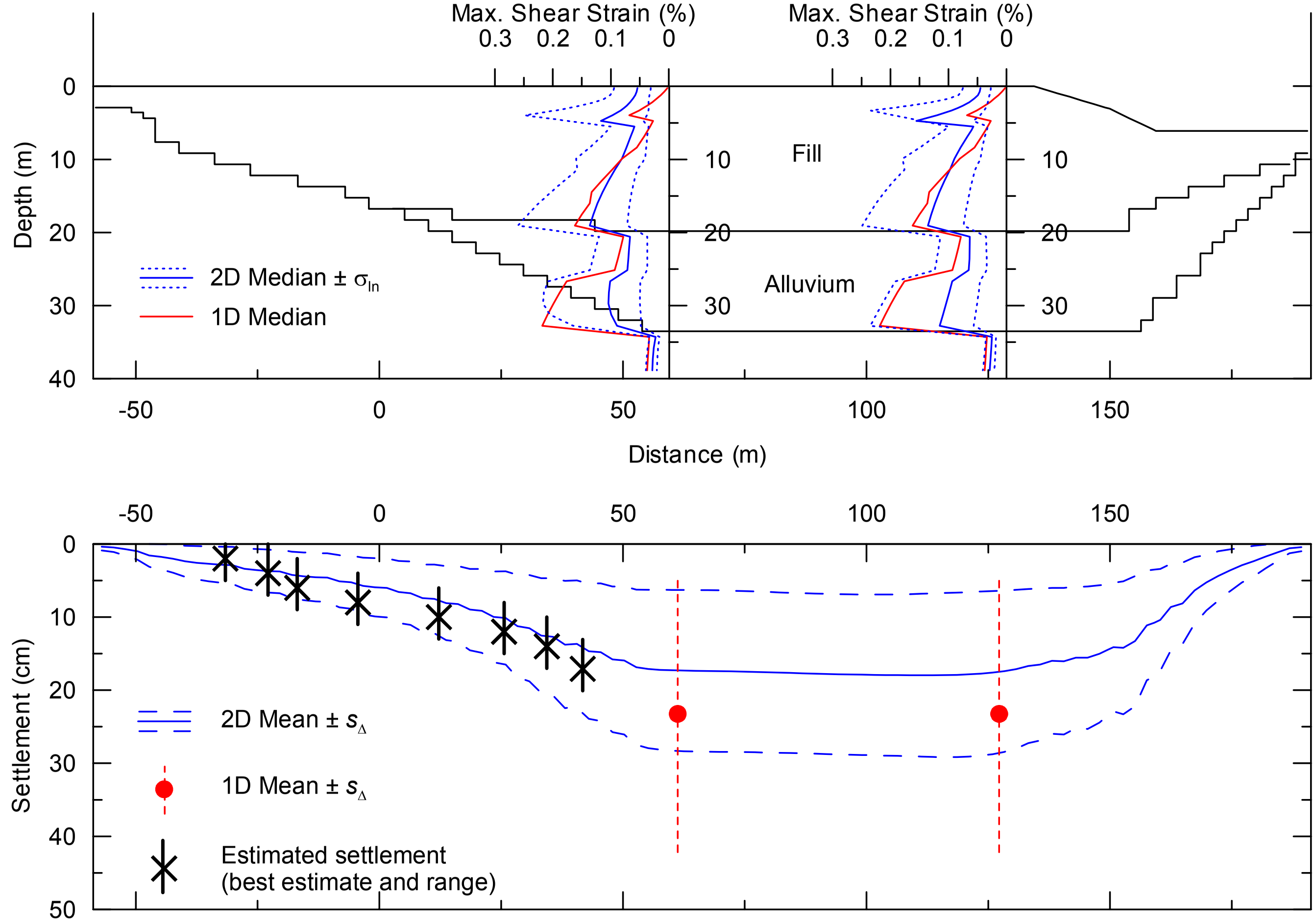

Fig. 7.36. Site A, Section A-A', vertical profiles of shear strain and lateral profiles of estimated and calculated settlement

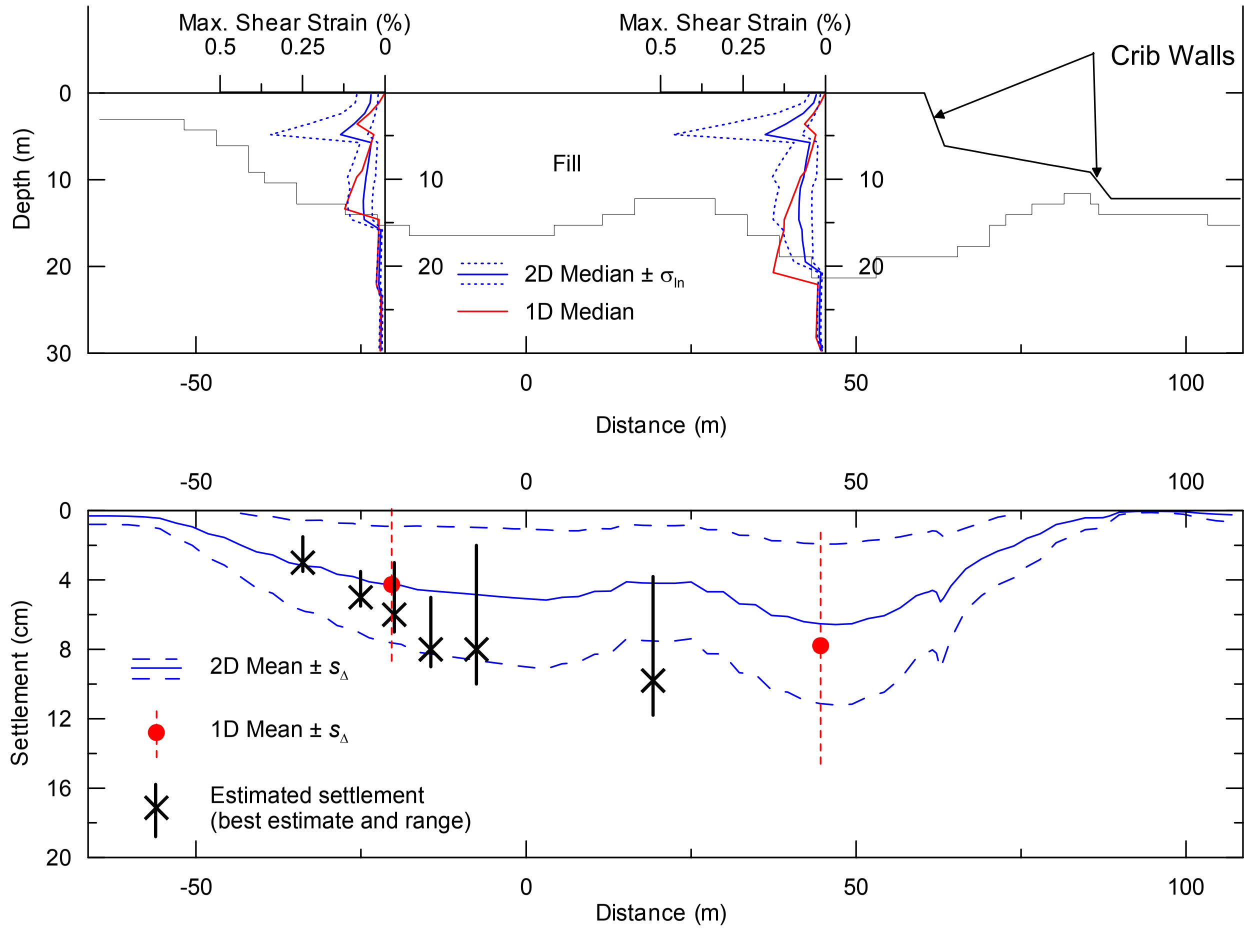

Fig. 7.37. Site A, Section B-B', vertical profiles of shear strain and lateral profiles of estimated and calculated settlement

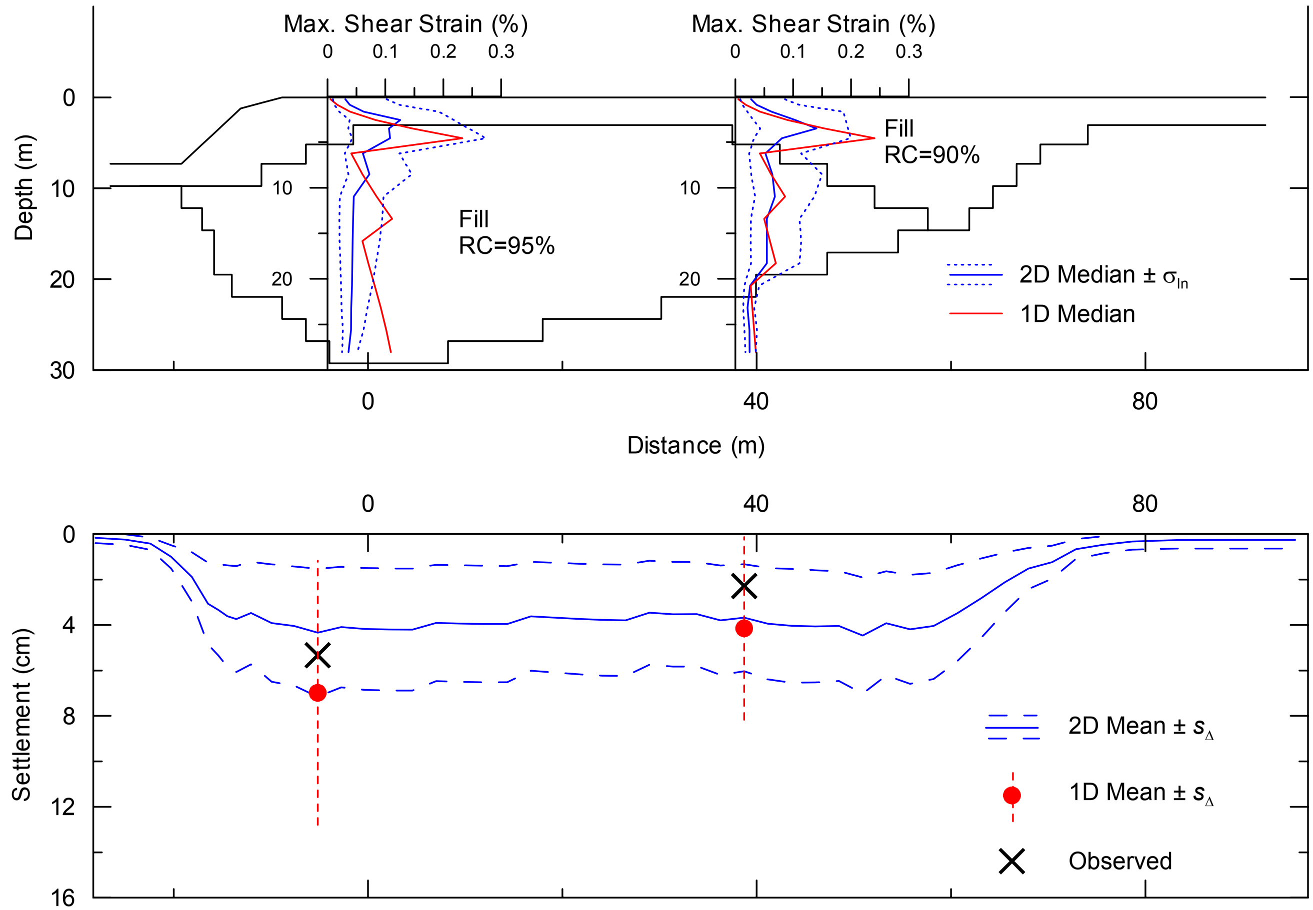

Fig. 7.38. Site B, Section A-A', vertical profiles of shear strain and lateral profiles of observed and calculated settlement

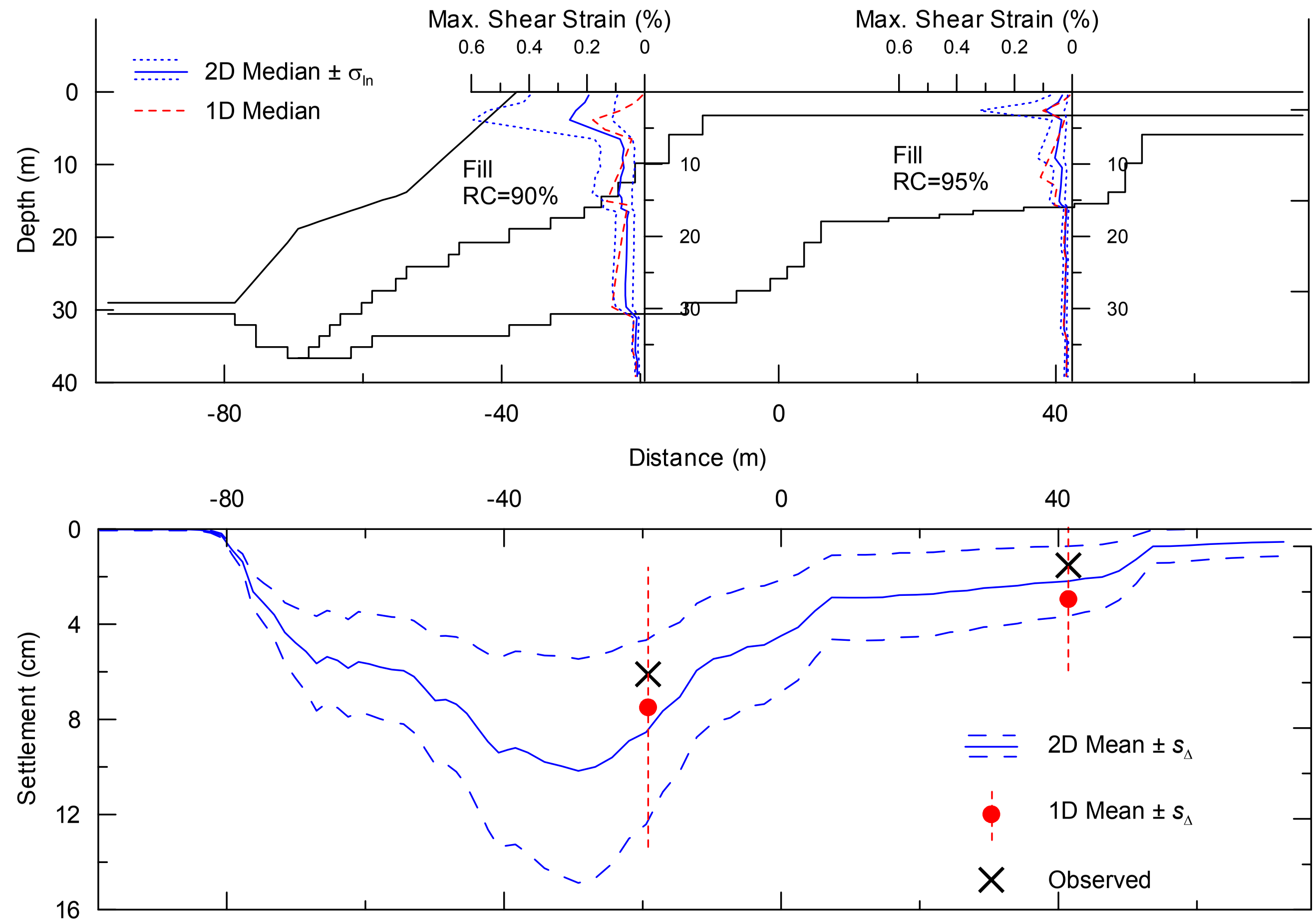

Fig. 7.39. Site B, Section B-B', vertical profiles of shear strain and lateral profiles of observed and calculated settlement

For Site A Section A-A (Figure 7.36), the mean settlement predictions from the 2-D analyses generally underpredict "best estimate" field settlements, although the trend of the calculated settlements along the section is consistent with observation. The estimated settlements are generally consistent with about the 50th–70th percentile of calculated settlements. There are several plausible explanations for this apparent bias in the mean:

1. The location and depth of the alluvium along the left (north) side of the section is not well known (drilling to identify alluvial depth in this area was not possible because it is overlain by a structure). The location of the edge of alluvium shown in Figure 7.36 is assumed based on top-of-alluvium elevations from boreholes south of the building. However, because the section passes up through a natural canyon (see Figure 3.2a), it is possible that alluvium extends further up the canyon, and that this alluvium contributed additional seismic compression not accounted for in our analyses.
2. The shear-volumetric strain relationship used for the fill may contain bias related to larger clods in the field than in the laboratory-prepared specimens. The tendency of the Site A soils to form clods was documented in Chapter 5. Laboratory specimens were prepared with controlled clod sizes by use of sieving. Larger clods would be expected in the field, which would lead to larger inter-clod void space and thus potentially greater seismic compression susceptibility.

The contribution of alluvium to the calculated settlements along Section A-A' ranges from null (where alluvium is absent) to about 50% (between distance stations 50 m and 150 m). Due to the significant contribution of the alluvium to the settlements in this portion of the site, and uncertainty regarding soil fabric effects on volumetric strains in alluvium (which may introduce unknown bias into our analysis results), we have less confidence in calculated settlements for these portions of the site underlain by significant thicknesses of alluvium.

Mean settlements for Section B-B' at Site A (Figure 7.37) are more significantly underpredicted between distance stations -25 m and 25 m than those for A-A'. This local underprediction is likely due to the presence of alluvium near the base of the section (see Item 1 above) and the possible removal of the bedrock "ridge" near station 25 m during site grading (which would significantly increase fill thicknesses and thus settlement in that area).

For Site B (Figures 7.38–7.39), the settlement predictions from 2-D analyses generally compare favorably to observation. The observed settlements are between the 30th and 70th

percentile predictions, and the comparisons are generally suggestive of no systematic bias in model predictions.

For Site A, the estimated settlements derived from 1-D and 2-D analyses differ significantly. The 1-D settlements are larger for Section A-A (Figure 7.36) because 1-D analyses do not restrain shear strains at depth, which occurs in the 2-D analyses as a result of the bowl-shaped bedrock-soil interface. For Section B-B, the 1-D and 2-D settlements are similar as a result of compensating differences, i.e., 2-D volumetric strains exceed 1-D near the surface of the fills, while 1-D exceeds 2-D near the base. A similar compensating effect occurs at the locations considered for Site B, which causes the 1-D and 2-D settlement predictions to be similar.

As shown in Table 7.15, coefficients of variation on the settlement quantities from the 2-D analysis range from about 0.5 to 0.7. Larger COVs of 0.8 to 1.0 are obtained from the 1-D analyses.

7.4.5 Analysis Results for Peak Horizontal Acceleration (*PHA*)

(a) Identification of Optimum Theoretical Model for Distribution of PHA

Peak horizontal accelerations (*PHA*) and *PHA* amplification ($PHA_{surface}/PHA_{input}$) along the surface of the sections at Sites A and B were compiled from the analysis results, and the statistical distributions of those parameters were investigated. The locations used for these tests are the points on the ground surface above the locations identified in Figures 7.24–7.25. Table 7.16 shows for these locations the point estimates of *PHA* calculated using Eqs. 7.23–7.25. Weighted frequency functions (*WFFs*) and candidate theoretical cumulative distribution functions for *PHA* are plotted by Smith (2002). Results of the *K-S* and Chi-square goodness-of-fit tests are summarized in Tables 7.17 and 7.18, respectively.

Table 7.16. Point estimates of *PHA* at selected surface locations, Sites A and B

Site	Analysis Type	Location	Weighted Avg. (g)	Std. Dev. (g)	Coeff. of Variation	Skewness Coeff.
A	2-D	Psecta1	0.496	0.139	0.281	-0.122
		Psecta2	0.595	0.204	0.342	0.149
		Psectb1	0.633	0.247	0.390	0.004
		Psectb2	0.609	0.253	0.415	0.095
	1-D	Psecta1	0.447	0.127	0.284	0.107
		Psecta2	0.447	0.127	0.284	0.107
		Psectb1	0.485	0.159	0.329	0.146
		Psectb2	0.563	0.233	0.414	0.256
B	2-D	Ssecta1	0.881	0.393	0.446	0.310
		Ssecta2	0.990	0.470	0.475	0.271
		Ssectb1	0.761	0.309	0.406	0.549
		Ssectb2	0.776	0.360	0.464	0.395
	1-D	Ssecta1	0.752	0.299	0.398	0.370
		Ssecta2	0.807	0.364	0.451	0.376
		Ssectb1	0.778	0.307	0.394	0.257
		Ssectb2	0.856	0.425	0.497	0.333

Table 7.17. *K-S* test results for *PHA* distribution

Site	Analysis Type	Location	Distribution Model D_n Values: Normal	Log-normal	Shift. Log-normal	Type II	D_n^α Reference Value	Best Fit*
A	2-D	psecta1	0.077	0.125	0.999	0.215	0.075	Null
		psecta2	0.091	0.106	0.09	0.16	0.075	Null
		psectb1	0.084	0.133	0.084	0.189	0.075	Null
		psectb2	0.071	0.113	0.071	0.188	0.075	Normal
	1-D	psecta1	0.05	0.084	0.053	0.134	0.075	Normal
		psecta2	0.05	0.084	0.053	0.134	0.075	Normal
		psectb1	0.065	0.111	0.069	0.19	0.075	Normal
		psectb2	0.075	0.111	0.069	0.182	0.075	Shifted
B	2-D	ssecta1	0.13	0.16	0.13	0.25	0.075	Null
		ssecta2	0.135	0.154	0.131	0.253	0.075	Null
		ssectb1	0.082	0.112	0.086	0.188	0.075	Null
		ssectb2	0.131	0.138	0.124	0.234	0.075	Null
	1-D	ssecta1	0.077	0.1	0.077	0.172	0.075	Null
		ssecta2	0.104	0.121	0.098	0.211	0.075	Null
		ssectb1	0.078	0.113	0.08	0.184	0.075	Null
		ssectb2	0.129	0.145	0.124	0.251	0.075	Null

* A "Null" value indicates that no distribution model passed the *K-S* test.

Table 7.18. Chi-square test results for *PHA* distribution

Site	Analysis Type	Location	Distribution Model *E* Values: Normal	Log-normal	Shift. Log-normal	Type II	$c_{1-\alpha,f}$ Reference Value	Best Fit
A	2-D	psecta1	36	98	10633	202	370	Normal
		psecta2	109	102	114	302	370	Log
		psectb1	87	182	83	346	370	Shifted
		psectb2	93	132	57	343	370	Shifted
	1-D	psecta1	35	59	44	109	370	Normal
		psecta2	35	59	44	109	370	Normal
		psectb1	50	136	58	253	370	Normal
		psectb2	82	95	77	321	370	Normal
B	2-D	ssecta1	173	155	149	584	370	Shifted
		ssecta2	139	164	140	587	370	Normal
		ssectb1	140	64	106	316	370	Log
		ssectb2	119	108	117	504	370	Log
	1-D	ssecta1	76	75	86	269	370	Log
		ssecta2	99	103	103	449	370	Normal
		ssectb1	90	84	91	322	370	Log
		ssectb2	154	125	130	559	370	Log

Table 7.16 shows that *PHA* results for Sites A and B have a positive skewness coefficient (skewed to the left). Table 7.17 indicates that few of the candidate theoretical distributions passed the *K-S* goodness-of-fit test, but the minimum error (D_n) among the distributions considered was generally associated with the normal distribution for Sites A and B. Similar results were found from the Chi-square goodness-of-fit tests, which are shown in Table 7.18. For the sake of consistency, we adopt a normal distribution model to represent the *PHA* at Sites A and B. Moments of this distribution are the point estimates listed in Table 7.16. Corresponding point estimates of the *PHA*-amplification are presented in Table 7.19. These distributions of *PHA* amplification are also assumed to be approximately normally distributed.

Table 7.19. Point estimates of *PHA* amplification at selected locations, Sites A and B

Site	Analysis Type	Location	Median (λ)	Std. Dev. (σ)
A	2-D	Psecta1	1.57	0.56
		Psecta2	1.87	0.73
		Psectb1	1.97	0.91
		Psectb2	1.90	0.91
	1-D	Psecta1	1.43	0.58
		Psecta2	1.43	0.58
		Psectb1	1.53	0.64
		Psectb2	1.76	0.85
B	2-D	Ssecta1	1.86	0.94
		Ssecta2	2.08	1.11
		Ssectb1	1.60	0.73
		Ssectb2	1.64	0.86
	1-D	Ssecta1	1.60	0.75
		Ssecta2	1.70	0.88
		Ssectb1	1.65	0.77
		Ssectb2	1.80	1.02

(b) Interpretation of Trends in the PHA and PHA Amplification Results

The distribution of the mean (μ) and mean ± one standard deviation ($\mu \pm \sigma$) of *PHA* along the surface of the fill are presented in Figures 7.40 through 7.43. Results are presented for both the 2-D and 1-D analyses. Also shown in these figures are the calculated *PHA* amplification levels based on the 2-D analysis results.

The largest mean *PHA* from the 2-D analyses for Site A are near the crest of the slope for Section A-A (μ= *0.60 g*) and near the crib walls for Section B-B (μ = *0.79 g*). These maximum *PHA* values are amplified relative to the mean input *PHA* = 0.33g by factors of approximately 1.9 at the crest of Section A-A and 2.4 near the crib walls for Section B-B. For Site B, the largest mean *PHA*s from the 2-D analyses are seen near the crest of the slopes of Section A-A (μ= *1.00 g*) and Section B-B (μ= *1.12 g*). These maximum *PHA* values are amplified relative to the median input of *PHA* = 0.50g by factors of approximately 2.1 at the slope crest in Section A-A and 2.3 at the slope crest in Section B-B.

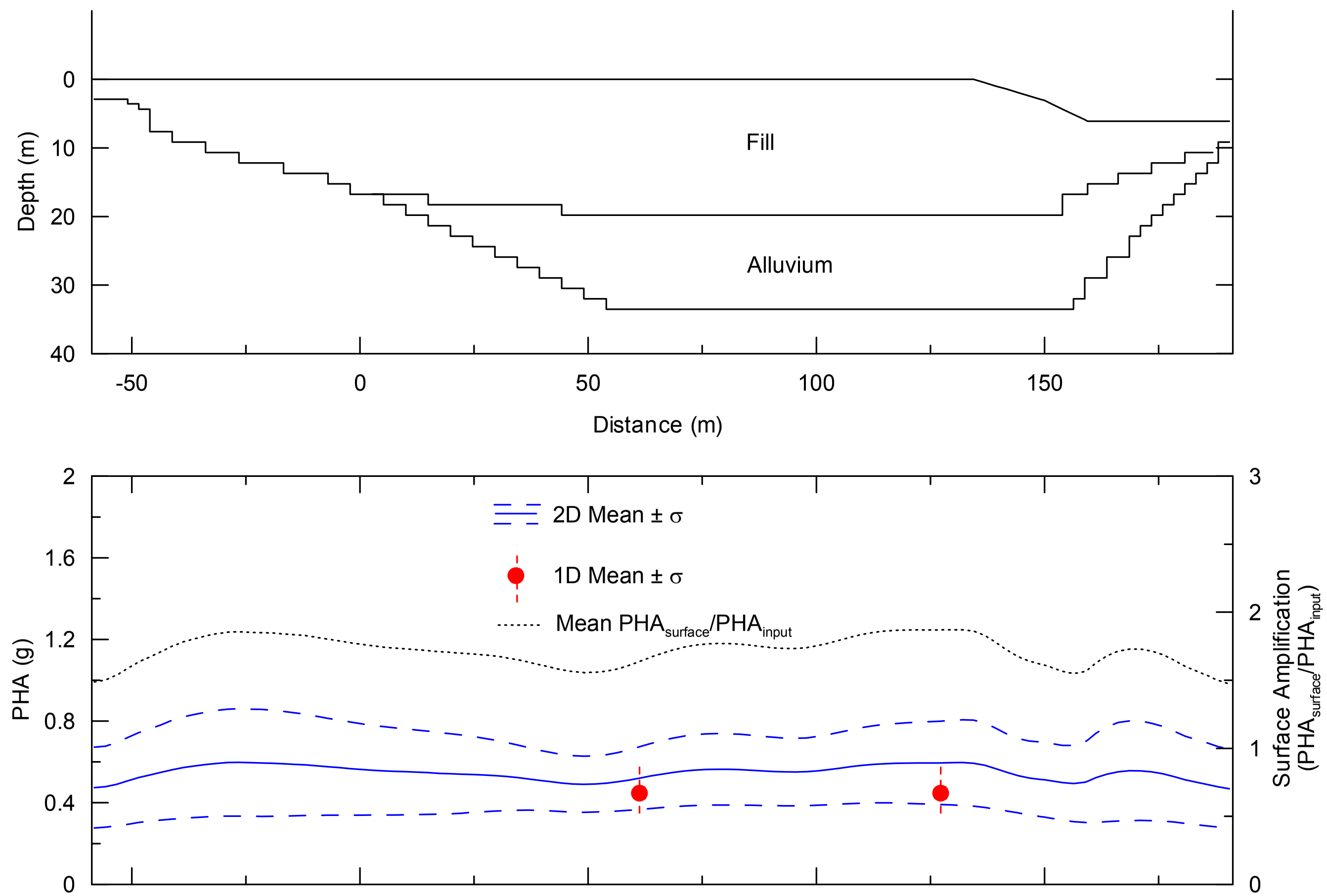

Fig. 7.40. Site A, Section A-A', variation of *PHA* and *PHA* amplification along section

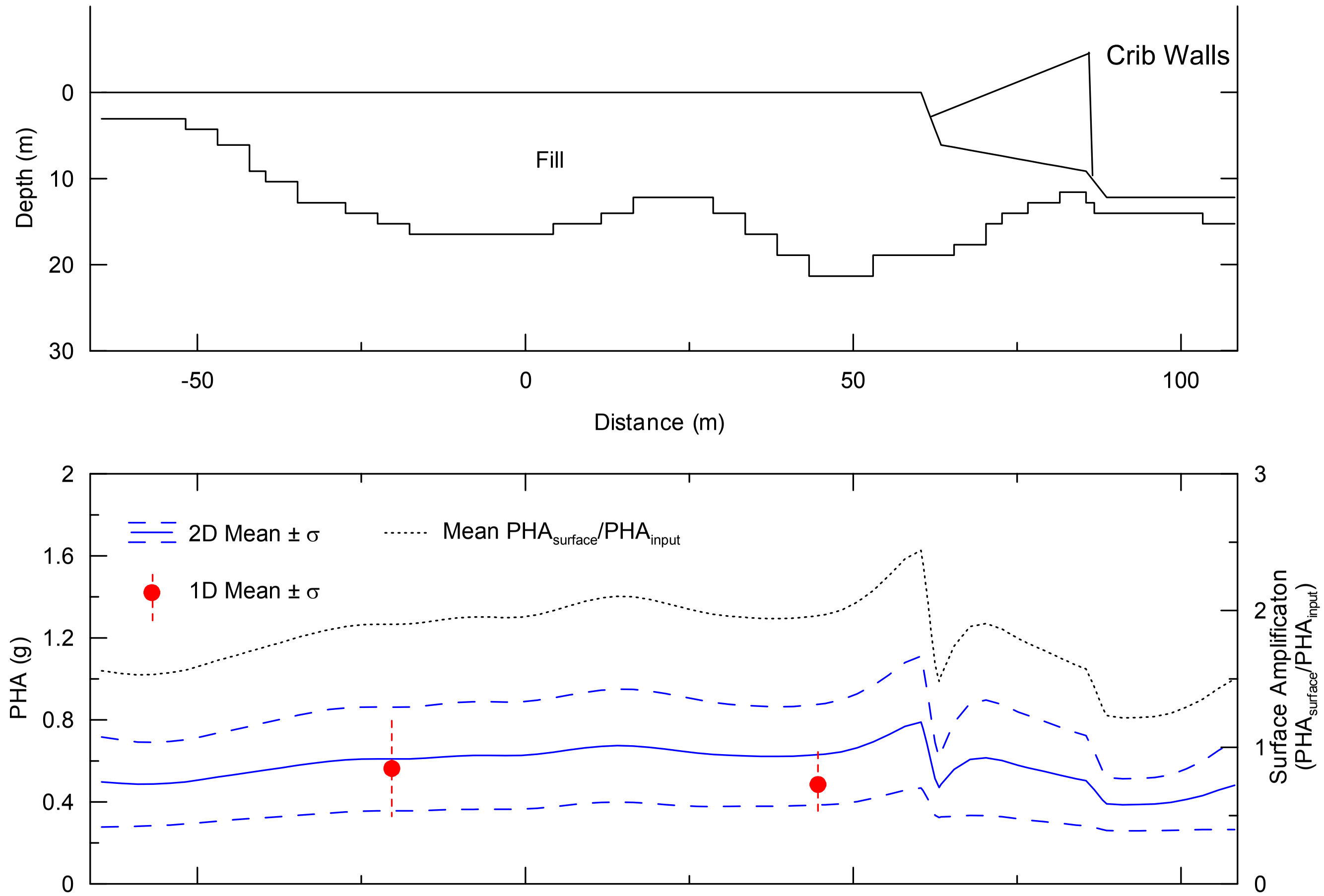

Fig. 7.41. Site A, Section B-B', variation of *PHA* and *PHA* amplification along section

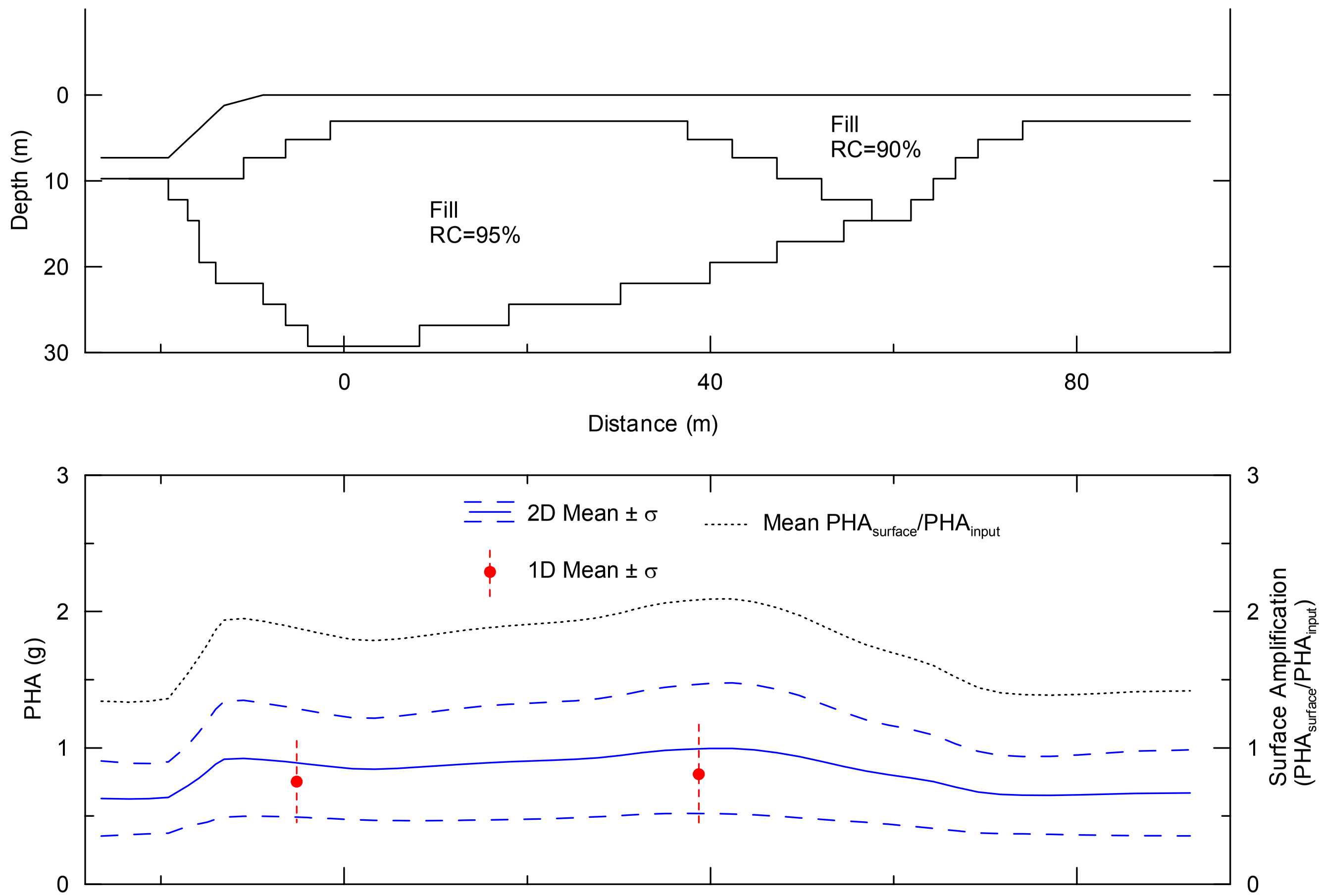

Fig. 7.42. Site B, Section A-A', variation of *PHA* and *PHA* amplification along section

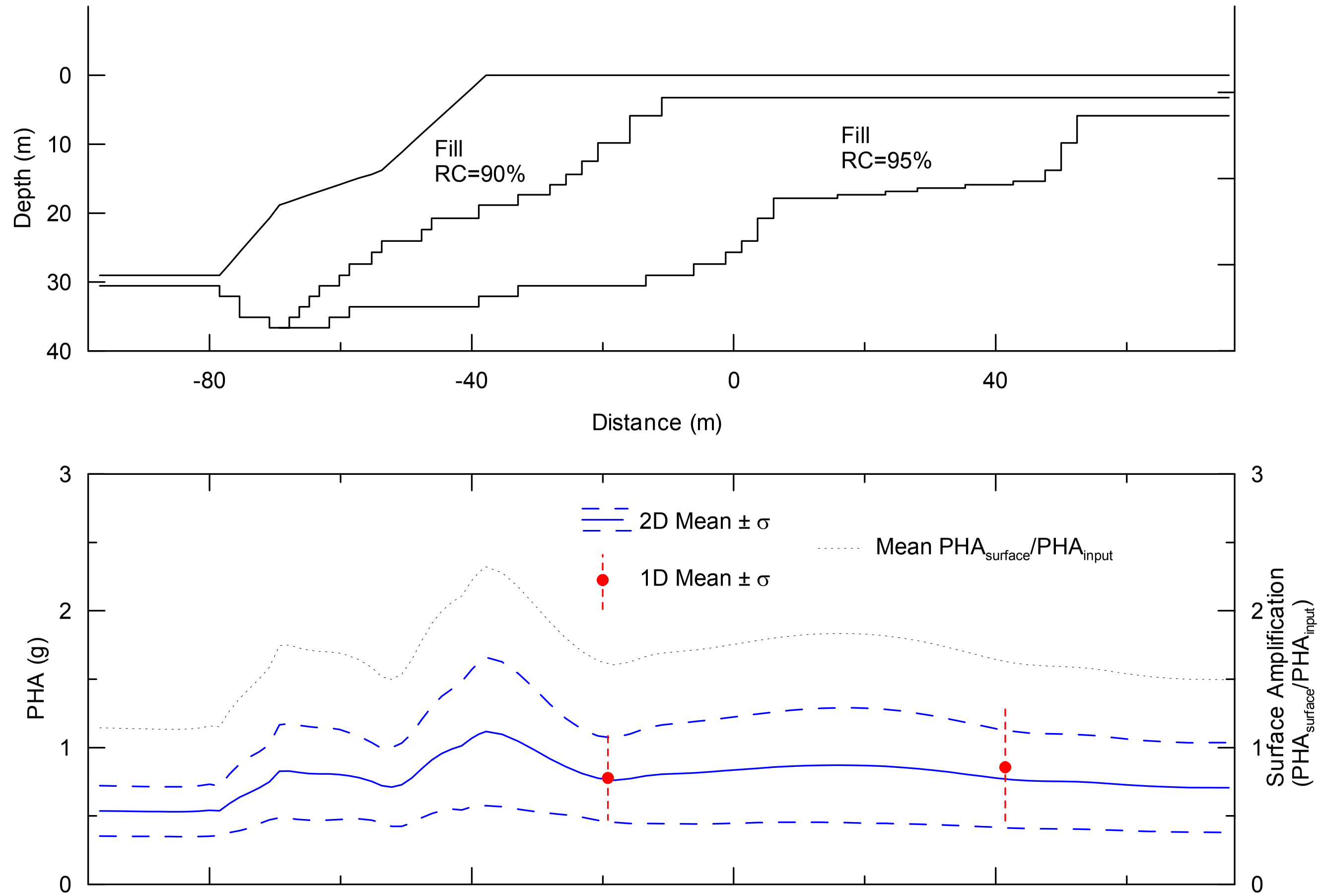

Fig. 7.43. Site B, Section B-B’, variation of *PHA* and *PHA* amplification along section

The amplification of slope crest accelerations (where topographic effects would be expected) relative to portions of the fill removed from the crest (where topographic effects should be absent) can be compared to topographic amplification models by Ashford et al. (1997). These models apply for single-sided slopes having a geometry similar to that present at the subject sites, and relate amplification levels to slope angle, the vertical angle of incident body waves, and a normalized frequency parameter. Amplification in the models is maximized for steep slopes whose height is approximately 20% of the wavelength (wavelength=$V_s \times T$, where V_s = shear wave velocity and T = period) of the incident wave field, and for waves propagating into the slope. The topographic amplification of crest accelerations from our 2-D analyses are compared in Table 7.20 to those from the Ashford et al. model (applied for vertically propagating incident waves). Our factors are slightly larger than those from Ashford et al., which may be related to nonvertically propagating incident waves.

Table 7.20. Crest amplification of *PHA* from topographic effects, Sites A and B

			Crest Amplification	
Section	Slope Height (m)	Slope Angle (degrees)	2-D analyses (this study)	Ashford et al. model (Vert. Incidence)
A-A	6.1	13.7	1.2 ± 0.28	1.0-1.1
B-B	12.2	24.3	1.3 ± 0.27	1.0-1.1
A-A	7.3	35.2	1.2 ± 0.19	1.0-1.2
B-B	29	35.5	1.4 ± 0.30	1.0-1.2

8 Sensitivity of Analysis Results to Parametric Variability

8.1 INTRODUCTION

In Chapter 7 we compared the observed settlements at two sites strongly shaken by the 1994 Northridge earthquake to predictions from back-analysis. Peak shear strains ($\gamma_{pk} = \gamma_{eff}/0.65$) were estimated using 1-D and 2-D ground response analyses, and these shear strains were then used to estimate profiles of volumetric strain (ε_v), which were integrated across the depth of fill to estimate settlements. Each of the parameters that enter the analysis has both aleatory and epistemic uncertainties, which were estimated for the purpose of these analyses in Section 7.3. The effects of these uncertainties on the analysis results were addressed using a logic tree approach in which parameter spaces were discretized and weighted with respect to their likelihood of occurrence. Each branch of the logic tree produced estimates of shear strain, volumetric strain, and settlement, and also produced weights associated with those estimates. The analysis results and their associated frequencies were analyzed to develop weighted frequency functions (*WFF*s) from which point estimates (e.g., weighted means and standard deviations) were calculated. The point estimates and *WFF*s were then used to identify the theoretical probability density function that best represents the distribution of γ_{pk} and ε_v at specific locations. The presentation of the results in this manner enabled the estimated / observed field settlements to be compared to distributions of calculated settlement. By comparing to field settlements, the calculated settlements were found to be unbiased for Site B, but biased low at Site A. Several possible explanations for the Site A bias are provided in Section 7.4.4. The dispersion of the calculated settlements was large, as measured by coefficients of variation, COV, on the order of 0.5 to 1.0.

In this chapter we further examine the analysis results to identify the sources of parametric variability that most significantly affect the computed shear and volumetric strains. The effects of parametric variability are assessed two ways:

- We identify the influence of parametric variability on the mean/median of the analysis results. For γ_{pk}, the median analysis result is considered, and is denoted as λ in arithmetic units (evaluated from Eq. 7.30). For ε_v, the mean analysis result is considered, and is denoted as $m_{\varepsilon v}$ (Eq. 7.23). The effect of parametric variability on the mean/median is of obvious practical interest because misidentification of a parameter to which the analysis results are sensitive would bias the mean/median. In design, it would be of utmost importance to properly characterize such parameters.
- We identify the effect of parametric variability on the dispersion of the analysis results. This is of practical interest because the larger the dispersion of an analysis result, the larger the number of analysis runs that is required to develop a statistically stable estimate of the mean/median. In a forward analysis (i.e., design), if this dispersion can be minimized by high-quality characterization of specific input parameters (and hence minimization of their parametric variability), one could then streamline computation time and have more confidence in the analysis results. For the purpose of this discussion, dispersion of γ_{pk} is parameterized by the standard deviation in natural log units (σ_{ln}, defined in Eq. 7.31) and dispersion of ε_v is parameterized by coefficient of variation, COV = $s_{\varepsilon v}/m_{\varepsilon v}$.

The chapter is organized into separate sections on shear and volumetric strain (Sections 8.2 and 8.3 respectively). These strains are examined for specific locations within the fill cross sections at Sites A and B, which are shown in Figures 7.24–7.25. In the sections that follow for shear and volumetric strain, the randomized input parameters are identified, and the results of 2-D ground response analyses are presented either for fixed values of the input parameter or for a narrow range of the input parameter space. In essence, this approach allows the analysis results to be interpreted for situations in which there is nearly perfect knowledge of the fixed input parameter (no uncertainty or randomness). We conclude in Section 8.4 by interpreting the results to formulate recommendations for design practice in terms of where parameter specification resources could be most effectively directed for forward analyses of seismic compression.

8.2 PARAMETRIC VARIABILITY OF CALCULATED SHEAR STRAINS

A number of factors affect the peak shear strain that is calculated for a particular location within a soil profile. The most significant of these are the input ground motion time history, the dynamic properties of the soil and underlying rock, and the method of analysis. It should be noted that we are concerned here only with the amplitude of shear strain as measured by the peak value, γ_{pk}. The number of strain cycles is considered in the volumetric strain analysis. The frequency content of shear strain time histories is not of direct interest for the calculation of volumetric strain at a point (although frequency content would affect the variation of strain in space, and hence settlement).

For the purpose of these sensitivity analyses, ground motions are parameterized by their amplitudes as measured by peak horizontal acceleration (*PHA*) and peak horizontal velocity (*PHV*), and by their frequency content as measured by mean period (T_m). The dynamic soil properties for which parametric variability was considered are the shear wave velocity (V_s) profiles and the models for modulus reduction and damping curves (variations of G/G_{max} and β with shear strain). The methods of analysis that are considered are 1-D and 2-D ground response analyses as implemented in the codes SHAKE91 (Idriss and Sun, 1991) and QUAD4M (Hudson et al., 1994). The effect of 1-D versus 2-D analyses on the computed shear strains was discussed previously in Section 7.4 and is not repeated here. The following is focused on the effects of the ground motion parameters and site parameters on the results of 2-D analyses.

Complete results of the sensitivity analyses are presented for each of the four considered locations at Site A in Figures 8.1–8.4 and at Site B in Figures 8.5–8.8. Each of the figures contains four frames that show results for "fixed" values of modulus reduction/damping curves, shear wave velocity profiles, and ground motion parameters. The values of the fixed parameters are indicated in the left margins of the figures. The results for each fixed value of a parameter are presented as a horizontal line with a circle at the median (λ) of γ_{pk} and dashes at $\exp[\ln\lambda \pm \sigma_{ln}]$. To the right of each line is written the corresponding value of dispersion, σ_{ln}.

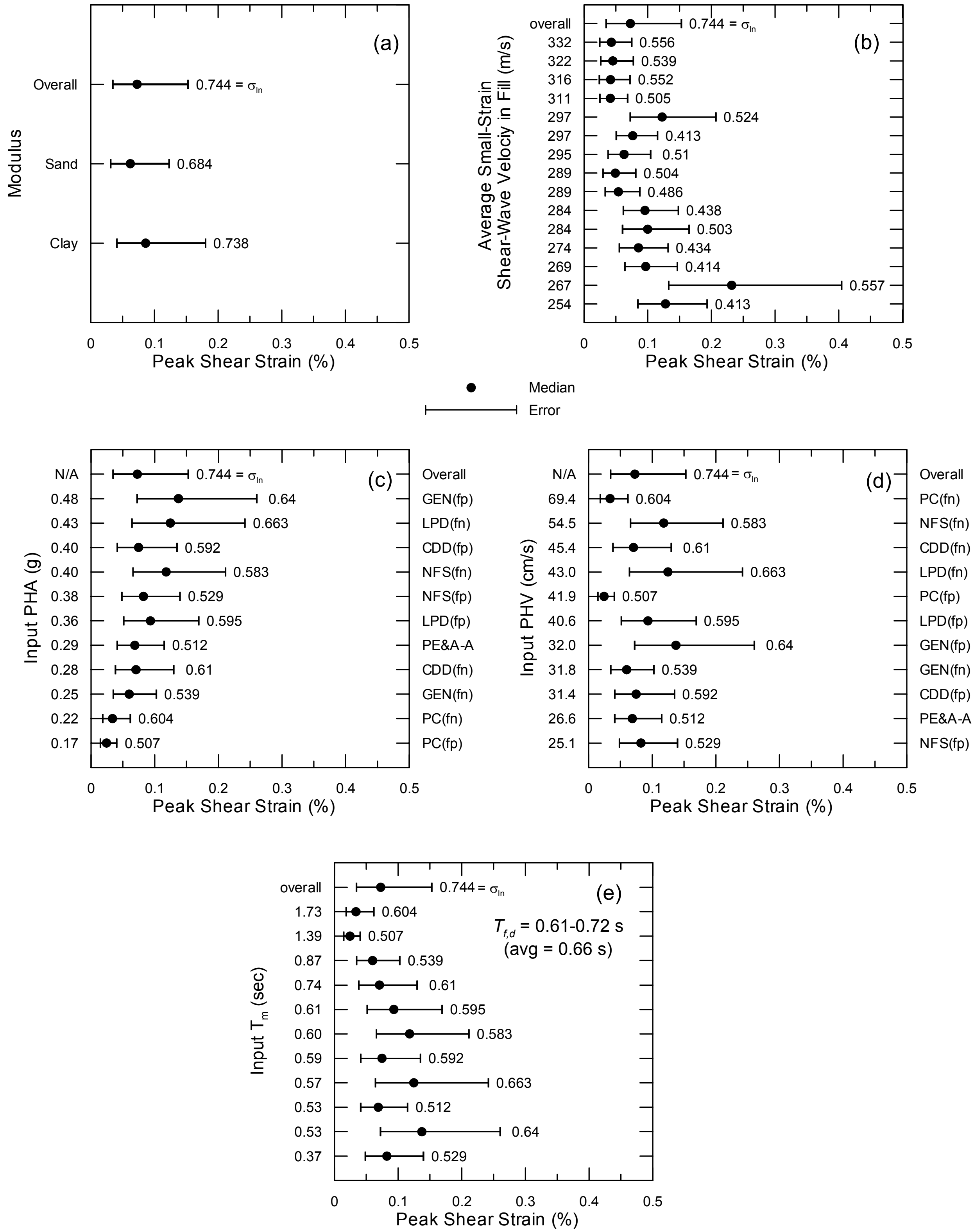

Fig. 8.1. **Site A, PSECTA1 (2-D analysis, depth=2.7m). Variability of γ_{pk} with (a) modulus reduction and damping curves; (b) average V_s in fill; (c) *PHA* of input motion; (d) *PHV* of input motion; (e) T_m of input motion**

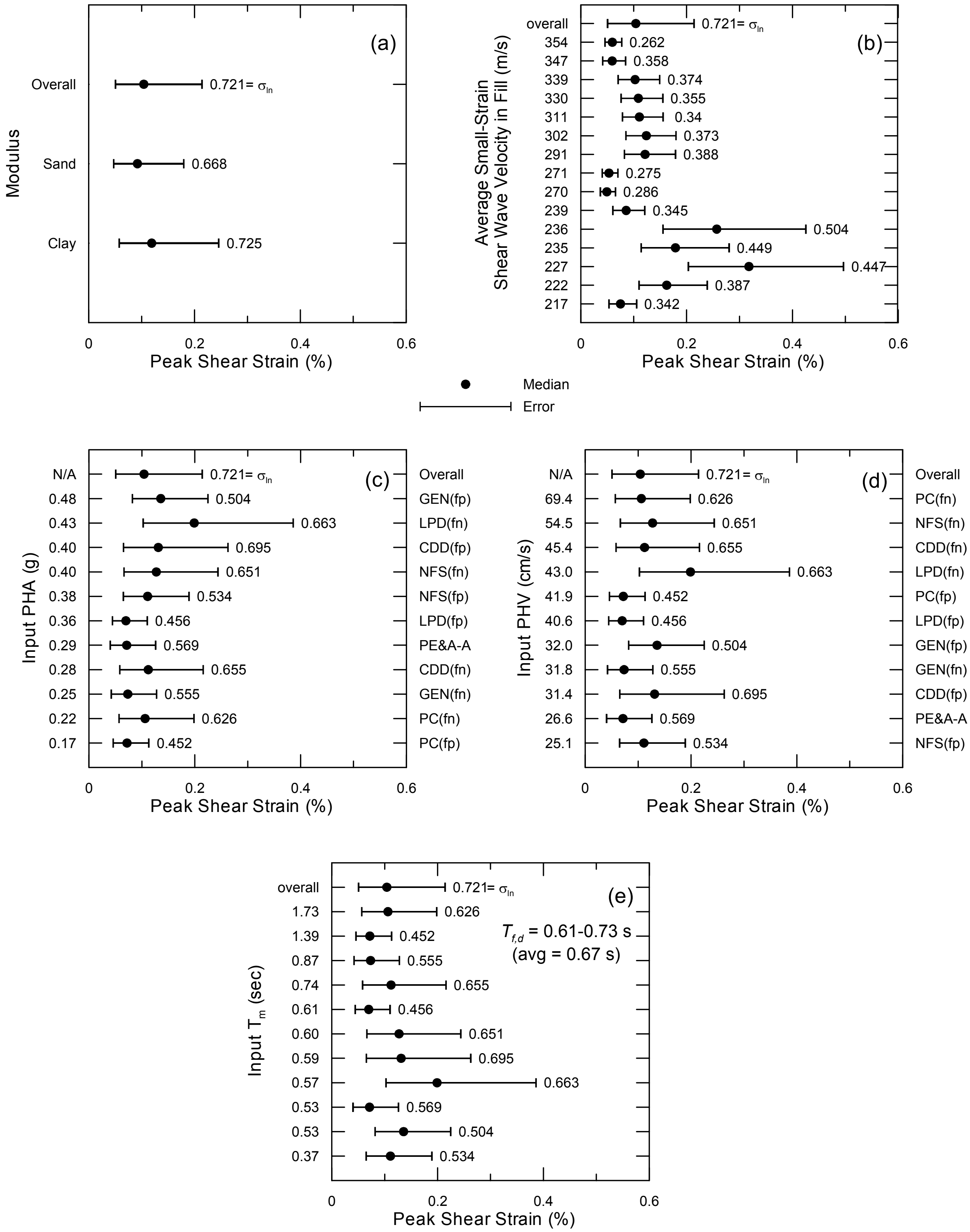

Fig. 8.2. **Site A, PSECTA2 (2-D analysis, depth=29.7m). Variability of γ_{pk} with (a) modulus reduction and damping curves; (b) average V_s in fill; (c) *PHA* of input motion; (d) *PHV* of input motion; (e) T_m of input motion**

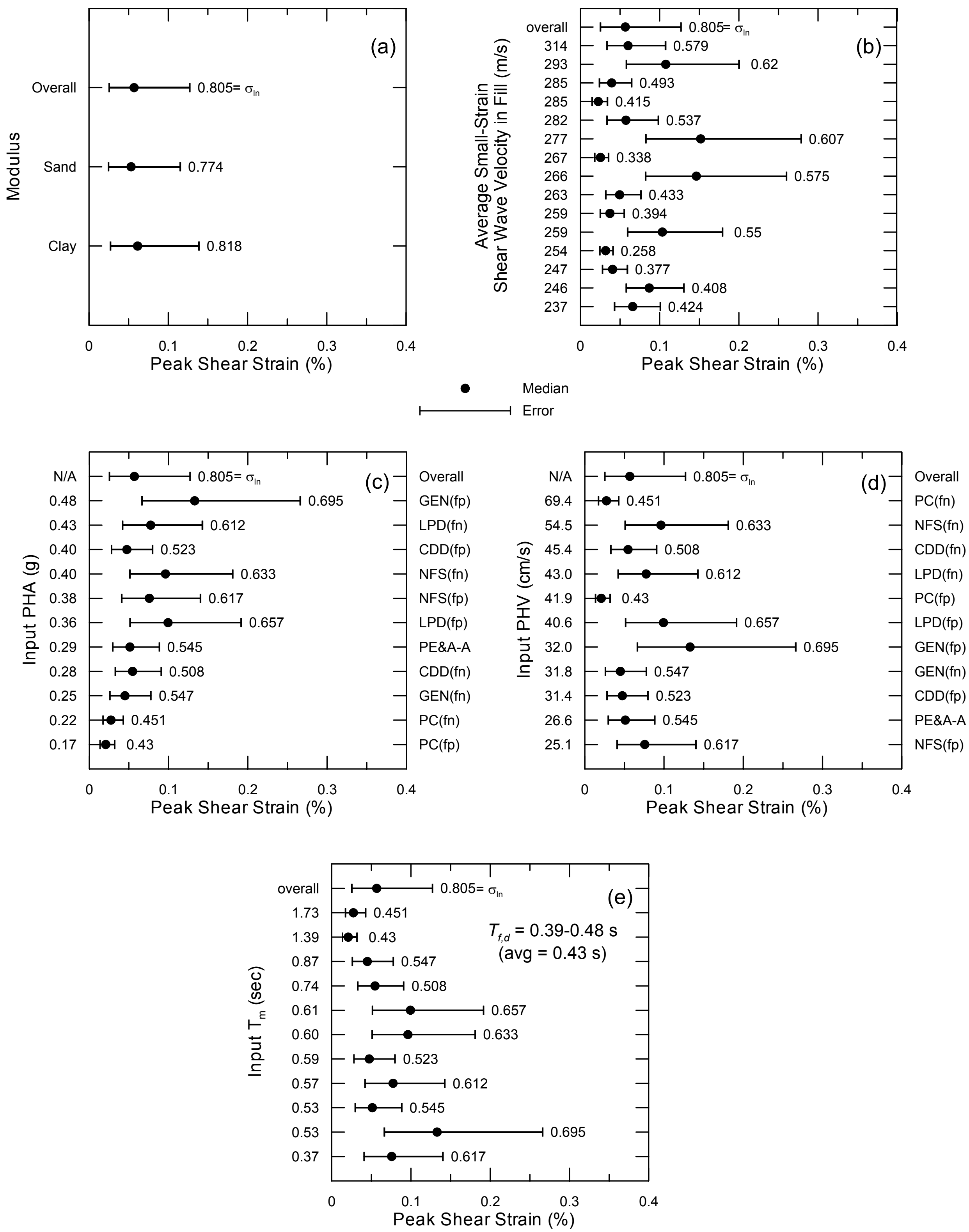

Fig. 8.3. Site A, PSECTB1 (2-D analysis, depth = 7.5m). Variability of γ_{pk} with (a) modulus reduction and damping curves; (b) average V_s in fill; (c) *PHA* of input motion; (d) *PHV* of input motion; (e) T_m of input motion

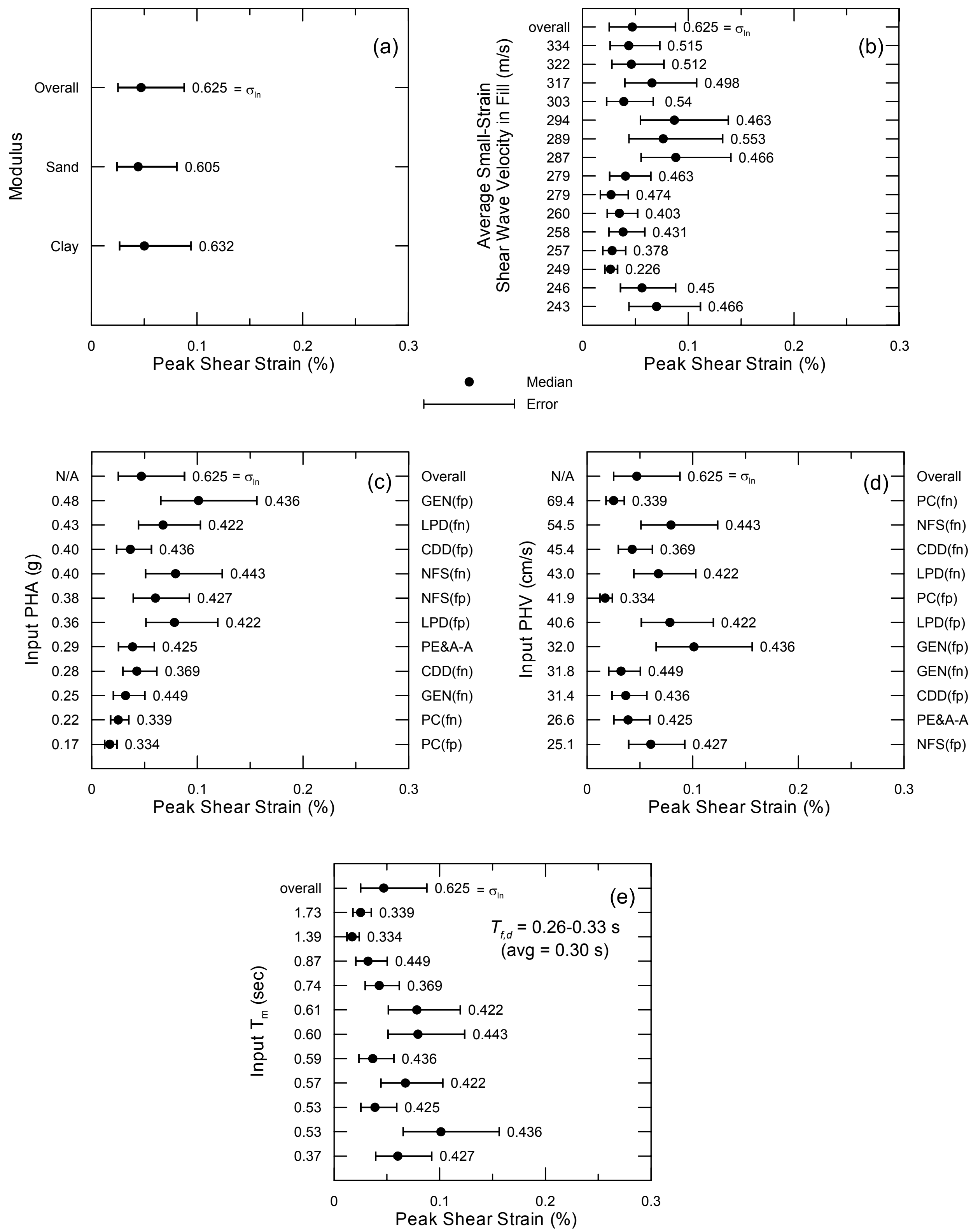

Fig. 8.4. Site A, PSECTB2 (2-D analysis, depth = 7.2m). Variability of γ_{pk} with (a) modulus reduction and damping curves; (b) average V_s in fill; (c) *PHA* of input motion; (d) *PHV* of input motion; (e) T_m of input motion

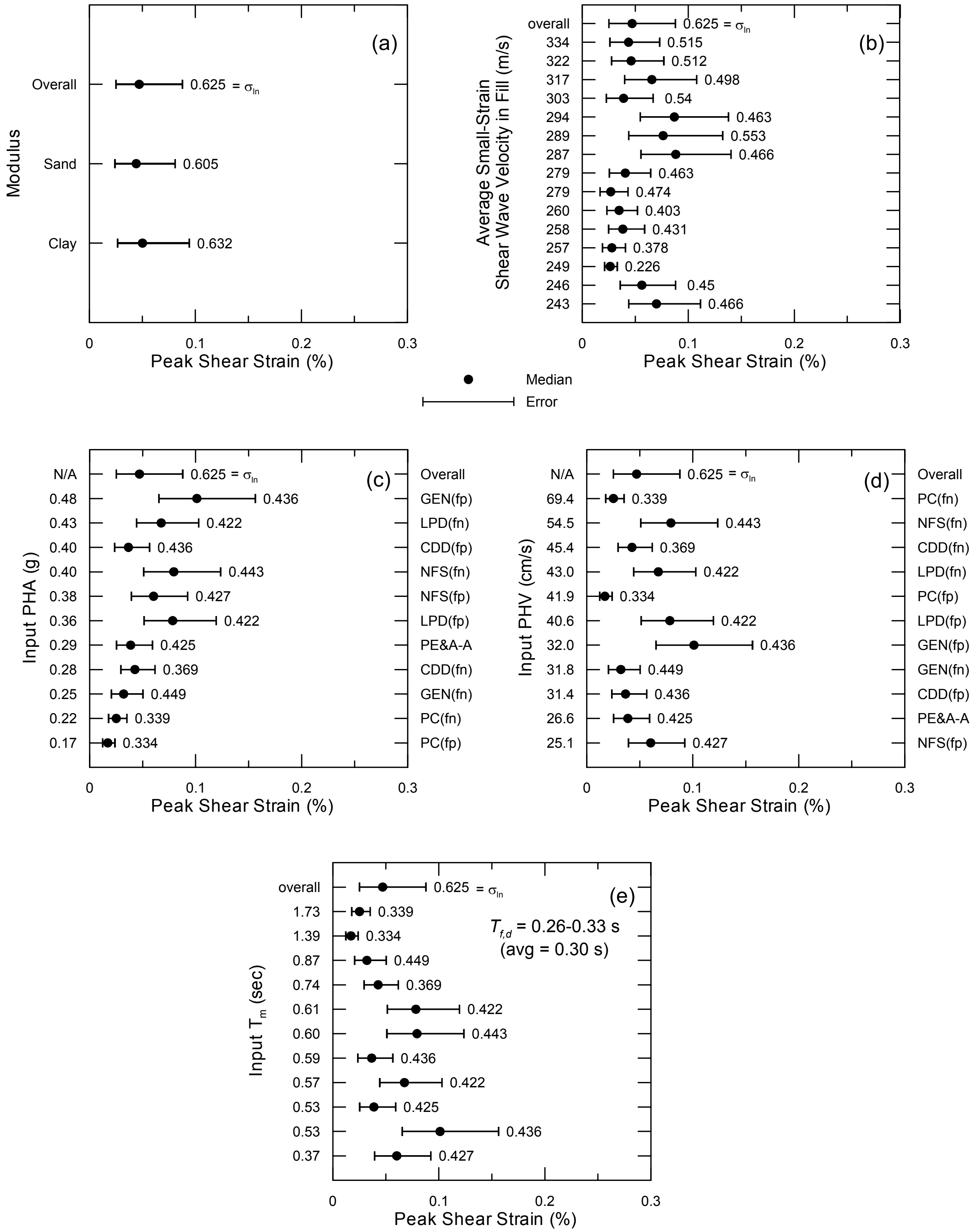

Fig. 8.5. Site B, SSECTA1 (2-D analysis, depth = 23.2m). Variability of γ_{pk} with (a) modulus reduction and damping curves; (b) average V_s in fill; (c) *PHA* of input motion; (d) *PHV* of input motion; (e) T_m of input motion

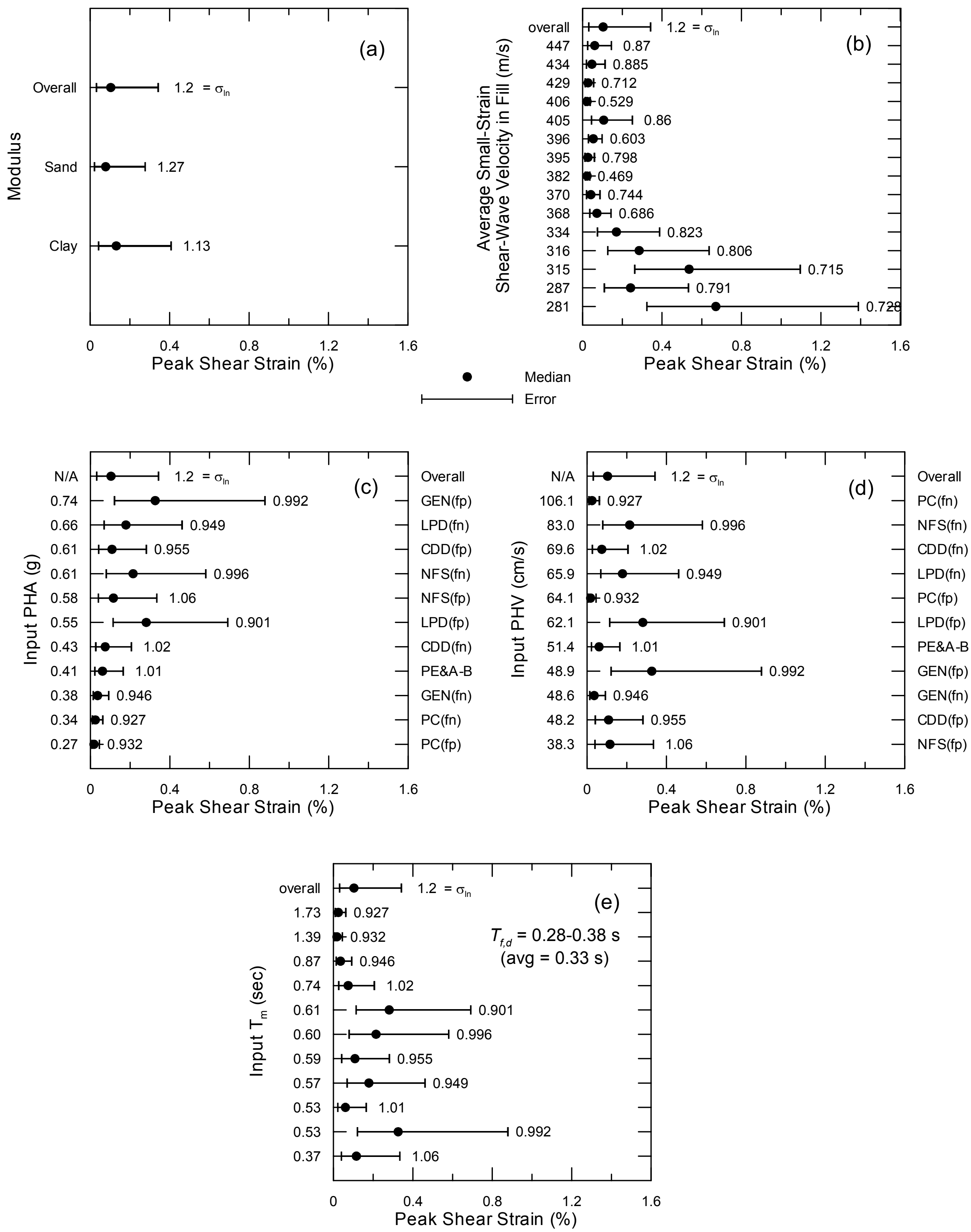

Fig. 8.6. Site B, SSECTA2 (2-D analysis, depth = 2.6m). Variability of γ_{pk} with (a) modulus reduction and damping curves; (b) average V_s in fill; (c) *PHA* of input motion; (d) *PHV* of input motion; (e) T_m of input motion

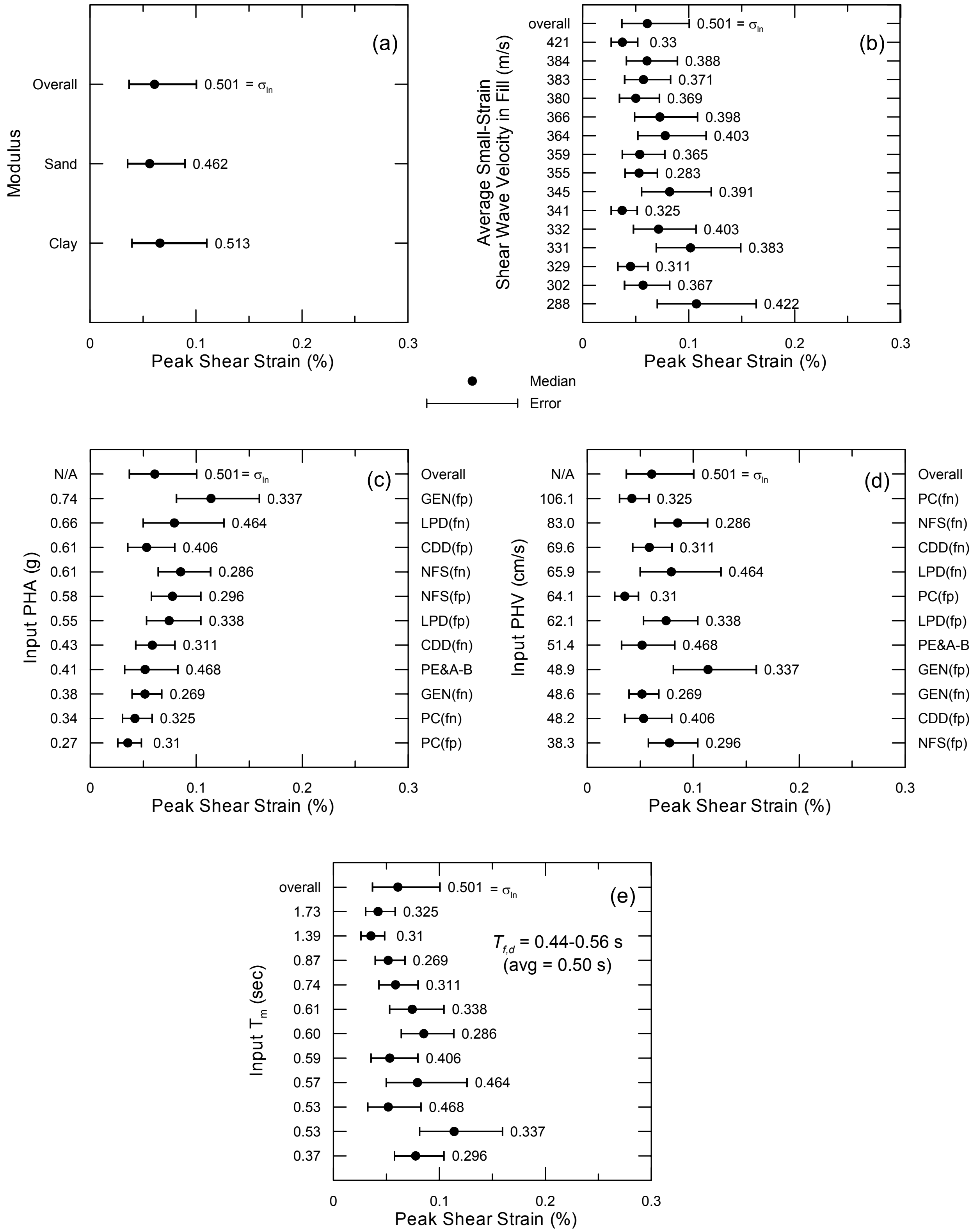

Fig. 8.7. Site B, SSECTB1 (2-D analysis, depth = 18.6m). Variability of γ_{pk} with (a) modulus reduction and damping curves; (b) average V_s in fill; (c) *PHA* of input motion; (d) *PHV* of input motion; (e) T_m of input motion

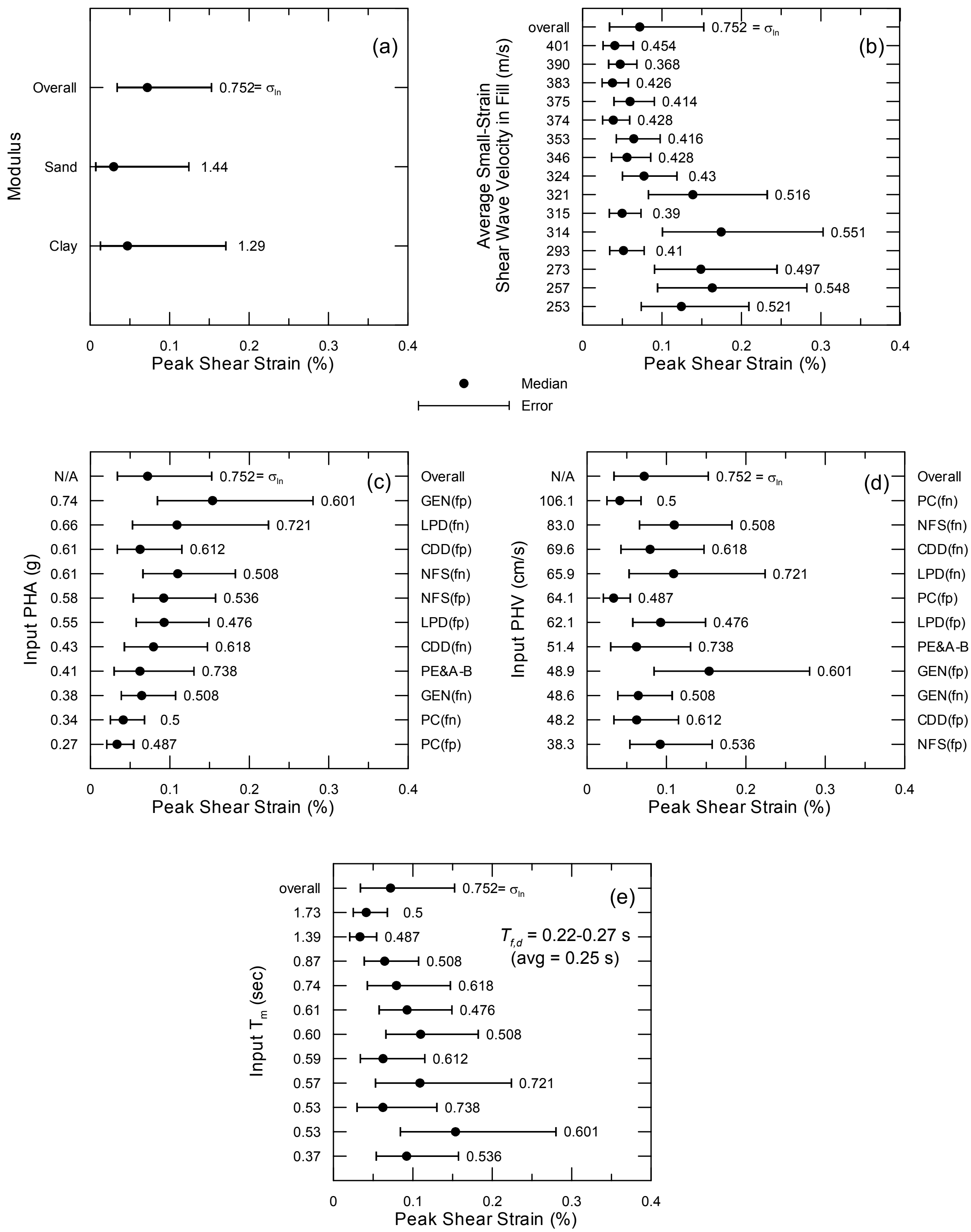

Fig. 8.8. **Site B, SSECTB2 (2-D analysis, depth = 10.5m). Variability of γ_{pk} with (a) modulus reduction and damping curves; (b) average V_s in fill; (c) *PHA* of input motion; (d) *PHV* of input motion; (e) T_m of input motion**

Part (a) of the figures shows the effect of the modulus reduction and damping models on γ_{pk} values. As described in Section 7.3.1, two alternative models were used — one denoted "sand," the other "clay." The computed median γ_{pk} values are slightly larger for the clay model than the sand model. However, the difference in these medians is not considered to be significant. The overall dispersion in estimated shear strains (e.g., 0.744 for PSECTA1) is reduced only by about null-0.05 by fixing the modulus reduction and damping curves. This is considered a negligibly small change.

Part (b) of the figures shows the effect of variability in the shear wave velocity profile on γ_{pk} values. As described in Section 7.3.2, 15 individual profiles were used, which are plotted in Figure 7.18. The average values of V_s (small-strain) across the fill height are shown on the left margin of the Part (b) figures. The average velocity is calculated as the ratio of the profile thickness to the shear wave travel time through the profile height. The computed median γ_{pk} values increase with decreasing average V_s in some cases (e.g., PSECTA1-A2; SSECTA2, B2), but in other cases there is no trend (e.g., PSECTB1-B2; SSECTA1, B1). This inconsistent trend should not be taken to indicate that shear strains are not significantly dependent on V_s, rather the range of V_s for these well-characterized sites is sufficiently small that a consistent trend does not emerge. The overall dispersion in estimated shear strains is reduced by amounts ranging from about 0.2 to 0.5 by fixing the V_s profile. These changes in dispersion are significant.

Parts (c)–(e) of the figures show the effect of variability in the input ground motions on γ_{pk} values. As described in Chapter 6, 11 individual time histories were used for each site, and the various intensity measures for these motions are listed in Table 6.4. The specific values of *PHA*, *PHV*, and T_m are listed on the left margin of the Part (c), (d), and (e) figures, respectively. The values listed in the figures represent the amplitudes after scaling the motions. As shown in Parts (c) and (d) of the figures, the computed median γ_{pk} values increase significantly with increasing *PHA*, but not with *PHV*. Part (e) of the figures shows that median γ_{pk} values are maximized for motions having mean periods that are nearly in resonance with the 1-D period of the fill section at the location under consideration. These 1-D periods are indicated on Parts (e) of the figures as the weighted average ± one standard deviation of $T_{f,d} = 4H/V_{sd}$, where H = fill section height and V_{sd} = degraded shear wave velocity. These results indicate that for these sites and input motions, *PHA* is a better predictor of ground strain than *PHV*, and that T_m, or more precisely the proximity of T_m to $T_{f,d}$, is also a good predictor. Fixing the input time history reduces the overall dispersion in estimated shear strains by amounts ranging from about null to 0.4, but reductions are generally about 0.1–0.3. These are considered significant reductions.

8.3 PARAMETRIC VARIABILITY OF CALCULATED VOLUMETRIC STRAINS

The volumetric strain (ε_v) that is calculated for a particular location within a soil profile is controlled by the shear strain time history and the soil behavioral model that relates γ_{pk} to ε_v. For the purpose of volumetric strain analysis, shear strain time histories are parameterized by an amplitude γ_{pk} and a number of equivalent shear strain cycles (*N*). As described in Section 7.2.3, the volumetric strain material model relating γ_{pk} to ε_v is dependent on the soil compaction condition as represented by the Modified Proctor relative compaction (*RC*) and the formation degree of saturation (*S*).

Complete results of the sensitivity analyses are presented for each of the four considered locations at Site A in Figures 8.9–8.12 and at Site B in Figures 8.13–8.16. Each of the figures contains three frames that show in Part (a) results for "fixed" values of *RC* and water content (*w*), in Part (b) results for narrow ranges of γ_{pk}, and in Part (c) results for particular values of *N* from the input time histories. The values of the fixed parameters (or for γ_{pk}, the narrow range of the parameter) are indicated in the left margins of the figures. The results for each fixed value of a parameter are presented as a horizontal line with a circle at the mean ($m_{\varepsilon v}$) of ε_v and dashes at $m_{\varepsilon v} \pm s_{\varepsilon v}$. To the right of each line is written the corresponding value of coefficient of variation, $COV = \sigma_{\varepsilon v} / \mu_{\varepsilon v}$.

Part (a) of the figures shows the effect on ε_v of the compaction condition, which is represented by combinations of formation relative compaction (*RC*) and formation water content (*w*). Note that for Site B soils, ε_v is independent of *S* and hence *w*, so the compaction condition is parameterized only with respect to *RC*. These models for ε_v are presented in Section 7.2.3, and the ranges of *RC* and *w* used to represent the site for ε_v analyses are presented in Section 7.3.4. As expected, computed $m_{\varepsilon v}$ values generally vary strongly with compaction condition. For Site A, the largest volumetric strains in fill occur in the bin having the lowest *RC* and *w*, and $m_{\varepsilon v}$ decreases with increasing *RC* and increasing *w*. The variation of $m_{\varepsilon v}$ between the least-favorable and most-favorable compaction condition is approximately a factor of ten. The overall coefficient of variation for estimated volumetric strains (e.g., 0.94 for PSECTA1) is reduced by about 0.06–0.23 by fixing the compaction condition. This is considered a modest change. Results for Site A in the alluvium (PSECTA2) show no sensitivity to compaction condition, which is because compaction condition was fixed for this layer (see Sections 3.2.4 and 7.3.5). For Site B, there appears to be no appreciable effect of *RC* on $m_{\varepsilon v}$ over the *RC* range of 90–95%. This weak trend can be explained by the insensitivity of ε_v to *RC* in the volumetric strain models derived from laboratory testing (see Figures 7.8–7.9 and 7.11). Because of this small effect of *RC*, $m_{\varepsilon v}$ and COV are not significantly affected by fixing the compaction condition for Site B.

Part (b) of the figures shows the effect of peak shear strain (γ_{pk}) on ε_v. The range of γ_{pk} used in these analyses matches that found in Section 8.2 for the corresponding locations within the fill sections. For the purpose of these sensitivity analyses, the γ_{pk} values are discretized into bins defined by percentile (i.e., 0–10, 10–20, etc.), with the corresponding range of γ_{pk} values shown on the left side of the figures. For both Sites A and B, the computed $m_{\varepsilon v}$ values increase significantly with increasing γ_{pk}, which is expected. The overall coefficient of variation for estimated volumetric strains (e.g., 0.941 for PSECTA1) is reduced by about 0.4–0.5 by fixing the shear strain level. This is a very substantial change.

Part (c) of the figures shows the effect of equivalent number of strain cycles (*N*) on ε_v. The analysis of *N* values from the time histories was described previously in Section 6.3.2. These *N* values are given on the left side of the figures, with the corresponding time history listed on the right side of the figures. Note that the *N* values apply for a bi-directional set of accelerograms, i.e., there is a single *N* value for both orthogonal components. There is a general increase of $m_{\varepsilon v}$ with *N*, although the trend is fairly weak. The weakness of the trend is associated with the variations of shear strain across these time histories, which is not controlled in the Part (c) comparisons. In other words, the effect of *N* is of second order importance relative to the effect of γ_{pk}. The overall coefficient of variation for estimated volumetric strains (e.g., 0.941 for PSECTA1) is reduced by null to about 0.3 by fixing *N* (which is the same as conditioning on an orthogonal pair of input motions). This is considered a significant change.

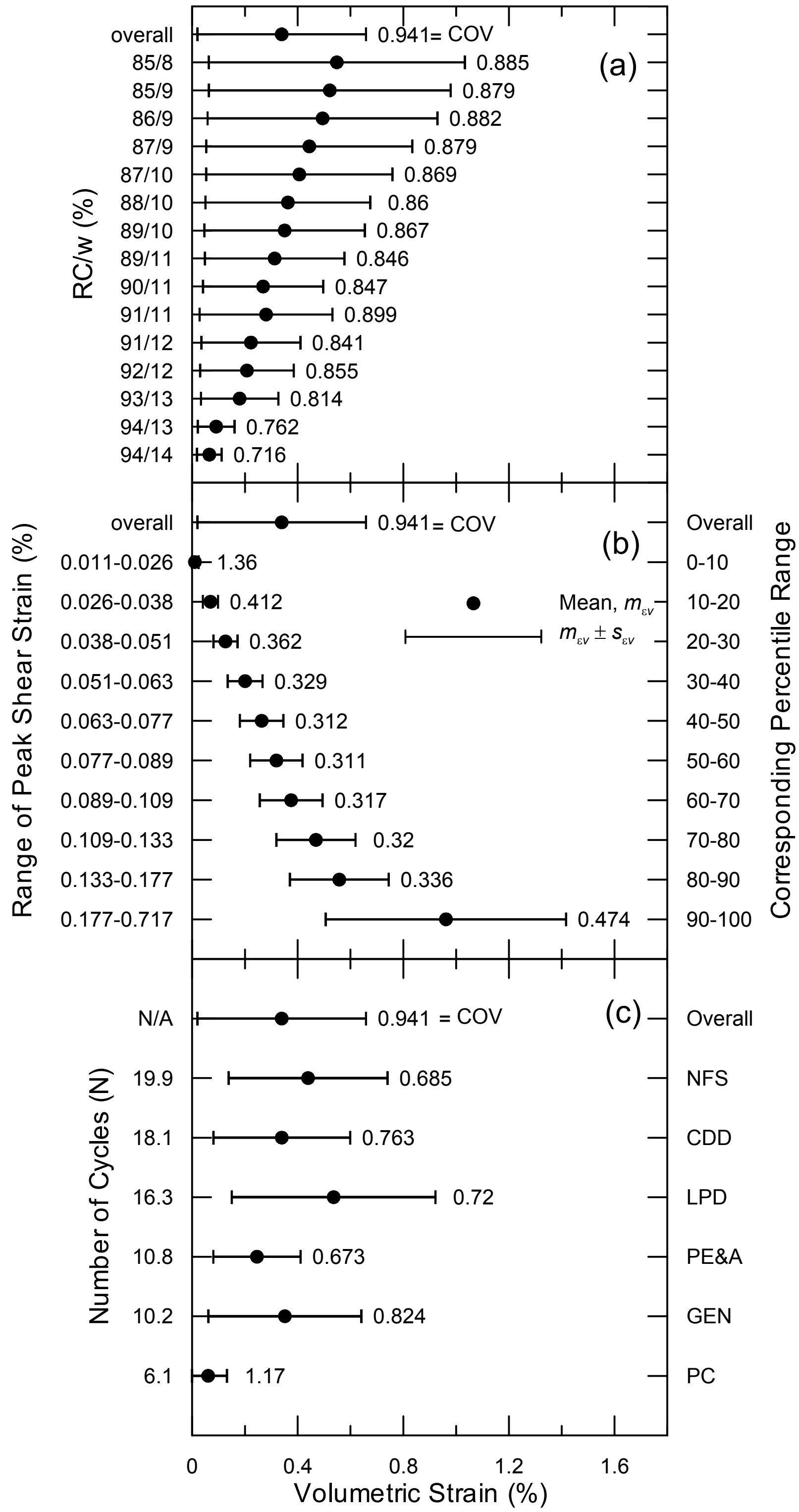

Fig. 8.9. Site A, PSECTA1, variability of ε_v with (a) compaction condition; (b) γ_{pk} (in 10-percentile increments); (c) equivalent number of uniform strain cycles (N)

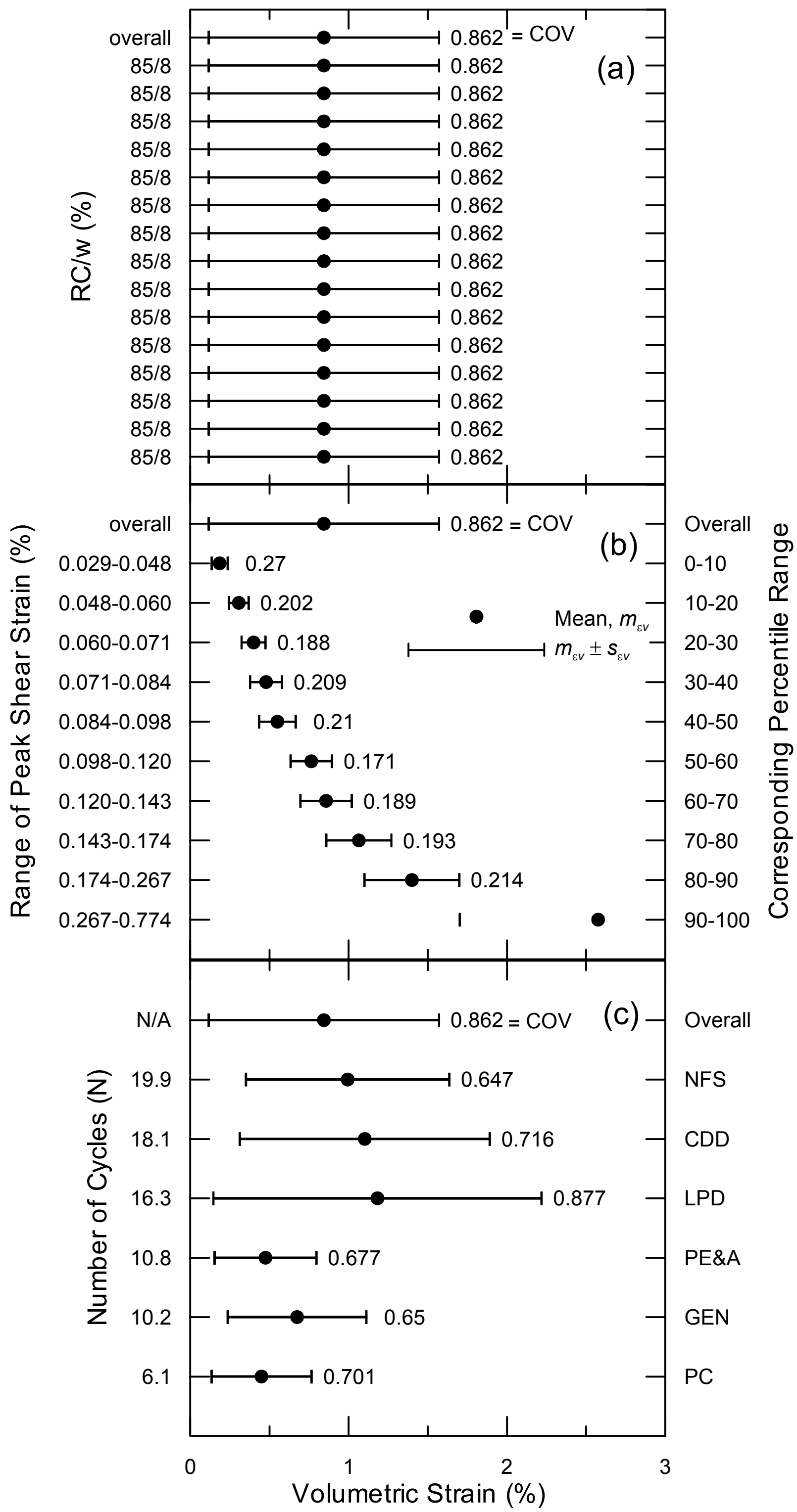

Fig. 8.10. Site A, PSECTA2, variability of ε_v with (a) compaction condition; (b) γ_{pk} (in 10-percentile increments); (c) equivalent number of uniform strain cycles (N)

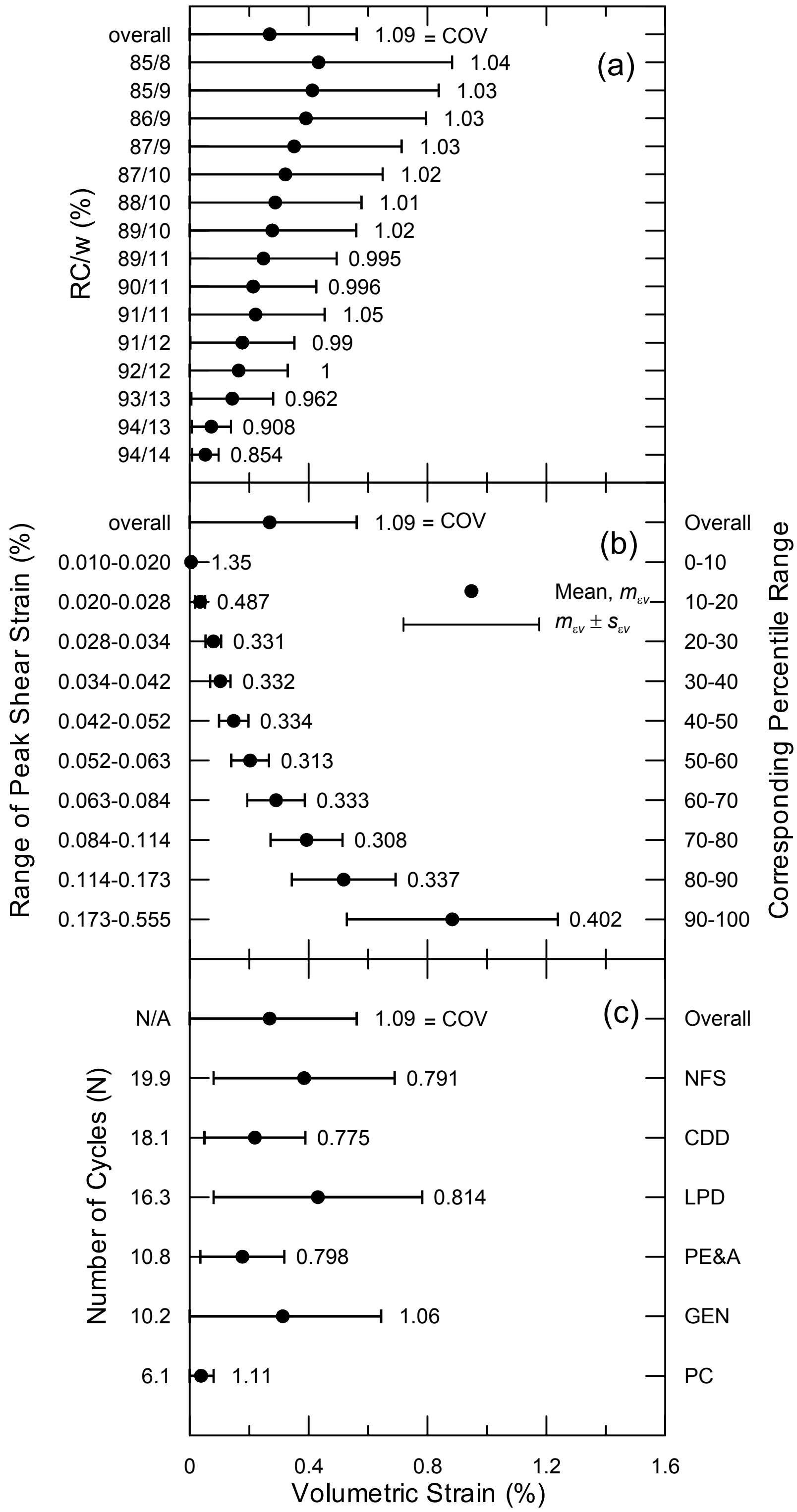

Fig. 8.11. Site A, PSECTB1, variability of ε_v with (a) compaction condition; (b) γ_{pk} (in 10-percentile increments); (c) equivalent number of uniform strain cycles (N)

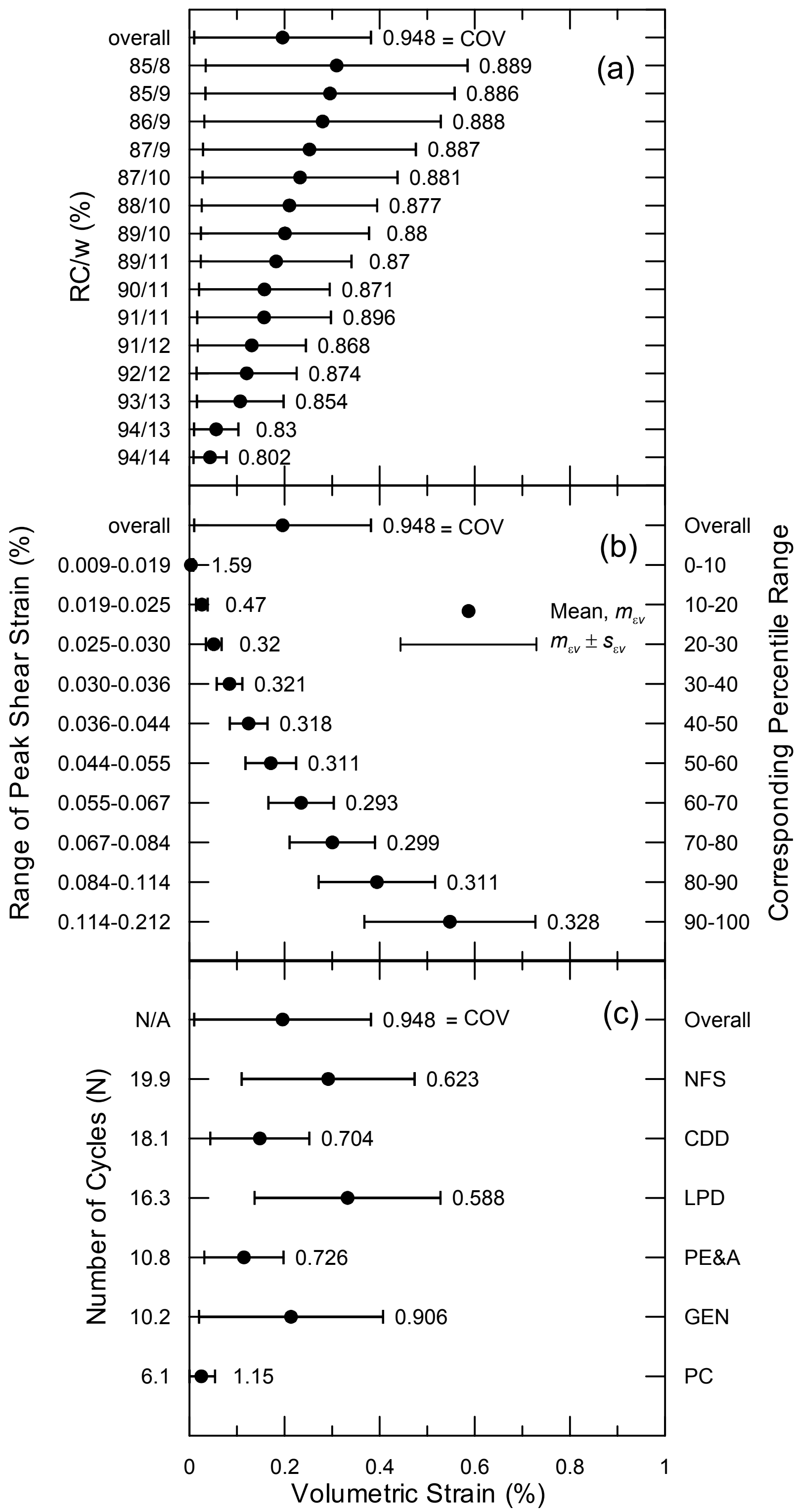

Fig. 8.12. Site A, PSECTB2, variability of ε_v with (a) compaction condition; (b) γ_{pk} (in 10-percentile increments); (c) equivalent number of uniform strain cycles (N)

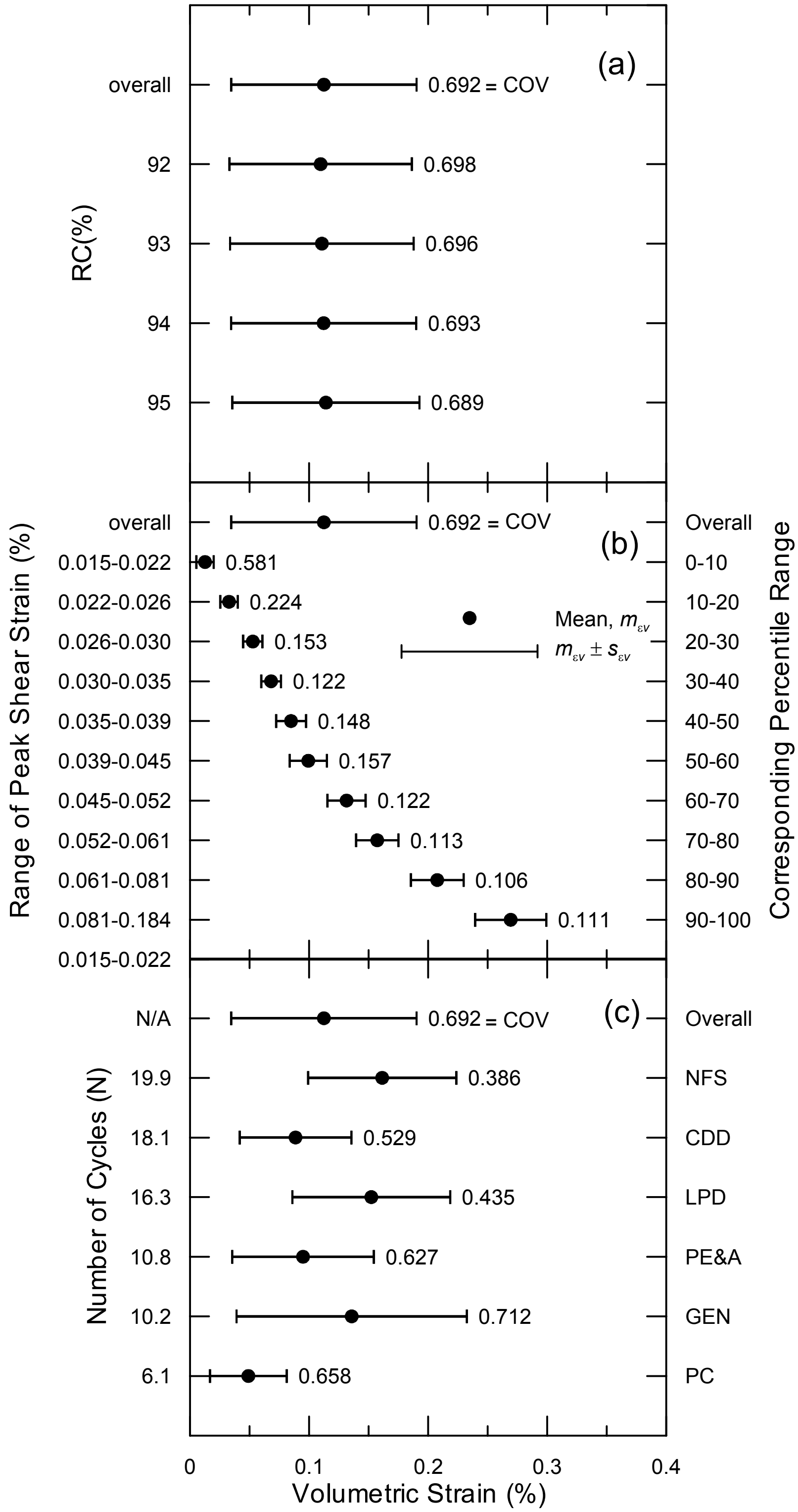

Fig. 8.13. Site A, SSECTA1, variability of ε_v with (a) compaction condition; (b) γ_{pk} (in 10-percentile increments); (c) equivalent number of uniform strain cycles (N)

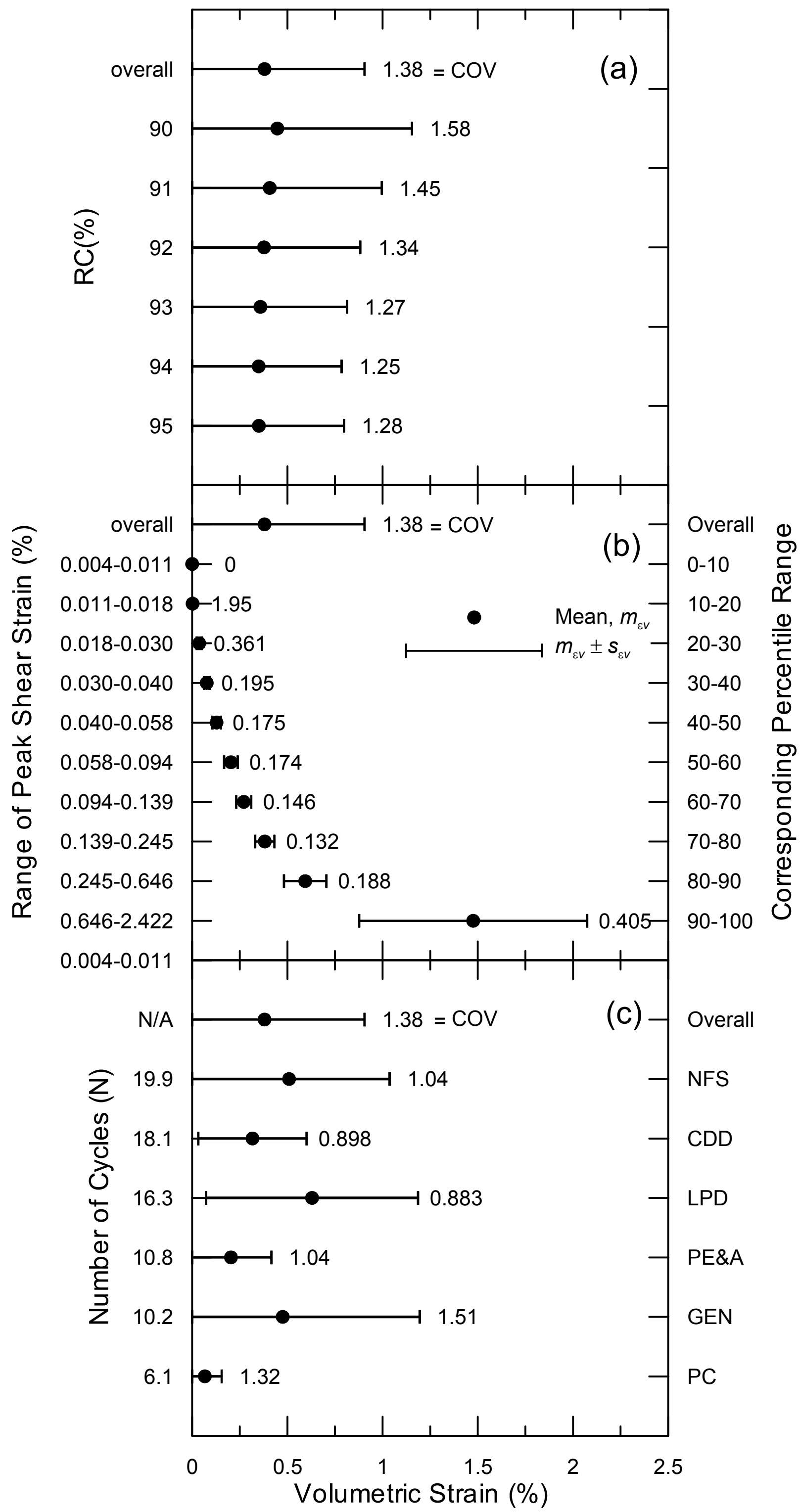

Fig. 8.14. Site A, SSECTA2, variability of ε_v with (a) compaction condition; (b) γ_{pk} (in 10-percentile increments); (c) equivalent number of uniform strain cycles (N)

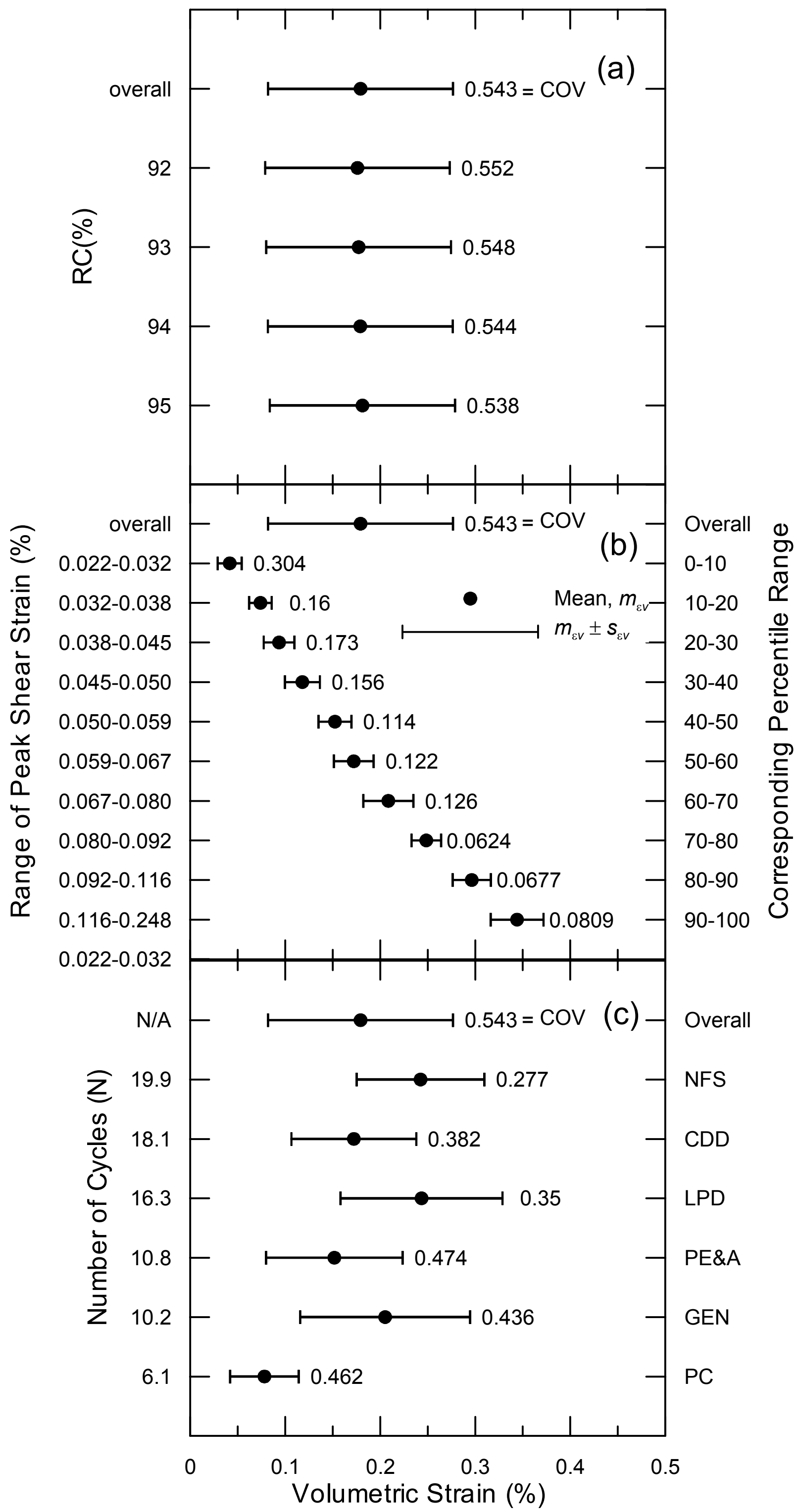

Fig. 8.15. Site A, SSECTB1, variability of ε_v with (a) compaction condition; (b) γ_{pk} (in 10-percentile increments); (c) equivalent number of uniform strain cycles (N)

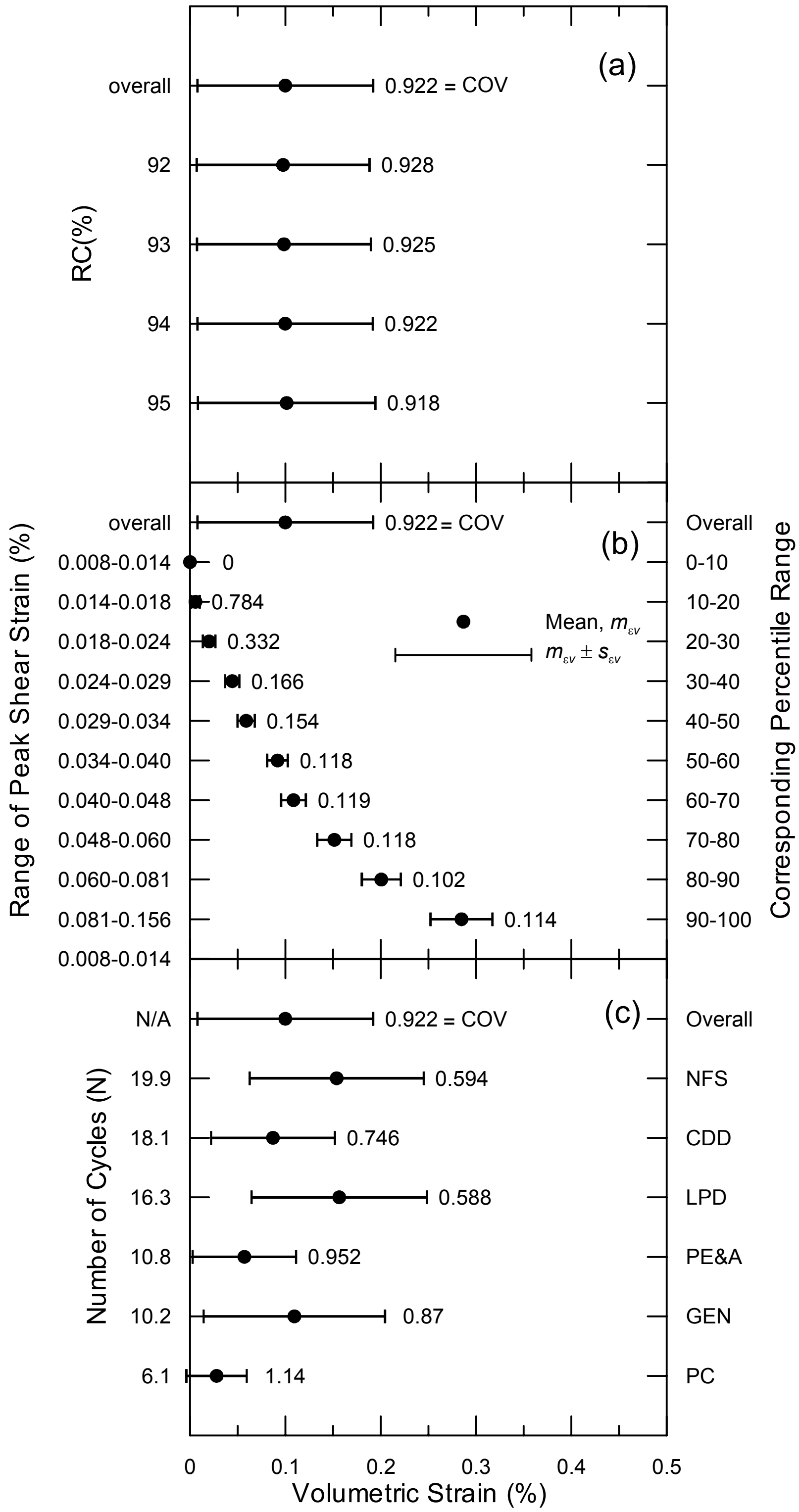

Fig. 8.16. Site A, SSECTB2, variability of ε_v with (a) compaction condition; (b) γ_{pk} (in 10-percentile increments); (c) equivalent number of uniform strain cycles (N)

8.4 SYNTHESIS OF RESULTS

The sites considered in this research are well characterized in terms of their shear wave velocity profiles and compaction conditions. For these sites, we find that the most important factors affecting the statistical properties of the calculated shear strains are the shear wave velocity profile and the input ground motion (as parameterized by *PHA* and T_m). Statistical properties of the calculated volumetric strains, in turn, are most sensitive to the compaction condition and the shear strain amplitude. Accordingly, for the sites considered, the sources of parametric variability most significantly influencing the calculated volumetric strains and settlements are the shear wave velocity profiles, input ground motions, and the soil compaction conditions.

Given the above, resource allocation for the development of input data for seismic compression analyses should be structured so that each of the following is reliably estimated: (1) site-specific measurement of the shear wave velocity profile at the site; (2) characterization of input ground motions, with particular emphasis on the intensity measures of *PHA*, T_m, and *N*; (3) characterization of compaction conditions in the fill (i.e., formation *RC* and *S*). Issues of less critical importance include the modulus reduction and damping curves and the peak velocity of the input motions.

9 Summary and Conclusions

9.1 SCOPE OF RESEARCH

Earthquake-induced ground deformations resulting from contractive volumetric strains in unsaturated soils have been observed in numerous earthquakes. This process, termed seismic compression, resulted in major economic losses during the 1994 Northridge earthquake, which has caused this phenomenon to be acknowledged as a critical design issue. In this research program, we performed detailed investigations of seismic compression for two sites with unusually well-documented field performance during the 1994 Northridge earthquake. In addition to the documentation of these important case histories, the objectives of the work were to shed light on physical soil characteristics that control seismic compression susceptibility through a laboratory testing program, and through analyses to (1) investigate the degree to which seismic compression can explain the observed ground displacements and (2) evaluate the sensitivity of calculated settlements to variability in input parameters as well as the dispersion of calculated settlements given the overall parametric variability.

To realize the stated objectives, this research involved the following phases of work:

1. Detailed characterization of the geotechnical conditions at the sites and documentation of the observed field performance (Chapter 3);
2. Laboratory studies to characterize the seismic compression susceptibility of the fill soils at these sites (Chapters 4–5);
3. Estimation of the ground motions that were likely to have occurred at the sites during the 1994 Northridge earthquake (Chapter 6);
4. Back-analyses of ground settlements from the 1994 Northridge earthquake using the available site and earthquake data to assess whether seismic compression can explain the observed ground deformation (Chapter 7); and

5. Analytical studies to evaluate the sensitivity of the computed results to parametric variability in key input parameters (Chapter 8).

Our site characterization work began with the collection of existing borehole data and information from as-built grading plans. To obtain more detailed information on subsurface conditions, we drilled boreholes to clarify the subsurface stratigraphy and to collect samples for laboratory testing; performed cone penetration testing (CPT) to further characterize soil conditions; and performed geophysical logging to evaluate shear wave velocity profiles at the borehole and CPT locations. We also carefully reviewed the available field performance data from the 1994 Northridge earthquake to identify the ground deformations at the subject sites that can be attributed to the earthquake.

Our laboratory testing of the seismic compression of soils from the selected sites was performed using cyclic simple shear test equipment. This testing was performed under drained conditions to evaluate the vertical strain accumulation of samples subjected to uniform shear strain cycles. All tests were performed for a vertical stress of 101.3 kPa and a sinusoidal loading frequency of 1 Hz. A total of four different sands and four distinct fill samples were tested. The sands were tested to provide a baseline set of results against which the test results for fills (which contain fines) could be compared. The reconstituted fill soils were tested to provide soil-specific seismic compression test results for the two field sites. Accordingly, the formation water content and dry densities of the tested specimens were chosen to represent the range of estimated in situ conditions at the field sites.

A number of ground motion acceleration time histories were selected to represent possible realizations of the ground shaking at the subject sites. The selected motions consist of time histories from the 1994 Northridge earthquake recorded at nearby accelerograph stations as well as site-specific time histories estimated using a simulation procedure. All time histories were corrected, as necessary, to a rock site condition, which required deconvolution of recordings from soil sites. The recordings were also scaled to correct for the different site-source distances at the recording sites and the subject fill sites.

The back-analysis of settlements at the two subject fill sites was performed using an analysis procedure that decouples the computation of shear and volumetric strains. Peak shear strains (γ_{pk}) were estimated using 1-D and 2-D ground response analyses, and these shear strains were then used to estimate profiles of volumetric strain (ε_v), which could be integrated across the depth of fill to estimate settlements. Each of the parameters that enter the analysis has both aleatory and epistemic uncertainty, and these uncertainties were estimated. The effects of these uncertainties on the analysis results were addressed using a logic tree approach in which parameter spaces were discretized and weighted with respect to their likelihood of occurrence. Each branch of the logic tree produced an estimate of shear strain, volumetric strain, and settlement and weights associated with those estimates. The analysis results and their associated frequencies were combined to develop weighted frequency functions (*WFF*s) from which point estimates (e.g., weighted means and standard deviations) were calculated. The *WFF*s were then used to identify the theoretical probability density function that best represents the distribution of γ_{pk} and ε_v at specific locations. The presentation of the results in this manner enabled the observed settlements to be compared to probabilistic distributions of calculated settlement.

The final stage of work involved detailed examination of analysis results for the two subject sites to identify the effects of parametric variability on the calculated shear and volumetric strains. In particular, we assessed the sensitivity of peak shear strains to variations in the input ground motions and variations of dynamic soil properties. Moreover, we assessed the sensitivity of volumetric strains to variations in compaction conditions, shear strain amplitude, and equivalent number of uniform cycles of shear strain.

9.2 RESEARCH FINDINGS AND RECOMMENDATIONS

Our discussion of the research findings and consequent recommendations is structured to parallel the statement of project objectives. As a reminder, the objectives of the work are to shed light on physical soil characteristics that control seismic compression susceptibility, and through analysis to (1) investigate the degree to which seismic compression can explain the observed ground displacements and (2) evaluate the sensitivity of calculated settlements to variability in input parameters as well as the dispersion of calculated settlements given the overall parametric variability.

9.2.1 Soil Compositional Characteristics Controlling Seismic Compression

Simple shear testing of fill specimens containing fines indicates a strong effect of fines plasticity on seismic compression. Soils with nonplastic fines experience less seismic compression than clean sands for a common set of baseline conditions, but these two materials behave similarly in the sense that Modified Proctor relative compaction (*RC*) is the principal construction-related factor affecting seismic compression. Soils with low-plasticity fines (PI ~ 15) demonstrate different behavior, with seismic compression decreasing not only with increasing *RC*, but also at a given *RC* decreasing with increasing as-compacted degree of saturation (*S*). At low *S*, volumetric strains from seismic compression are comparable to those for sand (at a common *RC*), whereas at high *S* the strains are 10 to 50% of those for sand. The observed behavior is postulated to be associated with macrostructural features. At low to moderate *RC*, clayey soils form a clod-like structure when compacted at low *S*, but a nearly continuum structure when compacted at high *S*. We speculate that these variations of clod structure with compaction condition control the seismic compression susceptibility (i.e., seismic compression should increase with interclod void space). Nonplastic fine-grained soils lack the tendency to form clods, which explains the observations from these materials that seismic compression is independent of *S*.

9.2.2 Analysis of Seismic Compression for Sites A and B

The analytical studies of seismic compression at Sites A and B provided the insights outlined in the following paragraphs.

The peak shear strain at selected locations within the fill sections was found to have a lognormal distribution which can be described by a median (λ) in arithmetic units and standard deviation (σ_{ln}) in natural logarithmic units.

Median shear strains are strongly influenced by shear wave velocity and ground motion characteristics. Among the ground motion intensity measures considered, strains were found to increase significantly with increasing peak acceleration, but to be relatively insensitive to peak velocity. The shear strains are also affected by resonance effects between the input motion and site period, with the largest shear strains occurring when the mean period of the ground motion is similar to the degraded site period. Median shear strains were not significantly different for the two soil modulus reduction and damping models used herein. The standard deviation of the shear strains is most strongly influenced by variations in shear wave velocity and input ground motions.

Median shear strains calculated using 1-D and 2-D ground response analyses are similar in areas of nearly 1-D site geometry but can differ significantly near slopes or sloping bedrock/fill interfaces. The lack of ground restraint near slopes increases the shear strains behind the slope in 2-D analyses relative to 1-D analyses. Conversely, the added restraint against shear deformation provided by a sloping bedrock-fill interface decreases shear strains in fill overlying this interface.

The volumetric strains at selected locations within the fill sections were not found to have the shape of any standard, theoretical probability density function. Accordingly, we chose to describe the distribution of the volumetric strain results with the point estimates of weighted mean ($m_{\varepsilon v}$) and weighted standard deviation ($s_{\varepsilon v}$), both in arithmetic units. These quantities happen to correspond to the statistical moments of a theoretical normal distribution, although it should be emphasized that the data are not normal.

Calculated mean volumetric strains are most sensitive to the compaction condition and the shear strain amplitude. Volumetric strains increase as compaction conditions become less favorable, which generally occurs with decreasing formation moisture content and decreasing Modified Proctor relative compaction. Volumetric strains are very strongly dependent on shear strain amplitude, and thus are dependent on those factors that control shear strain amplitude. The dependence of volumetric strain on equivalent number of uniform strain cycles (N) was second-order relative to the above dependencies on strain and compaction condition. The primary factor controlling the coefficient of variation of volumetric strains is variability in shear strains, which in turn is controlled by the variability of the velocity profiles and the input ground motions.

Calculated ground settlements from seismic compression at Site B match observations between the 30th and 70th percentile levels. Settlements at Site A are underpredicted (observed settlements are generally matched at the 50–70th percentile level). We speculate that the underprediction at Site A results from imperfect knowledge of site stratigraphy and/or underestimation of volumetric strains from the laboratory tests as a result of the nonreproducibility of the field soil's clod structure. These comparisons to data are inadequate to demonstrate the presence of a bias or lack of bias in the analysis procedure.

The coefficient of variation on the predicted settlements ranges from about 0.5 to 1.0, being closer the low end of the range if 2-D analyses are performed (~0.5–0.7) and the upper end of the range if 1-D analyses are performed (~0.8–1.0).

9.2.3 Recommendations for Analysis of Seismic Compression

It is important to emphasize that the analysis procedure employed herein cannot be considered to be calibrated based on the analyses presented in this report, because two case histories are not a sufficiently large calibration data set. Nonetheless, the limited available data suggest that the general analysis approach employed in this study can provide an effective means by which estimate the general magnitude of settlements from seismic compression and their distribution across a project site. To employ this approach in practice, the following general steps are required:

1. The site stratigraphy must be carefully evaluated, especially the distribution of fill depth across the site. In situ measurements of shear wave velocity in the fill and underlying native materials should be made.
2. The fill compaction conditions must be reliably characterized, including their mean and the dispersion about the mean.
3. Earthquake ground motion time histories must be selected that are appropriate for the seismic hazard at the site and the site condition present beneath the fill. The records should be scaled to the *PHA* obtained from appropriate ground motion hazard analyses. A suite of scaled time histories is needed to characterize the natural variability of phasing and frequency content of motions that might occur during the design event. At a minimum, 5–10 time histories should be considered in the analyses.
4. Ground response analyses should be performed using the input motions and velocity profiles. Two-dimensional analyses are highly desirable for sites having irregular surface topography or irregular subsurface stratigraphy. The distribution of peak shear strains in the fill mass should be assessed, and the number of shear strain cycles should be assessed using procedures outlined in Section 6.3.2.

5. Volumetric strains should be evaluated from the shear strains using an appropriate volumetric strain material model. For clean sands, previous models presented by Silver and Seed (1971) can be used for this purpose. For soil with significant fines, such as silty sands/sandy silts or low-plasticity clays, the test results in Chapter 5 can be used to provide a first-order estimate of volumetric strains, although additional testing of fine-grained soils is needed before generalized volumetric strain material models can be formulated for fine-grained soils. Volumetric strains at 15 cycles of loading [$(\varepsilon_v)_{N=15}$] need to be corrected for the actual expected number of cycles (N), and should be multiplied by two to account for multi-directional shaking effects.
6. Ground settlements are evaluated by integrating volumetric strains over the height of the fill section. This should be repeated at a sufficient number of locations to describe the lateral variability of settlement across the surface of the fill.

Several caveats should be noted with respect to the above procedure. First, these analyses do not provide an estimate of lateral ground displacements that may arise from seismic compression of soil sections having significant static shear stresses. This can be accounted for by integrating volumetric strains in the direction of the major principal stress in lieu of the more common practice of integrating vertically across the fill thickness. Second, engineers should also consider the potential for permanent shear deformations, especially when significant driving static shear stresses are present and / or slope materials have low shear strength.

9.3 RECOMMENDATIONS FOR FUTURE RESEARCH

There are several major classes of research needs that remain on the topic of seismic compression. These research needs can be subdivided into several categories: (1) development of generalized volumetric strain material models for seismic compression from more comprehensive laboratory testing; (2) update existing simplified procedures for seismic compression analysis by Tokimatsu and Seed (1987) to account for recent advances in dynamic soil property characterization and other relevant factors; and (3) identification of additional case histories of seismic compression to enable calibration of simplified and more detailed analysis procedures.

Perhaps the most important of the above research needs is that for predictive models of volumetric strain from seismic compression. The models should be developed from laboratory testing of a broad variety of soil types, soil compaction conditions, and sample environmental conditions (e.g., overburden pressure, age, postcompaction wetting, etc.). Such models are needed before seismic compression analyses can be performed with confidence in the absence of material-specific laboratory testing of seismic compression.

REFERENCES

Abrahamson, N.A. and Silva, W.J. (1997). "Empirical response spectral attenuation relations for shallow crustal earthquakes," *Seism. Research Letters*, 68(1): 94–127

Ang, A.H. and Tang, W.H. (1975). *Probability concepts in engineering planning and design*, John Wiley and Sons, Volume 1.

Ashford, S.A., Sitar, N., Lysmer, J., and Deng, N. (1997). "Topographic effects on the seismic response of steep slopes," *Bull Seism. Soc. Am*., 87(3): 701–9.

Benjamin, J.R. and Cornell, C.A. (1970). *Probability, statistics and decision theory for civil engineers*, McGraw-Hill Book Company.

Benson, C.H. and Daniel, D.E. (1990). "Influence of clods on hydraulic conductivity of compacted clay," *J. Geotech. Engrg.*, ASCE, 116(8): 1231–48.

Casagrande, A. (1932). "The structure of clay and its importance in foundation engineering," *Contributions to soil mechanics*, Boston Society of Civil Engineers, Boston, pp. 72–112.

Chang, S.W., Bray, J.D., and Seed, R.B. (1996). "Engineering implications of ground motions from the Northridge earthquake," *Bull Seism. Soc. Am*., 86(1B): S270–88.

Chu, H.-H. and Vucetic, M. (1992). "Settlement of compacted clay in a cyclic direct simple shear device," *Geotech. Testing J.*, 15 (4), 371–79.

Coduto, D.P. (1994). *Foundation design: principles and practices*, Prentice Hall, Englewood Cliffs, NJ.

Cressie, N.A.C. (1991). *Statistics for spatial data*, John Wiley and Sons, Inc., New York, 900 pp.

Crouse, C.B. and Ramirez, J.C. (2003). "Soil-structure interaction and site response at the Jensen Filtration Plant during the 1994 Northridge, California mainshock and aftershocks," *Bull Seism. Soc. Am*. in press.

Fumal, T.E., Gibbs, J.F., Roth, E.F. (1982). "In-situ measurements of seismic velocity at 22 locations in the Los Angeles, California region," *OFR 82-833*, U.S. Geological Survey, Menlo Park, CA.

Geo-Resources Consultants, Inc. (1994). Confidential geotechnical report.

Hudson, M., Idriss, I.M., Beikae, M. (1994). "QUAD4M: A computer program to evaluate the seismic response of soil structures using finite element procedures and incorporating a compliant base," Ctr. for Geotech. Modeling, Univ. of California, Davis.

Idriss, I.M. (1991). *Procedures for selecting earthquake ground motions at rock sites,* Report to U.S. Department of Commerce, revised 1993.

Idriss, I.M. (1994). Personal communication regarding revision to Idriss 1991 document to incorporate Northridge recordings.

Idriss, I.M. and Sun, J.I. (1991). "User's manual for SHAKE91: A computer program for conducting equivalent linear seismic response analyses of horizontally layered soil deposits," Ctr. for Geotech. Modeling, Univ. of California, Davis.

Lawson, A. C., ed. (1908). "Minor geologic effects of the earthquake," *California earthquake of April 18, 1906*, Publ. 87, Vol. 1, Part 2, Carnegie Institute of Washington, D.C., 384–409.

Lawton, E., Fragaszy , R.J. and Hardcastle, J.H. (1989). "Collapse of compacted clayey sand," *J. Geotech. Engrg.*, ASCE, 115(9), 1252–66.

Liu, A.H., Stewart, J.P., Abrahamson, H.A., and Moriwaki, Y. (2001). "Equivalent number of uniform stress cycles for soil liquefaction analysis," *J. Geotech. & Geoenv. Engrg.*, ASCE, 127 (12) 1017–26.

Mann, H. and Wald, A. (1942). "On the choice of the number of class intervals in the application of the Chi square test," *Ann. Math. Stat.* 13: 306–17.

McClure, F.E. (1973). *Performance of single family dwellings in the San Fernando earthquake of February 9, 1971*. NOAA, U.S. Dept. of Commerce, May.

Pearson, D. (1995). "L.A. County 'Section 309' statement," *Geogram*, California Geotechnical Engineers Association, Placerville, Calif.

Pyke, R., Seed, H.B., Chan, C.K. (1975). "Settlement of sands under multidirectional shaking," *J. Geotech. Engrg.*, ASCE, 101 (4) 379–98.

Rathje, E.M., Abrahamson, N.A., and Bray, J.D. (1998). "Simplified frequency content estimates of earthquake ground motions," *J. Geotech. & Geoenv. Engrg*., ASCE, 124(2): 150–59.

Roblee, C.J., Silva, W.J., Toro, G.R., and Abrahamson, N.A. (1996). "Variability in site-specific seismic ground motion design predictions," *ASCE Geotech. Special Publication No. 58*, Uncertainty in the Geologic Environment: From Theory to Practice, C.D. Shakelford, P.P. Nelson (eds.), Vol. 2, 1113–33.

Rodriguez-Marek, A., Bray, J.D., and Abrahamson, N.A. (2001). "An empirical geotechnical seismic site response procedure," *Earthquake Spectra*, 17(1) 65–87.

Sadigh, K., Chang, C.-Y., Egan, J.A., Makdisi, F., and Youngs, R.R. (1997). "Attenuation relations for shallow crustal earthquakes based on California strong motion data," *Seism. Res. Letters*, 68(1): 180–89.

Schnabel, P.B. (1973). "Effects of local geology and distance from source on earthquake ground motions," Ph.D. Dissertation, U.C. Berkeley.

Seed, H.B. (1967). "Soil stability problems caused by earthquakes," Soil Mech. and Bituminous Mat. Res. Lab., U.C. Berkeley, January.

Seed, H.B. and Idriss, I.M. (1970*). Soil moduli and damping factors for dynamic response analysis,* Rpt. No. UCB/EERC-70/10, U.C. Berkeley, December.

Seed, H.B., Idriss, I.M., Makdisi, F., and Banerjee, N. (1975). *Representation of irregular stress time histories by equivalent uniform stress series in liquefaction analyses,* Rpt. No. UCB/EERC-75/29, Earthquake Engrg. Research Ctr., U.C. Berkeley.

Seed, H.B., Mitchell, J.K., and Chan, C.K. (1960). " The strength of compacted cohesive soils," *in Shear Strength of Cohesive Soils*, ASCE, Boulder, CO. 877–964.

Seed, H.B. and Silver, M.L. (1972). "Settlement of dry sands during earthquakes," *J. Soil Mechanics and Foundations Div.*, ASCE, 98 (4): 381–97.

Seismic Safety Commission (SSC) (1995). *Northridge earthquake, turning loss to gain: Report to Governor Pete Wilson in response to governor's executive order W-78-94,* SSC Rpt. No. 95-1, Seismic Safety Commission, State of California, Sacramento.

Silva, W. (1986). *Soil response to earthquake ground motion,* Rpt. No. RP2556-07, Electrical Power Research Institute, Palo Alto, CA.

Silva, W.J., Darragh, R.B., Stark, C., Wong, I., Stepp, J.C., Schneider, J.F., and Chiou, S.-J. (1990). "A methodology to estimate design response spectra in the near-source region of large earthquake using the band-limited-white noise ground motion model," *Proceedings of the 4th U.S. National Conference on Earthquake Engineering*, Palm Springs, CA, May 20–24, Earthquake Engineering Research Institute, El Cerrito, CA, vol. 1, pp. 487–94.

Silver, M.L. and Seed, H.B. (1971). "Volume changes in sands due to cyclic loading," *J. Soil Mech. & Foundations Div.*, ASCE, 97(9): 1171–82.

Slosson, J.E. (1975). "Chapter 19: Effects of the earthquake on residential areas." *San Fernando, California, Earthquake of 9 February 1971*, Bulletin 196, California Division of Mines and Geology, Sacramento Calif.

Smith, P.M. (2002). "Documentation and analysis of field case histories of seismic compression during the 1994 Northridge, California earthquake," Ph.D. Dissertation, University of California, Los Angeles.

Somerville, P.G., Smith, N.F., Graves, R.W. and Abrahamson, N.A. (1997). "Modification of empirical strong ground motion attenuation relations to include the amplitude and duration effects of rupture directivity," *Seism. Research Letters*, 68 (1): 199–222.

Stewart, J.P., Bray, J.D., McMahon, D.J., Smith, P.M., and Kropp, A.L. (2001). "Seismic performance of hillside fills," *J. Geotech. & Geoenv. Engrg.*, ASCE, 127 (11): 905–19.

Stewart, J.P., Seed, R.B., and Bray, J.D. (1996). "Incidents of ground failure from the Northridge earthquake," *Bull. Seism. Soc. Am.*, 86(1B): S300–18.

Tokimatsu, K. and Seed, H.B. (1987) "Evaluation of settlements in sands due to earthquake shaking," *J. Geotech. Engrg.*, ASCE, 113(8): 861–78

Toro, G. R. (1997). *Probabilistic models of shear-wave velocity profiles at the Savannah River Site, South Carolina,* Report to Pacific Engineering and Analysis.

Vucetic, M. (1994). "Cyclic threshold shear strains in soils," *J. Geotech. Engrg.*, ASCE, 120(12): 2208–28.

Vucetic, M. and Dobry, R. (1991). "Effect of soil plasticity on cyclic response," *J. Geotech. Engrg.*, ASCE, 117(1): 89–107.

Wald, D.J. and Heaton, T.H. (1994). *A dislocation model of the 1994 Northridge, California, Earthquake determined from strong ground motions,* Open-File Report 94-278, U.S. Geological Survey.

Whang, D. (2001). "Seismic compression of compacted fills," Ph.D. Thesis, University of California, Los Angeles.

Youd, T.L. (1972). "Compaction of sands by repeated shear straining," *J. Soil Mech. & Foundations Div.*, ASCE, 98 (7): 709–25.

Appendix Borehole and CPT Logs

UCLA Dept. of Civil and Environmental Engineering

Sponsored by:
USGS/PEER

Project: Site A
Location: Santa Clarita, CA
Date: 03/26/1998
Field Log by: J. Stewart
Operator: Cascade Drilling
Water Table Elevation: Not encountered

Drilling Method: 8" Hollow Stem Auger
Drilling Equipment: CME85
Velocity Measurements: Law/Crandall
SPT System: Rope, pulley and cathead method. AWJ rods.
Hammer Type: Safety hammer
Notes: Boring B-1

Depth Scale (m)	Lithology	Description & Remarks	Sample Type and No.	Pitcher Tube Recovery Lth. (cm)	SPT (N)	Field Moisture (%)	Plasticity Index/ Liquid Limit	%Fines/%Clay	D10/D30/D60 (mm)	MP W_{opt}	MP γ_{dmax} (g/cm^3)
0		SM: Sand, medium to fine, silty, slightly clayey, brown, FILL				12.5	12/32	45/14	0.001/0.019/0.22		
			B-1 SH-1	61							
						14.4	10/29	43/12	0.001/0.033/0.33		
			B-2 SP-1		28	14.3	12/31	47/16	0.001/0.017/0.18	8.4	2.20
		CL: Clay, silty, sandy, brown, FILL	SH-2	61			13/32	53/17	0.001/0.010/0.13		
		Increasing rock fragments below 6.9 meters	B-3 SP-2		30		13/32	54/17	0.001/0.013/0.12		
			SH-3 B-4	23			15/32	54/17	0.001/0.010/0.13		
10			B-5 SP-3		54	14.3	15/34	53/20	0.001/0.009/0.13	8.6	2.15
			SP-4		73	10.0	15/33	55/18	0.001/0.010/0.12		
			B-6 SH-4	46							
			SP-5		38	12.3	16/34	57/17	0.001/0.009/0.10	8.4	2.18
			SH-5 B-7	46							
			SP-6		30	12.9	13/32	52/20	0.001/0.008/0.14		
			B-8 SH-6	46							
			SP-7		38	11.5	14/33	54/20	0.001/0.008/0.13		
			SH-7 B-9								

Shear Wave Velocity (m/s)

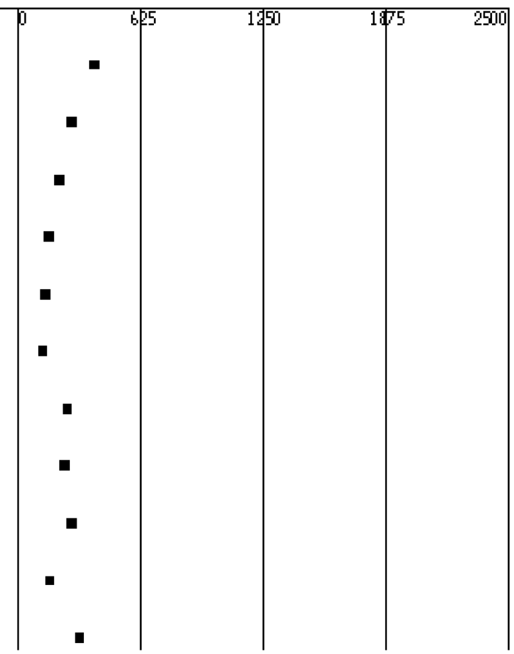

Legend SP: Spit Spoon (SPT) SH: Shelby tube P: Pitcher tube B: Bag Sample

Depth Scale (m)	Lithology	Description & Remarks	Sample Type and No.	Pitcher Tube Recovery Lth. (cm)	SPT (N)	Field Moisture (%)	Plasticity Index/ Liquid Limit	%Fines / %Clay	D10/D30/D60 (mm)	MP W_{opt}	MP $\gamma_{d\,max}$ (g/cm^3)
			SP-8	46	44	9.4	14/32	58/20	0.001/0.010/0.09	7.9	2.17
		SC: Sand, medium, clayey, brownish gray, FILL	B-10 SP-9		46	8.4	14/32	46/16	0.001/0.019/0.21		
20			B-11 SP-10		49	8.8	12/30	43/14	0.001/0.032/0.30	7.4	2.17
		ALLUVIUM: Clay, sandy, silty, brown	B-12 SP-11		36	7.9	10/31	49/16	0.001/0.015/0.15		
			B-13 SP-12		30	10.9	10/27	50/46	0.001/0.018/0.14		
			B-14 SP-13		27	11.3	12/31	51/18	0.001/0.010/0.13		
			B-15 SP-14		24	7.0	13/30	69/20	0.001/0.008/0.08		
			B-16 SP-15		27	4.0					
30			B-17								
			SP-16		61	14.4					
		SAUGUS BEDROCK, Claystone: Silty, sandy, weathered, severly fractured, caliche streaks	SP-17		83	16.4					
			SP-18		Ref.	12.8					
						10.5					

Shear Wave Velocity (m/s)

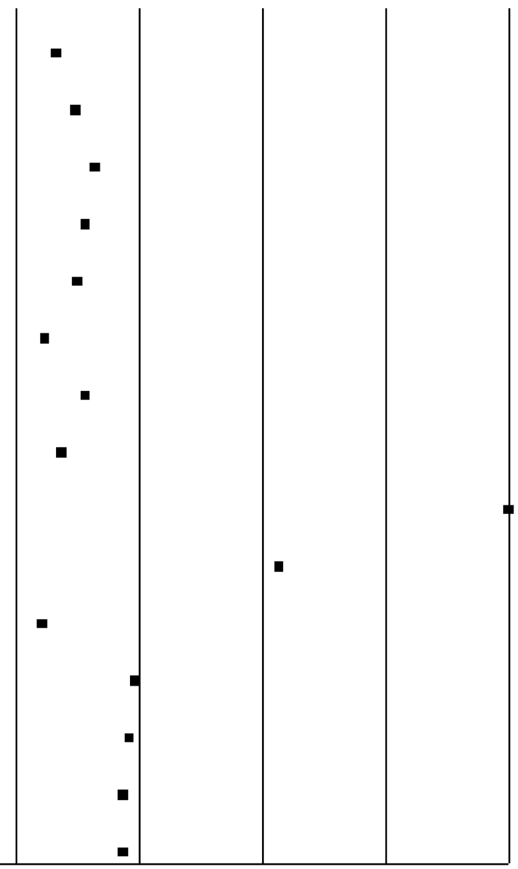

Legend SP: Spit Spoon (SPT) SH: Shelby tube P: Pitcher tube B: Bag Sample

UCLA Dept. of Civil and Environmental Engineering

Page 1 of 2

Sponsored by: USGS/PEER

Project: Site A
Location: Santa Clarita, CA
Date: 03/26/1998
Field Log by: J. Stewart
Operator: Cascade Drilling
Water Table Elevation: Not encountered

Drilling Method: 8" Hollow Stem Auger
Drilling Equipment: CME85
Velocity Measurements: Law/Crandall
SPT System: Rope, pulley and cathead method. AWJ rods.
Hammer Type: Safety hammer
Notes: Boring B-2

Depth Scale (m)	Description & Remarks	Sample Type and No.	Pitcher Tube Recovery Lth. (cm)	SPT (N)	Field Moisture (%)	Plasticity Index/ Liquid Limit	%Fines/%Clay	D10/D30/D60 (mm)	MP W_{opt}	MP γ_{dmax} (g/cm^3)
0	CL: Clay, silty, sandy, brown, FILL									
		B-1				11/31	51/14	0.001/0.019/0.18		
		SH-1	61						8.5	2.18
						11/31	49/13	0.001/0.019/0.17		
					14.0					
		B-2 SP-1		24						
		B-3				15/35	56/17	0.001/0.011/0.10		
		SH-2	46						9.7	2.15
		SP-4 B-4		19	15.8	14/33	58/14	0.001/0.018/0.09		
	Increasing rock fragments below 6.9 meters	B-5 SP-5		21	12.9	14/33	57/15	0.001/0.016/0.09		
					13.2					
10		SP-6		25						
		B-6			14.0	13/32	56/56	0.001/0.010/0.13		
		SP-7		22						
		B-7			15.3	14/33	55/16	0.001/0.017/0.10	9.3	2.11
	Becoming brownish gray below 12 meters	SP-8		28						
		B-8			9.6	14/33	53/15	0.001/0.012/0.10		
		SP-9		34						
		SP-10		40						
	SAUGUS BEDROCK, Claystone: Silty,	B-9			15.2	14/33	53/15	0.001/0.016/0.13		
									9.5	2.16

Shear Wave Velocity (m/s)

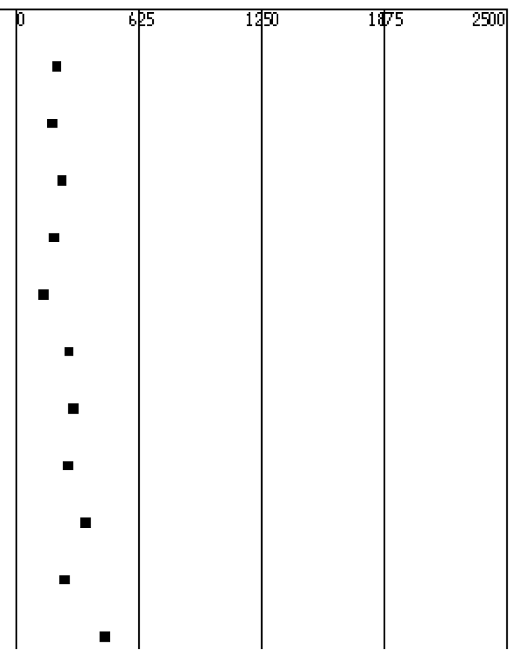

Legend SP: Spit Spoon (SPT) SH: Shelby tube P: Pitcher tube B: Bag Sample

Depth Scale (m)	Lithology	Description & Remarks	Sample Type and No.	Pitcher Tube Recovery Lth. (cm)	SPT (N)	Field Moisture (%)	Plasticity Index/ Liquid Limit	%Fines / %Clay	D10/D30/D60 (mm)	MP W_{opt}	MP $\gamma_{d\,max}$ (g/cm^3)	Shear Wave Velocity (m/s)
		sandy, weathered, severly fractured, caliche streaks	SP-11		Ref.	19.4						
20			SP-12		71	14.0	14/34	61/21	0.001/0.006/0.07			
			SP-13		Ref.							

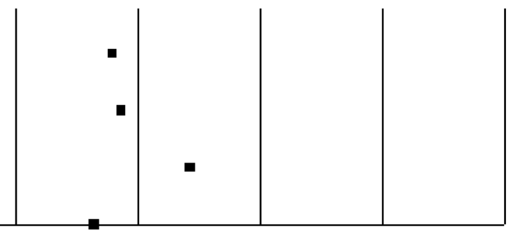

Legend SP: Spit Spoon (SPT) SH: Shelby tube P: Pitcher tube B: Bag Sample

UCLA Dept. of Civil and Environmental Engineering

Sponsored by:
USGS/PEER

Project: Site B
Location: Santa Clarita, CA
Date: 08/07/1998
Field Log by: J. Stewart
Operator: Pitcher Drilling
Water Table Elevation: Not encountered

Drilling Method: Rotary Wash
Drilling Equipment: Rotary Wash
Velocity Measurements: Geovision
SPT System: Rope, pulley and cathead method. AWJ rods.
Hammer Type: Safety hammer
Notes: Boring B-1

Depth Scale (m)	Lithology	Description & Remarks	Sample Type and No.	Pitcher Tube Recovery Lth. (cm)	SPT (N)	Field Moisture (%)	Plasticity Index/ Liquid Limit	%Fines/%Clay	D10/D30/D60 (mm)	MP W_{opt}	MP γ_{dmax} (g/cm^3)
0		SM/ML: Sand, silty, and silt, sandy. Gravels at intervals, mottled brown,. and brownish gray									
			SP-1		26	13.8	2/26	50/8	0.0025/0.031/0.14		
			SP-2		20						
			SP-3		32	12.6	2/26	44/6	0.0044/0.038/0.18		
			P-1	91			14/35	40/5	0.0031/0.030/0.14	8.3	2.07
			SP-4		34	13.9	9/33	50/5	0.0029/0.029/0.15		
			SP-5		29	14.4	6/29	52/6	0.0045/0.026/0.13		
			SP-6		55						
		Occasional cobble	P-2	61			9/30	48/4	0.0032/0.040/0.29	9.0	2.11
			P-3	91			2/27	44/10	0.0090/0.020/0.17	8.2	2.11
10			SP-7		68						
			SP-8		82	10.9	2/27	45/5	0.0050/0.034/0.18		
			SP-9		81						
			P-4	91						9.2	2.08
		Difficult drilling, significant gravel content at intervals	SP-10		60		4/27	52/2	0.0075/0.038/0.11		
			SP-11		76	13.2	5/28	45/5	0.0050/0.035/0.17		

Shear Wave Velocity (m/s)

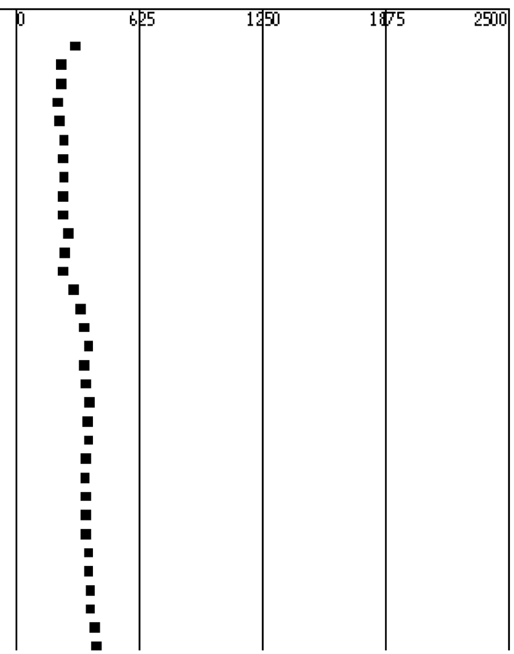

Legend SP: Spit Spoon (SPT) SH: Shelby tube P: Pitcher tube B: Bag Sample

Depth Scale (m)	Lithology	Description & Remarks	Sample Type and No.	Pitcher Tube Recovery Lth. (cm)	SPT (N)	Field Moisture (%)	Plasticity Index/ Liquid Limit	%Fines / %Clay	D10/D30/D60 (mm)	MP W_{opt}	MP $\gamma_{d\,max}$ (g/cm^3)
		Difficult drilling (gravels)	SP-12		>100						
			P-5	91							
20			SP-13		>100						
			SP-14		>100		5/27	46/5	0.0058/0.036/0.16		
			SP-15		>100	8.5	5/28	36/8	0.0034/0.046/0.21		
		SAUGUS BEDROCK: Sandstone and interbedded comglomerate, severly to compelety weathered, mottled, light olive brown									
30			SP-16		>100						
			SP-17		>100						
		Difficult drilling from 38-43m									
40											

Shear Wave Velocity (m/s)

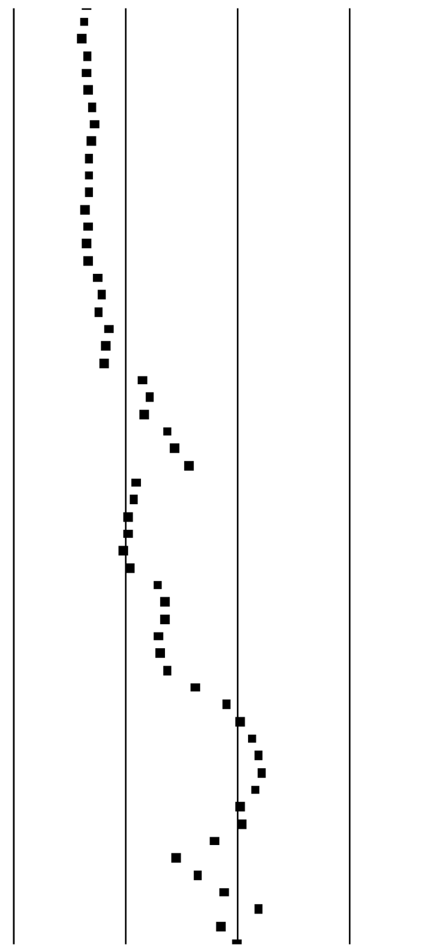

Depth Scale (m)	Lithology	Description & Remarks	Sample Type and No.	Pitcher Tube Recovery Lth. (cm)	SPT (N)	Field Moisture (%)	Plasticity Index/ Liquid Limit	%Fines / %Clay	D10/D30/D60 (mm)	MP W_{opt}	MP $\gamma_{d\,max}$ (g/cm^3)	Shear Wave Velocity (m/s)

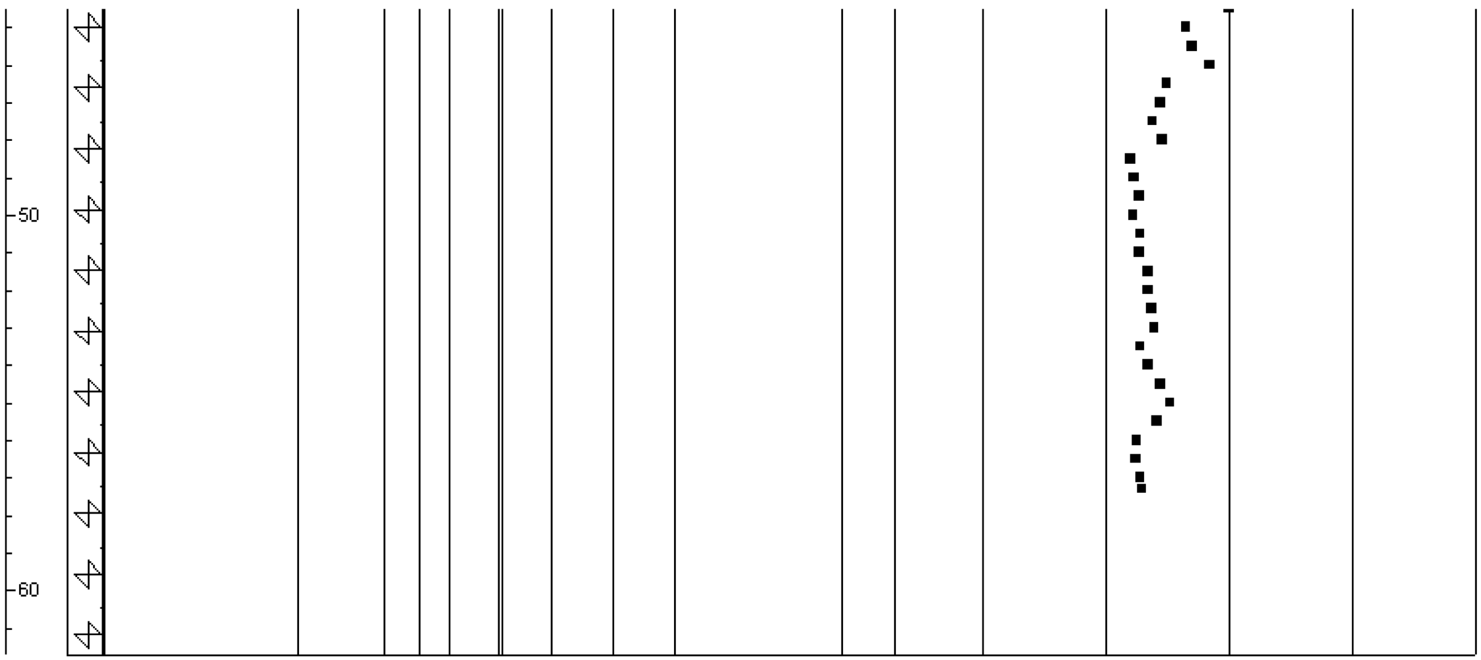

Legend SP: Spit Spoon (SPT) SH: Shelby tube P: Pitcher tube B: Bag Sample

UCLA	**Project Name:** Site A		**Page:** 1 of 1
	Location: Santa Clarita, California		
	GPS Coordinates: 33° 55' N, 118° 21' W		
	Test Number: SCPT-1	**Elevation:** Top of fill	
	Type of Cone: Electric	**Date:** June 23, 1997	
Sponsored by:	**File Name:** Cptlog.xls	**Water Table Elevation:** Not encountered	
USGS/PEER	**Operator:** Holguin Fahan & Associates	**Responsible Engineers:** Patrick Smith and Jonathan Stewart	
	Notes:		

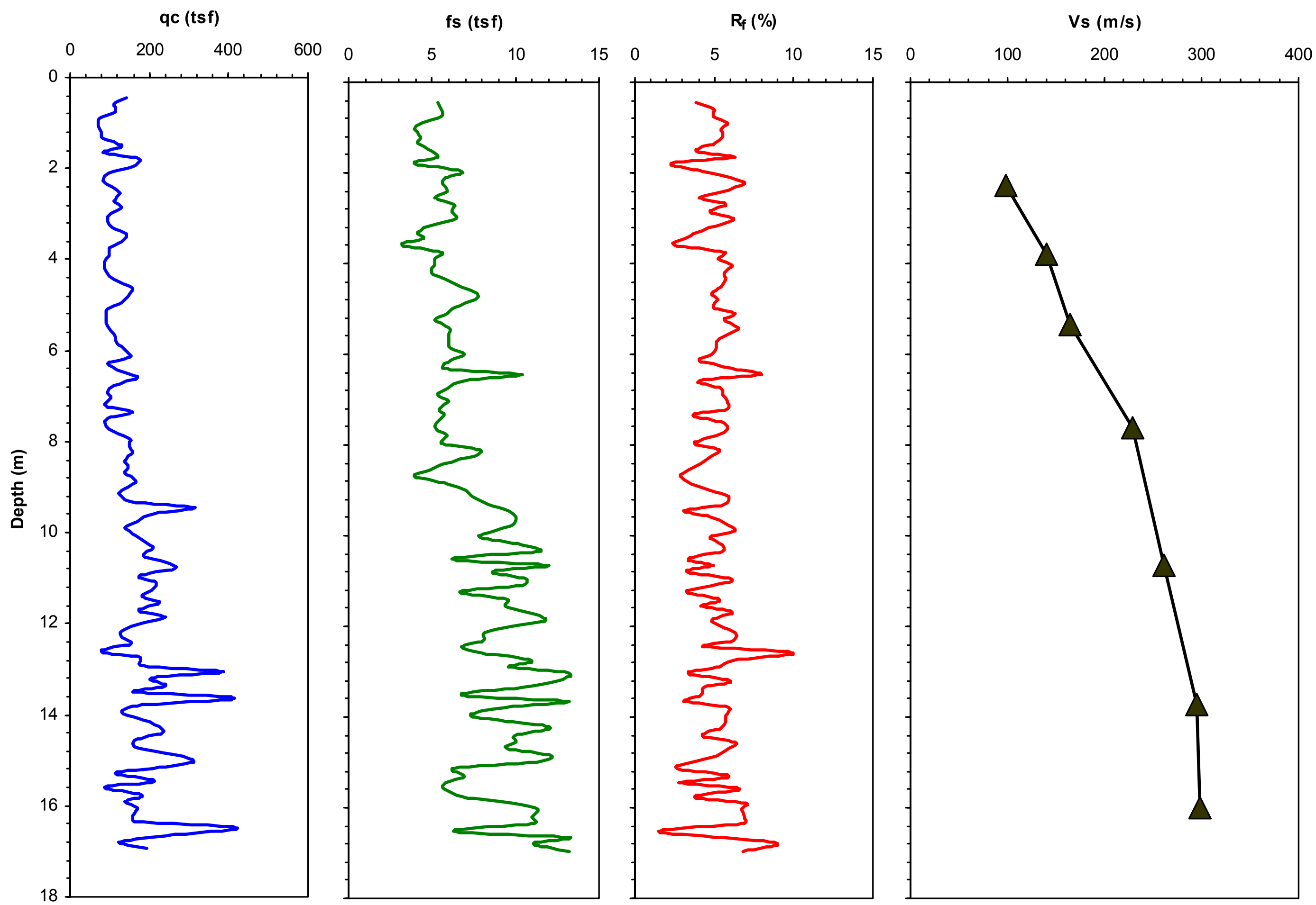

UCLA	**Project Name:** Site A		**Page:** 1 of 1
	Location: Santa Clarita, California		
	GPS Coordinates: 33° 55' N, 118° 21' W		
	Test Number: SCPT-2	**Elevation:** Top of fill	
	Type of Cone: Electric	**Date:** June 23, 1997	
Sponsored by:	**File Name:** Cptlog.xls	**Water Table Elevation:** Not encountered	
USGS/PEER	**Operator:** Holguin Fahan & Associates	**Responsible Engineers:** Patrick Smith and Jonathan Stewart	
	Notes:		

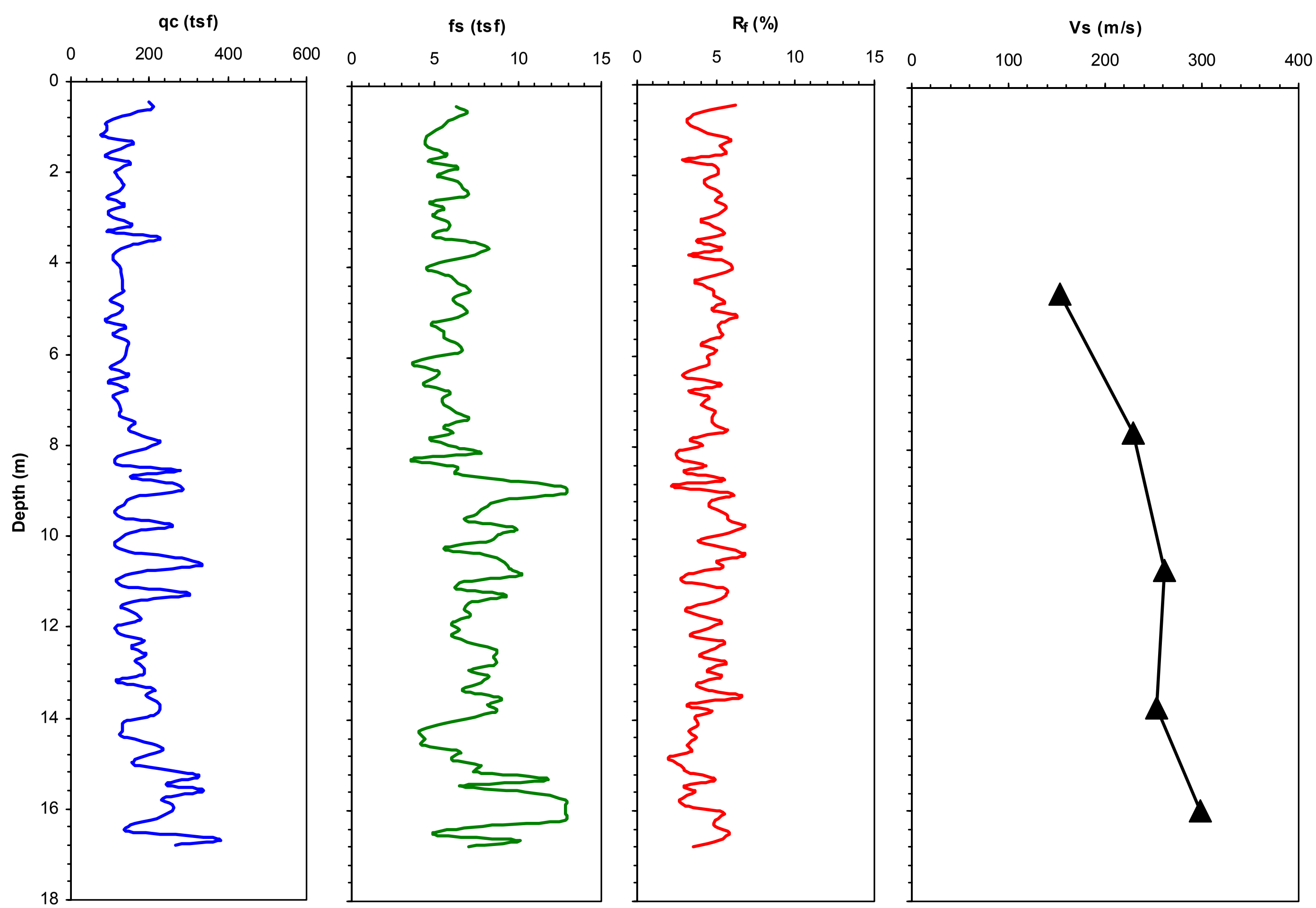

UCLA	**Project Name:** Site A		**Page:** 1 of 1
	Location: Santa Clarita, California		
	GPS Coordinates: 33° 55' N, 118° 21' W		
	Test Number: SCPT-3	**Elevation:** Top of fill	
	Type of Cone: Electric	**Date:** June 23, 1997	
Sponsored by:	**File Name:** Cptlog.xls	**Water Table Elevation:** Not encountered	
USGS/PEER	**Operator:** Holguin Fahan & Associates	**Responsible Engineers:** Patrick Smith and Jonathan Stewart	
	Notes:		

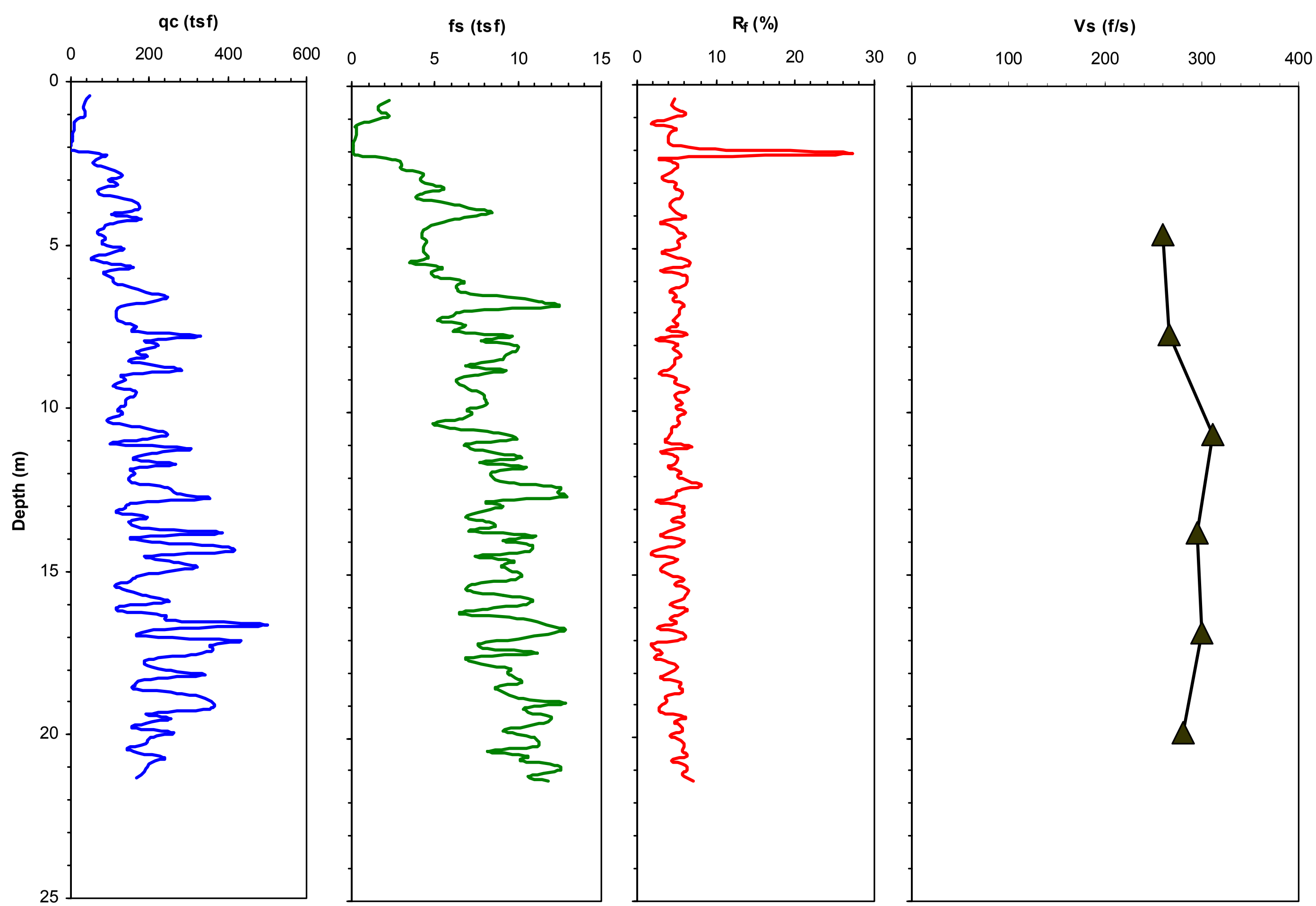

UCLA	**Project Name:** Site B		**Page:** 1 of 1
	Location: Santa Clarita, California		
	GPS Coordinates: 33° 55' N, 118° 21' W		
	Test Number: SCPT-1	**Elevation:** Top of Fill	
	Type of Cone: Electric	**Date:** August 08, 1998	
Sponsored by:	**File Name:** Cptlog.xls	**Water Table Elevation:** Not encountered	
USGS/PEER	**Operator:** Gregg InSitu	**Responsible Engineers:** Patrick Smith and Jonathan Stewart	
	Notes:		

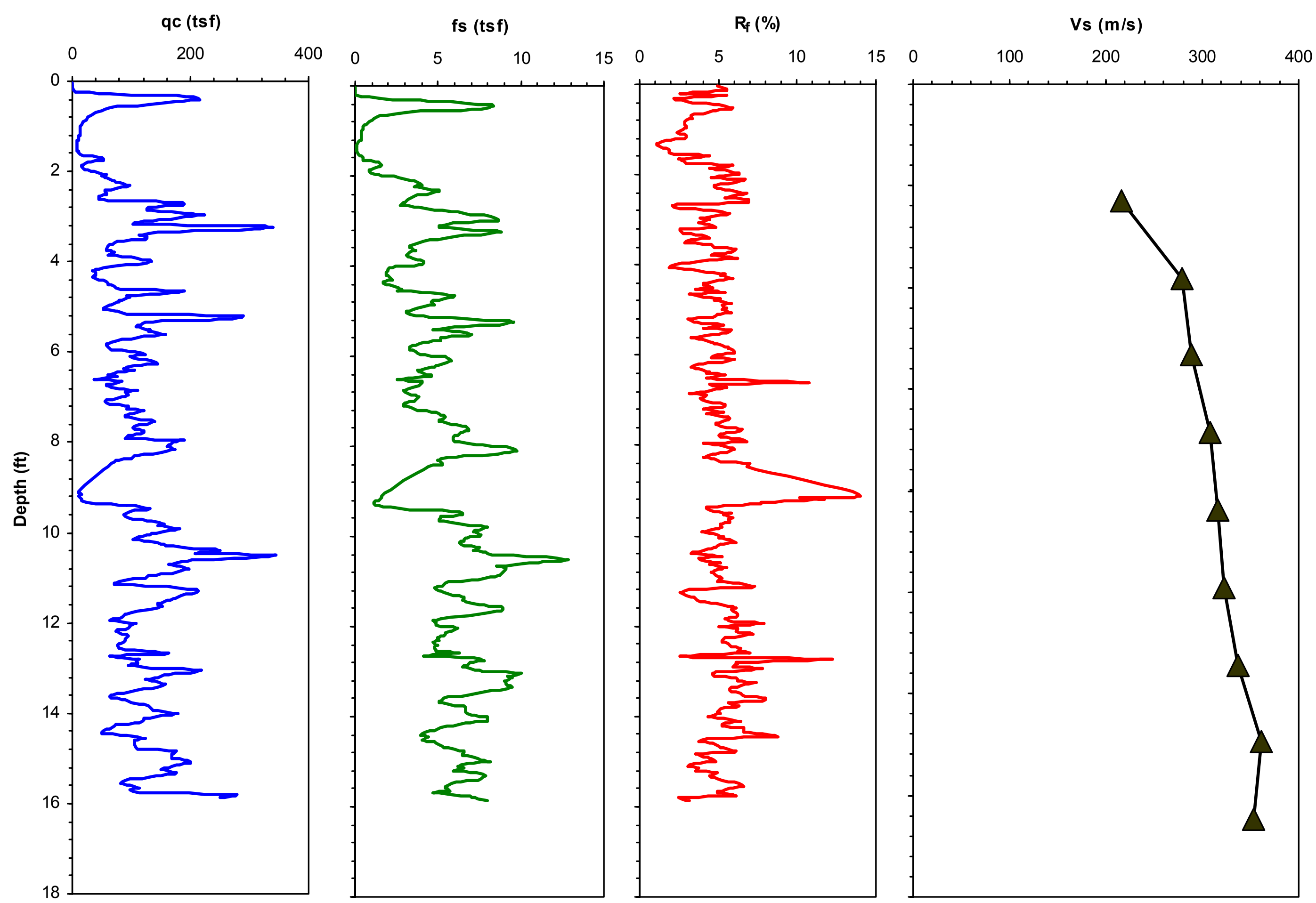

UCLA	**Project Name:** Site B		**Page:** 1 of 1
	Location: Santa Clarita, California		
	GPS Coordinates: 33° 55' N, 118° 21' W		
	Test Number: SCPT-2	**Elevation:** Top of Fill	
	Type of Cone: Electric	**Date:** August 08, 1998	
Sponsored by:	**File Name:** Cptlog.xls	**Water Table Elevation:** Not encountered	
USGS/PEER	**Operator:** Gregg InSitu	**Responsible Engineers:** Patrick Smith and Jonthan Stewart	
	Notes:		

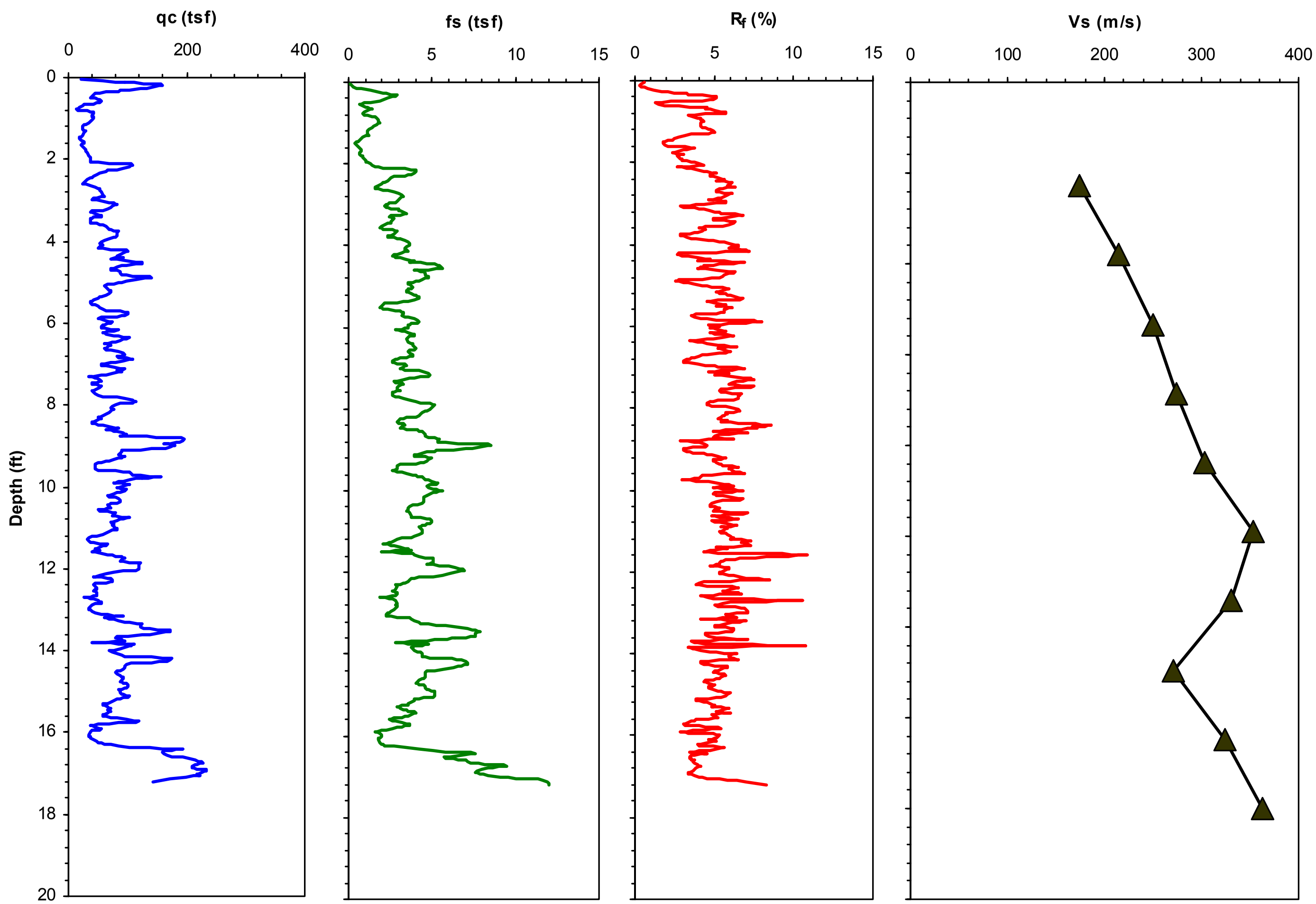

PEER REPORTS

PEER reports are available from the National Information Service for Earthquake Engineering (NISEE). To order PEER reports, please contact the Pacific Earthquake Engineering Research Center, 1301 South 46th Street, Richmond, California 94804-4698. Tel.: (510) 231-9468; Fax: (510) 231-9461.

PEER 2002/13 *Probabilistic Models and Fragility Estimates for Bridge Components and Systems.* Paolo Gardoni, Armen Der Kiureghian, and Khalid M. Mosalam. June 2002.

PEER 2002/11 *Analytical and Experimental Study of Fiber-Reinforced Strip Isolators.* James M. Kelly and Shakhzod M. Takhirov. September 2002.

PEER 2002/09 *Documentation and Analysis of Field Case Histories of Seismic Compression during the 1994 Northridge, California, Earthquake.* Jonathan P. Stewart, Patrick M. Smith, Daniel H. Whang, and Jonathan D. Bray. October 2002.

PEER 2002/08 *Component Testing, Stability Analysis and Characterization of Buckling-Restrained Unbonded Braces™.* Cameron Black, Nicos Makris, and Ian Aiken. September 2002.

PEER 2002/07 *Seismic Performance of Pile-Wharf Connections.* Charles W. Roeder, Robert Graff, Jennifer Soderstrom, and Jun Han Yoo. December 2001.

PEER 2002/06 *The Use of Benefit-Cost Analysis for Evaluation of Performance-Based Earthquake Engineering Decisions*. Richard O. Zerbe and Anthony Falit-Baiamonte. September 2001.

PEER 2002/05 *Guidelines, Specifications, and Seismic Performance Characterization of Nonstructural Building Components and Equipment*. André Filiatrault, Constantin Christopoulos, and Christopher Stearns. September 2001.

PEER 2002/03 *Investigation of Sensitivity of Building Loss Estimates to Major Uncertain Variables for the Van Nuys Testbed.* Keith A. Porter, James L. Beck, and Rustem V. Shaikhutdinov. August 2002.

PEER 2002/02 *The Third U.S.-Japan Workshop on Performance-Based Earthquake Engineering Methodology for Reinforced Concrete Building Structures*. July 2002.

PEER 2002/01 *Nonstructural Loss Estimation: The UC Berkeley Case Study. Mary C. Comerio and John C. Stallmeyer.* December 2001.

PEER 2001/16 *Statistics of SDF-System Estimate of Roof Displacement for Pushover Analysis of Buildings.* Anil K. Chopra, Rakesh K. Goel, and Chatpan Chintanapakdee. December 2001.

PEER 2001/15 *Damage to Bridges during the 2001 Nisqually Earthquake.* R. Tyler Ranf, Marc O. Eberhard, and Michael P. Berry. November 2001.

PEER 2001/14 *Rocking Response of Equipment Anchored to a Base Foundation.* Nicos Makris and Cameron J. Black. September 2001.

PEER 2001/13 *Modeling Soil Liquefaction Hazards for Performance-Based Earthquake Engineering.* Steven L. Kramer and Ahmed-W. Elgamal. February 2001.

PEER 2001/12 *Development of Geotechnical Capabilities in OpenSees.* Boris Jeremic. September 2001.

PEER 2001/11 *Analytical and Experimental Study of Fiber-Reinforced Elastomeric Isolators*. James M. Kelly and Shakhzod M. Takhirov. September 2001.

PEER 2001/10 *Amplification Factors for Spectral Acceleration in Active Regions.* Jonathan P. Stewart, Andrew H. Liu, Yoojoong Choi, and Mehmet B. Baturay. December 2001.

PEER 2001/09 *Ground Motion Evaluation Procedures for Performance-Based Design.* Jonathan P. Stewart, Shyh-Jeng Chiou, Jonathan D. Bray, Robert W. Graves, Paul G. Somerville, and Norman A. Abrahamson. September 2001.

PEER 2001/08 *Experimental and Computational Evaluation of Reinforced Concrete Bridge Beam-Column Connections for Seismic Performance*. Clay J. Naito, Jack P. Moehle, and Khalid M. Mosalam. Nover

PEER 2001/07 *The Rocking Spectrum and the Shortcomings of Design Guidelines.* Nicos Makris and Dimitrios Konstantinidis. August 2001.

PEER 2001/06 *Development of an Electrical Substation Equipment Performance Database for Evaluation of Equipment Fragilities*. Thalia Agnanos. April 1999.

PEER 2001/05 *Stiffness Analysis of Fiber-Reinforced Elastomeric Isolators.* Hsiang-Chuan Tsai and James M. Kelly. May 2001.

PEER 2001/04 *Organizational and Societal Considerations for Performance-Based Earthquake Engineering.* Peter J. May. April 2001.

PEER 2001/03 *A Modal Pushover Analysis Procedure to Estimate Seismic Demands for Buildings: Theory and Preliminary Evaluation.* Anil K. Chopra and Rakesh K. Goel. January 2001.

PEER 2001/02 *Seismic Response Analysis of Highway Overcrossings Including Soil-Structure Interaction.* Jian Zhang and Nicos Makris. March 2001.

PEER 2001/01 *Experimental Study of Large Seismic Steel Beam-to-Column Connections.* Egor P. Popov and Shakhzod M. Takhirov. November 2000.

PEER 2000/10 *The Second U.S.-Japan Workshop on Performance-Based Earthquake Engineering Methodology for Reinforced Concrete Building Structures.* March 2000.

PEER 2000/09 *Structural Engineering Reconnaissance of the August 17, 1999 Earthquake: Kocaeli (Izmit), Turkey.* Halil Sezen, Kenneth J. Elwood, Andrew S. Whittaker, Khalid Mosalam, John J. Wallace, and John F. Stanton. December 2000.

PEER 2000/08 *Behavior of Reinforced Concrete Bridge Columns Having Varying Aspect Ratios and Varying Lengths of Confinement.* Anthony J. Calderone, Dawn E. Lehman, and Jack P. Moehle. January 2001.

PEER 2000/07 *Cover-Plate and Flange-Plate Reinforced Steel Moment-Resisting Connections.* Taejin Kim, Andrew S. Whittaker, Amir S. Gilani, Vitelmo V. Bertero, and Shakhzod M. Takhirov. September 2000.

PEER 2000/06 *Seismic Evaluation and Analysis of 230-kV Disconnect Switches.* Amir S. J. Gilani, Andrew S. Whittaker, Gregory L. Fenves, Chun-Hao Chen, Henry Ho, and Eric Fujisaki. July 2000.

PEER 2000/05 *Performance-Based Evaluation of Exterior Reinforced Concrete Building Joints for Seismic Excitation.* Chandra Clyde, Chris P. Pantelides, and Lawrence D. Reaveley. July 2000.

PEER 2000/04 *An Evaluation of Seismic Energy Demand: An Attenuation Approach.* Chung-Che Chou and Chia-Ming Uang. July 1999.

PEER 2000/03 *Framing Earthquake Retrofitting Decisions: The Case of Hillside Homes in Los Angeles.* Detlof von Winterfeldt, Nels Roselund, and Alicia Kitsuse. March 2000.

PEER 2000/02 *U.S.-Japan Workshop on the Effects of Near-Field Earthquake Shaking.* Andrew Whittaker, ed. July 2000.

PEER 2000/01 *Further Studies on Seismic Interaction in Interconnected Electrical Substation Equipment.* Armen Der Kiureghian, Kee-Jeung Hong, and Jerome L. Sackman. November 1999.

PEER 1999/14 *Seismic Evaluation and Retrofit of 230-kV Porcelain Transformer Bushings*. Amir S. Gilani, Andrew S. Whittaker, Gregory L. Fenves, and Eric Fujisaki. December 1999.

PEER 1999/13 *Building Vulnerability Studies: Modeling and Evaluation of Tilt-up and Steel Reinforced Concrete Buildings.* John W. Wallace, Jonathan P. Stewart, and Andrew S. Whittaker, editors. December 1999.

PEER 1999/12 *Rehabilitation of Nonductile RC Frame Building Using Encasement Plates and Energy-Dissipating Devices.* Mehrdad Sasani, Vitelmo V. Bertero, James C. Anderson. December 1999.

PEER 1999/11 *Performance Evaluation Database for Concrete Bridge Components and Systems under Simulated Seismic Loads.* Yael D. Hose and Frieder Seible. November 1999.

PEER 1999/10 *U.S.-Japan Workshop on Performance-Based Earthquake Engineering Methodology for Reinforced Concrete Building Structures.* December 1999.

PEER 1999/09 *Performance Improvement of Long Period Building Structures Subjected to Severe Pulse-Type Ground Motions*. James C. Anderson, Vitelmo V. Bertero, and Raul Bertero. October 1999.

PEER 1999/08 *Envelopes for Seismic Response Vectors.* Charles Menun and Armen Der Kiureghian. July 1999.

PEER 1999/07 *Documentation of Strengths and Weaknesses of Current Computer Analysis Methods for Seismic Performance of Reinforced Concrete Members.* William F. Cofer. November 1999.

PEER 1999/06 *Rocking Response and Overturning of Anchored Equipment under Seismic Excitations.* Nicos Makris and Jian Zhang. November 1999.

PEER 1999/05 *Seismic Evaluation of 550 kV Porcelain Transformer Bushings.* Amir S. Gilani, Andrew S. Whittaker, Gregory L. Fenves, and Eric Fujisaki. October 1999.

PEER 1999/04 *Adoption and Enforcement of Earthquake Risk-Reduction Measures.* Peter J. May, Raymond J. Burby, T. Jens Feeley, and Robert Wood.

PEER 1999/03 *Task 3 Characterization of Site Response General Site Categories*. Adrian Rodriguez-Marek, Jonathan D. Bray, and Norman Abrahamson. February 1999.

PEER 1999/02 *Capacity-Demand-Diagram Methods for Estimating Seismic Deformation of Inelastic Structures: SDF Systems*. Anil K. Chopra and Rakesh Goel. April 1999.

PEER 1999/01 *Interaction in Interconnected Electrical Substation Equipment Subjected to Earthquake Ground Motions.* Armen Der Kiureghian, Jerome L. Sackman, and Kee-Jeung Hong. February 1999.

PEER 1998/08 *Behavior and Failure Analysis of a Multiple-Frame Highway Bridge in the 1994 Northridge Earthquake.* Gregory L. Fenves and Michael Ellery. December 1998.

PEER 1998/07 *Empirical Evaluation of Inertial Soil-Structure Interaction Effects.* Jonathan P. Stewart, Raymond B. Seed, and Gregory L. Fenves. November 1998.

PEER 1998/06 *Effect of Damping Mechanisms on the Response of Seismic Isolated Structures.* Nicos Makris and Shih-Po Chang. November 1998.

PEER 1998/05 *Rocking Response and Overturning of Equipment under Horizontal Pulse-Type Motions.* Nicos Makris and Yiannis Roussos. October 1998.

PEER 1998/04 *Pacific Earthquake Engineering Research Invitational Workshop Proceedings, May 14–15, 1998: Defining the Links between Planning, Policy Analysis, Economics and Earthquake Engineering.* Mary Comerio and Peter Gordon. September 1998.

PEER 1998/03 *Repair/Upgrade Procedures for Welded Beam to Column Connections.* James C. Anderson and Xiaojing Duan. May 1998.

PEER 1998/02 *Seismic Evaluation of 196 kV Porcelain Transformer Bushings.* Amir S. Gilani, Juan W. Chavez, Gregory L. Fenves, and Andrew S. Whittaker. May 1998.

PEER 1998/01 *Seismic Performance of Well-Confined Concrete Bridge Columns.* Dawn E. Lehman and Jack P. Moehle. December 2000.